WEAR OF LOW ALLOY STEELS

AT

ELEVATED TEMPERATURES

BY

SUKDEV SINGH ATHWAL, B.Sc., M.Sc.

A thesis submitted for the degree of

DOCTOR OF PHILOSOPHY

THE UNIVERSITY OF ASTON IN BIRMINGHAM

JANUARY 1983

* * *

D E D I C A T E D T O

M Y

L A T E B R O T H E R - I N - L A W

M O H I N D E R

A N D

T O M Y

B E L O V E D P A R E N T S

* * *

WEAR OF LOW ALLOY STEELS AT ELEVATED TEMPERATURES

By SUKDEV SINGH ATHWAL

A thesis submitted for the degree of

DOCTOR OF PHILOSOPHY

1983

Summary

A pin on disc wear machine was used to study the wear behaviour of EN8 and EN31 low alloy steels at various loads and at disc temperatures ranging from room temperature to 500°C. Wear rate, frictional force and temperatures of the pin and disc were continuously monitored during each test. The wear debris and worn samples were examined using x-ray diffraction techniques for the identification of compounds produced by the wear process. Scanning electron microscopy of worn samples provided not only valuable topographical information but also a direct measurement of the thickness of surface oxide films. Auger electron spectroscopy was employed to study oxygen and iron concentration depth profiles on some selected worn pin surfaces.

Under all loads and temperature conditions the mechanism which was prevalent in the wear process was mild oxidational wear. It was found that transitions occur in the wear rate versus load curves at certain critical loads, the magnitude of which increase with temperature. These transitions were found to be associated with change in surface oxide, lower wear rates being recorded when the predominant oxide was the spinel Fe_3O_4. At disc temperatures above 300°C out of contact oxidation appears to be the most important wear limiting factor.

A method was developed enabling contact temperature, numbers and size of contacts and critical oxide film thickness to be deduced from direct measurements of heat flow into the pin. Remarkable agreement was found between oxide thicknesses estimated from this method and measured values using a scanning electron microscope.

Wear/Friction/Low Alloy Steels/Oxidation

A C K N O W L E D G E M E N T S

I am greatly indebted to my supervisor, Mr. J.L. Sullivan, for his continued advice and encouragement during the work contained in this thesis. Thanks are due to Drs. T.F.J. Quinn and D.M. Rowson for their comments and suggestions. Thanks are also due to my colleague, Dr. C.B. Allen, for the many helpful discussions we had during the course of this work.

I am grateful to Messrs. H. Arrowsmith, C.J. Chapman and A. Abbot for their technical assistance. I wish to thank Professor S.E. Hunt for providing the laboratory facilities. Gratitude is also extended to the Metallurgy and Production Engineering Departments for the liberal use of facilities.

The financial support of the Science Research Council is gratefully acknowledged.

My special thanks to Mrs. Susan Glendon, Miss Manjit Seera and Miss Surbjit Basi for their help in the preparation of this thesis.

Finally, I would like to express my deepest gratitude to my family for their moral support, and my fiancee for her patience, understanding and continued encouragement.

CONTENTS

FIGURES

Figures (Cont.)

Figures (Cont.)

Figures (Cont.)

Figures (Cont.)

Figures (Cont.)

Figures (Cont.)

TABLES

Tables (Cont.)

Tables (Cont.)

CHAPTER 1

INTRODUCTION

1.1 Background to the problem

Wear has been a subject of practical interest for at least a thousand years. But because of the inherent difficulties and complications of the subject, most of the wear studies have been carried out over the last few decades when fairly sophisticated techniques have been applied to the subject. Wear may be defined as the removal of material from solid surfaces as a result of mechanical action. The rate at which material is removed will depend upon large number of variables. A list of these variables which are known to be important are given in Table 1.1.

Changes in these variables can cause considerable variations in the wear rates of rubbing surfaces. So, it is not surprising that early wear studies revealed that wear rates found with common engineering materials under unlubricated conditions can cover a range of approximately 10^5 while the coefficient of friction covers a range of only 3, and high values of wear rates are not necessarily associated with high values of friction. Archard(1) offers an explanation to why wear rates can vary over a very wide range, while coefficients of friction show little variation. He suggests that while every asperity encounter contributes to the frictional force, only a fraction K results in the formation of a wear particle. K is the probability factor. In other words, only one encounter in $^1/_K$ total encounters will produce a wear particle. The value of K will vary according to different combination of sliding materials and for different conditions of rubbing. Values of wear rates, coefficients of friction and K for various sliding combinations are shown in Table 1.2.

TEMPERATURE	ATOMSPHERE
LOAD	MATERIAL PROPERTIES
VELOCITY	TYPES OF LUBRICATION
CONTACT AREA	FINISH
SLIDING DISTANCE	TYPES OF MOTION

TABLE 1.1 Wear Variables

Materials	Wear Rate $X10^{-10}$ $cm^3 cm^{-1}$	μ	K
1. Mild Steel on itself	1570	0.62	$7.0x10^{-3}$
2. 60/40 Leaded Brass	240	0.24	$6.0x10^{-4}$
3. PTFE	20	0.18	$2.5x10^{-5}$
4. Stellite	3.2	0.60	$5.5x10^{-5}$
5. Ferritic Stainless Steel	2.7	0.53	$1.7x10^{-5}$
6. Polyethylene	0.3	0.65	$1.3x10^{-7}$
7. Tungsten Carbide on itself	0.02	0.35	$1.0x10^{-6}$

TABLE 1.2 Wear Rates, Coefficient of Friction and K-Values from Pin on Ring Tests. Rings are hardened Tool Steel except in Tests 1 and 7. Load 400gm; Speed 180cm/sec (90).

As technology progresses, many mechanical systems are required to operate at high temperatures and under unlubricated (dry wear) conditions of continuous sliding, e.g. in Nuclear Power and Aerospace applications. Though there has been a marked increase in the amount of research devoted to investigating the dry wear of materials, very little has been concerned with wear at elevated temperatures. Consequently there is an increasing demand for experimental data on friction and wear behaviour of materials, in particular of steels because of its technological importance, at elevated temperatures. The aim of the present research was to investigate the unlubricated sliding wear of two low-alloy steels (EN8 and EN31) at elevated temperature using a pin-on-disc machine.

1.2 Characterisation of Wear of Metals

As a broad classification, Archard and Hirst (2) proposed that wear of metals could be divided into two types which were called "mild wear" and "severe wear". Severe wear is characterised by intermetallic contact, large scale damage to the surfaces and production of loose metallic particles up to a fraction of a millimeter or so in size. In mild wear the surfaces become smooth and are usually protected by surface layers generated during rubbing. The wear debris consists of small particles of the oxide.

Although this classification of wear has been quite widely adopted, it has been criticised as being arbitrary. The alternative is to classify wear in terms of the mechanism by which material is removed, but the problem here is to decide what the mechanism is. Kragelskii (3) suggests that the proper classification should be based upon the way the junctions are broken; that is, elastic displacement, plastic displacement, cutting, destruction of surface films, and destruction of bulk material. On the other hand, Peterson (4) suggests that the classification should be based upon how the particle is removed and whether the event takes place at

the asperity level, in bulk, or via a surface film. The following methods of removal were suggested: adhesion and shear of junctions, surface fracture or break up, fatigue, cutting, melting, reactions, plastic deformation, scraping loose reaction products and tearing.

In his excellent 'Survey of Possible Wear Mechanisms', Burwell (5) lists four mechanisms, namely:

(a) Adhesive (or severe) wear;
(b) Corrosive (or mild or oxidational) wear;
(c) Abrasive wear;
(d) Surface fatigue.

He also includes a fifth classification under the heading 'Minor Types' of wear, which covers erosion, cavitation and impact chipping. In the sub-sections that follow we shall consider each one of these four mechanisms separately. In Section 1.2.5 another wear phenomena, known as fretting, will be considered which arises due to a combination of the above mechanisms.

1.2.1 Adhesive Wear

Adhesive wear occurs when surfaces slide against each other, and the pressure between the contacting asperities is high enough to cause local plastic deformation and adhesion (6). Adhesive forces between surfaces arise from atomic attraction and result in local cold welding of neighbouring asperities. Adhesion is favoured by clean surfaces and non-oxidising condition (7). Adhesion occurs between a few asperities which increase in size as motion continues. Eventually the junctions rupture at their weakest point, usually resulting in metal transfer from one surface to the other (8). These transferred particles may be transferred back to the original surface, or else come off the surface to form loose wear particles. Very severe adhesive wear resulting in gross surface damage is known as "scuffing".

1.2.2 Corrosive Wear

Corrosive wear is a form of chemical wear which results from the interaction of the environment with sliding surfaces, followed by the rubbing off of the products of the reaction. If the environment is "hostile" (e.g. liquid sodium), then one has a form of wear which proceeds rapidly and truly is "corrosive". If however, the environment is the normal atmosphere, it is possible to obtain a mild form of corrosive wear known as oxidational wear (9, 10).

In oxidational wear the reaction products are oxides. For a wide range of material combinations and environments, the oxide films present on the surface are sufficient to prevent intermetallic contact and hence reduce friction and wear. In these circumstances the rate of removal of oxide achieves an equilibrium with the rate of regeneration of the film by oxidation at the surface. Thus, oxidational wear will occur when the oxidation rate at the surface is sufficient to maintain a protective oxide film between the interacting asperities.

1.2.3 Abrasive Wear

The term 'abrasive wear' covers two types of situation. In both cases wear is occasioned by the ploughing out of softer material by a harder surface. In the first instance, known as 2 body abrasion, a rough hard surface slides against a softer surface (11). In the second case, known as 3 body abrasion, abrasion is caused by loose hard particles sliding between rubbing surfaces (12). During abrasive wear smooth surfaces become roughened with fairly regular grooves. This type of damage is usually described as scratching, scoring or gouging, the difference being mainly in the degree of severity. The presence of hard oxides can increase abrasive wear. Burwell (5) suggested that abrasive wear occurs most readily when the abrasive particles are sharp rather than rounded and when the abrasive material is significantly harder than the abraded material.

1.2.4 Surface Fatigue Wear

This form of wear is observed during repeated sliding or rolling over a track. The repeated loading and unloading cycles to which the materials are exposed may induce the formation of surface and subsurface cracks, which eventually will result in a break-up of the surface with the formation of large fragments ($\sim 100 \mu m$ in size) leaving large pits in the surface (13,14). Surface fatigue wear does not occur in a system in which other forms of wear are occurring since these other forms of wear will continuously remove surface material before it has a chance to become fatigued. Only in cases of rolling contact (e.g. ball bearings or gears), in which cases other forms of wear are very low, does fatigue wear occur.

Kragelskii (3) attaches much importance to this mode of wear, as is implied by his definition of wear, given earlier in this chapter. He interprets many of his results and those of other investigators in terms of fatigue. Archard and Hirst (2) have suggested that the metal transferred by adhesion is finally detached by a fatigue process. Oxidational wear is also likely to be due finally to a surface fatigue process.

1.2.5 Fretting Wear

Fretting can be considered as a form of wear which occurs when wear mechanisms act together under conditions of small oscillatory displacement (15). This is a common occurrence, since most machinery is subjected to vibration, both in transit and in operation. Because of the oscillating small amplitude motion ($130 \mu m$) the surfaces are never brought out of contact and therefore there is little opportunity for the wear debris to escape. Most commonly, fretting is combined with corrosion in which case the wear is known as fretting corrosion (16). In air the corrosion product is oxide. Since many commonly occurring films, notably iron oxides, are abrasive, the trapped oxide particles can cause

abrasive wear of the surface. Fretting wear of steels at high temperatures (17,18) has received much attention these days since this type of wear is likely to be encountered in the nuclear power stations.

1.3 General Studies of Unlubricated Wear

In 1930, Fink (19) published the first paper in which oxidation was identified as a new component in the unlubricated wear of steels. Rosenberg and Jordan (20) in 1934 suggested that the oxide film which forms on the surface while sliding in air is able to prevent severe wear of steel of any hardness, while the comparatively thin layer formed in nominally oxygen-free atmosphere is protective only when the substrate hardness is sufficiently high. In other earlier work by Mailander and Dies (21,22) and Siebel and co-workers (23), the complicated wear behaviour of steels was studied and attempts were made to account for changes in the magnitude and character of wear with changes in load and speed.

The most notable early work in the study of wear was that of Raynar Holm (24). He showed that when the wear rate was expressed as the volume removed per unit sliding distance (which has dimensions of an area) the severity of the wear rate might be assessed by comparing it with the true area of contact.

The wear of a steel pin rubbing on a flat steel disc under a chemically inert lubricant was studied by Burwell and Strang (25). They found that, in general, the rate of wear was proportional to the load and independent of the area of apparent contact. However, when the pressure over the apparent area of contact approached a value of one-third of the hardness (P_m), the wear rate then increased rapidly to a high value. It was found that at these higher loadings, large scale welding and seizure occur. Burwell and Strang suggest that as pressure approaches a value of $P_m/3$ the plastic zones

under individual asperities begin to interact causing the whole surface to become plastic so that the real area of contact is no longer proportional to load. This could result in an increased area of contact and a lowering of the shear strength of the peaks.

Archard (1) and Archard and Hirst (2) studied the wear of a wide range of material combinations (mainly metallic materials) under unlubricated condition. They found that each wear test began with a period of changing wear rate then became constant and independent of the apparent area of contact. For most of the materials the relation between wear rate and load was close to direct proportionality. From their comprehensive series of wear tests, Archard and Hirst(2) proposed that wear of metals could be divided into two types which were called "mild" wear and "severe" wear.

Both Burwell and Strang (25) and also Archard and Hirst(2) drew upon the earlier work of Holm (24) and the studies of friction by Bowden and Tabor (6) to provide an explanation of their results. It was assumed that the magnitude of wear was related to the true area of contact.

The pioneer study of transfer between sliding surfaces was made in 1951 by Rabinowicz and Tabor (8) using radioactive tracers. They showed that transfer consisted of discrete particles and that the volume of transferred material per unit sliding distance was approximately proportional to the load. The presence of discrete transfer particles confirmed Bowden and Tabor's (6) contention that welded junctions are formed between solids in contact. They also revealed the important distinction between wear and transfer. In most wear studies, one is concerned with the removal of material from both rubbing surfaces. Transfer implies a stronger bond between the transferred fragment and the surface to which it adheres than that which exists between the fragment and its parent body. The mechanisms by which loose particles are produced were thus shown to require more detailed study.

Rabinowicz (26) extended the radiographic method to obtain estimates of the size distribution of transferred particles. He then argued that these sizes (of the order of 10^{-5}m diameter) would be comparable with the sizes of the actual contact areas from which they were produced. Holm(24) and Bowden and Tabor (6), using contact resistance measurements, deduced that the diameter of a typical junction was of the same order.

The way in which adhesive wear particles are produced was graphically illustrated by the experiments of Green (27) and of Greenwood and Tabor (28) who used two-dimensional models of various metals and plasticene to denote asperities, and then sheared the asperities. They showed that, under some circumstances, especially when the plane of the junction was not parallel to the sliding direction, transferred particles are formed.

Kerridge (29) has shown that information about detailed mechanisms in wear can be obtained by combining tracer techniques with conventional methods of wear measurement. He found that with a soft-steel pin rubbing unlubricated on a hard-steel ring, the metallic transfer from a soft pin to a hard ring could be the first stage of a wear process. With steels, however, it was suggested that the subsequent stages of the wear mechanism were the slow oxidation of the transferred layer (accelerated by frictional heating) and its removal as loose oxidised debris. The material worn away was then replaced by new transferred material. The transferred material was found to be in a hardened condition. Further tests in an inert atmosphere showed a decrease in wear rate so Kerridge concluded that the oxidation and removal of the transferred material was the rate-determining process. This work reveals the important fact that wear particles may be produced directly when localised regions of the surface come in contact.

Kerridge and Lancaster (30) developed the radiographic method of Kerridge (29) to study the severe wear of 60/40 brass pin rubbing on hardened steel ring - a material combination which gives very reproducible wear rate results and a wear rate proportional to the load (2). It was found that during the initial stages of sliding, no wear particles were produced, but a transferred film of brass builds up on the steel surface. As the film thickness approached a steady value, wear particles started to appear until an equilibrium condition was reached. When the brass pin was replaced by an otherwise similar irradiated pin and sliding continued it was found that wear continued as before but initially these wear particles were not radioactive. Thus they could not have originated from the radioactive pin, but must have been detached from the inactive transfer film on the steel ring. As sliding continued with an active pin, the inactive film was gradually replaced by active brass and the wear debris therefore eventually became active. By a similar technique it was established that the material in the transferred film remained there until it was detached as debris. In other words, there was no back transfer from the film to the pin. Further experiments showed that the wear was a two-stage process starting from the transfer of the material from the pin to the ring followed by the removal of transferred material as wear particles. The transfer from the pin to the ring occurred as discrete particles, and the material was removed from the ring as aggregates of about 50 such transferred particles. Archard and Hirst (31), in a study of mild wear using hardened steel rubbing on a hardened steel surface, showed that back transfer was possible.

Many materials undergo a transition from mild wear to severe wear (or vice versa) when the rubbing conditions are changed, and Hirst and Lancaster (32) have described some of the factors which influence the magnitude of the transition load. These researchers, in agreement with an observation of Moore and Tegart (33), show that the early stages of

rubbing induces changes in the surface layers of the materials so that in general the wear rate after prolonged rubbing depends upon the properties of the generated skins rather than on the properties of the original materials. In consequence the wear rate usually changes with time until the equilibrium surface condition becomes established. By measuring the wear rates of newly prepared surfaces of various degrees of roughness, Hirst and Lancaster showed that the transition load is lowered by increasing the roughness amplitude.

The influence of temperature on the severe wear of 60/40 brass rubbing on hardened steel has been investigated by Lancaster (34). Low sliding speed (1.3cm sec^{-1}) was used to minimise frictional heating and temperature was increased by external heating. Two regimes of wear were found. At light loads protective surface films were generated during sliding and there was little intermetallic contact (mild wear). At heavier loads the wear rate increased by several orders of magnitude and there was extensive intermetallic contact (severe wear). At the transition load between these two regimes of wear, it was suggested that there was an equilibrium between the rate of formation of a protective surface film and its rate of destruction. The magnitude of the transition load was found to increase with temperature, i.e. an increase in temperature of the sliding metals facilitates the formation of a protective film.

In further investigations, Hirst and Lancaster (35) and Lancaster (36) studied in detail the conditions under which the wear of this same combination of materials changes from the severe to mild regime. The load, speed and ambient temperature of the system were varied over a very wide range. It was found that the mechanism of severe wear exposed clean metal surfaces and this was the condition which favoured the continuation of the process. On the other hand the exposure of the surfaces to the atmosphere leads to the formation of oxide films and, if sufficiently protective, lead to the

onset of mild wear. Mild wear takes place at light loads, low speeds and low temperatures, when there was sufficient time between contacts for a surface film to be established. In addition, mild wear also occurred at heavy loads, high speeds and high temperatures because of an increase in the rate of oxidation. Figure 1.1 shows the wear rate of 60/40 brass on hardened steel as a function of speed for various ambient temperatures (36). At an ambient temperature of 20°C severe wear occurs over a range of speeds from approximately 10^{-2} cmsec^{-1} to 10^{-3} cmsec^{-1}. As the ambient temperature was increased the range of severe wear was reduced by the increased rate of oxidation until at 400°C the wear was mild throughout. A similar effect may be produced by carrying out the experiments in an atmosphere of oxygen, as demonstrated by curve F in Figure 1.1. In addition, it may be noted that the change from mild to severe wear, and vice versa, is much more abrupt than that occurring in air at the same temperature (curve D). The increase in the wear rate at high speeds was shown to be due to thermal softening of the brass since when specimens were adequately cooled a fall in wear rate was observed (35).

The wear rate of hardened steel rubbing on hardened steel was investigated by Archard and Hirst (37) using such techniques as radioactive tracers, electron microscopy, and electron diffraction. It was found that metal transfer occurred in the early stages of rubbing, but in the later stages, when the surfaces had run in, the wear process was primarily governed by oxides. They concluded that oxidation of the sliding surfaces is an important phenomenon in the mild wear region.

Perhaps the most definitive work in separating modes of dry wear of steel is that of Welsh (38,39). He showed that great changes in wear rate could result from small changes in applied load when sliding a steel pin against a steel ring as shown in Figure 1.2. These sharp transitions which Welsh observed between mild wear and severe wear he refers to as

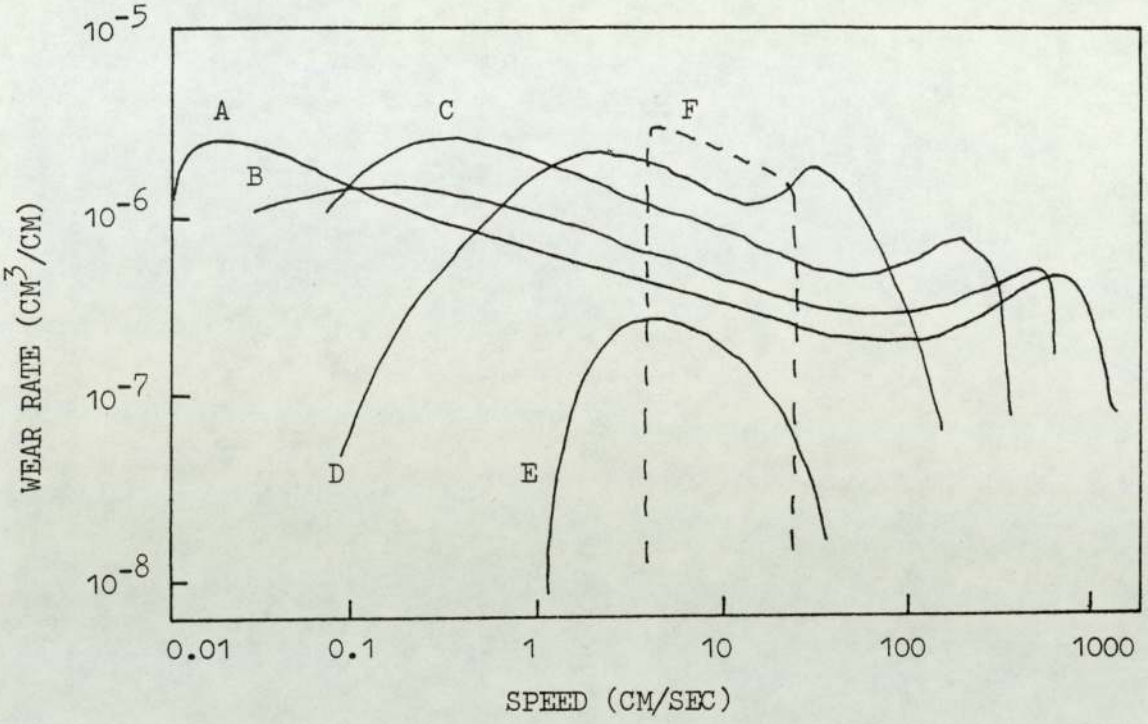

FIGURE 1.1 Variation of Wear Rate of 60/40 brass with Speed and Ambient Temperature. Load 3KG (36).

A 20°C
B 100°C
C 200°C
D 300°C
E 400°C
F 300°C (OXYGEN).

the T_1 and T_2 transitions. Below T_1, mild wear occurs by the removal of oxide debris from an oxidised surface supported on a work hardened substrate. T_1 is a transition to severe wear initiated by the breakdown of the protective surface oxide produced at lower loads. Plastic deformation of the substrate occurs, caused by a higher bulk temperature, and the wear rate increases considerably with the production of metallic debris. Between T_1 and T_2 severe wear occurs. At the T_2 transition the surface temperature is high enough for phase hardening (martensitic phase transformation) to produce a hard 'white layer' structure which prevents deformation and helps to establish an oxidised surface once more. The wear rate is reduced considerably but is not as low as the wear rate below the T_1 transition. At loads above the T_2 transition a third transition T_3 (not shown in Figure 1.2) has been reported by Welsh (39). Above T_3 permanent phase hardening occurs so that oxide formation is no longer necessary for the mild wear behaviour to be sustained.

Figure 1.2 also shows the effect of tempering on the pattern of wear. As the hardness increases, the range of loads over which severe wear occurs shrinks until at a hardness of between 360 and 436 VPN mild wear occurs over the full range of loads. An increase in speed reduces the loads at which the transitions take place and higher the carbon content of the steel, the smaller the range of loads over which severe wear is obtained (39). Steels with carbon content of 0.78% and 0.98% exhibited mild wear at all loads whereas a 0.026% carbon steel gave severe wear throughout the range of loads. The effect of oxidation was investigated by Welsh by testing in an inert atmosphere of argon. It was found that the critical load T_1 was decreased but the T_2 and T_3 loads are increased, i.e. the load range where severe wear will occur is therefore increased when the oxidising potential is decreased.

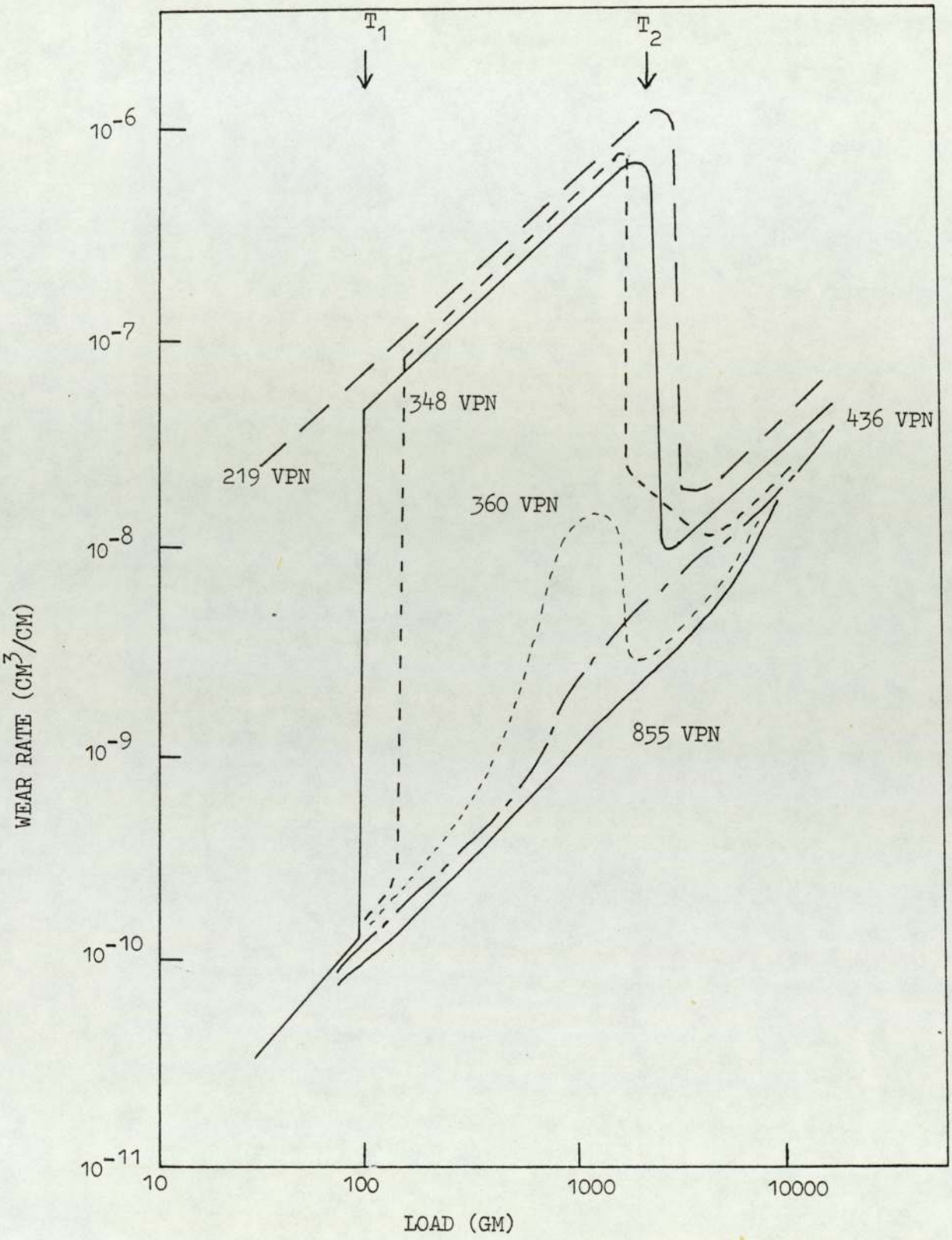

FIGURE 1.2 Effect of Heat Treatment upon the Pattern of Wear for a 0.52% Carbon Steel. Sliding speed 100cm/sec (39).

Welsh (39) determined two critical hardnesses using tempering and etching experiments, the first being that value which was required to support an oxide film and lay between 340 and 425 VPN. The second critical hardness was that minimum value required for mildwear without the intervention of an oxide film and fell between the limits 553 to 775 VPN. Welsh indicated that phase hardening can occur under conditions where the theoretical flash temperatures are sufficient, in terms of normal metallurgical behaviour, to cause hardening. Moreover, he remarks that the low carbon steels harden more intensively during rubbing than is possible during normal heat treatment.

Below T_1 Earles and Hayler (40) found that increases of speed in ENIA steels decreased wear rates while load increases increased wear rates. Increasing speed tends to raise surface temperature so that below T_1 more complete oxide coverage results and wear decreases. Load increases, however, increase the points of contact so that wear rates increase. Earles and Powell (41,42) examined the effect of speed on mild wear rates and found that speed increases do lead to lower mild wear rates.

Eyre and Maynard (43) suggest that it is possible to obtain load/speed transition graphs for materials which clearly indicate the boundary between mild and severe forms of wear, and that mild and severe wear may be related to both oxidation characteristics and the metallurgical changes taking place in the surface layers.

During running-in the hardness of the metal surfaces increases until a critical hardness dependent on the material composition is exceeded. This hardness (normally in the range 340 to 425 VPN for steels (39)) indicates that the substrate possesses the strength necessary to support an oxide so that fracture will occur within the oxide. Since mild wear depends on the uniform formation of an oxide layer,

altering the bulk composition to make the material more oxidation resistant has been found to prolong running-in. It has been found (43) that a 3% chromium steel has double the running-in distance of a 1% chromium steel under the same test conditions. Independent oxidation rates have shown that 3% chromium steel oxidised at a significantly slower rate.

A series of detailed studies of the oxidational wear of steels (above the T_2 transition) has been carried out by Quinn (44,45,46). He has proposed that in the conditions of his experiments the mechanism of wear is simply the growth of oxide (without metal transfer) until it reaches a critical thickness such that it breaks up to form a wear particle, allowing the process to start again. Quinn suggested that the wear rate was controlled by the oxidation rate rather than by the abrasion of the oxides from the surfaces as suggested by earlier mild wear studies (37). An oxidational theory of mild wear (44,47), appropriate to the mild wear of steels by oxide film removal, has been proposed by Quinn and is discussed in Section 4.5.

Suh and his co-workers (48,49,50) have studied the dry wear of steels below the T_1 transition using pin-on-ring and cross-cylinders machines. Loads from 10 to 20N and sliding speeds from 10 to 30 $mmsec^{-1}$ were used but protection and wear by oxidation observed in the earlier studies were suppressed by sliding in argon atmosphere. In these conditions the wear debris was metal flakes (of area $0.01mm^2$ and thickness 1 to 10μm) formed by fatigue failure of the sliding surfaces. The measured wear rates were one or two orders of magnitude less than observed in severe conditions. To distinguish it from mild or severe wear, this form of wear was called delamination wear.

A review of earlier studies on the sliding wear mechanism of metals has recently been made by Childs (51). He

concluded that, in general, the influence of sliding speed and load on the wear mechanisms observed during the dry wear of soft steels is as follows: at low loads and speeds surface work hardening and smoothing can occur under a protective oxide film, wear occurring either by removal of the film or by metal fatigue (delamination). At slightly higher loads and speeds oxide protection may break down leading to severe metallic wear and transfer but at higher speeds still enhanced oxidation caused by friction heating coupled with the possibility of surface transformation hardening of steels can restore oxide protectiveness. In hotter conditions still gross surface softening can cause a reversion to severe wear but in even hotter conditions a further regime of oxide domination exists.

1.4 The Influence of Surface Oxides on the Friction and Wear of Metals

The interactions between metals are profoundly affected by the oxide films present at the interface. Under normal atmospheric conditions most metals are covered by oxide films and clean metal surfaces will acquire such a film 5 to 50 molecules thick within a few seconds.

The effect of the oxide layer on friction coefficient was observed by Whitehead (52) in the sliding of copper on itself and on steel. He carried out a series of tests with various normal loads at a low sliding speed at which frictional heating would be negligible. As the load was increased, the friction coefficient μ remained virtually constant until a load of 1 gram was reached. Further increase in load caused an increase in μ, but above 10 grams it became constant at a new higher value. In this higher load range, the surface showed signs of metallic adhesion and large scale plastic deformation whereas below the transition the oxide layer appeared unbroken. Whitehead suggested that the oxide layer produced in air provides protection against

metallic contact, but breaks down if the load exceeds 1 gram. Further experiments by Whitehead led him to suggest that for low μ, the surface oxide film should resist penetration and at the same time be easily sheared. For example, the hardness of copper oxide is comparable to that of the base copper metal, and the metal and oxide can, therefore, undergo plastic deformation together. For amorphous aluminium oxide, the greater hardness of the oxide layer when compared to the aluminium metal causes plastic deformation in the underlying metal before the stress is sufficient to cause plasticity in the oxide. This results in a rupture of the oxide film which leads to eventual metal-to-metal contact.

Wilson (53,54) confirmed the role of oxide films in preventing intermetallic contact at low loads by measuring the electrical contact resistance between sliding solids. Below the transition load, the contact resistance was high showing that the solids are separated by an insulating layer. Above the transition load, a low resistance was obtained, indicating the existence of appreciable metallic contact.

Cocks (55) showed that surface films in metallic contacts are seldom penetrated to any appreciable extent under normal loading. When shearing forces were applied to the contact it was found that the films were not broken up until the frictional force reached a critical value, and with certain metals they remained intact even during sliding. When the film was penetrated, the area of metallic contact was small first, and was distributed over a number of tiny junctions. As sliding proceeds these junctions grow, and eventually coalesce, so that nearly the whole of the contact area suffers damage.

An experimental study of the role of oxidation due to frictional heating in unlubricated high speed sliding of metals has been made by Cocks (56,57). With steel on steel (56), microscopic examination showed that at light loads the

surfaces were severely damaged indicating the formation and tearing of welds. At higher loads this tearing was much less severe and the surfaces were covered with dark film. The decrease severity of tearing with increasing load was attributed to the greater amount of protective oxidation resulting from the increased frictional heating at higher loads. The relative freedom from welding was also evidenced by the low value of friction coefficient observed at higher loads. With other material combination (57) the results indicate that the oxide generated due to frictional heating gives considerable protection against surface damage. The degree of protection and the way in which it responds to changing load varies considerably from one combination to another. Cocks suggested that the extent to which oxide film prevents metallic interaction must depend on such factors as the mechanical properties of the oxide and of the underlying metal and the adhesion between the metal and the oxide.

In a paper by Mølgaard (58) it was shown that the basic factors determining the oxidative wear process are mechanical characteristics of the oxide layer and that the oxidation process, while important, was a secondary influence. These will determine both the oxide thickness and the attrition rate which will, however, be such that on the average the oxidation rate will equal the attrition rate. This author also shows that an increase in oxidation temperatures in wear, e.g. through an increase in the sliding speed, can in some instances lead to a decrease in the attrition rate, an increase in the oxide layer thickness and hence a decrease in the oxidation rate.

Stott et alia (59,60) have shown that the development of compacted oxides, particularly so-called 'glazes', on sliding metal and alloy surfaces can result in significant decrease in friction coefficient and wear rates. The 'glaze' consists of a thin, physically homogeneous, surface layer on top of either highly compacted oxide particles above a grow-

ing steady-state oxide layer or a metal deformed to varying degrees (depending on time of sliding, ambient temperature and strength of alloy). All experiments reported by Stott et alia were carried out using either unidirectional or reciprocating sliding modes.

While the oxidation is important for the maintenance of mild wear, the oxide composition has also been found to be significant in determining the magnitude of the wear rate (17,40,61-65). Iron oxide formed during unlubricated sliding of ferrous materials changes it composition with temperature, that is, $\alpha - Fe_2O_3$ below 200°C, Fe_3O_4 from 200°C to 570°C and FeO above 570°C is predominant (66). Quinn (46) has suggested that by determining the oxide composition the asperity temperature could be estimated. Good et al. (61) and Bisson et al. (62) examined a number of surfaces after sliding and found that Fe_3O_4 offered better surface protection than $\alpha - Fe_2O_3$, resulting in lower surface friction and wear rate. Clark et al. (63) measured the wear rate of hardened steel sliding on hardened steel at various ambient temperatures. The wear rate increased with ambient temperature up to about 200°C after which the trend was reversed. At high temperatures, a complete unbroken film was found on the surface and the debris was identified as Fe_3O_4. Below 200°C, the film was generally incomplete and $\alpha - Fe_2O_3$ was produced. Available evidence on the wear properties of FeO seems to be slightly contradictory. Both Bisson et al. (62) and Cornelius et al. (64) found FeO to be protective whereas Earles et al. (40) and Hurricks (17) found a distinct increase in wear between 500°C and 600°C where FeO becomes predominant. Quinn et al. (65) suggest that FeO is less mechanically stable than the other iron oxides giving rise to low oxide film thickness and hence high wear rates.

1.5 Mechanisms of Oxide Formation and Removal

Most experimental observations of oxidation rates show that the rate of increase of oxide layer thickness decreases

as the thickness itself increases, since it becomes harder for the oxygen to reach the unoxidised material. Various growth laws have been proposed the most common and best understood being the parabolic law:

$$\xi \sim t^{\frac{1}{2}} \qquad (1.1)$$

and the logarithmic law:

$$\xi \sim \log (1 + t) \qquad (1.2)$$

where ξ is the film thickness and t is the time of oxidation. The parabolic dependence is almost universally applicable to thick oxide films (approximately greater than 0.5μm) as these are almost certainly produced by a diffusion process. Although oxidational data for iron and steel are available from static experiments with bulk samples (67,68), no reliable data are available for the small values of t which occur in the sliding process.

The growth of oxide film occurs in two stages. In the first stage the oxygen atom, after dissociation of the oxygen molecules, is chemisorbed onto the surface of the metal. The second stage of oxidation is due to the thermal diffusion of either the metal ions, oxygen ions or in some cases both. For example, Carter and Richardson (69) have shown that for the oxides of iron, oxygen diffusion is responsible for the growth of α-Fe_2O_3, iron and oxygen diffusion for that of Fe_3O_4, and iron diffusion for the growth of FeO.

Oxide formation depends on temperature, oxygen partial pressure and many other factors. At high temperature oxidation is accelerated. During sliding, any given part of the surface will be in actual contact for an extremely short time, but during this period its temperature will be very much higher than when it is not in contact. Quinn (9) reviewed both wear studies and oxidation experiments and showed a correlation between the oxides actually obtained in

wear tests and those to be expected from the oxidation experiments at the contact temperature. Quinn (9,44) therefore argues that, since the oxidation rate increases rapidly with temperature, most of the oxidation will take place during the contact period at the contact temperature T_c. He supports this theory with experimental observations of the oxides produced. In his experiments, Quinn (44,45) found evidence of Fe_3O_4 debris and therefore argued that the oxidation temperature must have exceeded 300°C, this being higher than the bulk (or non-contact period) temperature T_s in his sliding system. The alternative viewpoint advanced by Clark, Pritchard and Midgely (63) and implicit in the arguments of Lancaster (34) and Yoshimoto and Tsukizoe (70) is that oxidation takes place during the non-contact period and hence depends on the bulk temperature T_s only. Archard (71) carried out a rough calculation using typical values for T_s and T_c and found that most of the oxidation should take place during the actual contact period, which supports Quinn's hypothesis. However, the question is complicated by the fact that when an area is in actual contact, the free flow of oxygen to the interface is obstructed. A third possibility is that most of the oxidation takes place shortly after a period of actual contact, when the temperature is somewhere between T_c and T_s.

A wide range of mechanisms have been proposed to account for the removal of the oxide film by wear. The most straight forward assumption, advanced by Yoshimoto and Tsukizoe (70), is that the whole film is removed from the actual contact area at each interaction. Tao (10) proposed two idealised models representing two extreme cases for build-up and removal of oxides on the rubbing surface. These are shown in Figure 1.3. Model 1 assumes the gradual growth of an oxide layer which is removed instantaneously by the rubbing action when a certain critical thickness ξ is reached. Model 2 assumes that the time for oxide growth is negligibly small in comparison with the time for rubbing off the oxide layer. Another possibility is that once the oxide reaches a critical thickness it is continually abraded in some manner so that any further growth is removed (58). This is illustrated in Figure 1.4.

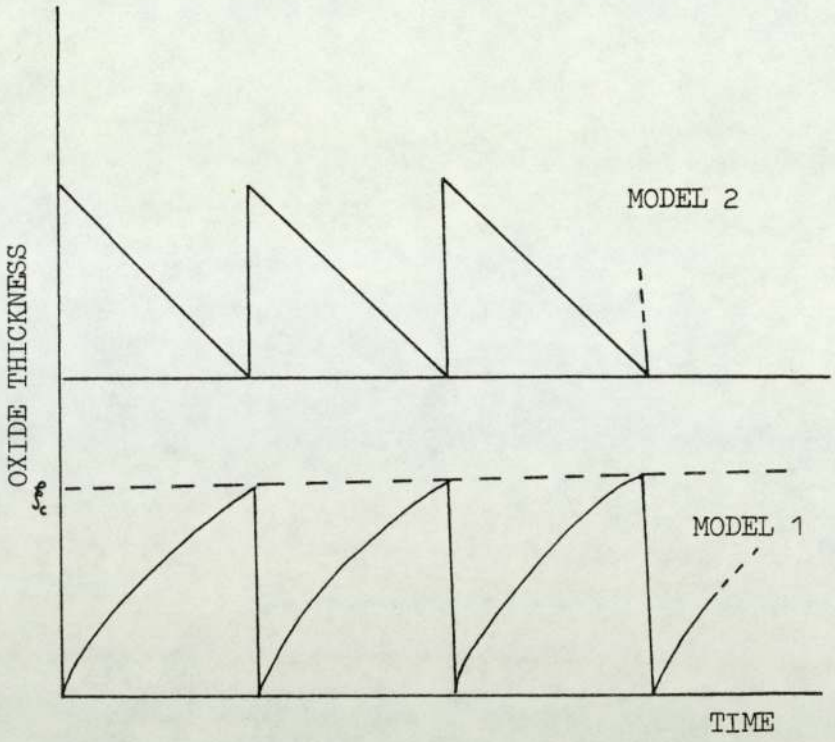

FIGURE 1.3 Theoretical Models for Oxidative Wear - I (10).

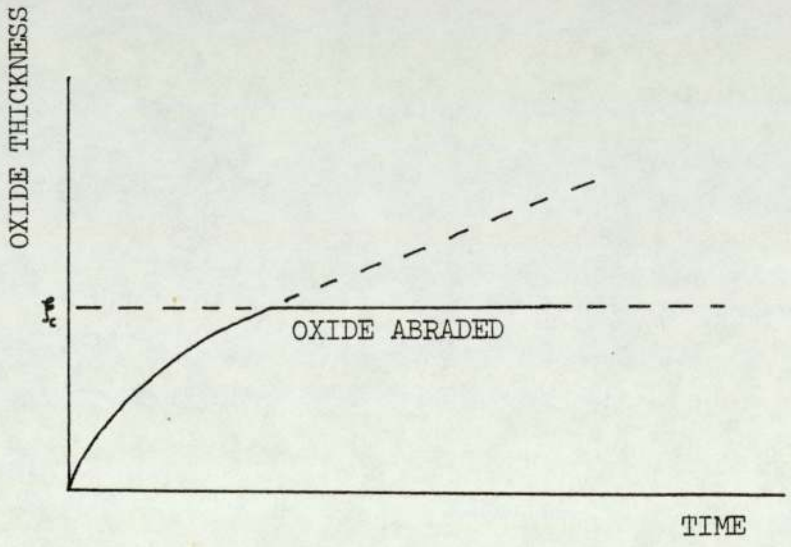

FIGURE 1.4 Theoretical Model for Oxidative Wear -II Continuous Abrasion of Oxide (58).

Quinn (44) suggests that the oxide thickness is built up over a number of traversals until at some critical thickness ξ it becomes unstable and cracks away from the surface to produce oxide flakes, after which a new layer begins to form. Electron micrographs of Quinn (45) show signs of cracking and detachment of the oxide layer, possibly caused by thermal or contact stresses.

The strength with which the oxide film adheres to the substrate will obviously depend upon the amount of mismatch between the lattices since a highly strained film will attempt to relieve the stresses by detaching itself from the metal. Kubackewski and Hopkins (67) suggest that the ratio of the unit cell volume in the oxide to the volume of the unit cell in the metal (known as Pilling-Bedworth Ratios) give an estimate of the stresses set up within the oxide. The stresses set up as a result of the differences in unit cell volumes will increase as the film thickness increases and may eventually overcome the attractive forces at the interface. In the case of iron, the volume ratios are 2.15, 2.1 and 1.7 for α-Fe_2O_3, Fe_3O_4 and FeO respectively. During sliding the internal stresses will be reinforced by external stresses arising from the applied load and frictional force.

Earles and Powell (72,73) found experimentally that the oxide layer generated by sliding builds up gradually to a critical thickness before becoming detached from the substrate to form a wear particle. Tenwick and Earles (74) suggested that, in addition to the adhesive strength between oxide and substrate and the volume ratio of oxide/metal, the critical thickness is also likely to be a function of applied load, friction, sliding speed and temperature.

Mølgaard (58) suggests that separation of oxide from a surface depends on the cohesion strength between oxide and bulk surface and on the mechanical properties of oxide, notably shear stress, fracture stress and ductility.

Aronov (75) has attributed the distruction of the oxide film to a fatigue process at the oxide/metal interface. The fatigue mechanism involves thermal and mechanical stresses within the oxide and at the oxide/metal boundary. Oxide elements under repeated stress subsequently develop cracks and eventually become detached as loose wear fragments.

1.6 Flash Temperature Theories

When two surfaces are placed together, contact is only made where small asperities meet. During sliding these asperities are heated by frictional contact with opposing asperities, resulting in localised sudden rises in temperature which may be sufficiently high to change the conditions of sliding. These high temperatures are often referred to as "flash temperatures". As sliding commences, contacts continue to be made and broken, and the "hot-spots" on the surface shift their location. The flash temperature reached at any of these hot spots, however, tends to be reasonably constant under constant sliding conditions (7).

Although the maximum temperature is made up of two components, a bulk temperature rise and a flash temperature rise, we are usually more interested in the latter, since the former is usually less, and is generally quite readily measured. The measurement of flash temperature is extremely difficult as they are commonly of only a few milliseconds duration and occur over an extremely small area in comparison with the geometric contact area. The best direct method of measurements of flash temperature is based on the principle of dynamic thermocouple (76,77). In brief, the method consists of using dissimilar metals and measuring the thermoelectric voltage generated. However, such measurements tend to be restrictive as regards the choice of sliding material combinations. This has led to a number of flash temperature theories being proposed. The classical work on flash temperature theory was performed by Blok (78,79) in 1937.

Blok investigated the problem of temperature rise at the centre of both stationary and moving sources of heat by assuming the bodies to which the heat is supplied have infinitely large heat capacity. The treatment involved relatively complicated mathematics. A theoretical study somewhat similar to Blok's was later made by Jaeger (80), who carried out the calculations in considerable numerical detail. In his theoretical analysis, Jaeger used uniform plane sources of heat of various shapes moving with constant velocity in the surface of a semi-infinite medium with no loss of heat from the surface. It was shown that for a wide range of shapes considered, the average temperature differed by a factor of less than two. Jaeger also conluded that the thermal properties of a thin surface layer can have a marked influence on the temperature of the surface.

Simpler mathematical studies have been made by Holm (81) and Bowden and Tabor (6), More recently, Jaeger's findings have been stated without its mathematical complexities by Archard (82) who considered contact area determined by both elastic and plastic deformation. Archard developed equations for the rise in surface temperature over the contact. The temperatures were calculated on the assumption that the heat is generated at the area of contact and that this heat is conducted away into the bulk of the rubbing members. The model used by Archard is a protuberance on the surface of body B forming a circular area of contact which moves with a velocity V over the flat surface of body C. Body B therefore receives heat from a stationary heat source while body C receives heat from a moving heat sources. It was shown that the mean rise in temperature over the contact area, θ_m, for a stationary heat source could be calculated from the following equation:

$$\theta_m = \frac{Q_B}{4aK_B} \qquad (1.3)$$

where Q_B is the quantity of heat supplied per second to body

B, a is the radius of contact and K_B is the thermal conductivity of body B. For a slow moving heat source, there is enough time for the temperature distribution of a stationary contact to be established in body C and therefore:

$$\theta_m = \frac{Q_c}{4aK_c} \qquad (1.4)$$

where Q_c and K_c refer to body C.

At higher speeds equation 1.4 will not apply because there is insufficient time for the temperature distribution of stationary contact to be established in body C. The speed at which this occurs is related by Jaeger (80) to the dimensionless parameter:

$$L = \frac{Va}{2\chi} \qquad (1.5)$$

where χ ($= K/\rho C$) is the thermal diffusivity of a material and K is its thermal conductivity, ρ the density and C is its specific heat. Therefore, at higher speeds, Archard showed that the average temperature is given by:

$$\theta_m = \frac{0.31Q_c}{aK_c} \left(\frac{\chi_c}{Va}\right)^{\frac{1}{2}} \qquad (1.6)$$

Archard states that to a reasonable approximation, Equation 1.4 applies for $L < 0.1$ and equation 1.6 for $L > 5$. For intermediate values ($0.1 < L < 5$), Archard presents a graphical procedure.

To apply the above results to a practical example, the proportion of the total heat supplied to each of the two bodies must be taken into account. Archard's method of dealing with the distribution of heat to the two bodies is summarized by the expression:

$$\frac{1}{\theta_m} = \frac{1}{\theta_B} + \frac{1}{\theta_C} \qquad (1.7)$$

where the flash temperature for each body (θ_B and θ_C) is calculated on the assumption that all the heat is supplied to it.

In his analysis Barber (83) considered the mechanism of a single interaction between two asperities on opposing surfaces. By making the assumption that the load is carried by a single asperity, Barber was able to calculate the average temperature rise produced on the surface of each of the contacting asperities. Powell and Earles (84,85) have shown that Barber's model predicted total temperatures which, on the basis of the worst comparison, are only 60°C lower than those predicted by the Archard theory.

There seems to have been only a few attempts to deduce surface temperatures from measurements of the heat flow from sources of frictional heating at the sliding interfaces. One of the first theoretical papers in which an attempt was made to estimate surface temperatures from heat flow parameters was that by Grosberg, McNamara and Mølgaard (86). In a later paper, Grosberg and Mølgaard (87) applied the theory to some pin and disc experiments to determine the contact temperature between the rubbing surfaces. In this paper the experimentally measured and theoretical derived values of division of heat were compared. The theoretical values of division of heat were deduced from a surface model consisting of N circular areas of contact (radius a), and each with a thin layer of oxide of thickness ξ. Quinn (88) uses a very similar model to that proposed by Grosberg and Mølgaard (14) to modify the expressions for flash temperature given by Archard (82). This is discussed in detail at a later stage.

1.7 Mechanisms of Friction

Friction is the resistance to motion which is experienced whenever one solid body slides over another. It has been found experimentally that there are two basic laws of friction:

1. The friction force F is proportional to the normal load W between the bodies, that is:

$$F = \mu W \qquad (1.8)$$

where μ is the coefficient of friction. μ is a constant only for a given pair of sliding materials under a given set of ambient conditions and varies for different materials and conditions.

2. The friction is independent of the apparent area of contact between the contacting bodies (true for most materials excluding elastomers).

When surfaces are loaded against each other they make contact only at the tips of the asperities. The pressure over the contacting asperities is assumed high enough to cause them to deform plastically. This plastic flow of the contacts causes an increase in the area of contact until the real area of contact is just sufficient to support the load. Under these conditions Bowden and Tabor (6) state that the real area of contact A is given by the expression:

$$A = W/P_m \qquad (1.9)$$

where P_m is the penetration hardness (yield pressure) of the softer material.

The adhesion theory of friction due to Bowden and Tabor (6) assumes that friction is mainly determined by the shear strength of the cold-welded junctions formed between bodies in contact. If s is the average shear stress required to

shear the welded junctions, then:

$$F = As + P_e \tag{1.10}$$

where P_e is a term introduced by Bowden and Tabor to take account of the force required to 'plough' hard asperities through a softer surface. Bowden and Tabor state that for most situations involving unlubricated metals, P_e is small compared with As and may be neglected.

Ignoring the ploughing term, from Equations (1.9) and (1.10) we can write:

$$F = As = \frac{Ws}{P_m} \tag{1.11}$$

and from Equation (1.8) we have:

$$\mu = \frac{F}{W} = \frac{s}{P_m} \tag{1.12}$$

Since shearing usually takes place in the softer material Bowden and Tabor suggest that we take s equal to S_o the critical shear stress of the softer material. Thus we may write:

$$\mu = \frac{\text{critical shear stress of the softer material } (S_o)}{\text{yeild pressure of the softer material } (P_m)} \tag{1.13}$$

This ratio S_o/P_m is fairly constant for most metals and the above analysis gives and indication of why μ lies within a fairly narrow range for a wide range of materials.

For most metals, S_o is about one-fifth of P_m and therefore the simple adhesion theory predicts that $\mu \simeq 0.2$. But many metal combinations in air give a friction coefficient higher than 0.5, and metals in high vacuum give much higher values of μ. This led Bowden and Tabor to re-examine some

of the assumptions in the simple theory and to present a modified and more realistic description of friction in terms of adhesion. By considering the phenomenon of junction growth (brought about by the superposition of the shear stress on the normal stress) and presence of thin contaminating film (of critical shear stress S_f) on the junctions, they showed that the coefficient of friction should be correctly given by the following relation:

$$\mu = \frac{\text{critical shear stress of the interface } (S_f)}{\text{yield pressure of the bulk metal } (P_m)} \qquad (1.14)$$

The interface, they maintain, is not usually one between metal and metal, and so it is incorrect to take critical shear stress of the bulk metal S_o instead of S_f. This interface may consist of thin film of boundary lubricant, or an oxide film, or even some contaminant. When the interface is no longer homogeneous and uniform, i.e. when it becomes damaged, then the situation becomes one in which there is a mixture of contacts between regions where the critical shear stress is S_f (undamaged film material) and where it is S_o (small metallic junctions). In this case the effective shear strength of the interface will lie between the shear strength of the metal and that of the oxide film, its exact value depending on the relative amount of metal to metal and metal to oxide contact.

Recently Wilson, Stott and Wood (89) have proposed a model based on the adhesion theory of friction to account for the influence of the developing compacted oxide "island" on the coefficient of friction. The model relates the coefficient of friction to the area of the compacted oxide in terms of several metal, oxide and metal/oxide interfacial parameters. In particular,

$$\mu = \frac{S_o}{P_m} \left\{ \alpha_m (1-Q)^2 + \alpha_{m-o} (2Q-2Q^2) + \alpha_o \frac{i}{k} Q^2 \right\} \qquad (1.15)$$

where Q is fraction of real area of contact covered by oxide layer

$1-Q$ is fraction of real area of contact not covered by oxide layer

α_m is junction growth constant for metal-metal asperity contact

α_{m-o} is junction growth constant for metal-oxide asperity contact

α_o is junction growth constant for oxide-oxide asperity contact

i is ratio of shear strength of oxide to that of metal

k is ratio of yield pressure of oxide to that of metal

Wilson, Stott and Wood (89) showed that the metal-oxide asperity interactions are not very critical in determining frictional behaviour although the oxide junction growth constant is important.

An alternative to traditional friction theories has recently been proposed by Rigney and Hirst (90). Their ideas are based on the work required for plastic deformation in the near surface region, described in terms of work hardening, recovery and the cellular microstructure existing during steady state sliding.

A recent paper by Tabor (91) gives a general critical picture of our present understanding of the frictional process. In particular it emphasizes the three main elements involved, namely the true area of contact, the nature and strength of the interfacial bonds formed at the regions of contact, and the way in which the material around the contacting regions is sheared and ruptured during sliding.

1.8 Oxidative Wear Theories

Oxidative wear consists of two processes, formation of oxide at the interface and its separation from the surface. A number of analytical theories have been proposed to estimate oxidative wear (44,70,74). Some theories differ by approach, others by interpretation of various parameters. However, the general assumption is that practically all of the material which is transformed by attrition to debris has previously undergone oxidation. Under equilibrium conditions the oxidation rate is then equal to the attrition rate. A critical review of the early development of oxidational wear theories during the 1960's and 1970's has recently been given by Quinn (92). Since this type of wear is of particular interest in the present work a brief outline of the main oxidational wear theories is given below.

Yoshimoto and Tsukizoe (70) based a wear theory on oxidation occurring during non-contact periods, the mechanism proposed was that the whole oxide film is removed from the actual contact area at each encounter and grows again to a constant thickness before the next encounter. Assuming a logarithmic growth rate, they showed that the thickness of the oxide film ξ in time t which elapses between two events at any given point on the surface is approximately given by:

$$\xi = \eta \frac{t}{\beta} \qquad (1.17)$$

where η and β are constants. During this time t the surfaces slide a distance l, where $l = ut$ and u is the sliding speed (see Figure 1.5).

Thus equation (1.17) becomes:

$$\xi = \frac{\eta l}{\beta u} \qquad (1.18)$$

The volume ΔV of a wear particle is given by:

$$\Delta V = \pi a^2 \xi \qquad (1.19)$$

where a is the contact radius.

Substituting equation (1.18) in equation (1.19):

$$\Delta V = \frac{\pi \eta l a^2}{\beta U} \qquad (1.20)$$

Assuming a simple model which represents the profile curve of the metal surface, Yoshimoto and Tsukizoe were able to deduce theoretically the number and size of the individual areas of contact, as well as the average distance l between two neighbouring asperities. They showed that the total wear rate per unit sliding distance for the whole surface is given by:

$$\omega = \frac{\pi \eta}{4\beta U} \{ (\frac{3}{\pi P_m})^{\frac{1}{2}} x W^{\frac{1}{2}} - \frac{3W}{\pi P_m} \} \qquad (1.21)$$

where x is the length of the profile curve.

Despite the fact that this was one of the first theories of oxidational wear, Yoshimoto and Tsukizoe did not produce any experimental validification of this expression. The assumption that every contact produces a wear particle is most unlikely, as suggested by Archard (1). Hence this theory has always been treated with some scepticism.

The theory advanced by Quinn (44) differs from that of Yoshimoto and Tsukizoe both in the proposition that oxidation takes place during the actual contact process and in the assumption of a different wear mechanism. He argues that the oxide film will continue to grow until at some critical thickness it become unstable and cracks away from the surface, after which a new layer begins to form. Quinn's oxidational wear theory is discussed in detail in Section 4.5.

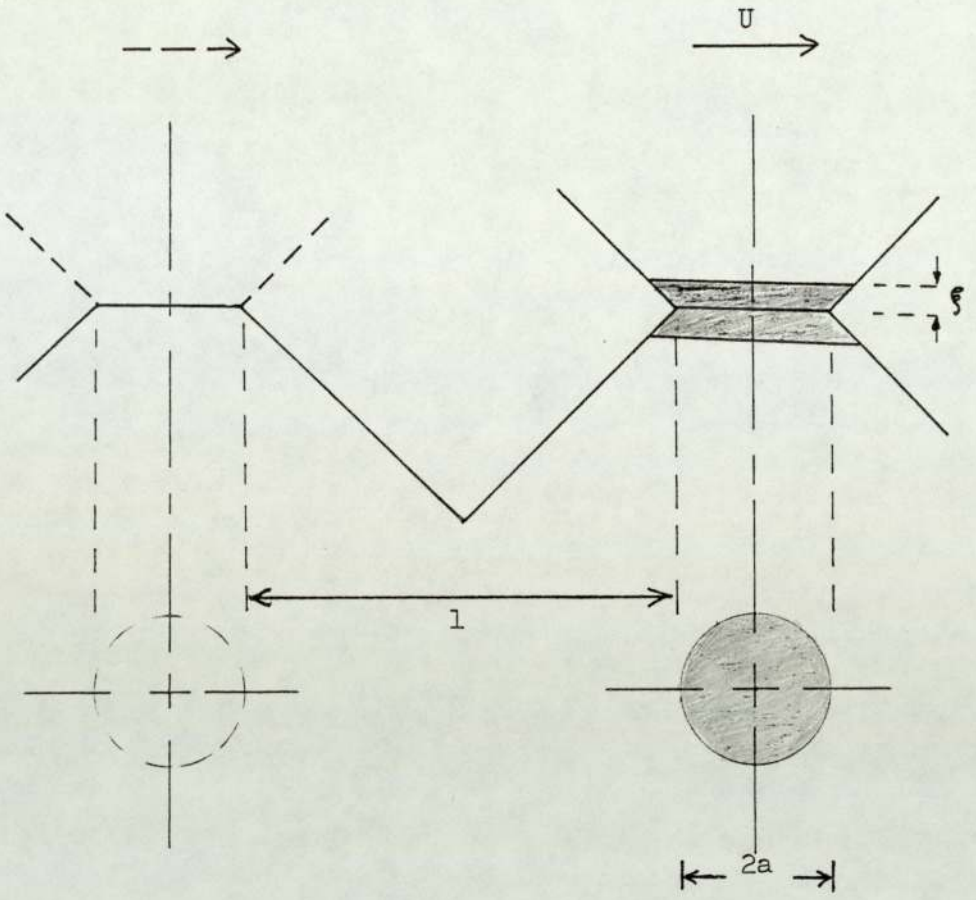

FIGURE 1.5 Idealized Model of Yoshimoto and Tsukizue (70).

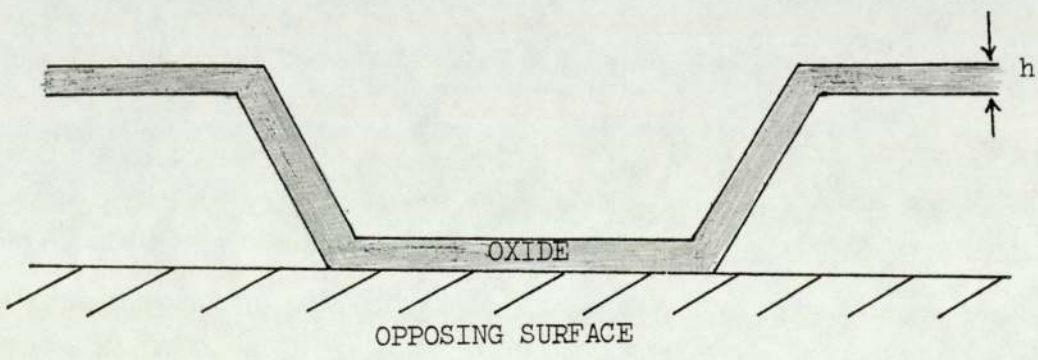

FIGURE 1.6 Typical Asperity Contact - Tenwick & Earles (74).

Tenwick and Earles (74) proposed a simple model, based on linear oxidation, to represent oxidative wear by flaking. In this model they assumed that contact between the sliding surfaces occurs at only one asperity. Figure 1.6 shows a schematic diagram of a typical asperity. It is further assumed that this asperity remains continuously in contact with the opposing surface until an oxide layer generated by sliding builds up gradually to a critical thickness (h_c) before becoming detached to form a wear particle. The process is then repeated with another asperity. Tenwick and Earles showed that the thickness of the oxide formed after time t can be expressed by:

$$h = (\frac{Co}{B})t \exp(-Qp/(R_g\theta)) \qquad (1.22)$$

where Co is the Arrhenius constant for linear oxidation, R_g is the universal gas constant, Qp is the activation energy, θ is the temperature and B is a constant.

Thus:

$$h_c = (\frac{Co}{B})t_c \exp(-Qp/(R_g\theta)) \qquad (1.23)$$

If A ($= W/P_m$) is the contact area of the asperity, then volume of the wear particle is given by:

$$\Delta V = h_c A = \frac{h_c W}{P_m} \qquad (1.24)$$

Therefore, the wear rate (volume removed/unit time) is:

$$\omega = \frac{h_c A}{t_c} = (\frac{WCo}{P_m B}) \exp(-Qp/(R_g\theta)) \qquad (1.25)$$

Tenwick and Earles suggested that general surface temperature T_s is the controlling temperature since any given point on the surface will spend more time out of contact, i.e. consecutive collisions for a given asperity will be infrequent. The experimental results showed reasonable agreement with the theoretical predictions for T_s values between 300°C and 500°C. Outside these limits, they suggested that wear mechanisms other than that employed in the theory become increasingly

important. However, oxidation of steel above 200°C is known to follow a parabolic law. Although Tenwick and Earles derived an expression for the wear rate (which involves h_c) assuming a parabolic rate law, they failed to apply this to their experimental results because of the difficulties in determining the critical oxide film thickness.

1.9 Research Programme

The unlubricated wear of steels at elevated temperatures has received very little attention from previous investigators, which is surprising in view of the great practical and economic importance of such materials.

The first aim in the present research was to investigate the unlubricated wear of two low-alloy steels (EN8 and EN31) sliding against EN8 steel at various loads and ambient temperatures. Tests were performed in air, using a pin-on-disc type machine. Wear rate, frictional force and temperatures of the pin and disc were continuously recorded during the tests with the aid of chart recorders. Wear debris collected from each test was examined using X-ray diffraction analysis and Glancing Angle X-ray Diffraction technique was used on selected worn pins to identify the compounds present on the surface. Bulk and microhardness tests were carried out on worn specimens' surface using a Vickers hardness tester and a Miniload hardness tester respectively. Taper sections were made through several worn pins to enable microhardness to be measured as a function of depth. The worn specimens were studied in a scanning electron microscope with the double purpose of examining surface topographies and for direct measurement of thickness of surface oxide films. These oxide films were also analysed by scanning Auger electron spectroscopy in an attempt to obtain in depth analysis through them. A method, based upon the theoretical expressions for the contact temperature of the rubbing surfaces and involving experimental and theoretical estimates of the

division of frictional heat at the sliding interface, is proposed whereby the contact temperature T_c, the number of contacts N, the contact radius a and the critical oxide film thickness ξ can be deduced. The validity of this method is confirmed by the reasonably good agreement obtained between the expected and predicted values for T_c (expected value estimated from the oxide composition in the wear debris) and ξ.

The theoretical estimates of T_c, N, a and ξ are used, together with the results from the various metallographical and physical techniques employed to examine the worn specimens and wear debris, to give a clearer picture of the wear behaviour of the steels investigated in this research.

It has always been assumed in the Oxidational Wear Theory that negligible oxidation occurs at those parts of the sliding interfaces not actually in contact at any given instant. However, for the study of wear at elevated temperatures, where temperatures are induced externally as well as by frictional heating, then we can no longer neglect the "out-of-contact" oxidation in our wear theories. Therefore, the second aim of this present research was to modify the existing Oxidational Wear Theory of Quinn (44) to take into account the "out-of-contact" oxidation.

CHAPTER 2

EXPERIMENTAL DETAILS

2.1 Introduction

Experimental details and description of the various physical the metallographical techniques of analysis that have been used in the examination of worn specimens and debris are given in this chapter. In Sections 2.2 - 2.5 the pin-on-disc type wear machine used in the present study is described. Details of specimen preparation and experimental procedures are given in Sections 2.7 and 2.8 respectively. Bulk and surface hardness measurements of worn specimens is described in Section 2.9, and in Section 2.10 a method used to estimate the wear rate of the disc material is given. Scanning electron microscopy (Section 2.12) was found most useful in the examination of surface topographies and oxide thickness measurements, whilst oxide composition and chemical structure was investigated by X-ray diffractometry (Section 2.11) and Auger electron spectroscopy (Section 2.13).

2.2 The Wear Test Rig

The wear test rig used for these experiments has already been described elsewhere (93). Essentially the test machine consisted of a pin and disc, in which the pin was loaded pneumatically against a rotating disc. A general view of the wear test rig is shown in Figure 2.1.

The disc was mounted on the main shaft of the machine with three $\frac{1}{4}$" BSF screws. A 2kW electrical resistance heater could be attached to the non-wearing side of the disc. The electrical power to the heater was supplied, via carbon brushes running on copper slip rings, from a 270 volt Auto-Transformer. This provided disc temperature up to 600°C. The heater and

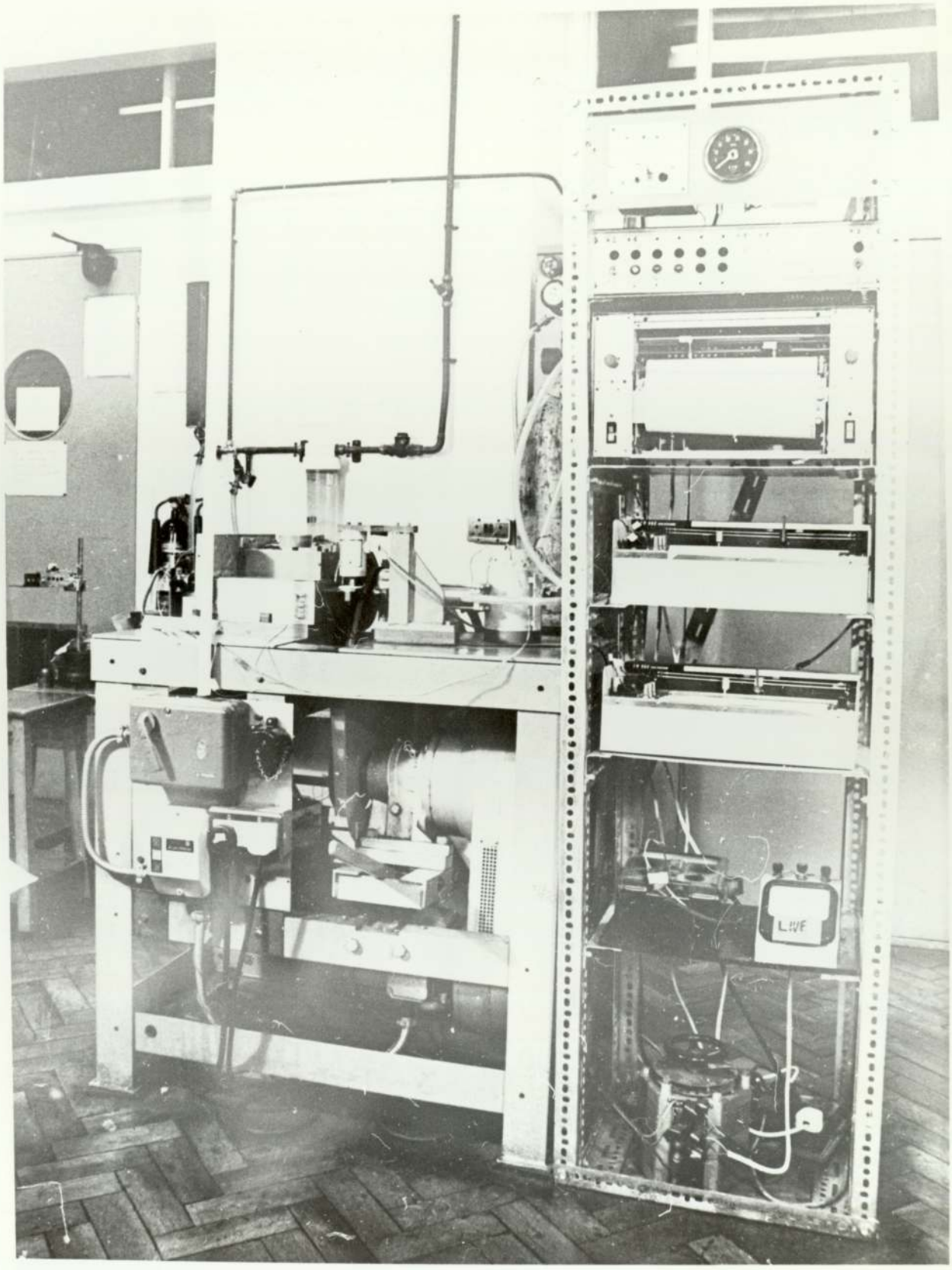

FIGURE 2.1 General View of the Pin on Disc Wear Test Rig.

copper slip rings, together with an insulating annulus and a securing plate, were mounted on a secondary shaft screwed into the main shaft.

The pin was held in a calorimeter fixed to the loading shaft. This shaft was mounted in linear and rotary bearings, in separate housings alongside the main shaft. See Figure 2.2. The loading shaft can move forward in its bearings when loaded and during the wearing process, and has the freedom to rotate slightly in order to measure the frictional force on the pin. Loads of up to 170N could be applied pneumatically by an air piston mounted along the axis of the load shaft. Because of the difficulty in regulating small pressures, and problems of friction in the loading shaft bearings and seals due to debris contamination, a simple dead weight system was used for loads below 10N.

The bulk temperature of the disc was measured by a thermo-couple connected via carbon slip rings mounted on the main shaft. To prevent overheating at higher temperatures, the bearings of the main shaft are water cooled, and an asbestos insulating ring (30mm thick) was sandwiched between the disc and carbon slip rings.

A 3-phase, 4 H.P. electric motor, a variable speed pulley and a reduction gear-box provided the main driving mechanism for the machine. This gave a range of disc speeds of 60 to 1440 rpm corresponding to linear velocities in the range 0.31 to 7.5 $msec^{-1}$.

Accilary equipment consists of devices to measure and continuously record the various temperatures, wear rates, friction and speeds.

One of the criticisms of using a pin-on-disc is that trapped debris (between pin and disc) could affect the wear process. In this present work this particular problem is largely overcome by using a horizontal pin on a vertical disc. Hence the majority of the debris will fall away from the sliding interface due to gravity.

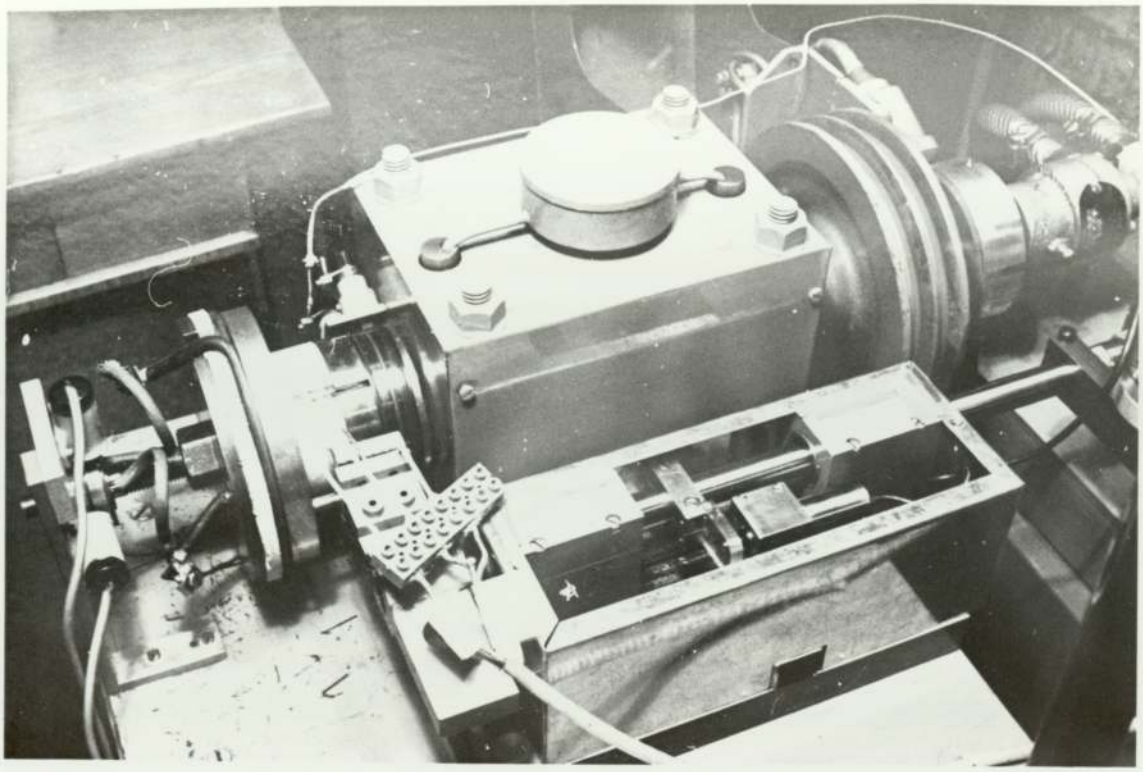

FIGURE 2.2 Pin Loading Assembly and the Heating Facility.

2.3 Wear Measurement

Equilibrium wear rate is expressed in this work as the volume of pin material removed per unit sliding distance (expressed as $m^3.m.^{-1}$). A Linear Voltage Differential Transformer (LVDT), which sensed the forward movement of a plate fixed to the load shaft, was used to measure wear on a continuous basis by means of a chart recorder. The sensitivity of the LVDT was 825mV per mm of distance moved by the pin as it wore down. The trace on the chart recorder gave the rate of decrease in the length of the pin and when multiplied by the cross-sectional area, the volume removed per unit time. Under equilibrium conditions, the slope of the trace divided by the linear track speed gave the volume removed per unit sliding distance, i.e. the wear rate.

Discrepancies are introduced in this method when the area of the pin increased, due to deformation of the pin surface. This occurred during either particularly severe wear or at the higher elevated disc temperature.

2.4 Friction Measurement

The frictional force of pin on disc was continously measured by a strain gauge dynamometer. The dynamometer was connected to the end of friction arm clamped to the loading shaft. This detected the torque exerted on the loading shaft by the frictional force. A miniature ball race was fitted to the dynamometer to act as a rolling line contact when the friction arm moved forward during the wearing process. Mechanical damping was introduced to reduce the effect of bouncing of the friction arm against the dynamometer. This was achieved by fixing a perpex strip to the friction arm. Output of the dynamometer was recorded via a strain gauge amplifier unit on the same chart as the wear trace on a 2-pen chart recorder. The sensitivity of the friction transducer was 25mV per 10N force on the pin.

By altering the sensitivities and chart speeds of the recorder, it was possible to resolve small variations in the wear and friction simultaneously.

2.5 Heat Flow

The cylindrical pin was held in a calorimeter, which enabled heat flow along the pin to be measured continuously. This is achieved by measuring temperatures at three positions along the pin with spot-welded chromel-alumel thermocouples. A schematic diagram illustrating the calorimeter is shown in Figure 2.3. This figure shows the three thermocouples T_1, T_2 and T_3 connected to the pin measuring temperatures T_A, T_B and T_C respectively. The cold junctions of the thermocouples were placed in a dewar of ice. Outputs from those thermocouples were connected to chart recorders for continuous monitoring. A method by which these temperatures were used in the Heat Flow Theory is given in reference 94. From this theory two parameters can be found, T_S the surface temperature of the pin and H_1 the heat flow per second at the interface. That is:

$$T_S = (T_A - T_C) \cosh \left(\frac{L_1}{ZR_t}\right) + \frac{ZH_2}{K_S \pi R_t} \sinh \left(\frac{L_1}{ZR_t}\right) + T_C \qquad (2.1)$$

and

$$H_1 = \frac{\pi R_t K_S}{Z} (T_A - T_C) \sinh \left(\frac{L1}{ZR_t}\right) + H_z \cosh \left(\frac{L_1}{ZR_t}\right) \qquad (2.2)$$

where :

$$Z = \left(\frac{K_s}{2R_t h_e}\right)^{\frac{1}{2}} \qquad (2.3)$$

h_e = heat transfer coefficient between cylindrical exposed surface of pin and the air

K_S = thermal conductivity of steel

R_t = radius of the pin

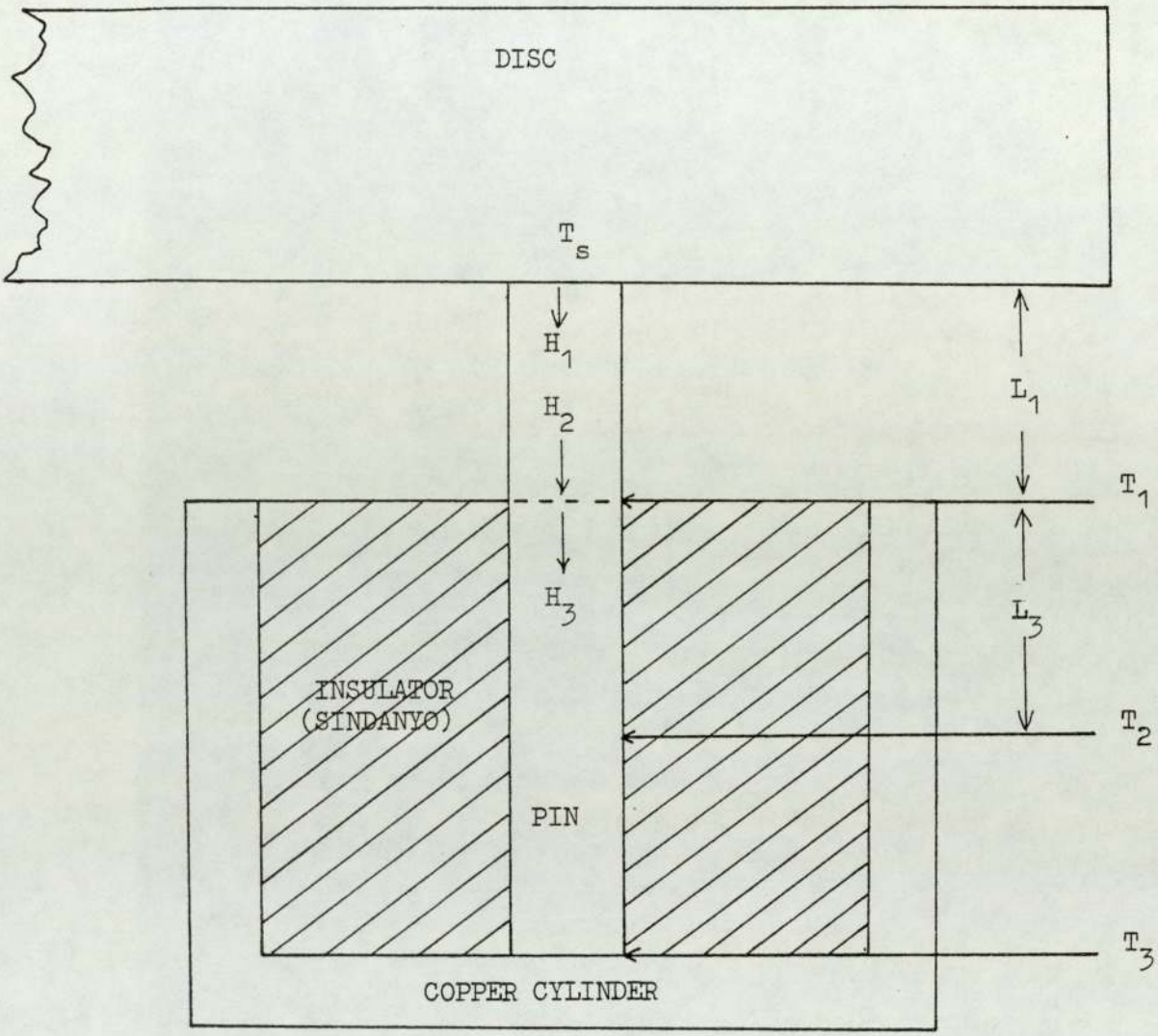

FIGURE 2.3 Cross-sectional diagram of the Pin and Pin-Holder showing Heat Flow and the Thermocouple Positions.

H_2 = heat flow per second entering the section of the pin where the thermocouple measuring T_A is conducting heat away

L_1 = length of pin exposed to the air between the holder and the disc

In the heat flow analysis, the values of K_S were taken at temperature T_A throughout. The variation of thermal conductivity of EN8 steel with temperature (95) is illustrated in Figure 2.4.

2.6 Specimen Materials

The wear of two low alloy medium-carbon steels, EN8 and EN31, was investigated in this work. The mass percentage composition of the alloys in these steels was as follows:

	C	Si	Mn	S	P	Cr	Fe
EN 8 (%)	0.35-0.45	0.05-0.35	0.6-1.0	0.06Max	0.06	-	Remainder
EN31 (%)	0.9 -1.2	0.1 -0.35	0.3-0.75	0.06Max	0.06Max	1-1.6	Remainder

Both EN8 and EN31 were used as pin material, but only EN8 as disc material throughout the experiments.

2.7 Specimen Preparation

The pins were 3.81cm in length and 0.625cm in diameter and were taken from cold-rolled rods and turned to a smooth finish of about 5μm Centre Line Average (CLA). The bulk hardness of the EN8 and EN31 pins was 250±10VPN and 280±10VPN respectively. Discs were cut from EN8 black bars and randomly ground to about 0.2±0.1μm CLA. The discs were 12cm diameter and 1.25cm thick. To provide specimens of the worn disc surface for analysis, two removable taper plugs were inserted into some of the discs. These could easily be removed by tapping out from the back face of the disc without damage to the surface. Bulk hardness of disc material was 200±10VPN.

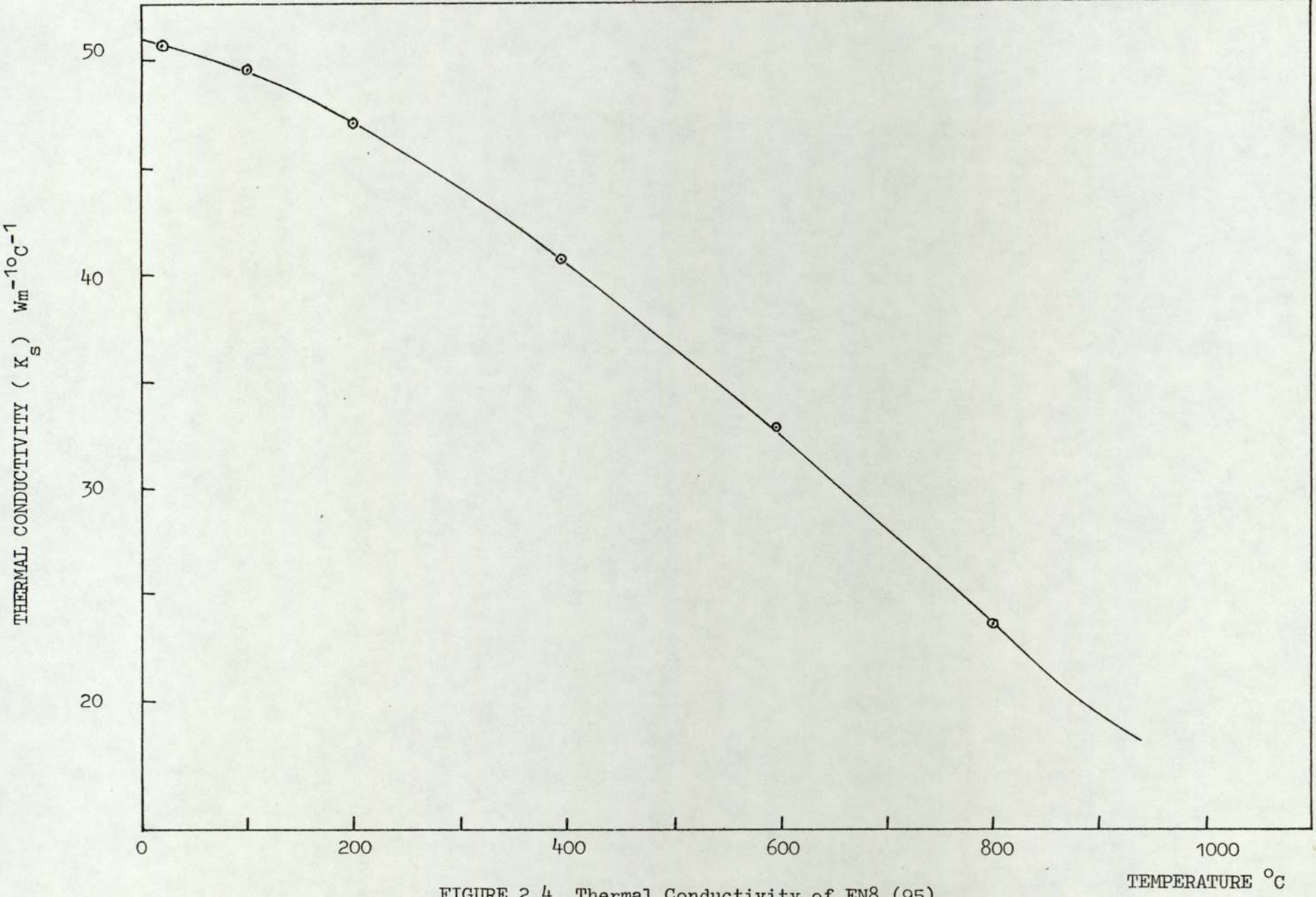

FIGURE 2.4 Thermal Conductivity of EN8 (95).

Before each run, both the pin and disc were washed in warm soapy water and rinsed in clean water. After this, they were thoroughly decreased in acetone and petroleum ether before being carefully mounted on the wear test machine.

2.8 Wear Tests

2.8.1 Room Temperature

Experiments were carried out at various loads between 4.9N and 120N, at a constant sliding speed of $2ms^{-1}$. Wear debris was collected when the initial severe wear rate gave way to a much milder wear rate after the surface had "run-in". This transition to mild wear was marked by a fall in the frictional force, the "levelling-off" of the pin temperatures, and more than an order of magnitude decrease in the wear rate. The severe wear rate was always associated with large metallic debris, while the mild wear rate was always associated with small oxidised wear debris. Normally equilibrium conditions were obtained after about half an hour.

2.8.2 Elevated Temperature

In these wear experiments, at a constant speed of $2ms^{-1}$, the disc temperature was raised by external electrical heating. The experiments were carried out at loads in the range 4.9N to 160N and at bulk disc temperature of 100,200, 300, 400 and 500°C. At the start of each elevated temperature run, the bulk disc temperature was raised to the desired value and maintained for about 15 minutes. When the load was applied to the pin, the voltage of the heater was reduced to compensate for the temperature rise of the disc due to frictional heating. The wear debris was collected once equilibrium conditions were reached.

2.9 Hardness and Microhardness Measurement

The microhardness of the worn pin and disc surfaces were measured using a Miniload Hardness Tester. The impressions were made by means of a diamond indenter, with a load of 100 or 200 grams. Because of the difficulty encountered in measuring microhardness on rough surfaces, it was too time consuming to carry out measurements on all of the pins and discs.

Bulk hardness of the worn pin surfaces were measured using a Vickers Hardness Tester for some selected experiments. The indentation load used throughout was 20Kg. All hardness readings were taken cold after completion of the relevant wear experiment.

Microhardness as a function of depth was measured from tapered microsections through worn pin surfaces. The specimens were prepared by moulding into conducting bakelite and tapered using 180, 240, 400, 600 and 1200 grit SiC abrasive paper (wet). This was followed by final polishing with 6μm and 1μm diamond wheels. Taper angles of about 10° were used throughout. The subsurface microstructure was examined after etching with 2% nital solution.

Hot bulk hardness were measured by Lucas Research Centre, West Midlands, on both EN8 and EN31 samples. Tests were carried out over a range of temperatures from $100^{\circ}C$ to $800^{\circ}C$. The variation of hot hardness with temperature for both EN8 and EN31 materials is illustrated in Figure 2.5. Unfortunately the hot hardness values obtained for EN31 material had an initial bulk hardness which was lower than that used in this work, i.e. 204VPN. The broken curve shown in Figure 2.5 was taken to represent the hardness/temperature variation for EN31 material having an initial bulk hardness of 280VPN.

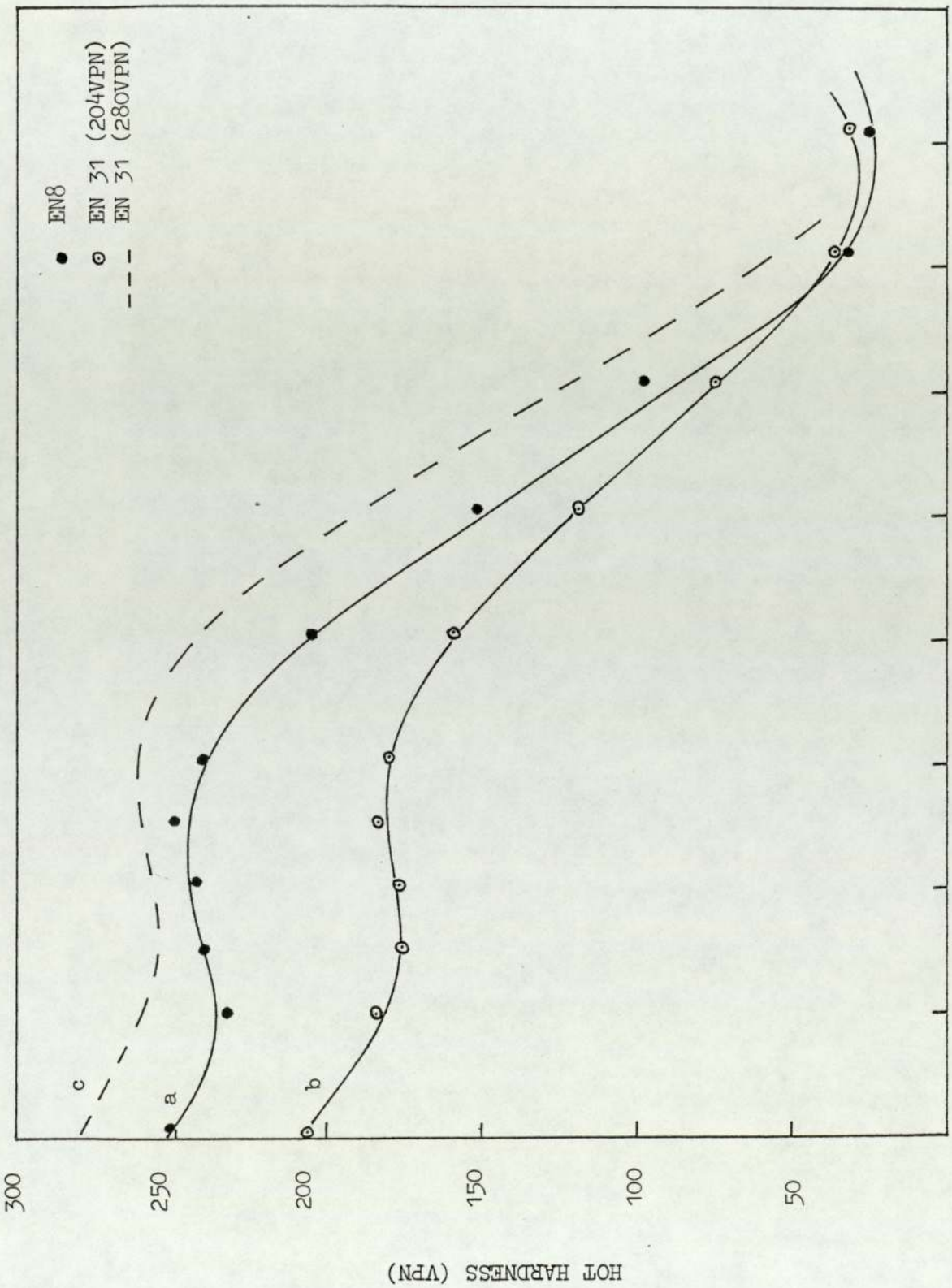

FIGURE 2.5 Hot Hardness Versus Temperature Curves for EN8 and EN31 Materials.

2.10 Surface Profile Measurements

Surface profiles of worn discs were measured using a Taylor-Hobson Talysurf. This comprises a stylus, mechanical system, electronic unit and a recording device. The vertical movements of the stylus relative to a suitable mechanical datum are magnified and a record made (this recording is usually referred to as a profile graph). The stylus was a pyramidal diamond with a rounded tip of 0.0001 inch (2.5μm) radius. Because of the mechanical arrangement of the instrument, difficulties arose when the surface profiles of the worn pins was measured.

Wear rate of the disc was estimated from the profile of the wear track. The volume of material removed from the disc, wear volume ω_D, was calculated according to the following equation:

$$\omega_D = \left(\frac{\Sigma Si}{m}\right) 2\pi R_m \qquad (2.4)$$

where Si was loss area of profile, m was the number of profiles taken from the disc and R_m is the mean radius of the wear track. The loss area was measured by a planimeter. The ratio of wear volume (m^3) to the total distance slid in metres by the pin gives the wear rate for the disc in $m^3 m^{-1}$.

2.11 X-Ray Analysis

The wear debris collected during the experiments was examined using an X-ray diffraction technique. A conventional 114.6mm diameter powder camera was used for the analysis. This enabled values of 2θ, where θ is the Bragg angle, to be measured directly from the film. Wear debris was placed inside a thin-walled glass capillary of 0.5mm diameter and irradiated with filtered Cobalt Kα radiation. Cobalt Kα radiation was used because its wavelength was longer than the K absorption edge of iron, therefore the mass absorption coefficient of the iron was relatively low.

The unwanted Kβ component which has a shorter wavelength was absorbed by an iron filter. The x-ray tube was operated at a potential and filament current of 40kV and 30mA respectively, and exposure times of about 45 minutes were used. The interplanar spacings (d_{hkl}) obtained from the powder pattern were compared with the interplanar spacings noted in the x-ray powder data file issued by the American Society for Testing and Materials (ASTM).

A glancing angle x-ray diffraction technique was used for some selected worn pin surfaces. The specimen was positioned in the powder camera so that the x-ray beam impinges on an edge of the surface. Cobalt Kα x-rays were used to irradiate the desired area of the specimen, at an x-ray tube setting of 40kV and 30mA, for one hour. Typically, the glancing angle used throughout was about 30°. At this angle, the maximum depth of penetration of the x-rays was about 20μm (96).

The line profile of each pattern was obtained using a microdensitometer. This instrument produces linear density profiles and the "density versus 2θ "curves obtained from the debris are directly proportional to the x-ray intensity. The relative integrated intensities of the diffraction lines can be determined from the product of "peak height" times "width of the peak at half its height" (97).

2.12 Scanning Electron Microscopy

A scanning electron microscope (SEM) was used for topographical study of the worn surfaces. In this instrument, a narrow beam of electrons is scanned across the specimen in a T.V. type raster, and the secondary electrons created by the scanning beam are utilised to give a picture of the specimen surface. The major advantages of the machine are that it has a very large effective depth of focus and after a little practice, studying surfaces with known topographical features, the micrographs can be easily

interpreted. The specimens required no special preparation apart from cementing them onto specimen holders provided, ensuring an electrical contact between the specimen and specimen holder.

With the aid of specimen tilt correction control, oxide film thickness were measured from the specimen micrographs. The tilt correction control unified the magnification over the area of the specimen under study, i.e. the vertical magnification was equal to the horizontal magnification. Only those oxide edges were selected which corresponded to the general oxide film thickness on the worn surface.

The wear debris particles were also examined directly with the scanning electron microscope. They were mounted by sprinkling them onto the surface of aqueous carbon which was placed on an aluminium specimen holder. This simple procedure was sufficient to fix them in position and to prevent charging.

2.13 Auger Electron Spectroscopy

Auger electron spectroscopy (AES) was used on some selected worn pin surfaces using a Kratos XSAM 800 instrument. The XSAM 800 is based on a hemispherical electrostatic electron energy analyser but it is fitted with a sophisticated electron optical system which is designed to combine high performance X-ray Photoelectron Spectroscopy (XPS) with high transmission Scanning Auger Microprobe (SAM), hence the name 'XSAM'.

The technique of AES was employed to study concentration-depth profiles of worn pins. Composition profiles were obtained after successive removal of atomic layers from the surface by sputtering with 2kV argon ions at a gas pressure of 5×10^{-5} torr. At this gas pressure the total ion current impinging the specimen was approximately 30±5 μamps.

All the Auger spectra were taken at an incident electron beam energy of 5keV. Approximate values for the relative concentration of the elements were obtained by measuring the peak-to-peak heights of selected Auger peaks and incorporating the appropriate sensitivity factors (98).

CHAPTER 3

EXPERIMENTAL RESULTS

3.1 Introduction

Friction and wear results, together with the results of various physical and metallographical techniques of analysis used to examine worn specimens and debris, are described in this chapter. In Section 3.2, the equilibrium wear results obtained for a series of wear tests are discussed extensively, and Section 3.4 gives the results of heat flow analysis performed on the pins. Hardness measurements and x-ray diffraction results are given in Sections 3.5 and 3.7 respectively. The technique of proportional analysis of wear debris is examined in Section 3.9, using pre-mixed samples of known concentrations. In the examination of worn specimens and wear debris, scanning electron microscopy was found most useful. The results obtained from this technique are discussed fully in Section 3.10. This section presents a selection of scanning electron micrographs of worn pin and disc surfaces to illustrate how the surface changed with applied load and temperature. In Section 3.11, the results of Auger electron spectroscopy are described in detail.

3.2 Wear

This section describes the wear results of EN8 and EN31 steels over a range of loads from 4.9N to 160N with no external heating and at constant disc temperature T_D of 100, 200, 300, 400 and 500°C. The experiments which were carried out with no external heating of the disc will be referred to as room temperature wear experiments. Those experiments which were carried out with external heating will be referred to as elevated temperature wear experiments. The graphs of the log wear rate against log applied load for EN8 and EN31 are shown in Figures 3.1 and 3.2 respectively.

3.2.1 Room Temperature Wear of EN8

From the room temperature wear results illustrated in Figure 3.1(a), it can be seen that the wear rate increases with applied load, and no transitional behaviour in the wear curve was observed. Initial severe running-in wear was always very high before mild wear was established. The wear debris, once equilibrium conditions prevailed, consisted of black oxide particles with traces of bright metallic particles. For loads up to 40N, the worn surfaces had a dull appearance and were covered with loose, black oxide particles. At 58.9N (not shown in Figure 3.1(a)), the running-in wear was so catastrophic, producing large metallic particles, that the experiment was terminated after only 10 minutes. The surface of the pin had experienced plastic flow causing considerable widening of the disc wear track. Because of the limitations of the rig, a longer pin could not be used to enable equilibrium wear to be established. Macroscopic islands of metallic transfer were clearly visible on the wear track of the disc at this particular load.

3.2.2 Elevated Temperature Wear of EN8

(i) $T_D = 100^{\circ}C$

The room temperature wear behaviour of EN8 sliding at $2m.s^{-1}$ was characterised by a distinctly non-transitional and a directly load dependent wear pattern. However, the effect of raising the disc temperature to 100°C was to induce a transition in the wear rate curve at 10N, as shown in Figure 3.1(a). At this transition the wear rate increases from $1.0 \times 10^{-13} m^3.m^{-1}$, to approximately $4.0 \times 10^{-13} m^3.m^{-1}$. For experiments carried out below this transition load, the surfaces were heavily oxidised and the wear debris was mainly brown in colour with traces of bright metallic particles. At the transition, the debris changed character and consisted of black oxidised particles. The appearance of worn surfaces, above the transition, was similar to room temperature experiments.

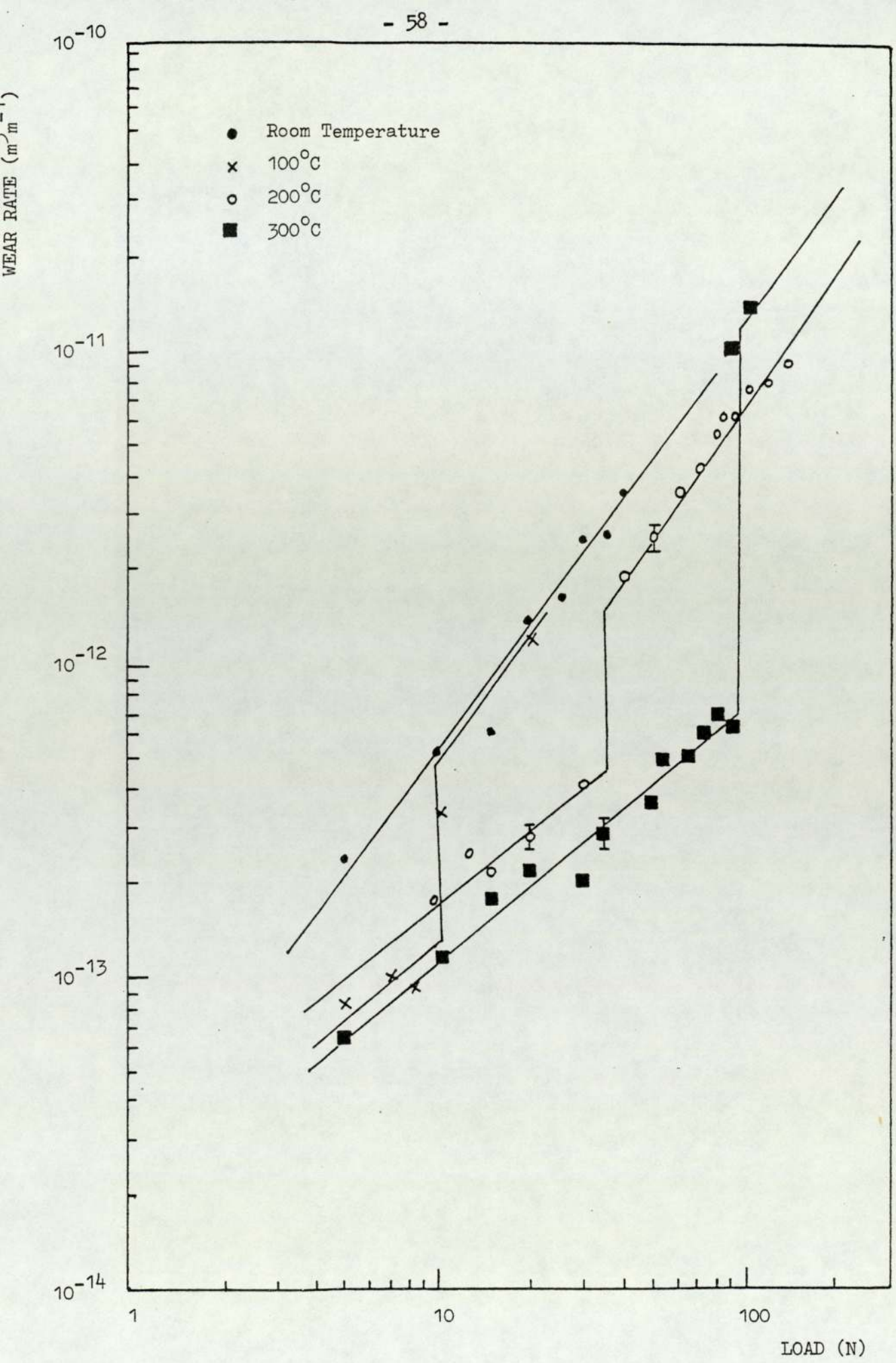

FIGURE 3.1(a) Wear Behaviour of EN8 at Room Temperature, 100°C, 200°C and 300°C.

(ii) T_D = 200°C

The effect of increasing the bulk disc temperature to 200°C by external heating was to increase the transition load observed at 100° C by about 25N. See Figure 3.1(a). At this transition the wear debris changed colour from brown to black. The wear rates above and below this transition were load dependent.

(iii) T_D = 300°C

The transition in the wear curve occurred at a load of 98.1N, as shown in Figure 3.1(a). In experiments below this load, the wear debris again consisted of red-brown oxide particles. Plastic deformation of the pin surface had taken place at 98.1N applied load and evidence of metallic transfer could be seen on the disc wear track. The debris at this load was metallic with black oxide particles. The wear rate for the 88.3N load experiment showed a transitory behaviour. The initial wear rate for a period of about one hour was very high with debris similar to 98.1N experiment. It then dropped by an order of magnitude and the debris changed character and consisted of light brown oxide particles. Both wear rates are plotted in Figure 3.1(a).

(iv) T_D = 400°C and 500°C

The wear behaviour of 400°C and 500°C, as shown in Figures 3.1(b) and (c) respectively, was non-transitional and load dependent. During the initial running-in period a negative wear rate was recorded due to thermal expansion of the pin. The debris was very fine red powder. Worn surfaces were heavily oxidised.

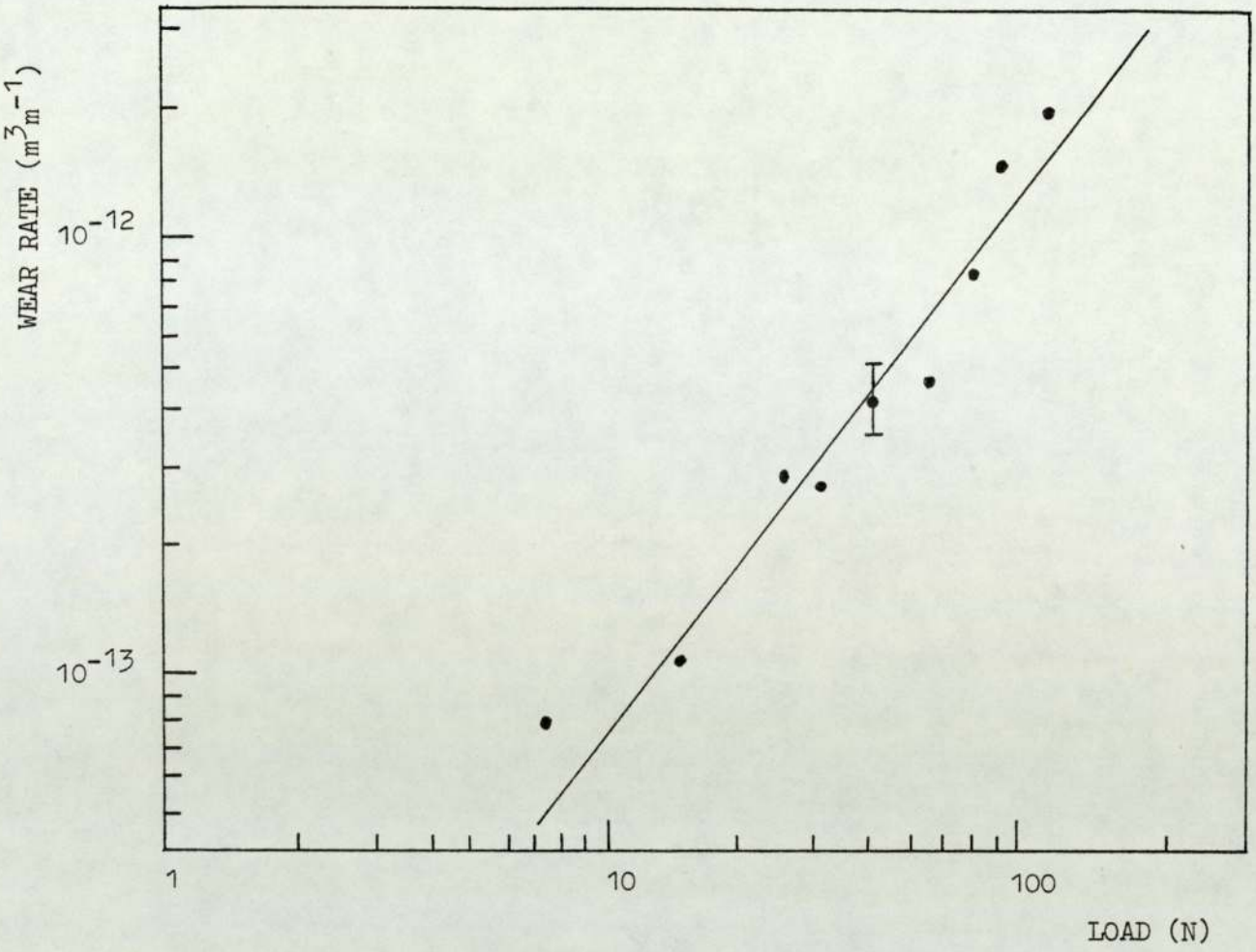

FIGURE 3.1(b) Wear Behaviour of EN8 at 400°C.

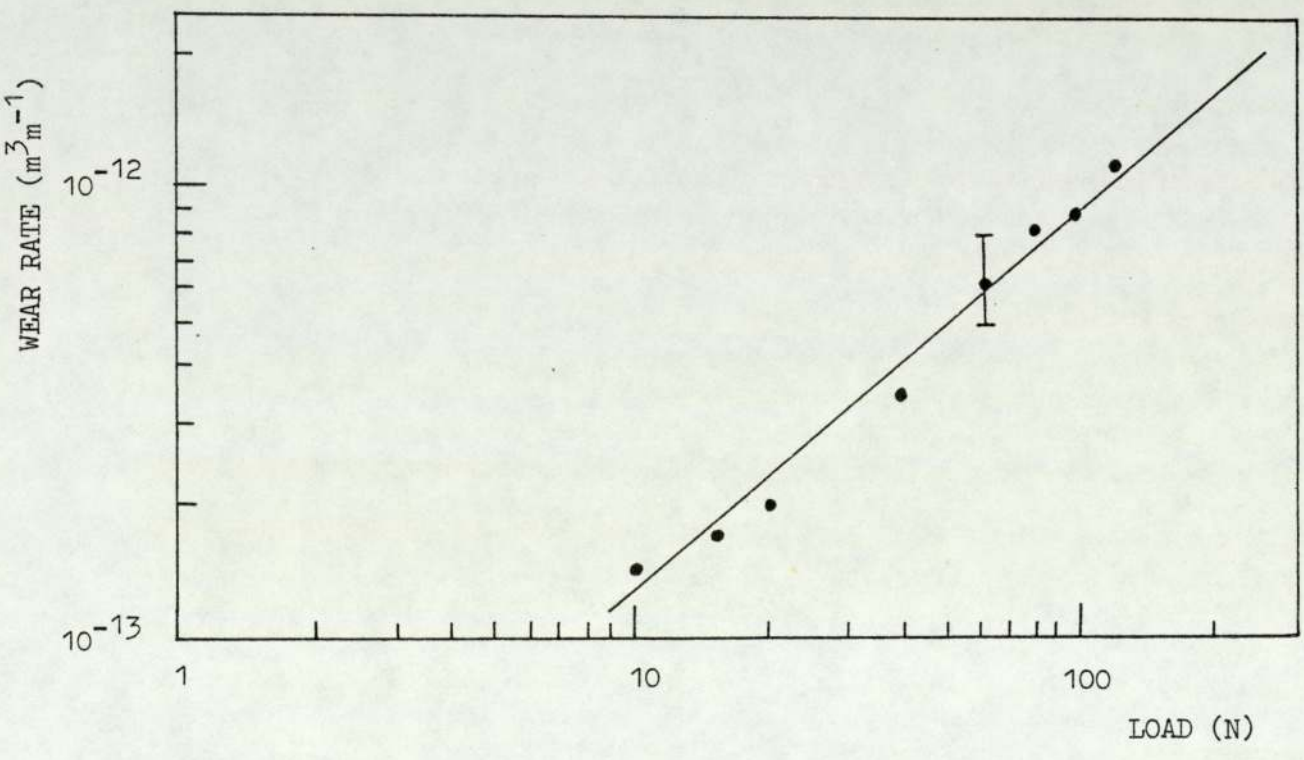

FIGURE 3.1(c) Wear Behaviour of EN8 at 500°C.

3.2.3 Room Temperature Wear of EN31

The wear behaviour of EN31 at room temperature was characterised by three distinct wear regimes as shown in Figure 3.2(a). In the first wear regime, at loads below 30N, the wear rate was strongly load dependent. The wear debris produced in this load range consisted of light brown oxide particles. Traces of metallic particles were also present in the debris, particularly so at low loads.

In the second wear regime, occurring between 30-80N, a decrease in the slope of the wear rate curve was noted. Experiments carried out in this load range were characterised by highly oxidised worn surfaces and production of fine dark brown wear debris. Another important feature of this wear regime was the fall in pin temperature once equilibrium wear was established. For example, in the 58.9N load experiment a fall of 55°C was recorded in temperature T_A measured by thermocouple T_1 (see Figure 2.3). Accompanying this fall was an increase of 30°C in the temperature T_D. The conclusion drawn from these observations was that a thick oxide film had developed on the wearing pin surface causing more frictional heat to flow into the disc. Results obtained from scanning electron microscopy and Auger electron spectroscopy verify this hypothesis.

Finally, in the third wear regime, occurring at loads greater than 80N, the wear rate once again was strongly dependent on load. The debris from these set of experiments consisted of black oxides with traces of bright metallic particles. Worn surfaces had a metallic appearance and were covered with loose black oxide particles.

3.2.4 Elevated Temperature Wear of EN31

(i) $T_D = 100°C$

The general characteristic wear behaviour was very much similar to that obtained with room

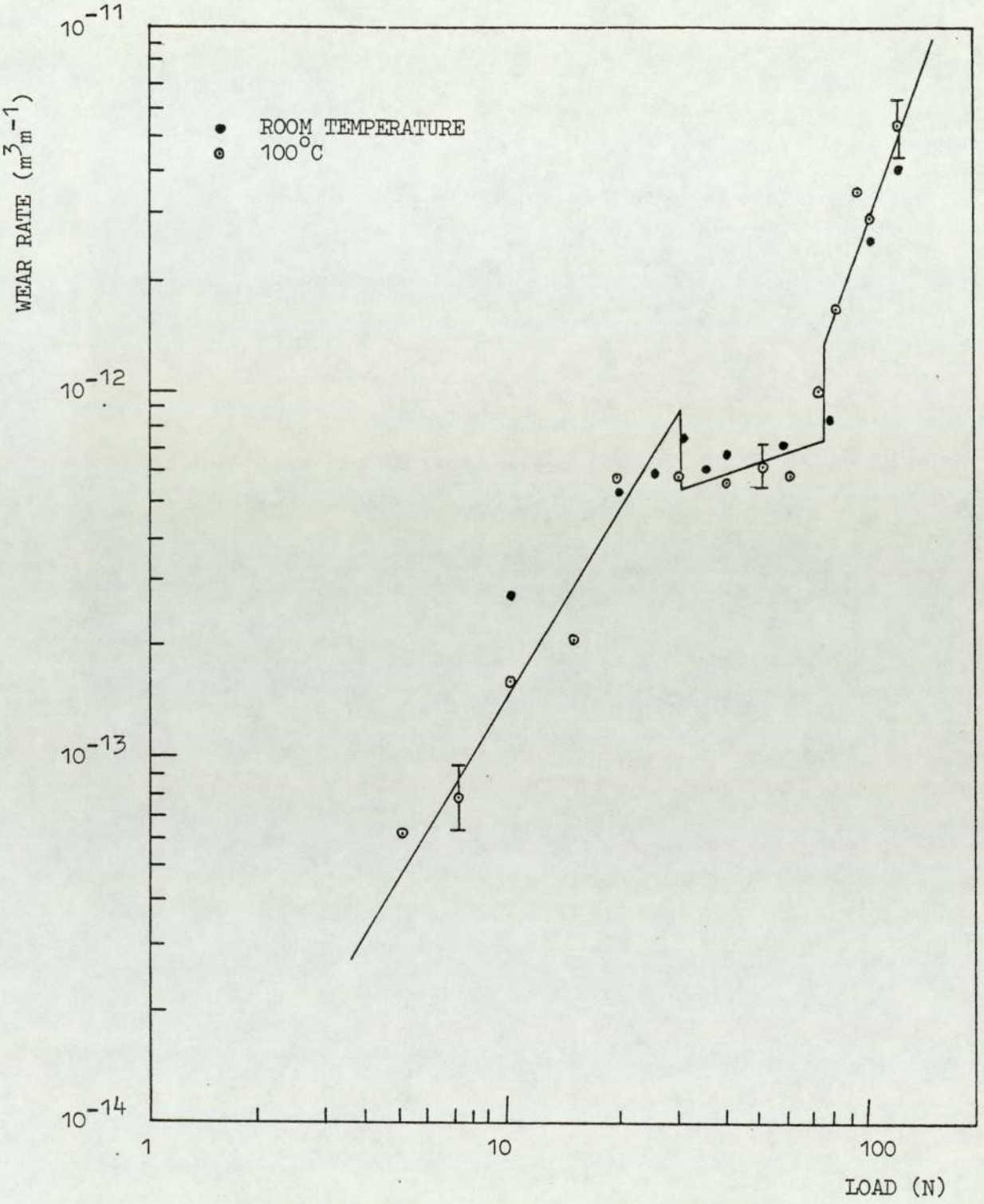

FIGURE 3.2(a) Wear Behaviour of EN31 at Room Temperature and 100°C.

temperature wear experiments. See Figure 3.2(a). External heating was only applied to experiments carried out at loads below 60N. At higher loads frictional heating was sufficient to take the disc temperature in excess of 100°C. The combined effect of frictional and external heating at low loads resulted in a small reduction in the wear rates.

(ii) T_D = 200°C

The effect of elevating the disc temperature to 200°C has produced some significant change in the wear behaviour of EN31, as shown by Figure 3.2(b). Only a single less well defined transition takes place in the wear pattern, and lies at a load a little over 80N. The wear rate on either side of the transition was load dependent. At low loads, the wear debris was light brown in colour but became darker brown as the load increased. Above the transition, the debris consisted of black oxide particles.

(iii) T_D = 300°C

Wear debris collected in experiments carried out at loads less than 120N was light brown in colour but became darker brown as the load increased. Worn surfaces were heavily oxidised giving a dull appearance. At 157.0N load the wear rate increased abruptly (see Figure 3.2(b)) but no characteristic change was observed in the wear debris, i.e. colour of debris was similar to that observed in the 117.7N experiment. Limitations of the rig prevented the carrying out of experiments at loads greater than 157.0N.

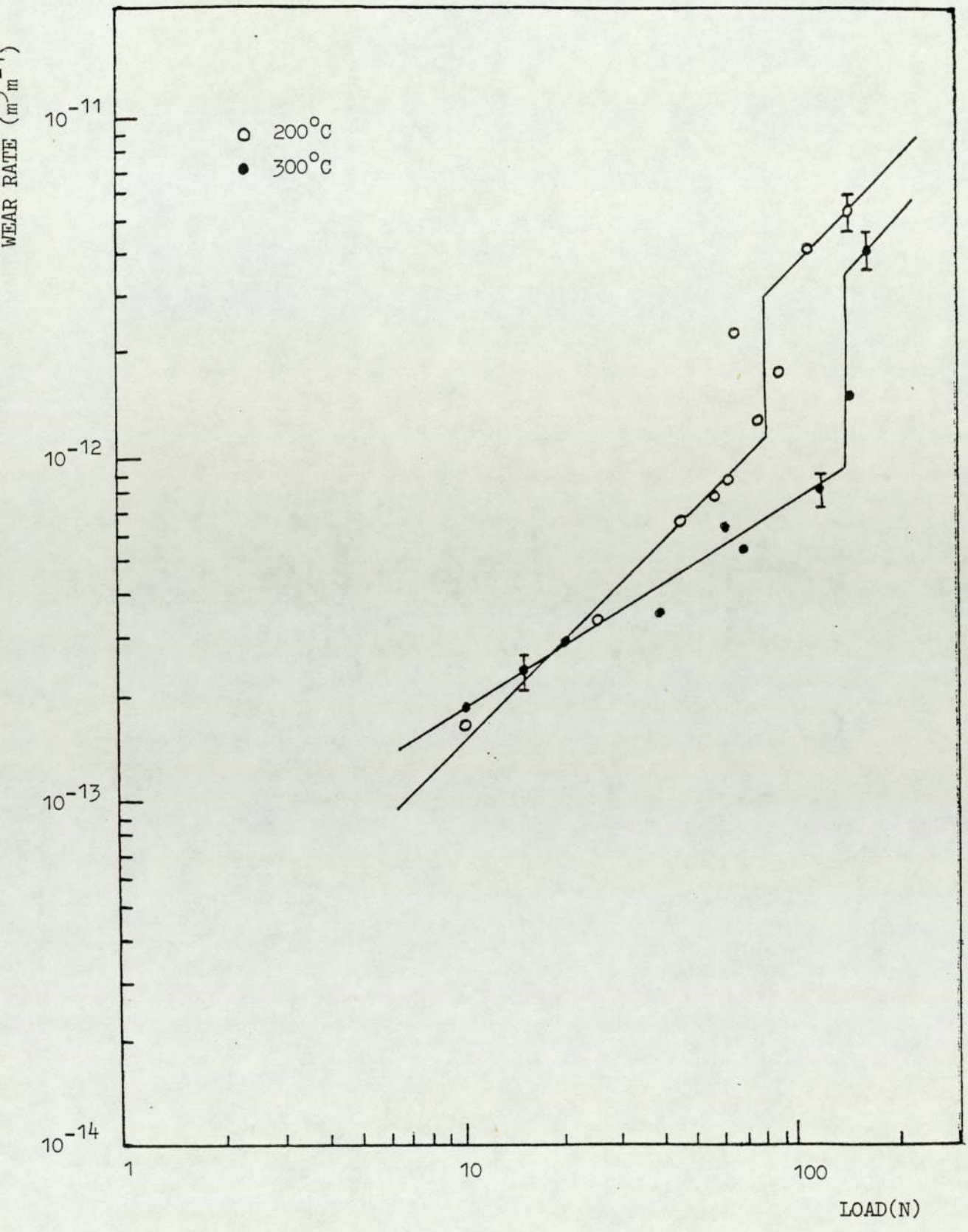

FIGURE 3.2 (b) Wear Behaviour of EN31 at 200°C and 300°C.

(iv) T_D = 400°C and 500°C

The wear results for 400°C and 500°C are shown in Figures 3.2(c) and 3.2(d) respectively. The general wear behaviour was similar to that obtained with EN8 at 400°C and 500°C, that is, the wear rate increased without obvious transitions. The debris from these experiments was very fine red powder and worn surfaces were heavily oxidised.

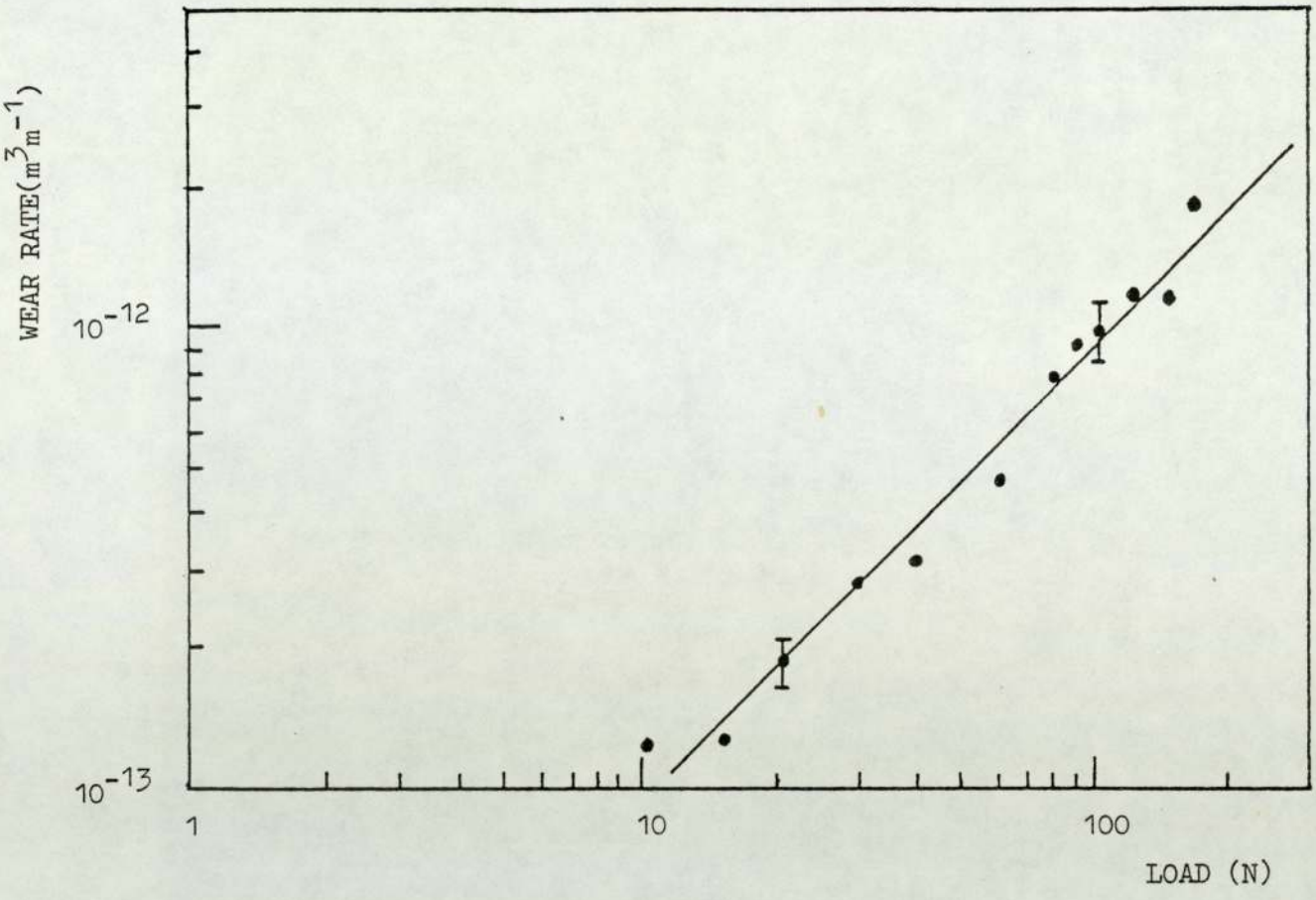

FIGURE 3.2 (c) Wear Behaviour of EN31 at 400°C.

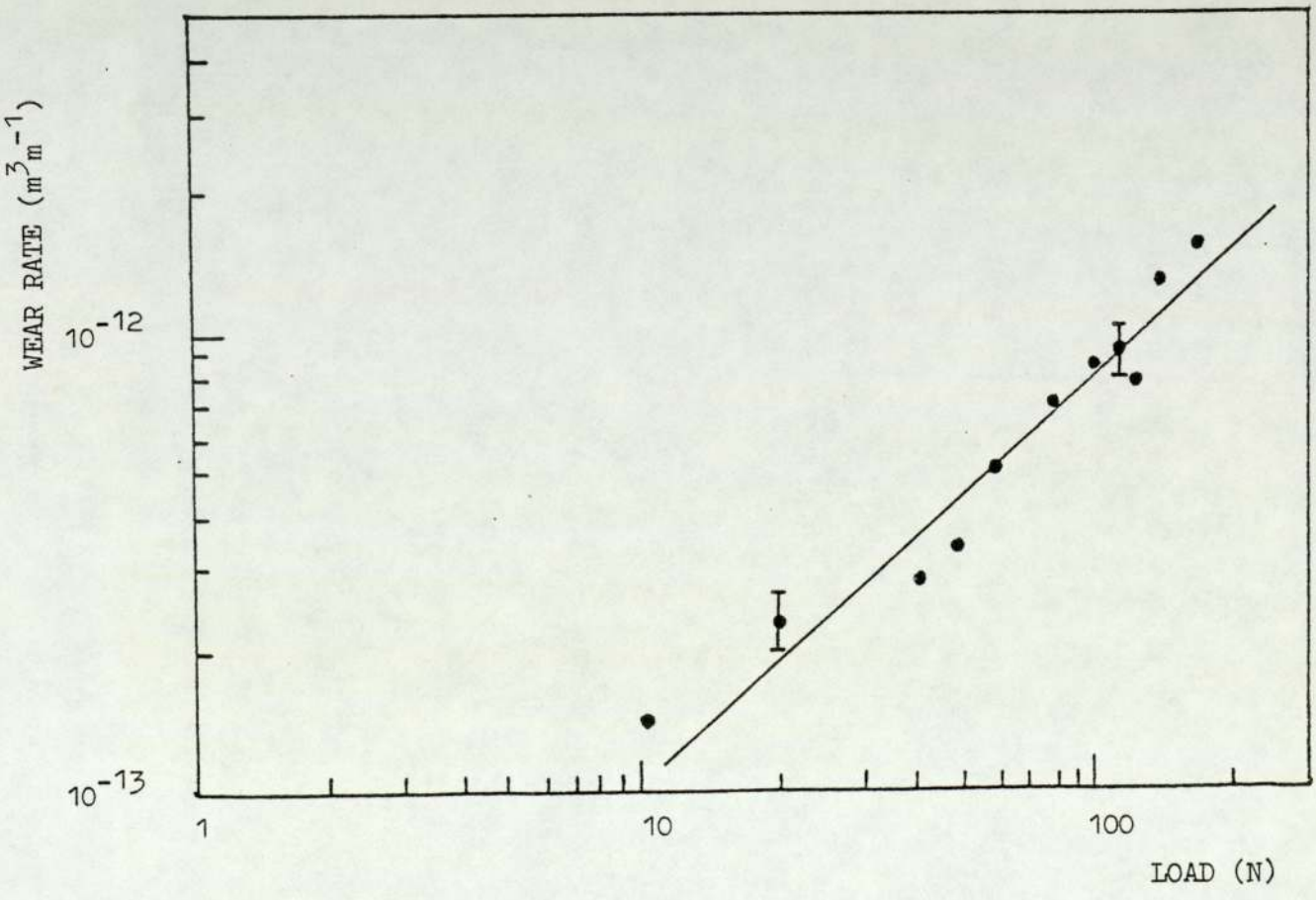

FIGURE 3.2 (d) Wear Behaviour of EN31 at 500°C.

3.2.5 Disc Wear

The wear rate of the disc versus load graphs for 200°C, 300°C, 400°C and 500°C EN8 experiments are shown in Figures 3.3(a), (b), (c) and (d) respectively. Disc wear rates versus load graphs for room temperature, 100°C, 200°C and 400°C EN31 experiments are shown in Figures 3.4(a), (b), (c) and (d) respectively. The values plotted are the mean of at least three separate talysurf measurements made on the disc wear track. Since this method includes the initial running-in severe wear, only a semi-quantitative assessment can be made for the disc wear. In general, the wear rate of the disc increases with applied load and was comparable in magnitude with that of the pin.

3.3 Friction

The frictional force was measured continuously for all the experiments in this present work. In general, during the running-in period, the friction had a very erratic behaviour and coefficient of friction values of 1 or greater were observed. However, once equilibrium conditions were established, the frictional force attained a reasonably stable value. For externally heated experiments, especially at 400°C and 500°C, the initial severe wear was very rapid and continuous sparking was evident from the pin/disc interface. This reduction in the amount of initial severe metallic wear was attributed to the pre-oxidised nature of the surfaces, i.e. before the start of each elevated temperature experiment the bulk disc temperature was raised to the desired value and maintained for about 15 minutes. This reduces the probability of metallic adhesion between the surfaces. The friction values referred to in this section are the steady-state values. Any changes occurring on the pin surface, such as oxide removal, were reflected by variation in the frictional force and mechanical noise of the rubbing.

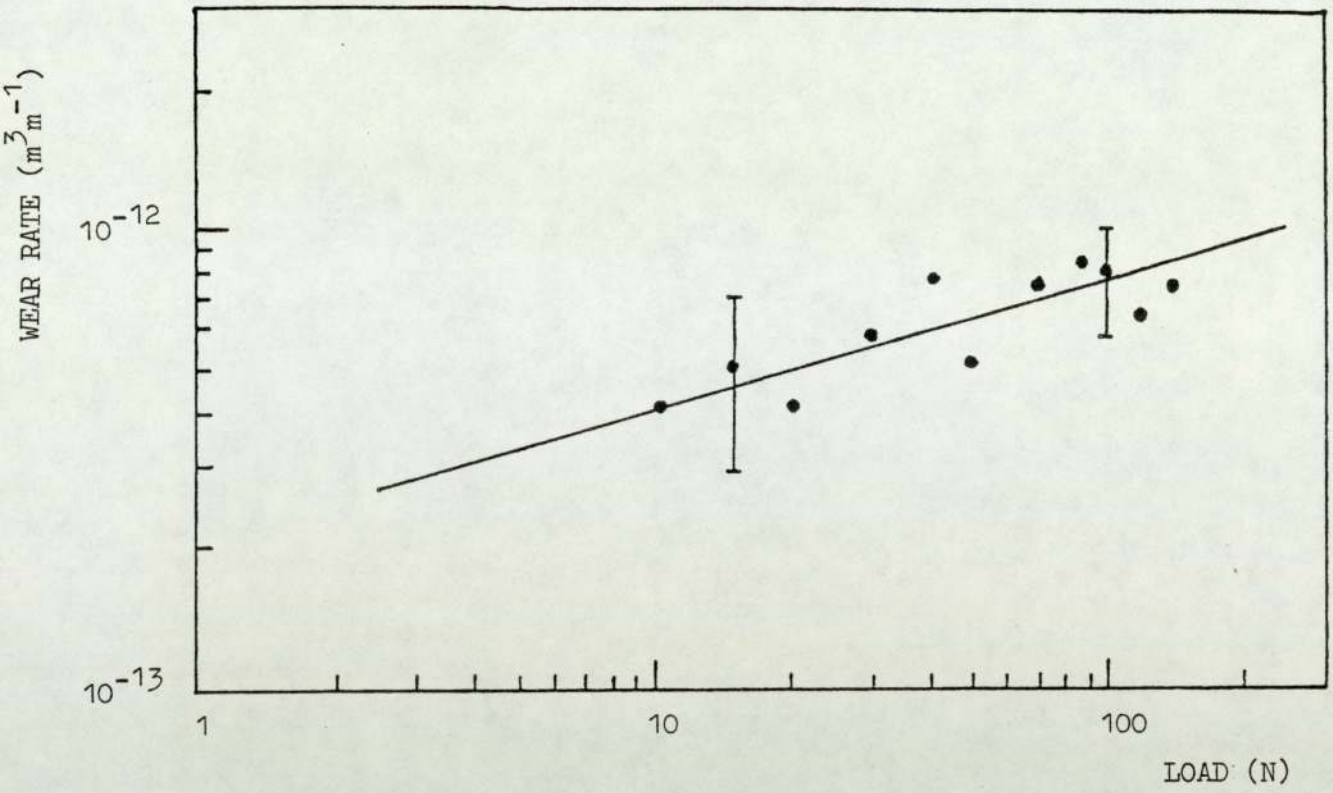

FIGURE 3.3(a) Disc Wear Rate Versus Load for EN8 at 200°c.

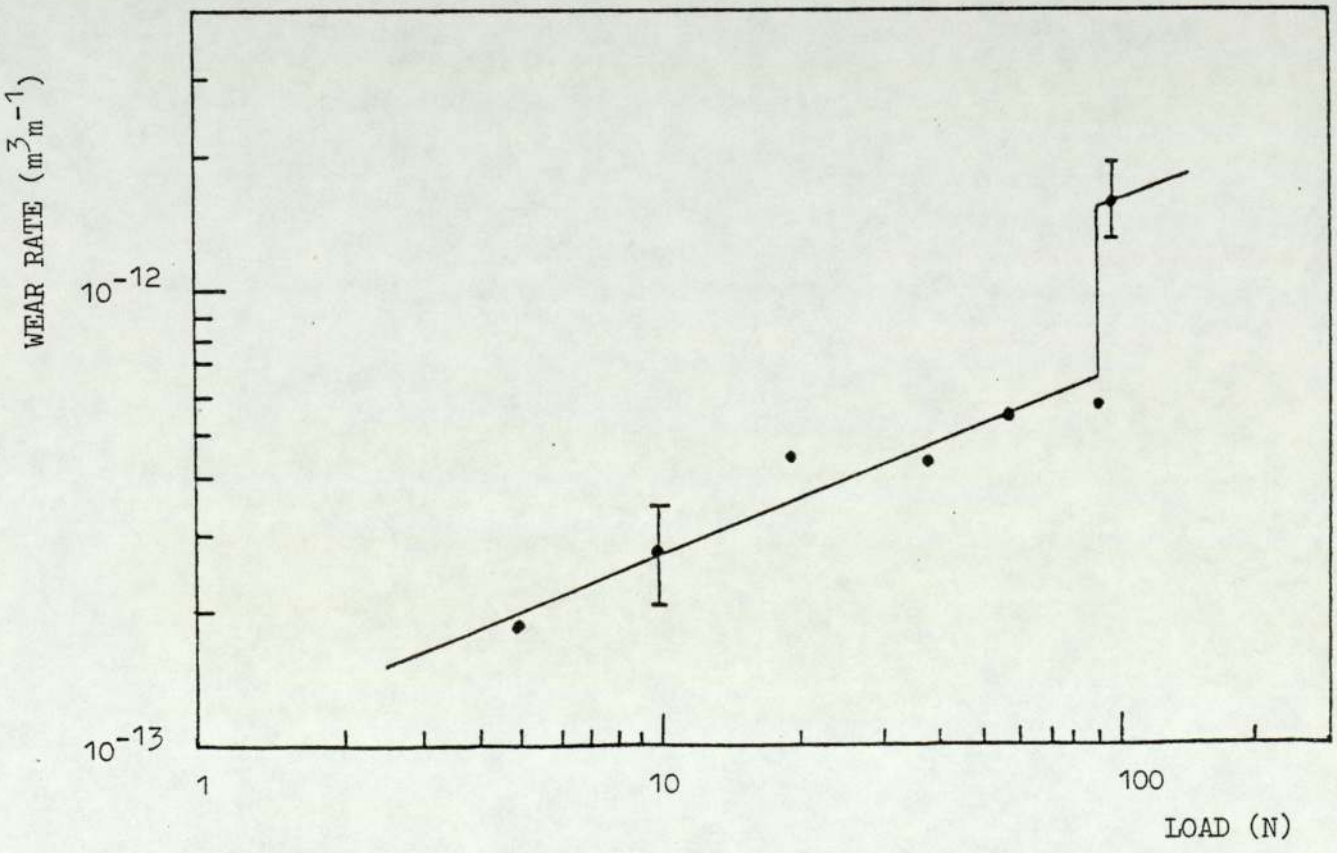

FIGURE 3.3(b) Disc Wear Rate Versus Load for EN8 at 300°C.

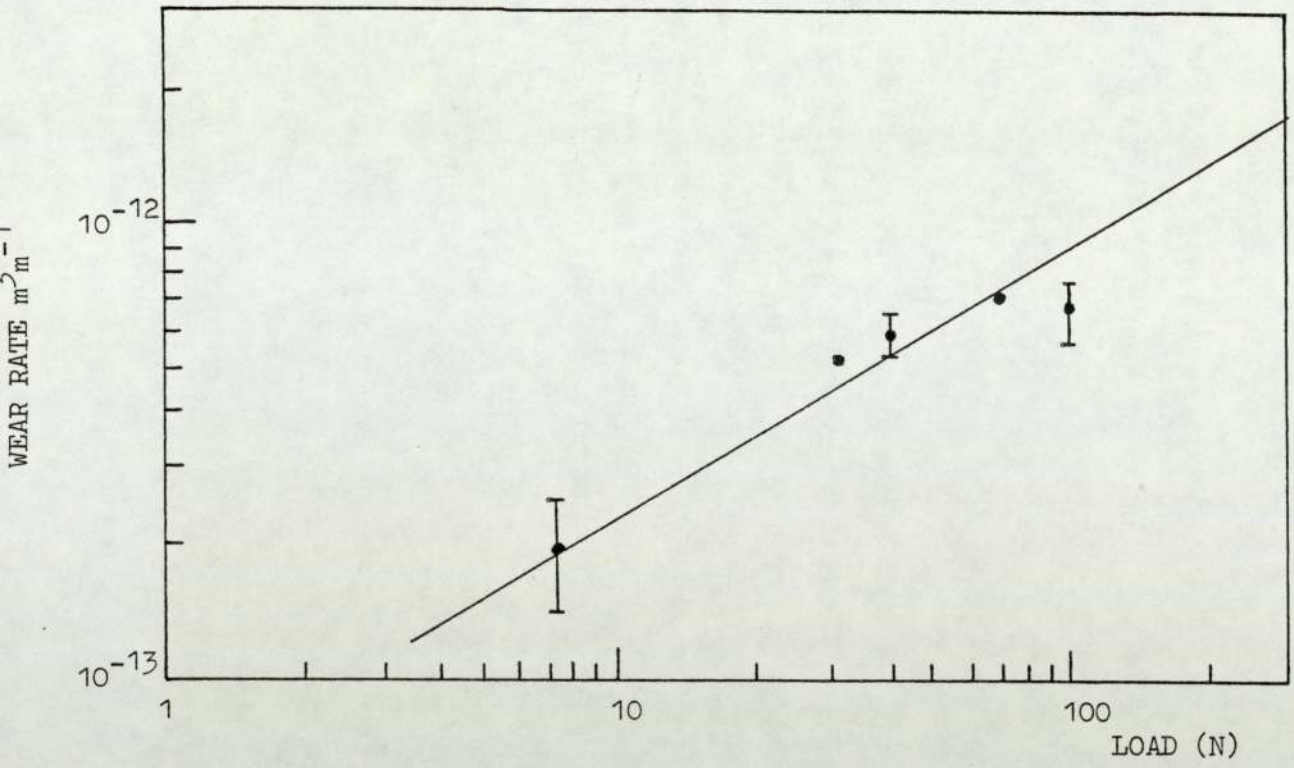

FIGURE 3.3(c) Disc Wear Rate Versus Load for EN8 at 400°C.

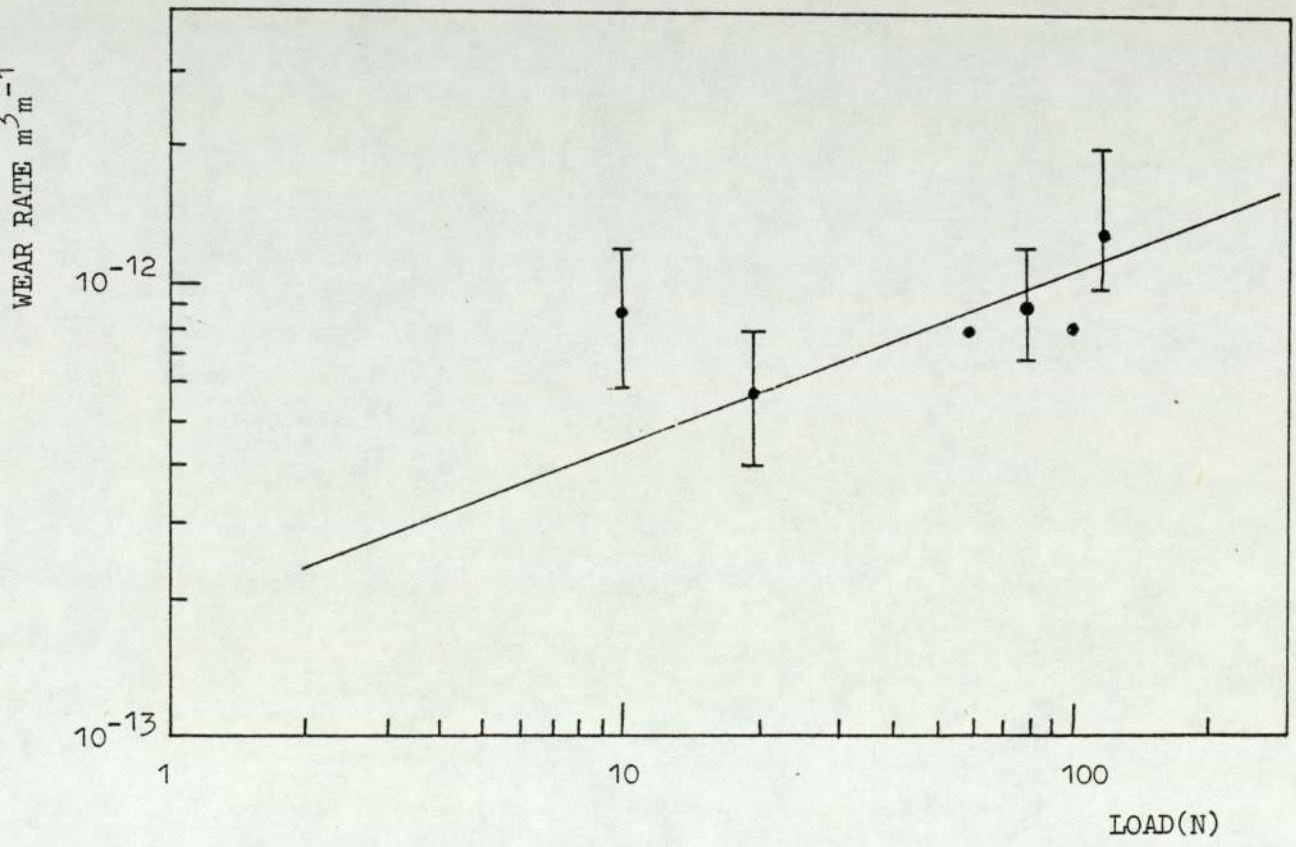

FIGURE 3.3(d) Disc Wear Rate Versus Load for EN8 at 500°C.

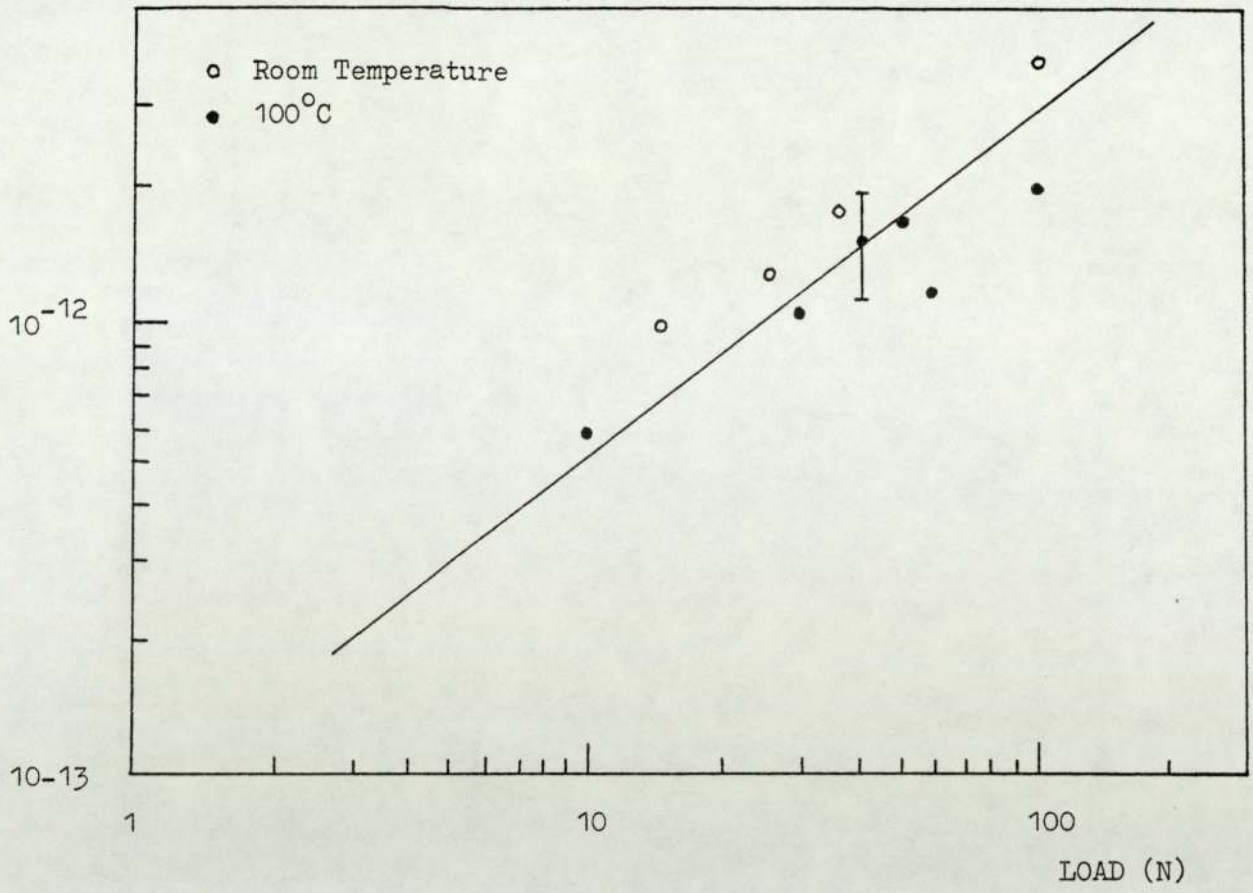

FIGURE 3.4(a) Disc Wear Rate Versus Load for EN31 at Room Temperature and 100°C.

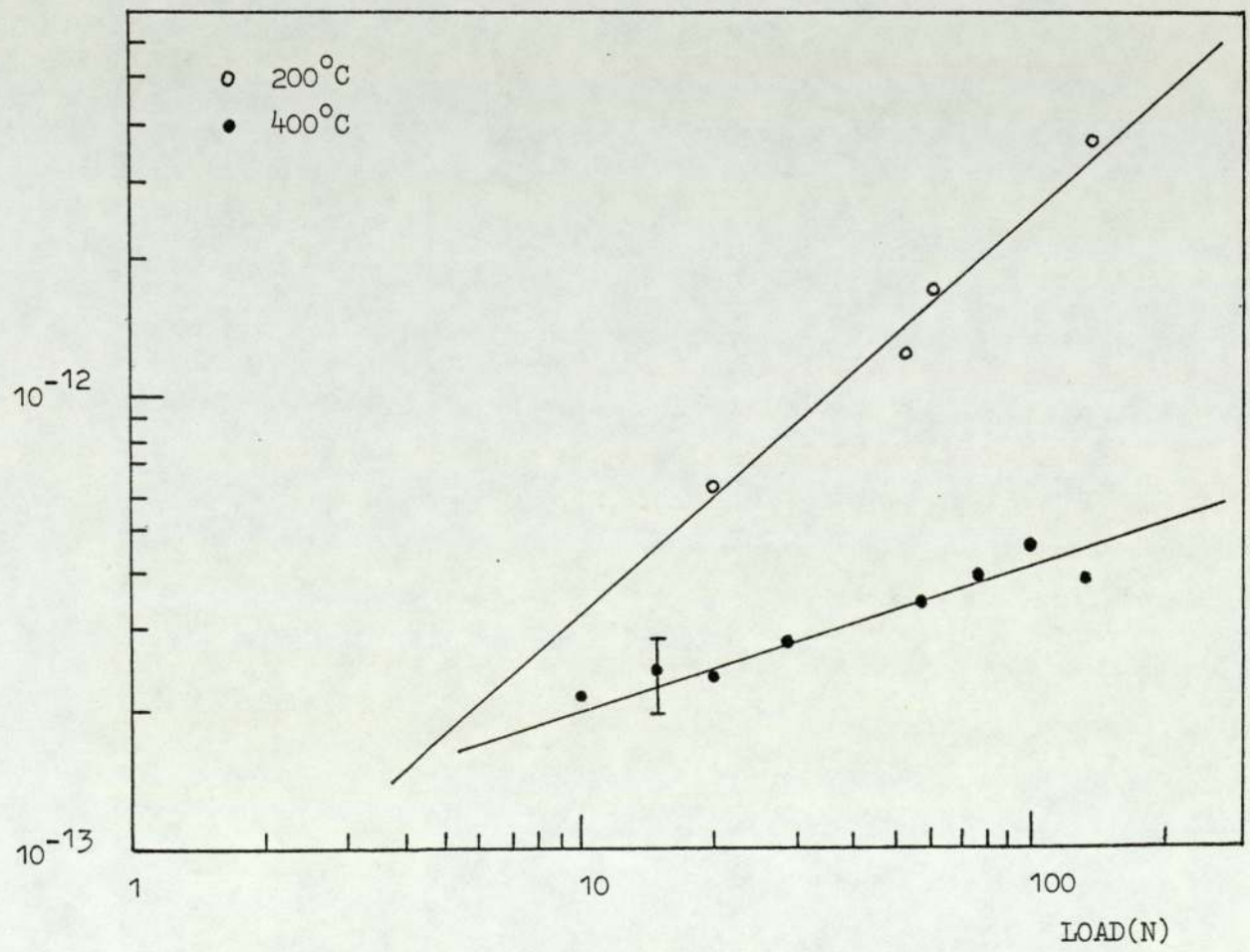

FIGURE 3.4(b) Disc Wear Rate Versus Load for EN31 at 200°C and 400°C.

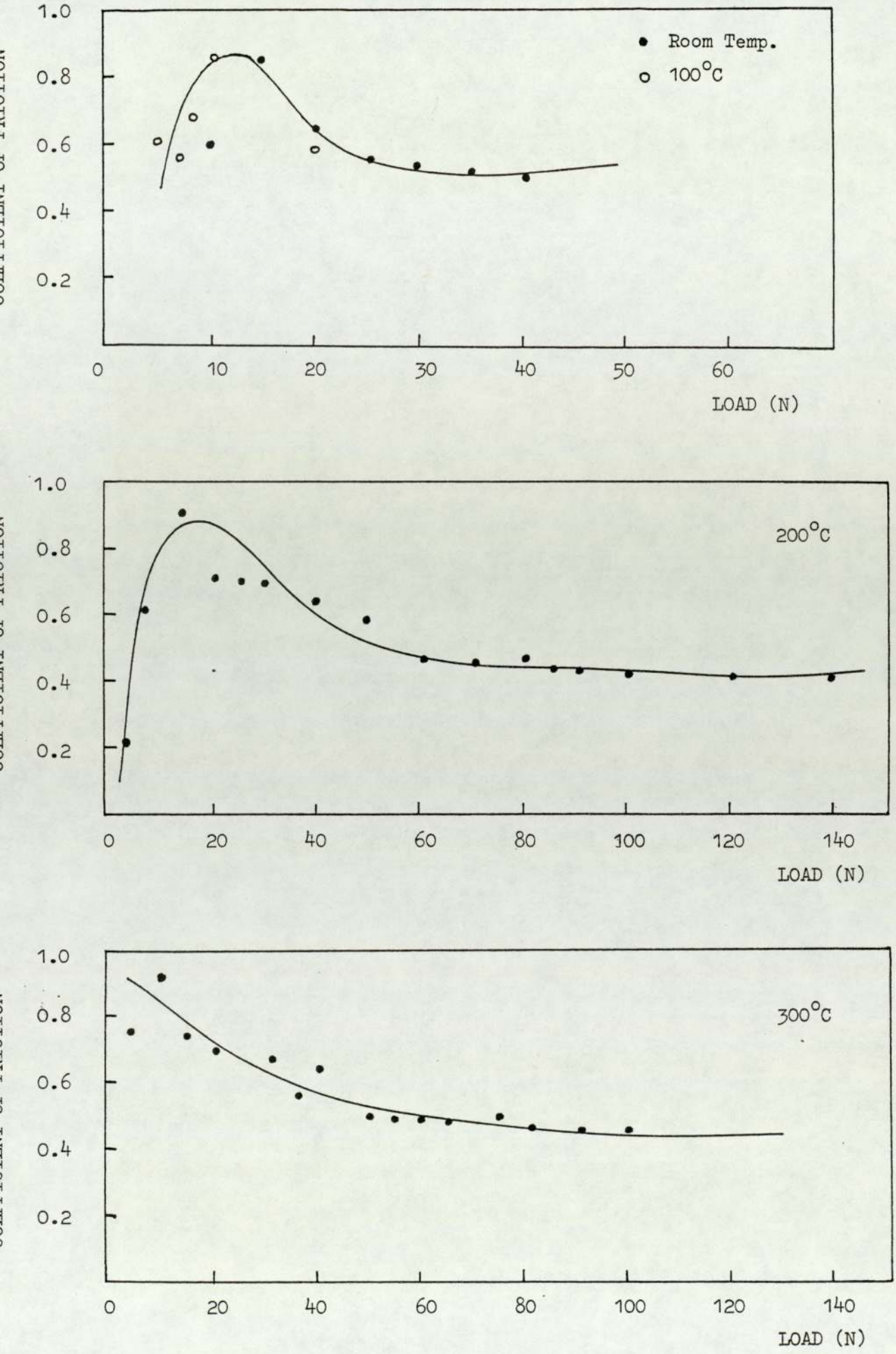

FIGURE 3.5(a) Coefficient of Friction Versus Load for EN8.

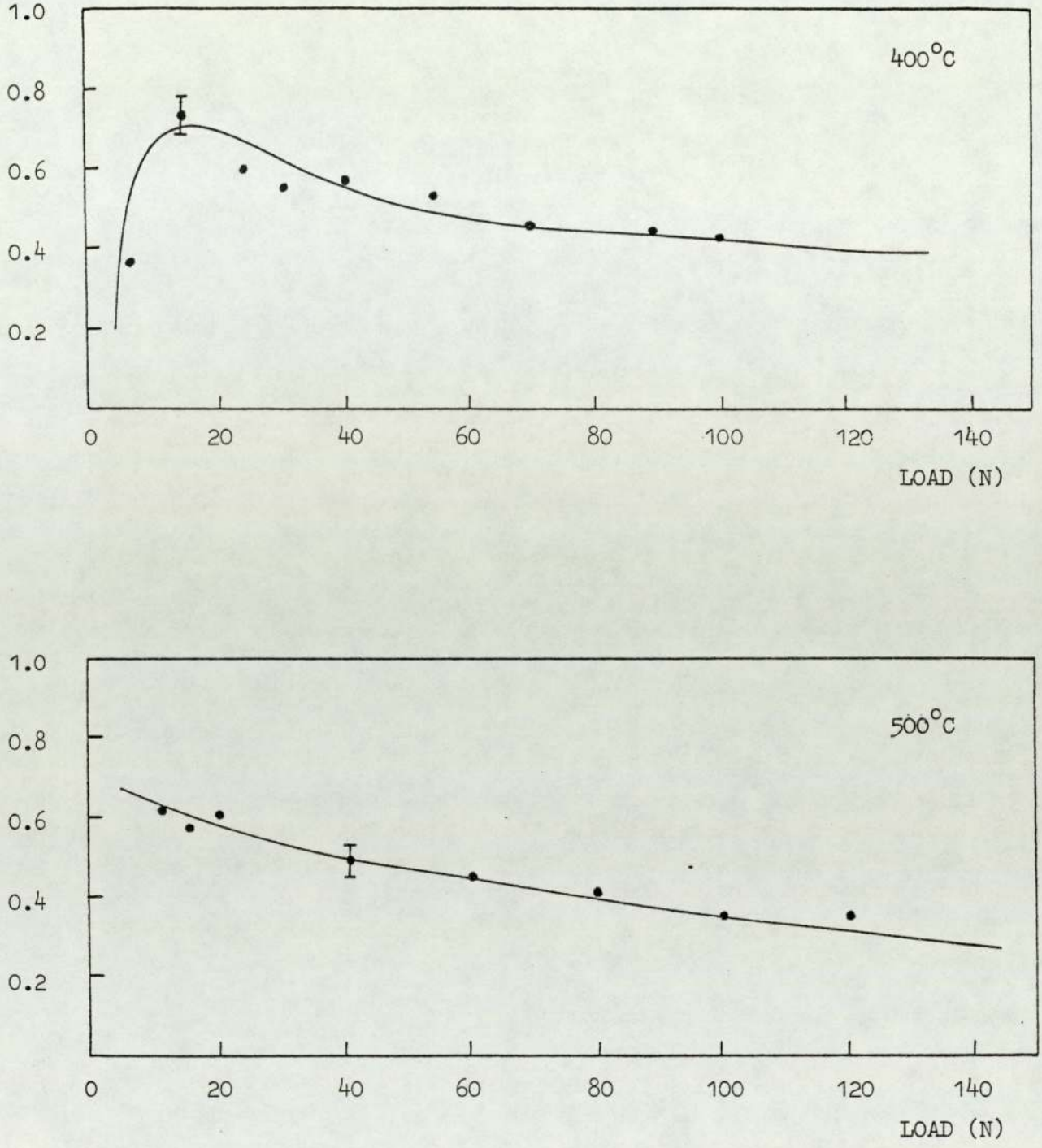

FIGURE 3.5(b) Coefficient of Friction Versus Load for EN8.

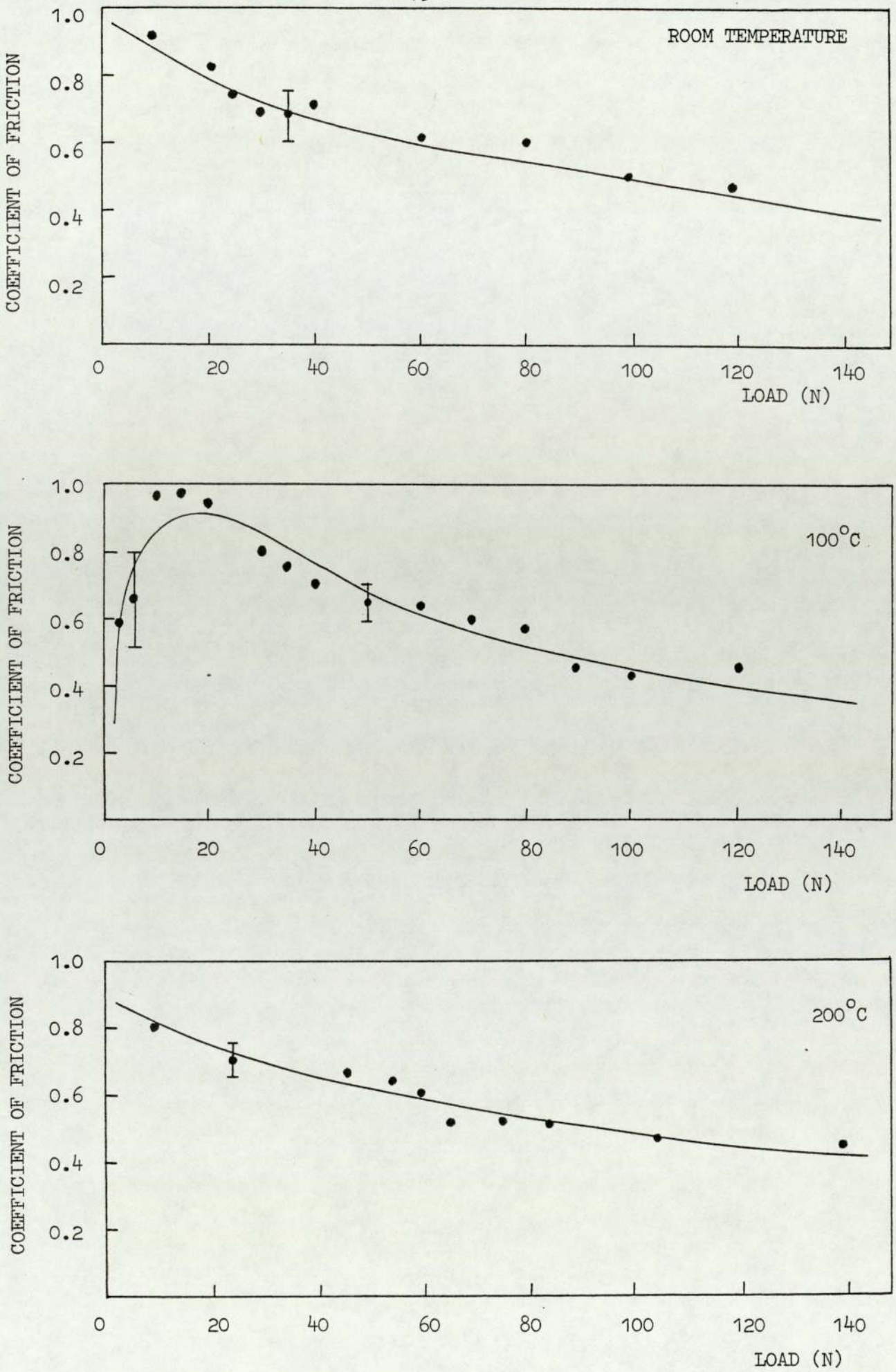

FIGURE 3.6(a) Coefficient of Friction Versus Load for EN31.

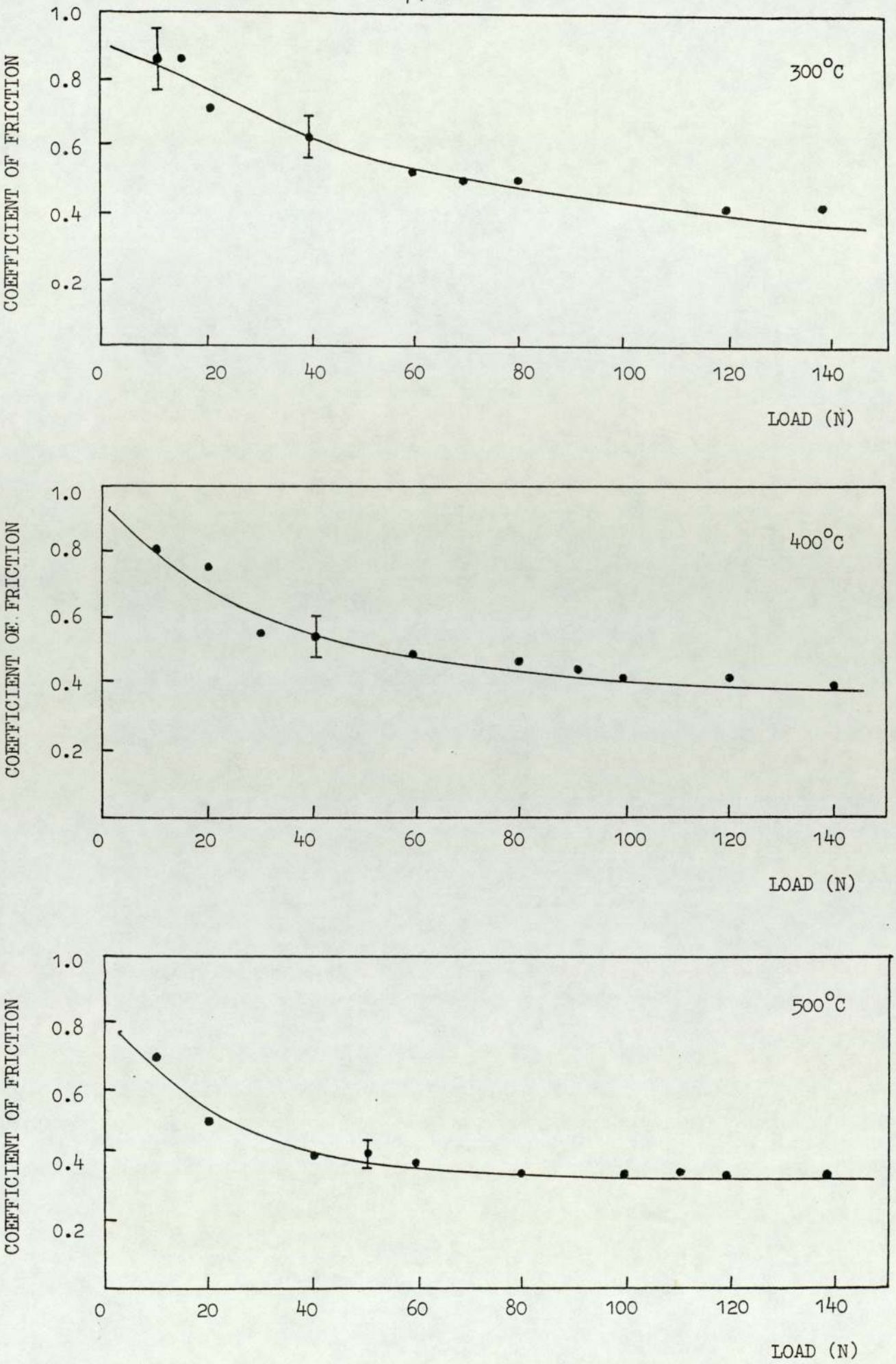

FIGURE 3.6(b). Coefficient of Friction Versus Load for EN31.

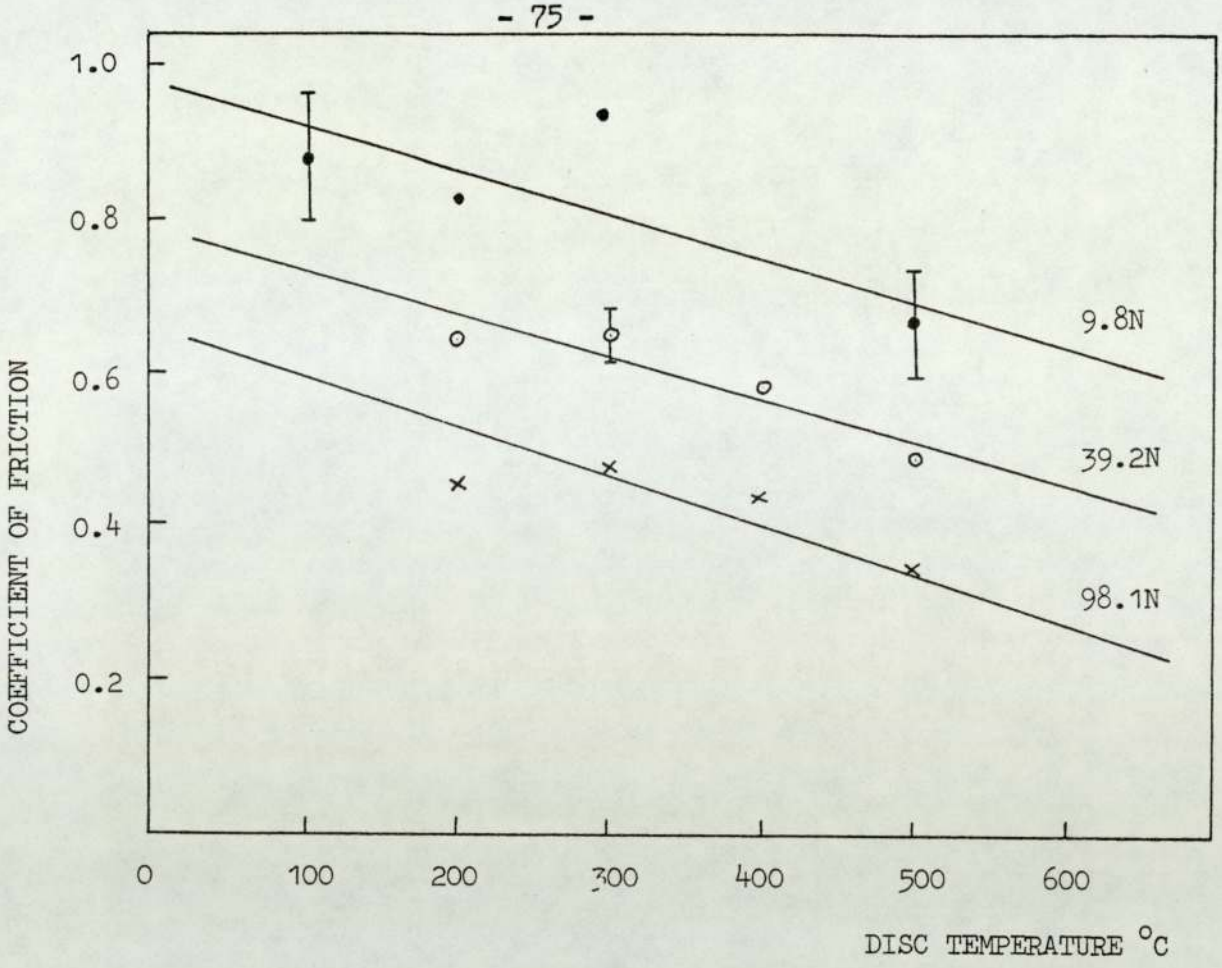

FIGURE 3.7 Variation of Friction Coefficient with Temperature for EN8 Experiments.

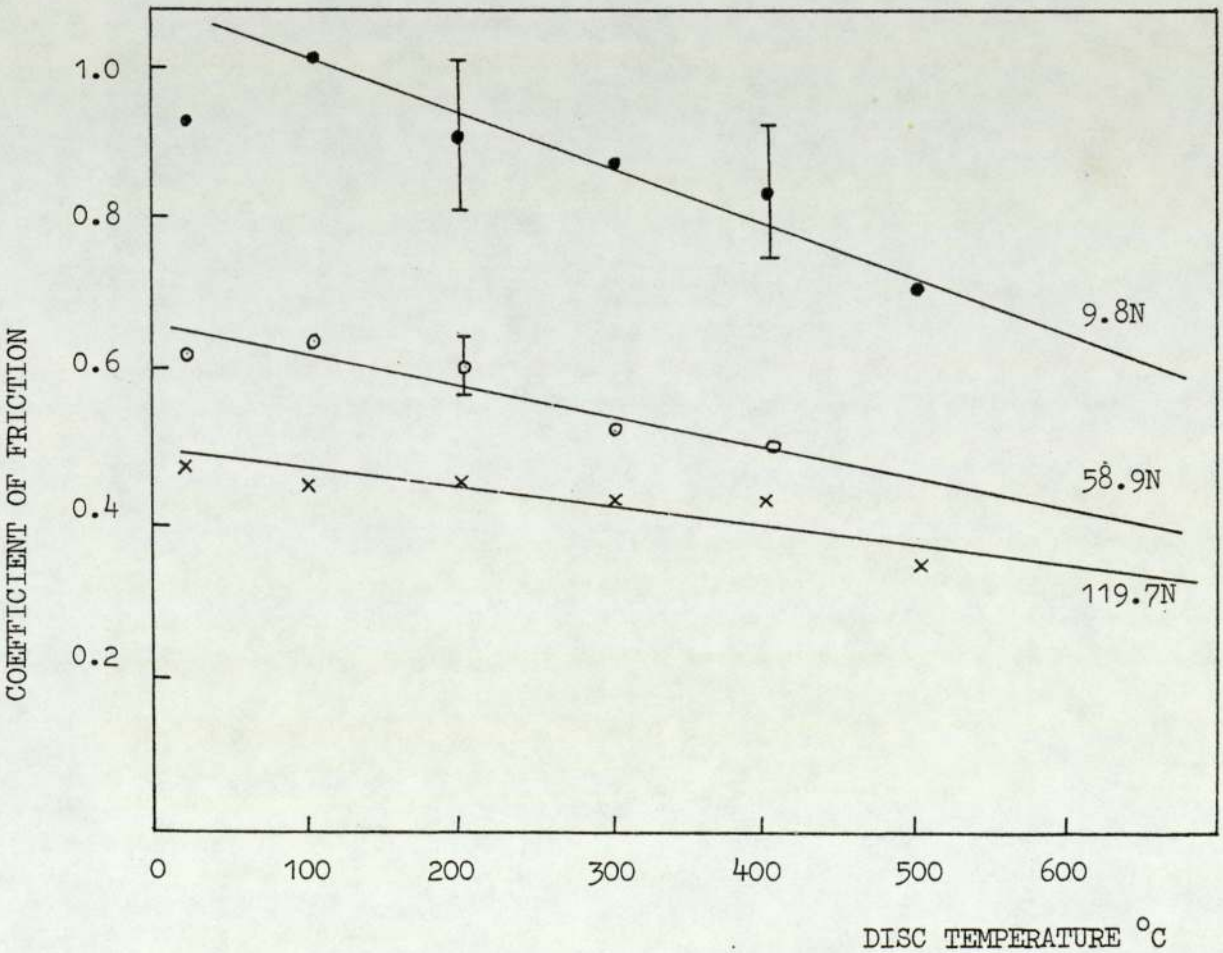

FIGURE 3.8 Variation of Friction Coefficient with Temperature for EN31 Experiments.

The variation of the coefficient of friction μ with applied load for EN8 and EN31 experiments is shown in Figures 3.5 and 3.6 respectively. In general, μ peaked at low loads (between 10N to 20N) and then tended to decrease with increasing load. Talysurf analysis, discussed in Section 3.6, shows that worn surfaces are generally rougher at low loads.

Figures 3.7 and 3.8 respectively, show the coefficient of friction of EN8 and EN31 steels versus disc temperature for a series of loads. All curves show the same general trend, that is, μ decreases with increasing disc temperature. This decrease was attributed to the formation of protective oxide films between the two rubbing surfaces.

By comparison with the general wear patterns, it appears from the non-transitory behaviour of μ that friction is independent of the wear rate.

3.4 Heat Flow

Heat flow results for EN8 and EN31 experiments at room temperature and elevated temperatures are given in Tables 3.1 to 3.6 and Tables 3.7 to 3.12 respectively. Tabulated here are three important parameters; namely the division of heat δ_{expt} at the interface between the pin and disc, the surface temperature T_s of the pin, and the heat flow rate H_1 entering the pin. The division of heat along the pin is given by the following expression:

$$\delta_{expt} = \frac{H_1}{H_T} \qquad 3.1$$

where H_T is the product of the frictional force at the pin (F) and the linear speed of the pin (V) with respect to the disc.

LOAD N	T_A ^oC	T_B ^oC	T_C ^oC	T_D ^oC	T_S ^oC	H_I W	H_T W	δ_{expt} %
4.9	42	35	30	25	45	0.83	13.4	6.2
9.8	49	46	36	34	51	0.48	11.4	4.2
14.7	106	73	48	42	119	3.7	24.8	14.9
24.5	154	96	61	39	173	6.1	26.8	22.8
29.4	153	98	69	53	168	5.7	32.0	17.8
34.3	183	93	76	49	208	8.9	39.6	22.5
39.2	218	112	78	52	247	9.9	40.0	24.8

TABLE 3.1. Heat flow data for EN8 Steel at room temperature

LOAD N	T_A ^oC	T_B ^oC	T_C ^oC	T_S ^oC	H_I W	H_T W	δ_{expt} %
4.9	83	57	48	94	2.7	6.0	45.0
6.9	89	63	45	101	2.9	7.4	39.2
8.3	100	69	52	116	3.4	11.4	29.8
9.8	130	77	58	153	5.5	16.8	32.7
19.6	143	98	71	159	4.8	22.8	21.1

TABLE 3.2. Heat flow data for EN8 steel at $T_D = 100^oC$

LOAD N	T_A °C	T_B °C	T_C °C	T_S °C	H_1 W	H_T W	δ_{expt} %
4.9	116	100	61	137	0.2	2.0	10.0
6.9	118	115	80	123	1.1	8.4	13.1
9.8	113	105	81	120	1.1	16.0	6.9
19.6	125	92	84	131	1.8	27.0	6.7
29.4	123	99	90	142	3.3	42.0	7.9
39.2	183	98	90	238	6.5	50.0	13.0
49.1	204	138	94	250	9.0	58.0	15.5
58.9	208	120	100	242	8.6	54.0	15.9
68.7	218	181	100	247	6.0	62.0	9.7
78.5	208	163	105	234	6.3	74.0	8.5
83.4	252	149	105	269	9.7	71.2	13.6
88.3	219	148	113	258	9.2	76.0	12.1
98.1	266	193	111	304	10.0	84.0	11.9
117.7	290	179	121	337	14.7	100.0	14.7
137.3	305	185	169	362	14.4	118.0	12.2

TABLE 3.3 Heat Flow Data for EN8 Steel at T_D = 200°C

LOAD N	T_A °C	T_B °C	T_C °C	T_S °C	H_1 W	H_T W	δ_{expt} %
4.9	285	210	148	339	11.2	-	-
9.8	280	175	154	332	11.7	18.2	64.3
14.7	292	188	127	337	11.0	22.2	49.5
29.4	310	185	130	360	13.8	39.6	34.8
34.3	321	173	130	363	14.5	37.0	39.2
39.2	341	208	146	398	14.8	50.4	29.4
49.1	315	215	141	365	12.1	50.0	24.2
54.0	344	189	150	384	14.3	53.0	27.0
58.9	338	220	150	409	14.6	57.2	25.5
63.8	330	231	165	396	12.5	61.4	20.4
73.6	362	224	169	419	15.3	77.2	19.8
78.5	270	240	161	424	14.5	72.0	20.1
88.3	357	246	174	449	15.7	76.0	20.7

TABLE 3.4 Heat Flow Data for EN8 Steel at T_D = 300°C

LOAD N	T_A °C	T_B °C	T_C °C	T_S °C	H_1 W	H_T W	δ_{expt} %
7.4	280	206	161	316	7.8	5.4	-
14.7	276	196	154	308	8.0	21.6	37.0
24.5	289	196	144	330	9.4	28.8	32.6
29.4	295	194	159	344	10.0	33.0	30.3
39.2	321	232	170	359	8.9	44.4	20.0
54.0	363	223	168	421	13.5	57.8	23.4
68.7	380	240	167	431	13.1	63.8	20.5
88.3	393	245	171	446	13.5	82.0	16.5
98.1	405	290	188	441	11.1	84.0	13.2

TABLE 3.5 Heat Flow Data for EN8 Steel at T_D = 400°C

LOAD N	T_A °C	T_B °C	T_C °C	T_S °C	H_1 W	H_T W	δ_{expt} %
9.8	361	242	190	414	11.3	12.2	92.6
14.7	362	242	190	416	11.4	16.8	67.9
19.6	381	246	175	438	12.6	24.2	52.1
39.2	387	265	194	440	11.5	37.6	30.6
58.9	397	257	190	457	12.9	53.8	24.0
78.5	405	258	180	462	13.5	66.6	20.8
98.1	420	295	199	468	13.3	65.8	20.2
117.7	419	274	202	473	13.0	84.0	15.5

TABLE 3.6 Heat Flow Data for EN8 Steel at T_D = 500°C

LOAD N	T_A °C	T_B °C	T_C °C	T_D °C	T_S °C	H_1 W	H_T W	δ_{expt} %
9.8	62	49	36	50	68	1.6	18.2	8.8
19.6	100	67	37	40	113	3.7	32.2	11.5
24.5	106	86	54	62	114	2.5	36.3	6.9
29.4	131	77	62	71	153	5.6	40.2	13.9
34.3	124	87	60	87	138	4.0	47.0	8.5
39.2	129	89	61	86	140	4.1	56.4	7.3
58.9	145	100	63	109	158	4.8	72.2	6.6
78.5	173	119	75	121	192	5.8	94.0	6.2
98.1	234	155	95	136	250	8.4	95.0	8.4
117.7	292	162	112	159	311	12.8	109.2	11.7

TABLE 3.7 Heat Flow Data for EN31 Steel at Room Temperature

LOAD N	T_A °C	T_B °C	T_C °C	T_S °C	H_1 W	H_T W	δ_{expt} %
4.9	81	50	45	93	3.1	5.8	53.4
6.9	83	55	44	96	3.0	8.8	34.1
9.8	113	68	46	130	4.8	20.2	23.8
14.7	107	77	51	119	3.2	29.6	10.9
19.6	131	69	50	156	6.4	37.0	17.3
29.4	117	90	58	129	3.2	46.4	6.9
34.3	133	80	56	152	5.5	51.1	10.8
39.2	130	81	57	147	5.0	53.8	9.3
49.1	140	84	57	158	5.5	62.2	8.8
58.9	155	89	62	176	6.5	75.2	8.6
68.7	200	107	75	217	9.1	82.4	11.0
78.5	224	115	75	252	10.2	89.0	11.5
88.9	257	159	100	274	9.3	77.2	12.0
98.1	268	148	86	290	10.9	82.4	13.2
117.7	311	173	107	326	12.1	105.2	11.4

TABLE 3.8 Heat Flow Data for EN31 Steel at $T_D = 100°C$

LOAD N	T_A °C	T_B °C	T_C °C	T_S °C	H_1 W	H_T W	δ_{expt} %
9.8	157	113	87	182	4.6	17.4	26.4
24.5	192	115	80	216	7.5	33.6	22.3
44.1	194	127	88	215	6.7	58.8	11.4
54.0	205	133	90	232	7.6	69.2	11.0
58.9	204	157	96	224	5.4	70.6	7.6
63.8	251	154	95	281	9.6	62.2	15.4
73.6	212	143	105	238	7.2	74.6	9.7
83.4	264	149	100	298	10.9	84.0	13.0
103.0	275	124	120	316	12.6	94.0	13.4
137.3	309	168	129	357	12.5	122.6	10.2

TABLE 3.9 Heat Flow Data for EN31 Steel at T_D = 200°C

LOAD N	T_A °C	T_B °C	T_C °C	T_S °C	H_1 W	H_T W	δ_{expt} %
9.8	203	131	121	230	7.0	16.8	41.7
14.7	236	161	118	268	7.8	25.5	30.6
19.6	245	152	104	283	9.7	27.6	35.1
39.2	250	162	121	284	8.8	49.7	17.7
58.9	277	176	131	315	10.0	61.2	16.3
68.7	292	195	120	331	9.8	69.2	14.2
78.5	295	182	128	335	11.2	78.6	14.2
117.7	302	181	137	356	12.1	100.8	12.0
137.3	337	183	144	385	13.9	119.2	11.7
157.0	374	192	152	433	15.4	129.4	11.9

TABLE 3.10 Heat Flow Data for EN31 at T_D = 300°C

LOAD N	T_A °C	T_B °C	T_C °C	T_S °C	H_1 W	H_T W	δ_{expt} %
9.8	294	209	159	337	8.9	16.2	54.9
19.6	324	200	164	379	11.9	29.6	40.2
29.4	355	231	161	418	12.2	33.0	37.0
39.2	334	208	171	400	12.8	42.0	30.5
58.9	346	208	167	419	13.9	57.2	24.3
78.5	374	220	157	432	14.3	74.0	19.3
88.3	365	216	154	436	14.7	77.2	19.0
98.1	408	234	173	447	14.7	84.0	17.5
117.7	408	261	176	476	14.2	100.8	14.1
137.3	400	221	192	472	15.9	107.5	14.8
157.0	416	242	192	488	15.9	122.6	13.0

TABLE 3.11 Heat Flow Data for EN31 Steel at T_D = 400°C

LOAD N	T_A °C	T_B °C	T_C °C	T_S °C	H_1 W	H_T W	δ_{expt} %
9.8	352	248	189	410	10.7	13.4	79.9
19.6	387	256	212	456	12.7	19.5	65.1
39.2	384	252	206	449	13.4	29.6	45.3
49.1	411	263	201	472	13.5	39.6	34.1
58.9	399	239	199	473	14.5	43.0	33.7
78.5	405	252	212	470	13.9	53.7	25.9
98.1	416	252	211	486	14.9	65.5	22.7
107.9	432	232	205	514	17.3	73.9	23.4
117.7	437	265	205	494	14.6	80.6	18.1
137.3	439	256	208	520	16.6	86.7	19.1
157.0	439	269	214	515	15.7	99.1	15.8

TABLE 3.12 Heat Flow Data for EN31 Steel at T_D = 500°C

The variation of surface temperature versus applied load for EN8 steel sliding against itself is illustrated in Figures 3.9, 3.10 and 3.11. Similarly, surface temperature versus load plots for EN31 steel pins sliding against EN8 steel discs are shown in Figures 3.12 and 3.13. In general, the surface temperature increases with load and the form of these curves are similar to "wear rate versus load" graphs.

In Chapter 4, values of δ_{th} calculated on the basis of a simple surface model to deduce the number of asperities in contact beneath the pin (N), the oxide film thickness (ξ), and the temperature at the real areas of contact (T_c).

3.5 Microhardness and Bulk Hardness

All results given in this section were obtained cold after completion of the relevant wear experiment. High accuracy cannot be claimed in the microhardness measurements owing to the roughness and highly oxidised nature of the surfaces which made measurements difficult. The hardness quoted is not the average hardness of the whole surface but only of those areas which appeared to be the contact regions at the moment rubbing ceased. In the mild wear state these usually consisted of burnished patches on a comparatively rough (and soft) background. The distinction between contact areas and out-of-contact areas disappears at elevated temperatures because most of the surface becomes oxidised. This was particularly important at disc temperatures of 400°C and 500°C. Another problem encountered at these high temperatures was the cracking of oxide under the impression load owing to its brittle nature.

3.5.1 Microhardness of Worn Pins

Under all experimental conditions, microhardness measurements indicated that the hardness of the EN8 and EN31 pins is

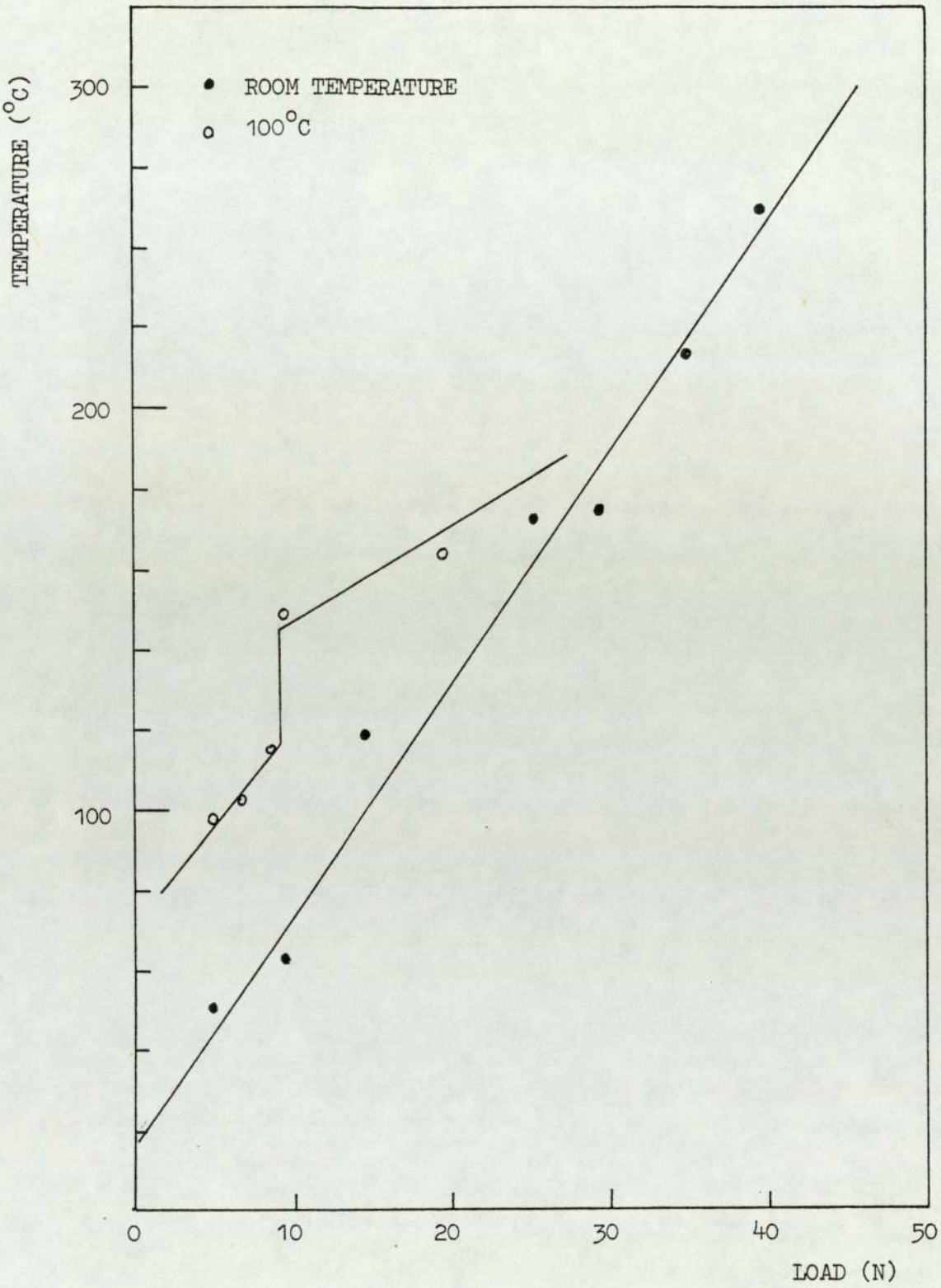

FIGURE 3.9 Surface Temperature Versus Load for EN8 at Room Temperature and 100°C.

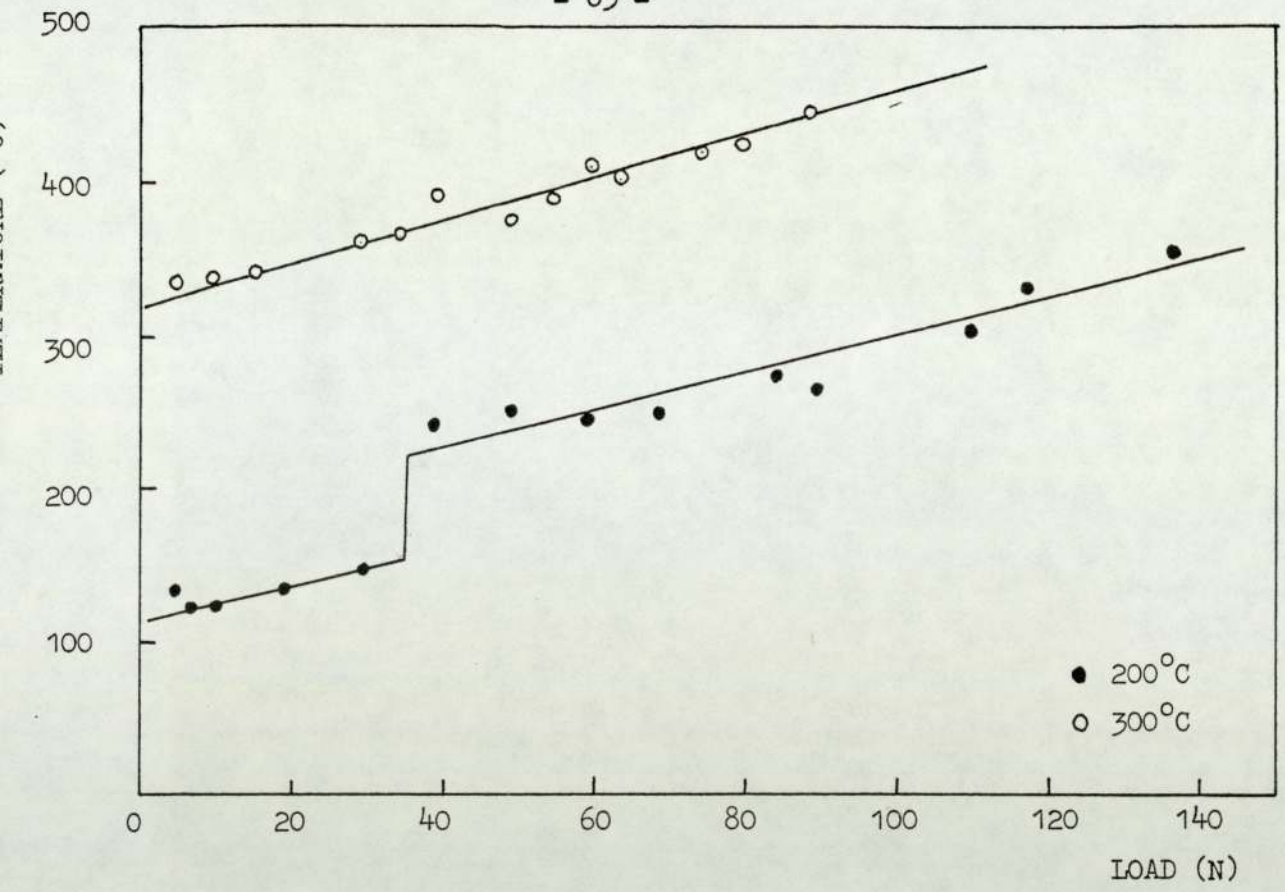

FIGURE 3.10 Surface Temperature Versus Load for EN8 at 200°C and 300°C.

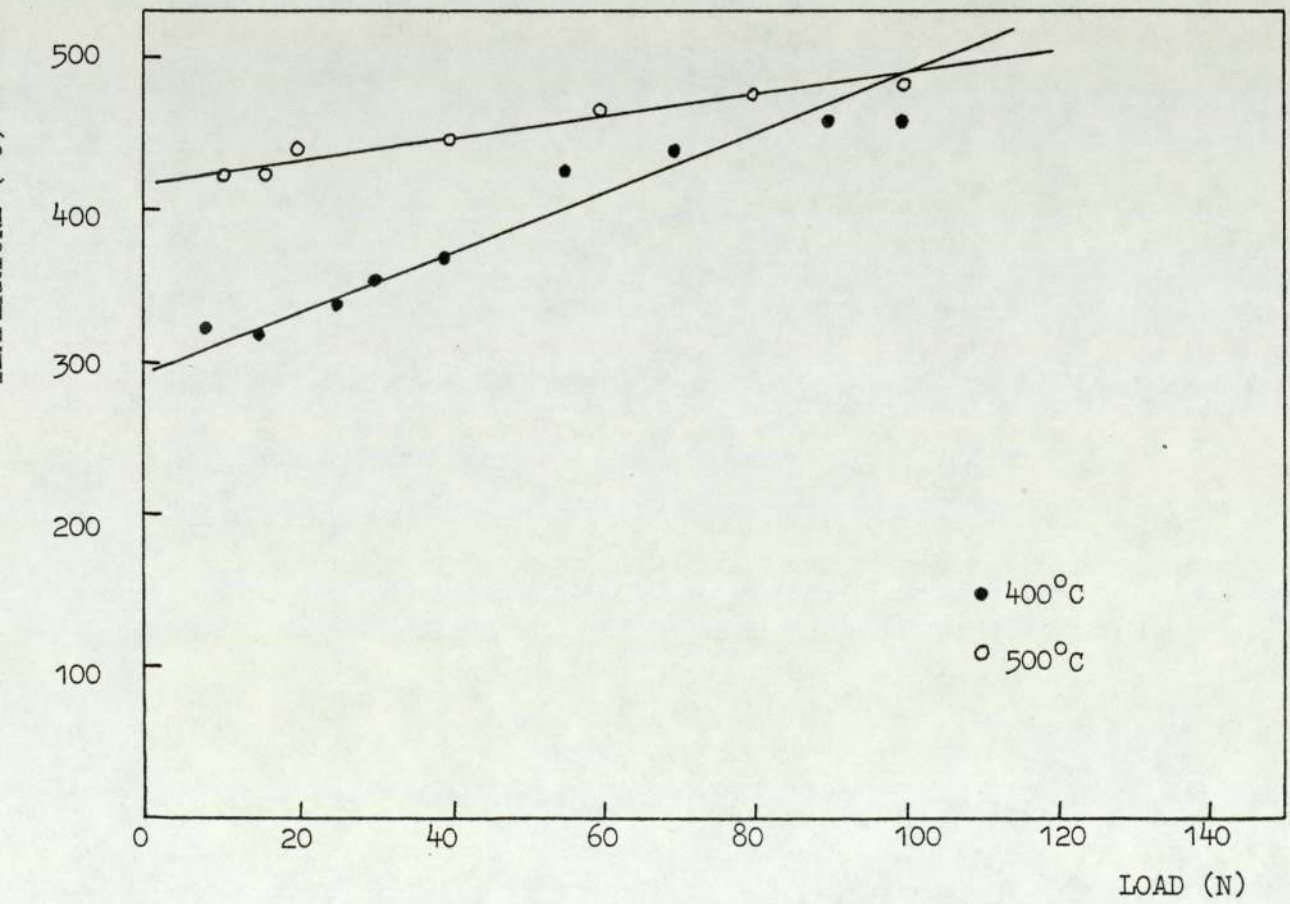

FIGURE 3.11 Surface Temperature Versus Load for EN8 at 400°C and 500°C.

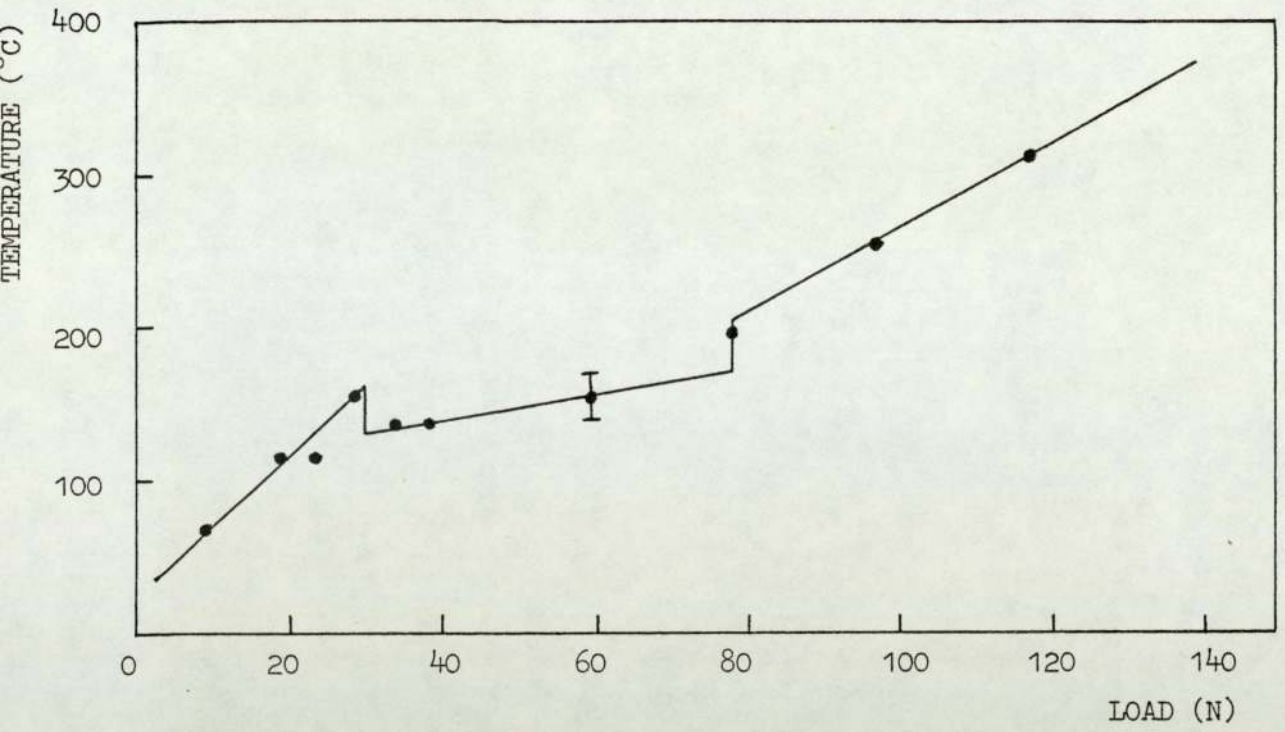

FIGURE 3.12 Surface Temperature Versus Load for EN31 at Room Temperature.

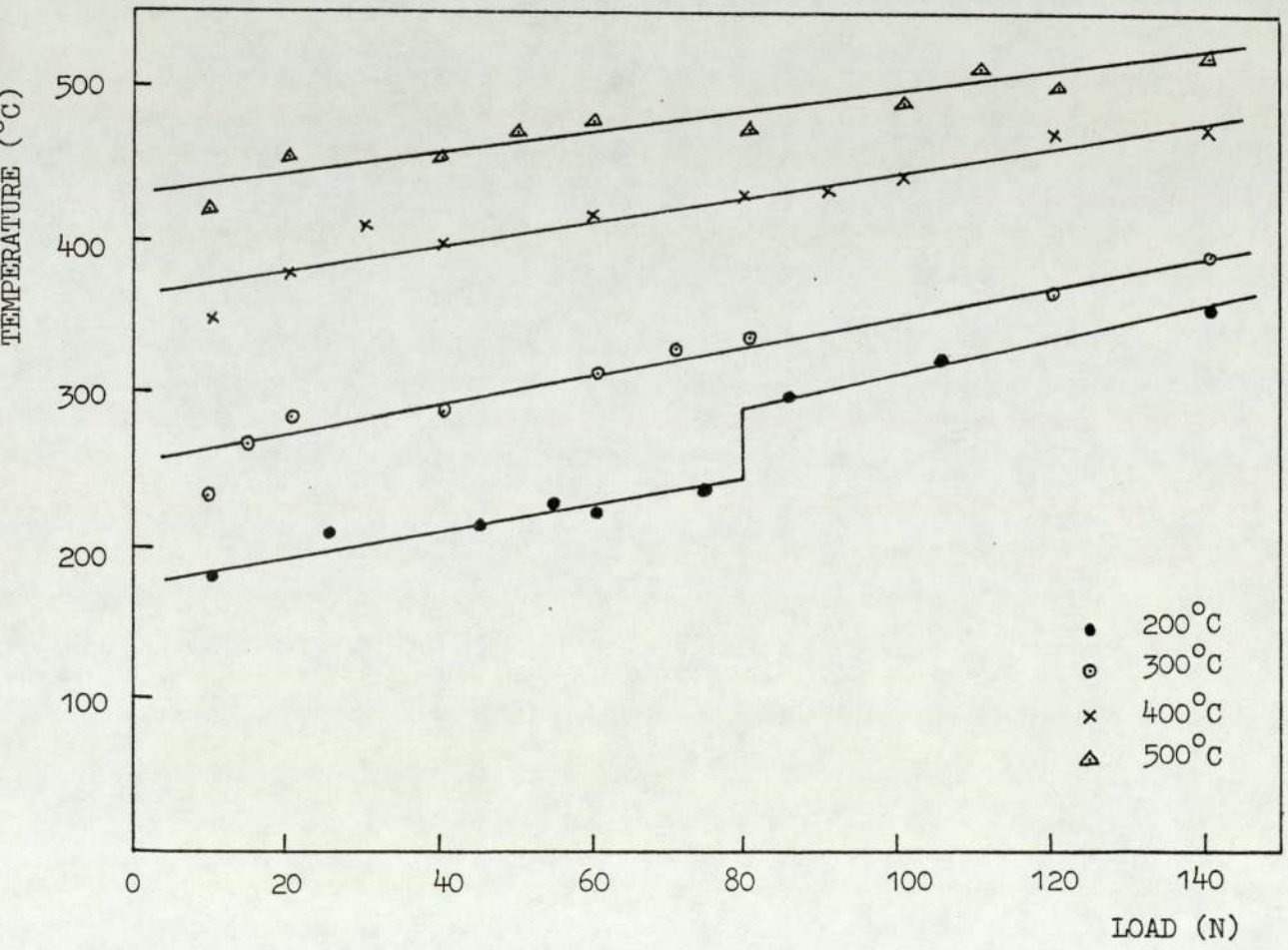

FIGURE 3.13 Surface Temperature Versus Load for EN31 at 200°C, 300°C, 400°C and 500°C.

in the range 500-800 VPN. These values are consistent with the range of critical hardness value for steels found by Welsh (39) associated with the T_2 transition (i.e. 553 to 775 VPN).

Figure 3.14 shows the microhardness of pin and disc from 200°C EN8 elevated temperature experiments plotted against load. Each point on the curve is an average of at least ten impressions. The results were illustrated in this manner so that comparison with the wear rate versus load curve given in Figure 3.1(a) can be made easily. For the 200°C experiments, Figure 3.1(a) showed a transition in the wear rate curve at about 35N applied load. However, it is clear from Figure 3.14 that no transition occurs in the microhardness versus load curve at this particular load. Some typical standard deviations are given in Figure 3.14.

3.5.2 Microhardness of Worn Discs

Illustrated in Figure 3.15 is the variation of microhardness of disc surface against applied load. Curves for two experimental disc temperatures (i.e. 300°C and 500°C) are shown in this figure. The results show a steady decrease in hardness with load.

3.5.3 Bulk Hardness of Worn Pins and Discs

Figures 3.16 and 3.17 show the variation in bulk hardness of worn EN8 and EN31 steel pin surfaces as a function of disc temperature respectively. Curves for two different loads are illustrated in each figure for comparison. Each point on the curve was an average of at least ten separate measurements. For both pin materials the result show a decrease in hardness with increasing experimental disc temperature. This is attributed to less work-hardening of subsurface layers at the high temperatures. The fall is more significant with the high load curve indicating the influence of frictional heating on the subsurface layers

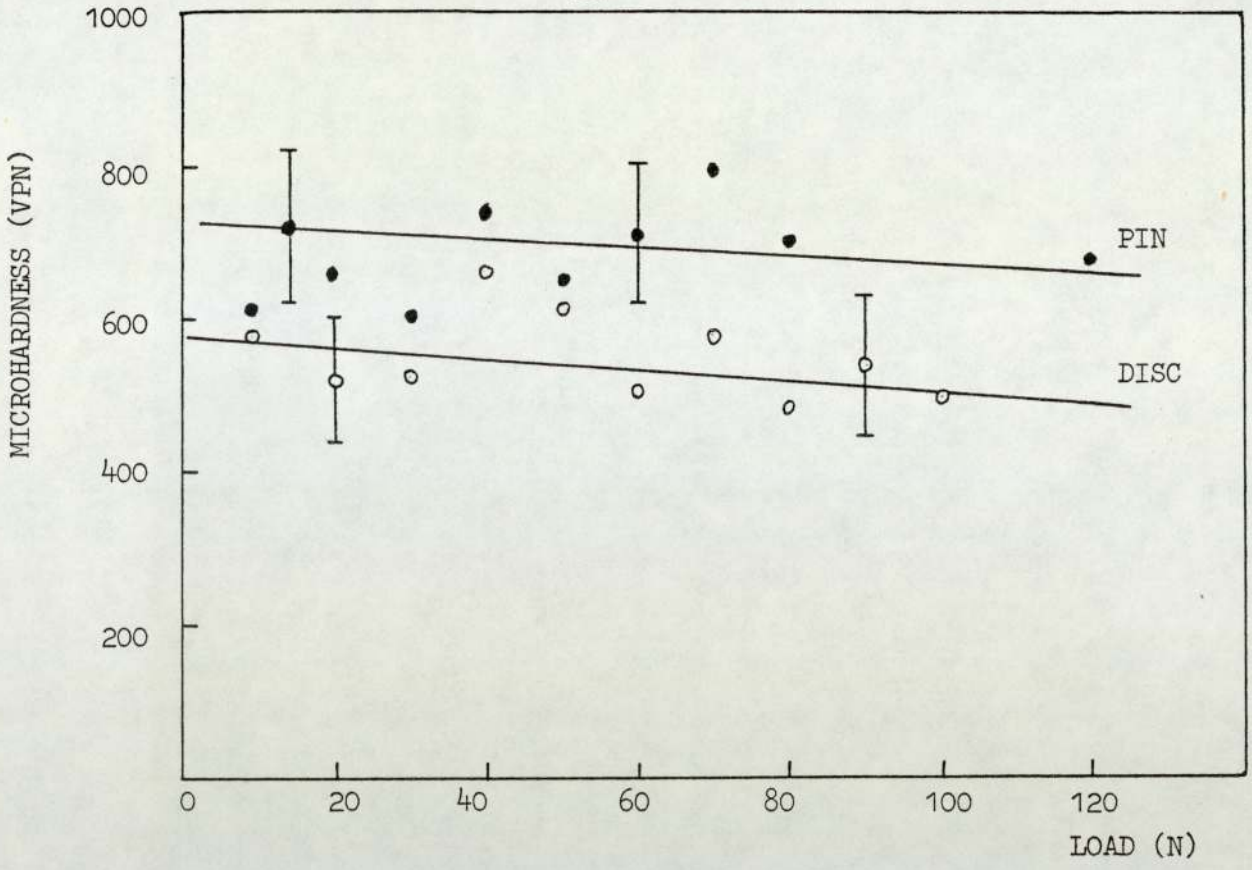

FIGURE 3.14 Microhardness of Pin and Disc Surfaces Versus Applied Load for EN8 at 200°C.

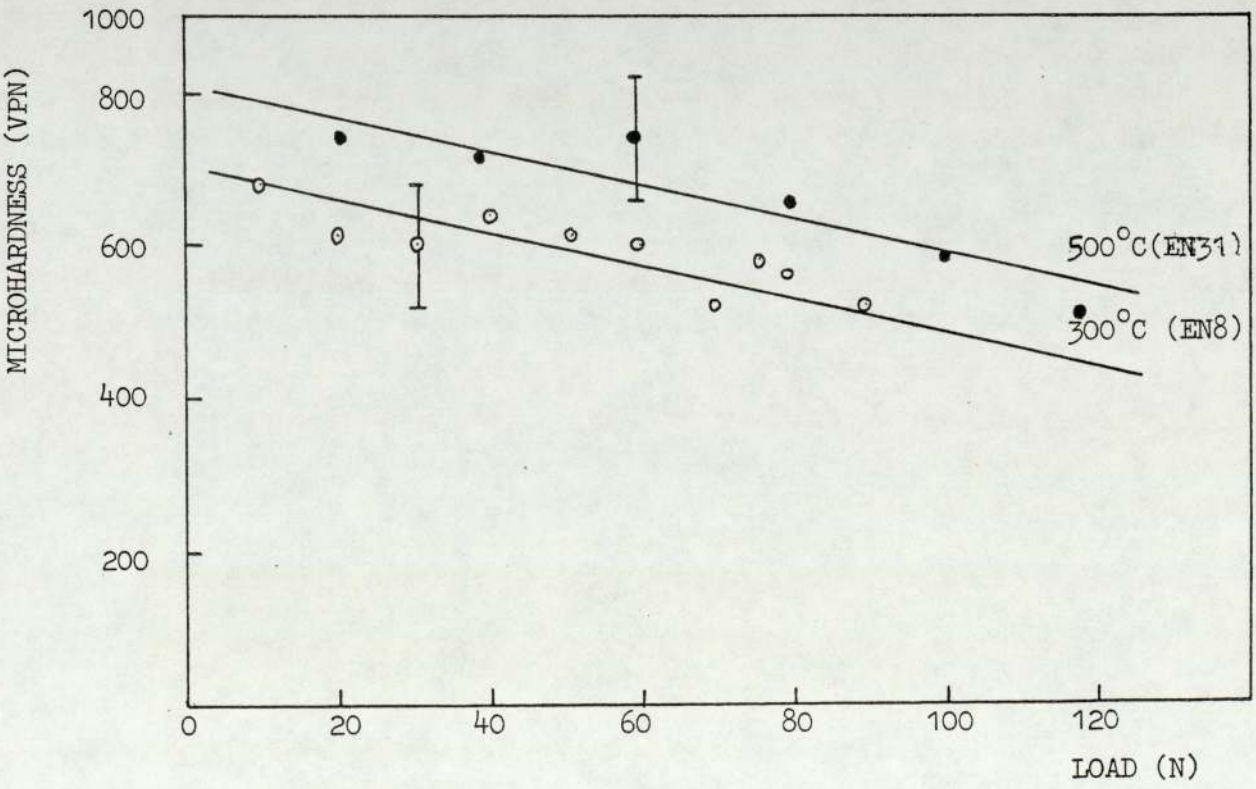

FIGURE 3.15 Disc Microhardness Versus Load.

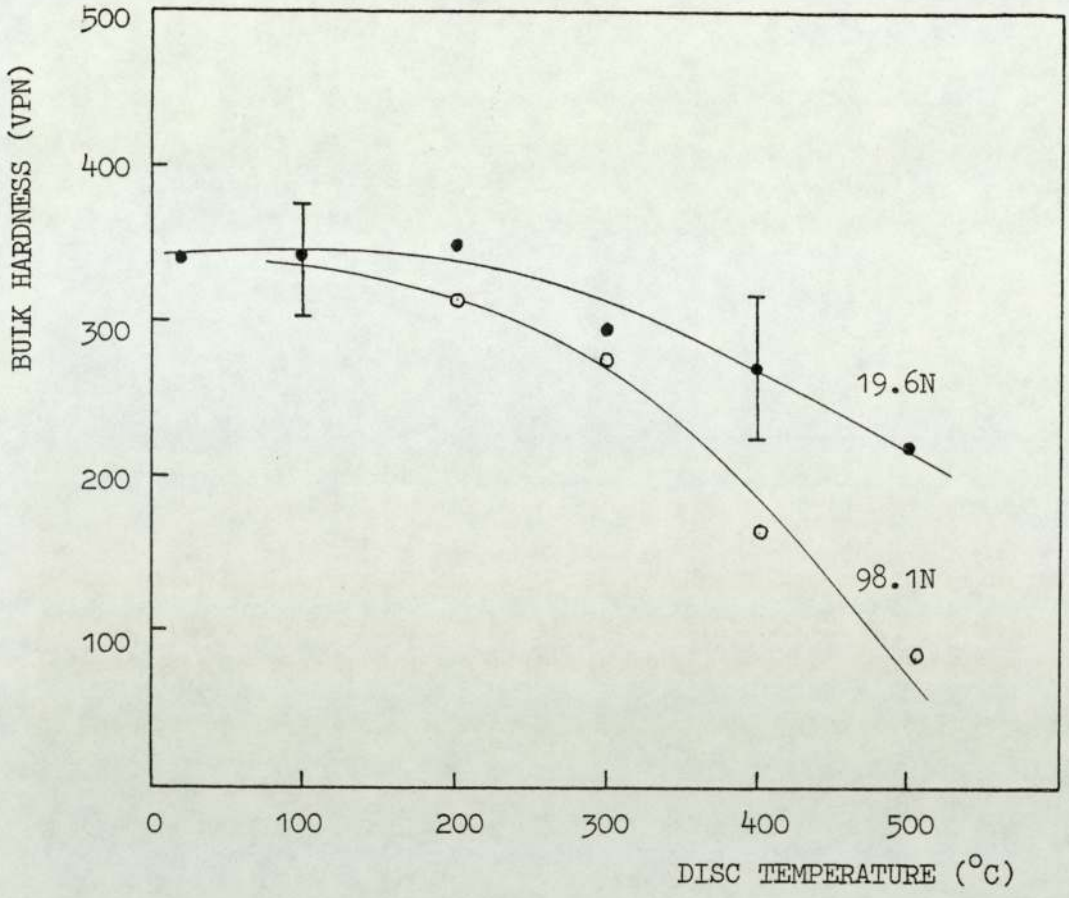

FIGURE 3.16 Bulk Hardness of EN8 Pin Versus Disc Temperature.

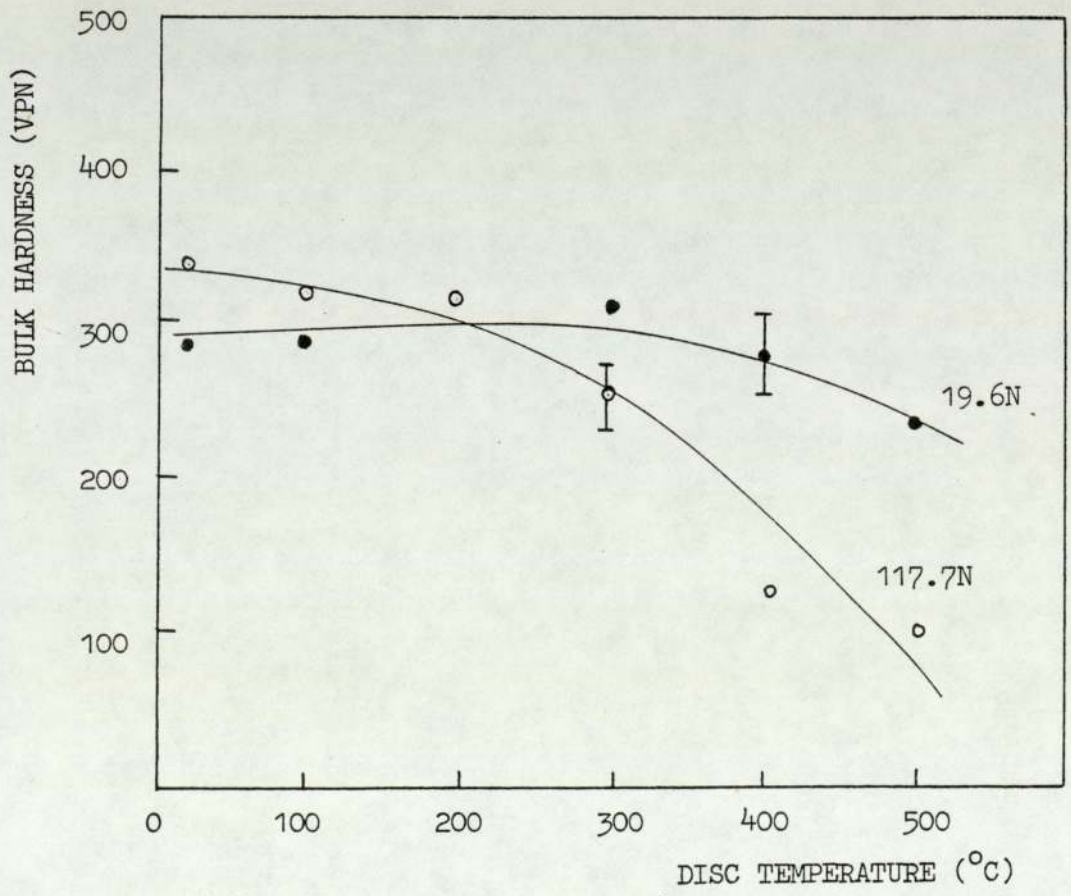

FIGURE 3.17 Bulk Hardness of EN31 Pin Versus Disc Temperature.

immediately below the real areas of contact. It is worth recalling that the original bulk hardness of EN8 and EN31 materials was 250 VPN and 280 VPN respectively.

Bulk hardness results of the disc showed a small decrease with temperature but the effect of applied load was negligible. For example, consider the 500°C EN31 elevated temperature experiments at 19.6N and 98.1N applied loads. The bulk hardness (disc) measured for these experiments was 199 ± 8 VPN and 197 ± 6 VPN respectively.

3.5.4 Microhardness Variation with Depth

Microhardness versus depth curves from some selected EN8 and EN31 experiments are shown in Figures 3.18 and 3.19 respectively. Both figures show that pronounced hardening had occurred below the worn pin surface (up to 800 VPN for some EN8 pins). This was attributed to the formation of work-hardened subsurface layers during sliding. The depth to which the pin surface was affected increased with applied load. All microhardness versus depth curves tended to the original bulk hardness value of the materials, i.e. 250 VPN and 280 VPN for EN8 and EN31 respectively.

The subsurface of a 137.3 EN8 200°C pin was very rough and dark which made measurements of microhardness near to the surface very difficult. However, measurements were made relatively easily at depths greater than 30μm below the surface. See Figure 3.18. Even at these depths pronounced hardening was evident. No evidence of subsurface hardening was detected on pins from 400°C elevated temperature experiments due possibly to less work-hardening of subsurface layers at high temperature.

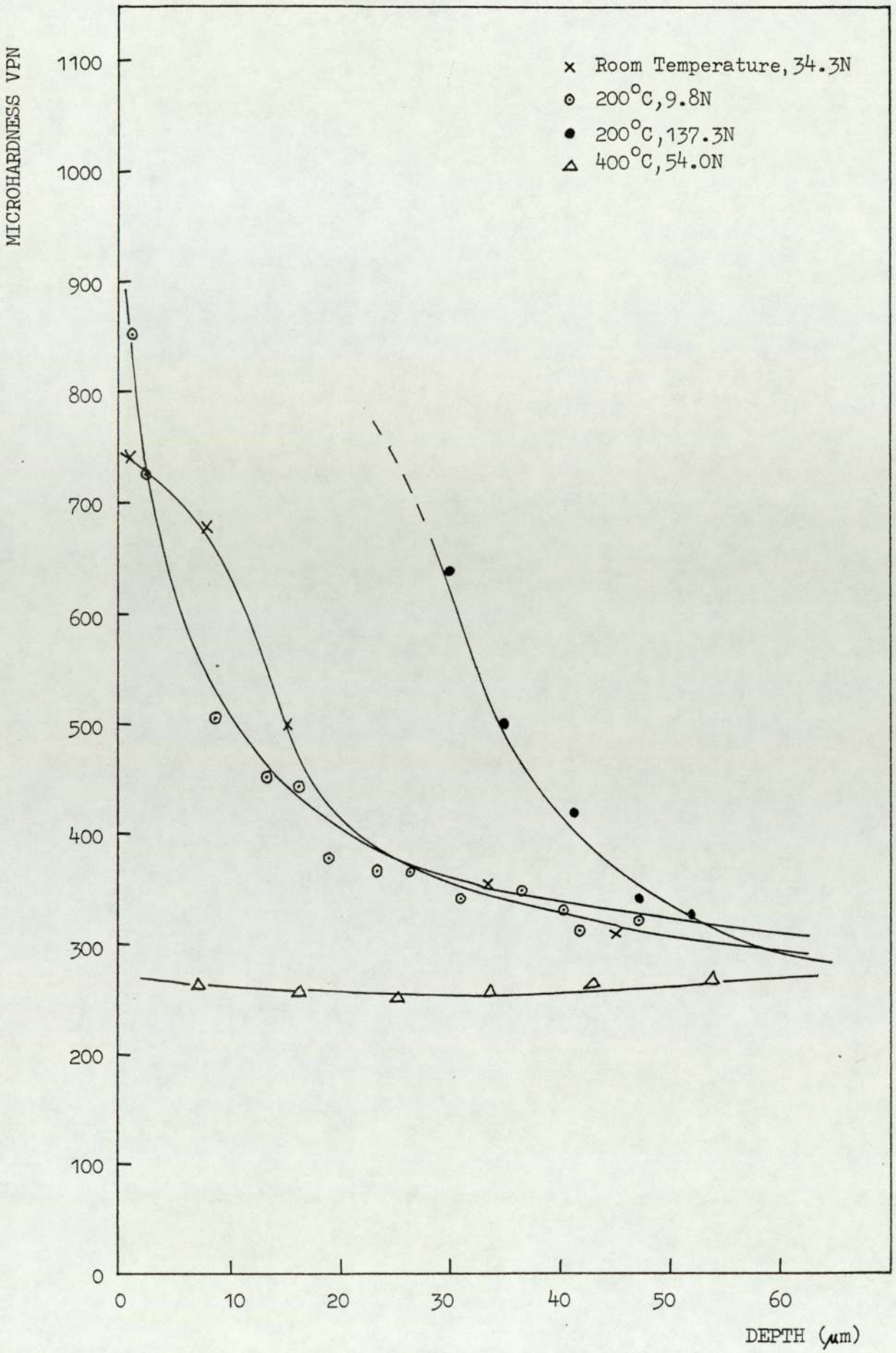

FIGURE 3.18 Microhardness Versus Depth Curves for EN8 Experiments.

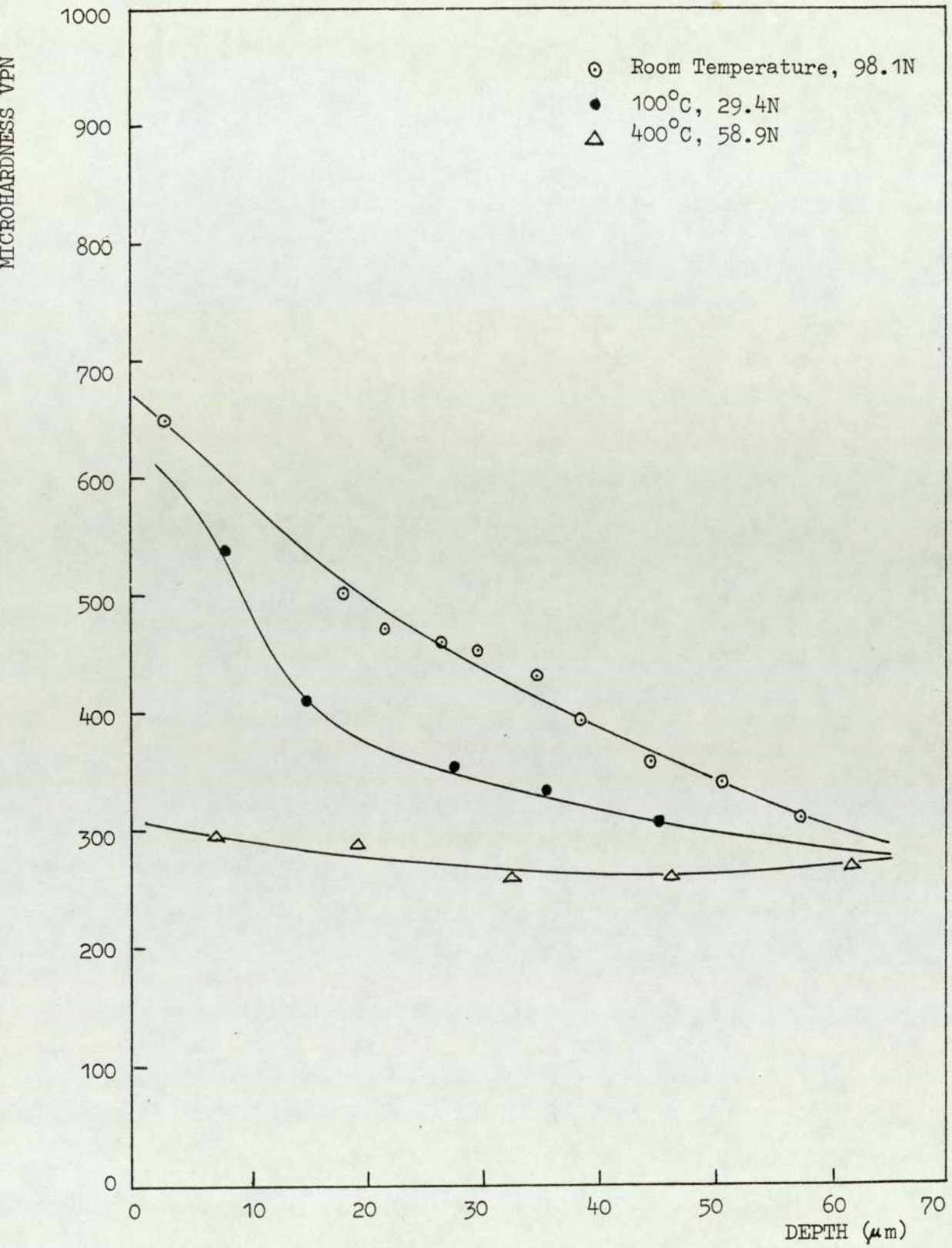

FIGURE 3.19 Microhardness Versus Depth Curves for EN31 Experiments.

3.6 Surface Profiles

This part of the work has only been partially fulfilled since talysurf profiles of the pin could not be obtained owing to the mechanical arrangement of the profilimeter. However, some typical talysurf profiles taken of worn disc surfaces are shown in Figures 3.20 and 3.21. The vertical and lateral magnification of these profiles was 1000× and 20× respectively. It is clear from these profiles that surface roughness decreases with applied load and surfaces tend to be much smoother at high disc temperatures.

3.7 Powder X-ray Diffraction of Debris

Experimentally measured d_{hkl} values and relative intensities of various constituents found in the wear debris, together with the d_{hkl} values and relative intensities noted in the x-ray powder data file (ASTM index), are given in Tables 3.13(a) and (b). In the sub-sections that follow the microdensitometer results will be referred to these tables.

3.7.1 EN8 Experiments

(i) Room Temperature

Analysis of x-ray diffraction patterns showed that the debris consisted mainly of FeO and α-Fe. Figure 3.22 shows the microdensitometer trace of x-ray diffraction pattern for 29.4N load experiment. As expected, in 58.9N load experiment only the α-Fe lines were present.

(ii) $T_D = 100^{\circ}C$

The oxide produced from the experiments below the transition load of 10N was a mixture of α-Fe_2O_3 and

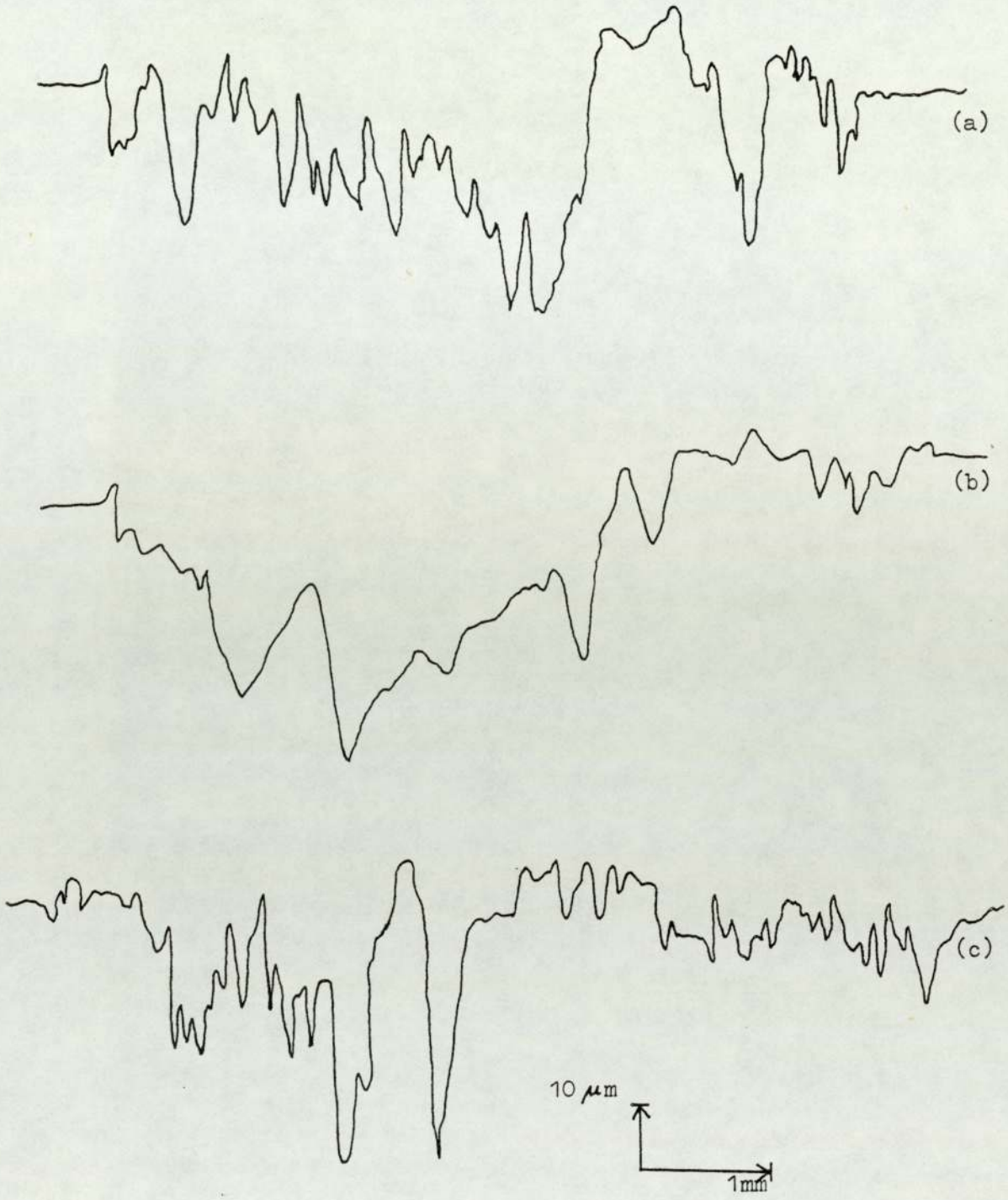

FIGURE 3.20 Profiles of Disc Surface.

(a) EN8, 9.8N, Room Temperature
(b) EN8, 9.8N, 200°C
(c) EN8, 98.1N, 200°C

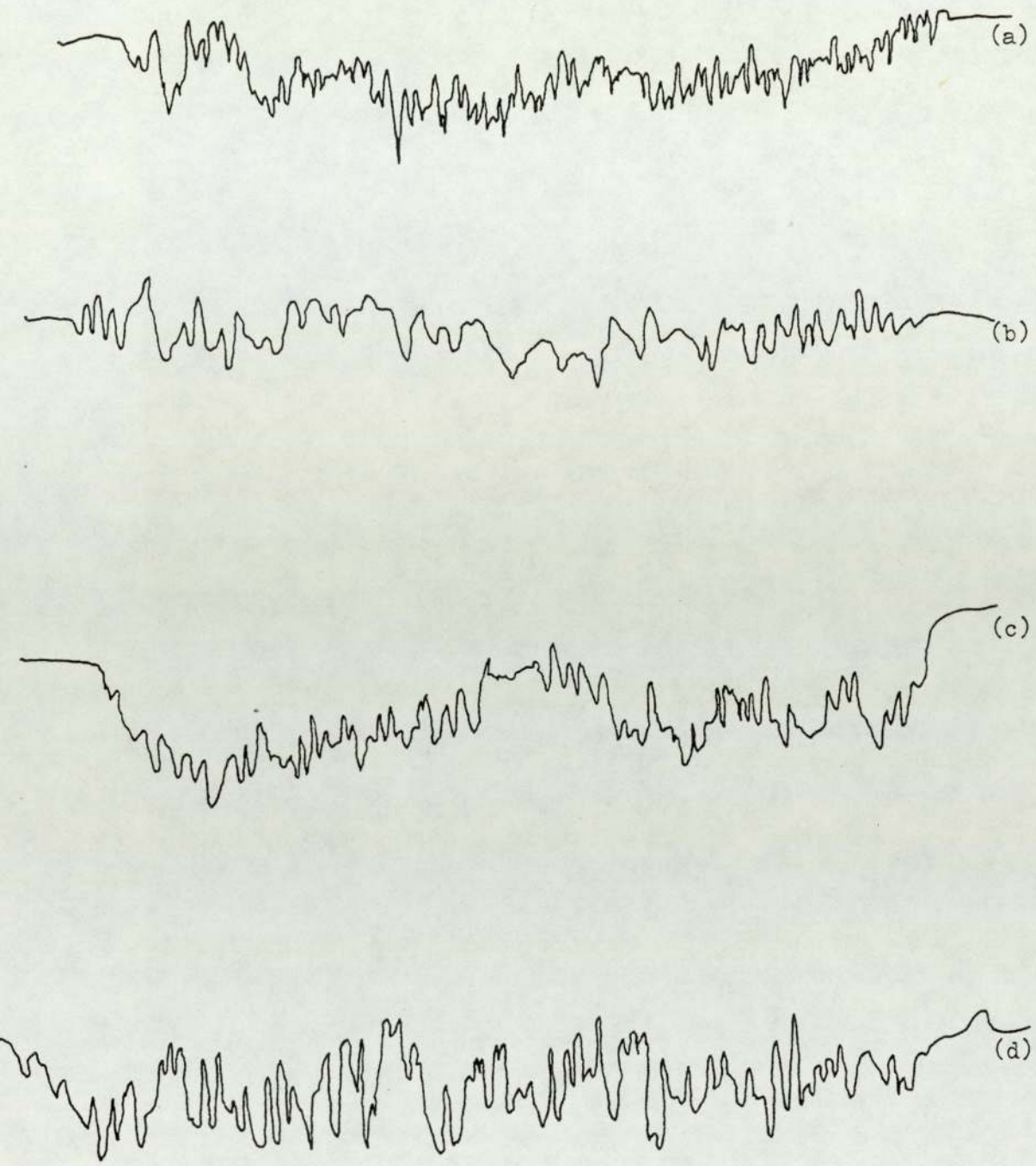

FIGURE 3.21 Profiles of Disc Surface.

(a) EN31, 39.2N, 400°C
(b) EN31, 78.5N, 400°C
(c) EN8, 9.8N, 500°C
(d) EN8, 98.1N, 500°C

EXPERIMENTAL VALUES			ASTM INDEX VALUES		
DIFFRACTION LINE	d_{hkl} (Å)	RELATIVE INTENSITY	IDENTITY	d_{hkl} (Å)	RELATIVE INTENSITY
1	4.795	13(4)	Fe_3O_4	4.850	8
2	3.672	34(7)	α-Fe_2O_3	3.686	25
3	2.950	29(8)	Fe_3O_4	2.967	30
4	2.680	100	α-Fe_2O_3	2.703	100
5	2.525	100	Fe_3O_4	2.532	100
6	2.513	73(13)	α-Fe_2O_3	2.519	50
7	2.468	51(13)	FeO	2.486	80
8	2.195	35(7)	α-Fe_2O_3	2.208	20
9	2.149	100	FeO	2.153	100
10	2.093	37(9)	Fe_3O_4	2.099	20
11	2.082	-	AUSTENITE	2.080	100
12	2.012	100	α-Fe	2.027	100
13	1.839	46(9)	α-Fe_2O_3	1.843	40
14	1.843	-	AUSTENITE	1.800	50
15	1.707	19(6)	Fe_3O_4	1.715	10
16	1.688	61(11)	α-Fe_2O_3	1.696	60
17	1.610	41(13)	Fe_3O_4	1.616	30
18	1.595	15(4)	α-Fe_2O_3	1.601	16

TABLE 3.13(a) Wear Debris Identification

EXPERIMENTAL VALUES			ASTM INDEX VALUES		
DIFFRACTION LINE	d_{hkl} (Å)	RELATIVE INTENSITY	IDENTITY	d_{hkl} (Å)	RELATIVE INTENSITY
19	1.520	91(21)	FeO	1.523	60
20	1.485	44(9)	α-Fe_2O_3	1.487	35
21	1.480	71(16)	Fe_3O_4	1.485	40
22	1.450	44(9)	α-Fe_2O_3	1.454	35
23	1.434	26(6)	α-Fe	1.433	19
24	1.349	5(2)	α-Fe_2O_3	1.351	4
25	1.322	3(2)	Fe_3O_4	1.328	4
26	1.309	20(5)	α-Fe_2O_3	1.313	20
27	1.297	34(9)	FeO	1.299	25
28	1.275	20(6)	Fe_3O_4	1.281	10
29	1.256	10(3)	α-Fe_2O_3	1.260	8
30	1.242	33(8)	FeO	1.243	15
31	1.211	8(2)	α-Fe_2O_3	1.215	4
32	1.189	9(2)	α-Fe_2O_3	1.191	8
33	1.168	64(13)	α-Fe	1.170	30
34	1.161	12(3)	α-Fe_2O_3	1.165	10
35	1.140	18(4)	α-Fe_2O_3	1.142	12
36	1.076	23(6)	FeO	1.077	15
37	1.013	45(10	α-Fe	1.013	9

TABLE 3.13(b) Wear Debris Identification

Fe_3O_4. The major α-Fe lines were also visible on the x-ray diffraction patterns. See Figure 3.23. This figure shows the microdensitometer trace of x-ray diffraction pattern for 8.3N load experiment. As the load increased above the transition the debris changed into predominantly FeO and α-Fe.

(iii) $T_D = 200^{\circ}C$

A transition was observed in the wear rate curve at a load of about 35N. See Figure 3.1(a). The constituents of wear debris below this transition was α-Fe_2O_3, Fe_3O_4 and α-Fe. Traces of FeO were also detected in 29.4N load experiment. The debris changed character for loads immediately above the transition and consisted of FeO, Fe_3O_4 and α-Fe with traces of α-Fe_2O_3. Figure 3.24 shows microdensitometer traces of x-ray diffraction pattern for 29.4N and 39.2N load experiments. The 39.2N load trace shows a marked increase in α-Fe and FeO. As the load increased, the oxide gradually changed into a mixture of FeO and Fe_3O_4, with FeO becoming more predominant. No α-Fe_2O_3 was detected at loads greater than 85N. The α-Fe lines were always present.

(iv) $T_D = 300^{\circ}C$

Wear debris collected for each experiment below 98.1N applied load was very fine light brown powder. X-ray diffraction examination of debris indicated that α-Fe_2O_3 was the main constituent with traces of α-Fe and Fe_3O_4. See Figure 3.25(a). However, the Fe_3O_4 lines became stronger as the load increased. At 98.1N load, the debris consisted mainly of FeO and α-Fe with traces of α-Fe_2O_3 and Fe_3O_4, as shown by the microdensitometer trace of the wear debris from this load given in Figure 3.25(b).

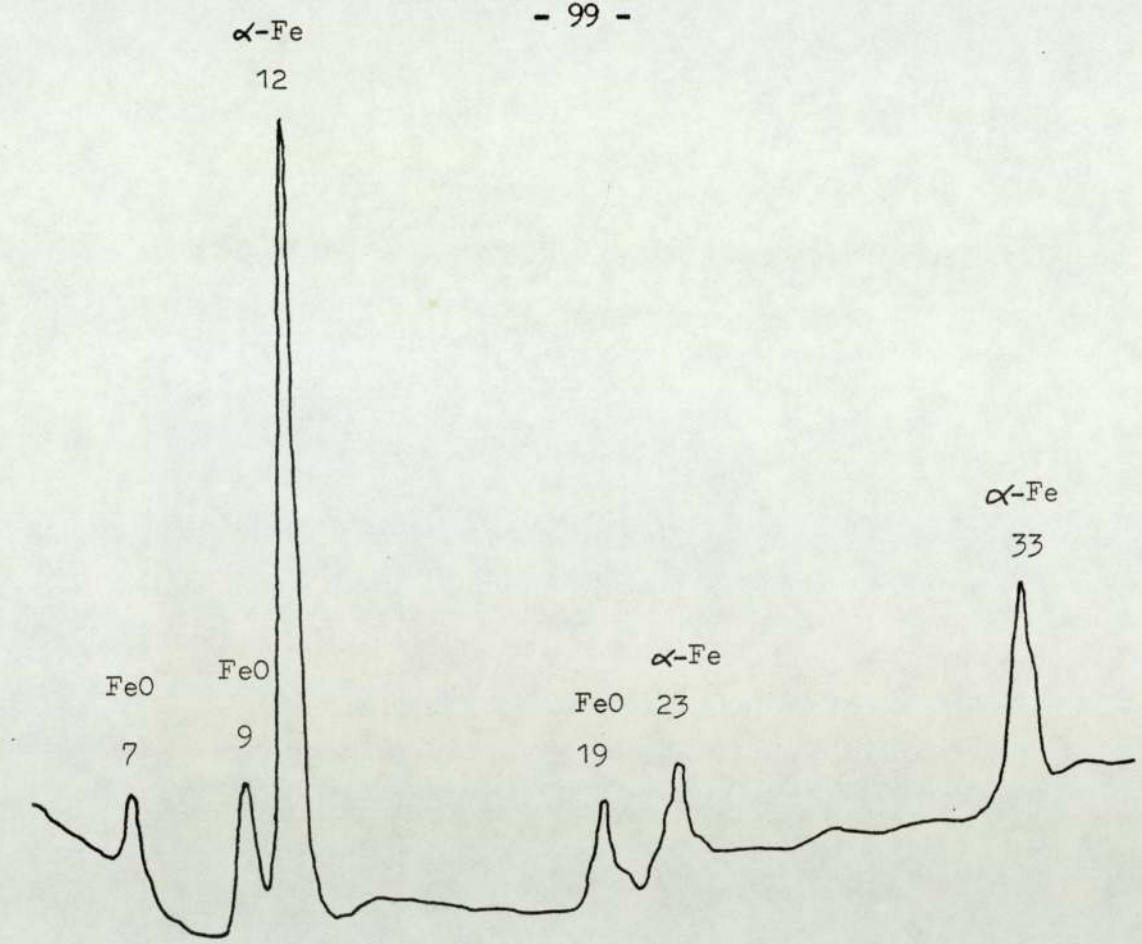

FIGURE 3.22 Microdensitometer Trace of the Wear Debris from 29.4N Load EN8 Experiment at Room Temperature.

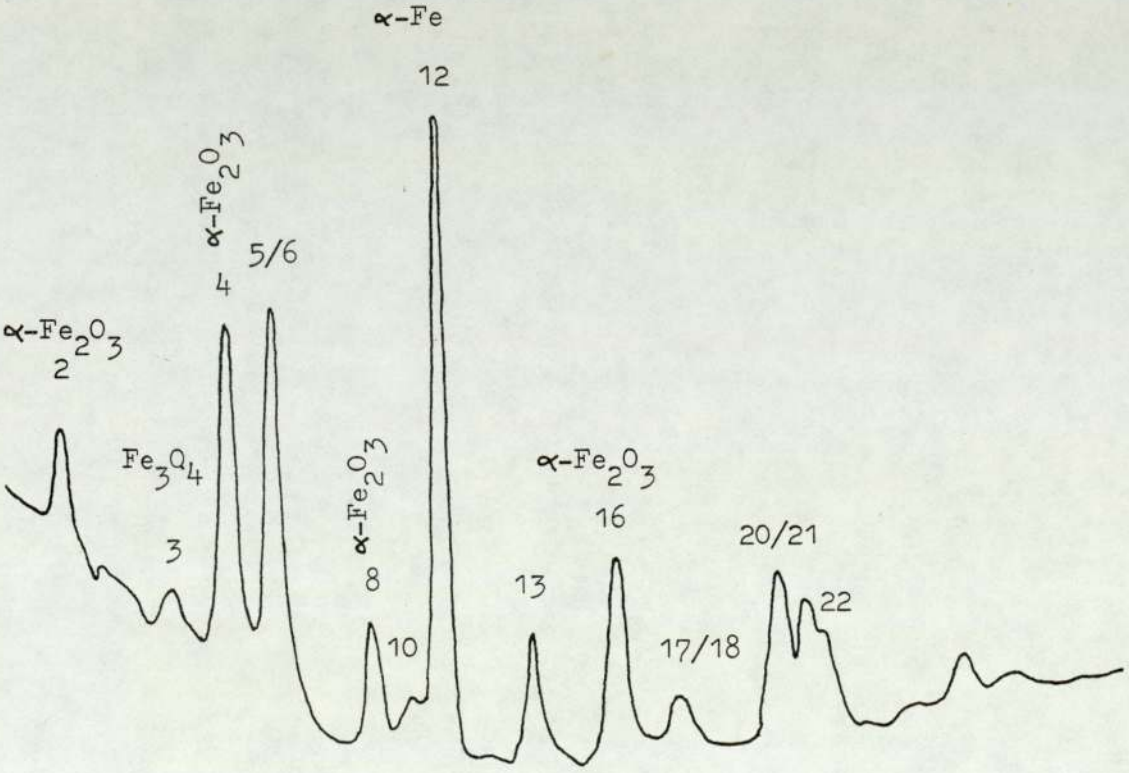

FIGURE 3.23 Microdensitometer Trace of the Wear Debris from 8.3N Load EN8 Experiment at 100°C.

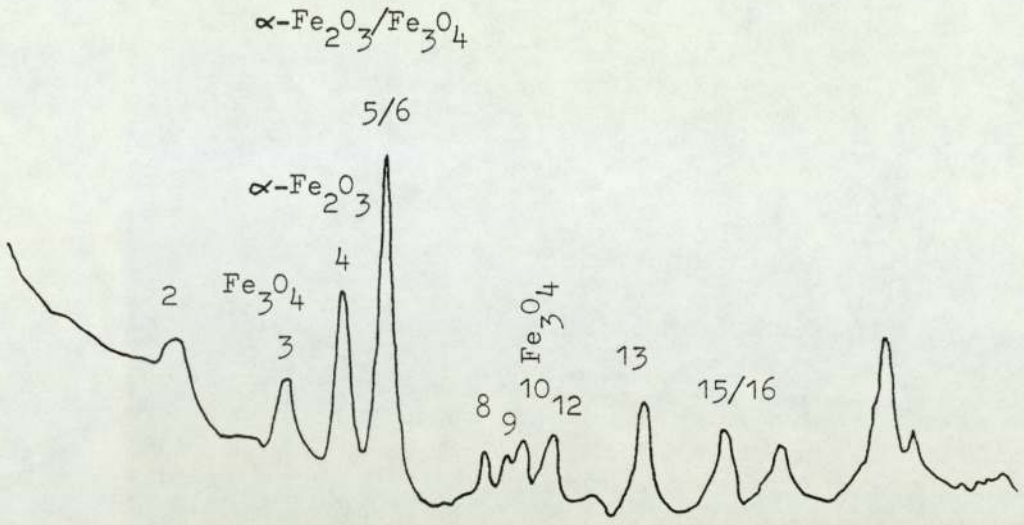

(a) 29.4N

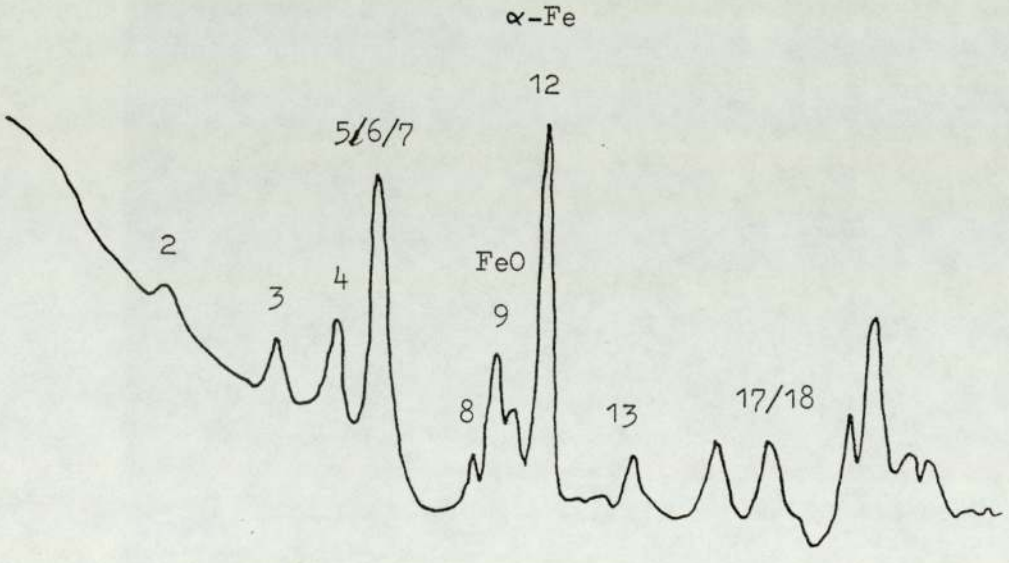

(b) 39.2N

FIGURE 3.24 Microdensitometer Traces of the Wear Debris from EN8 Experiments at 200°C.

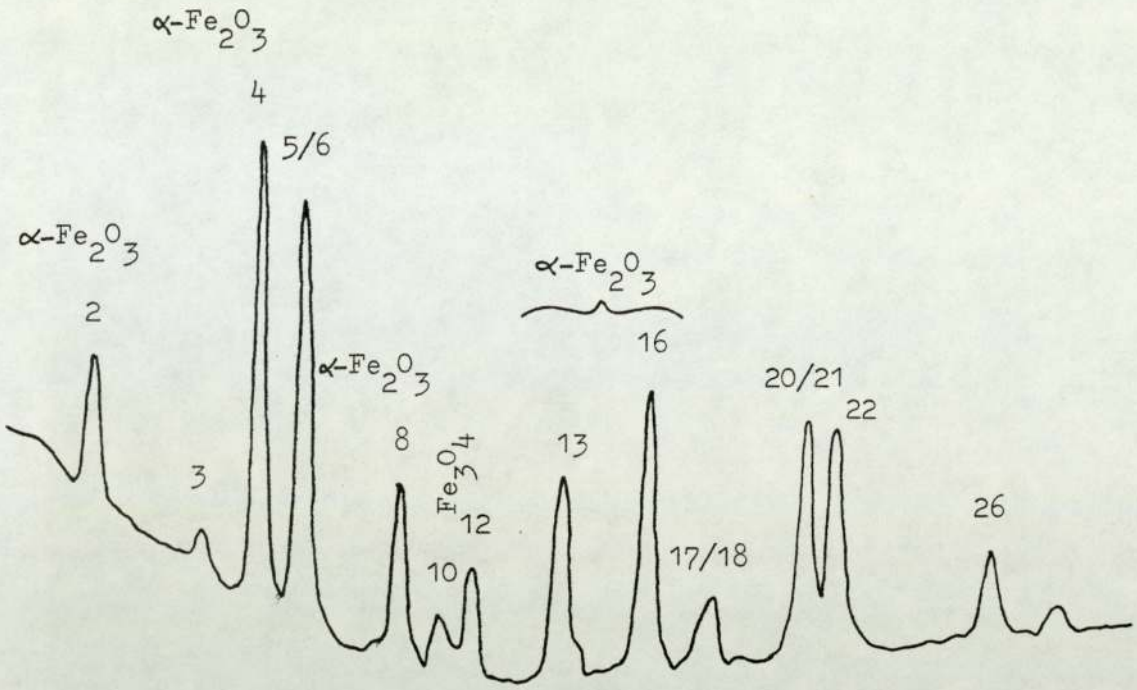

(a) 58.9N

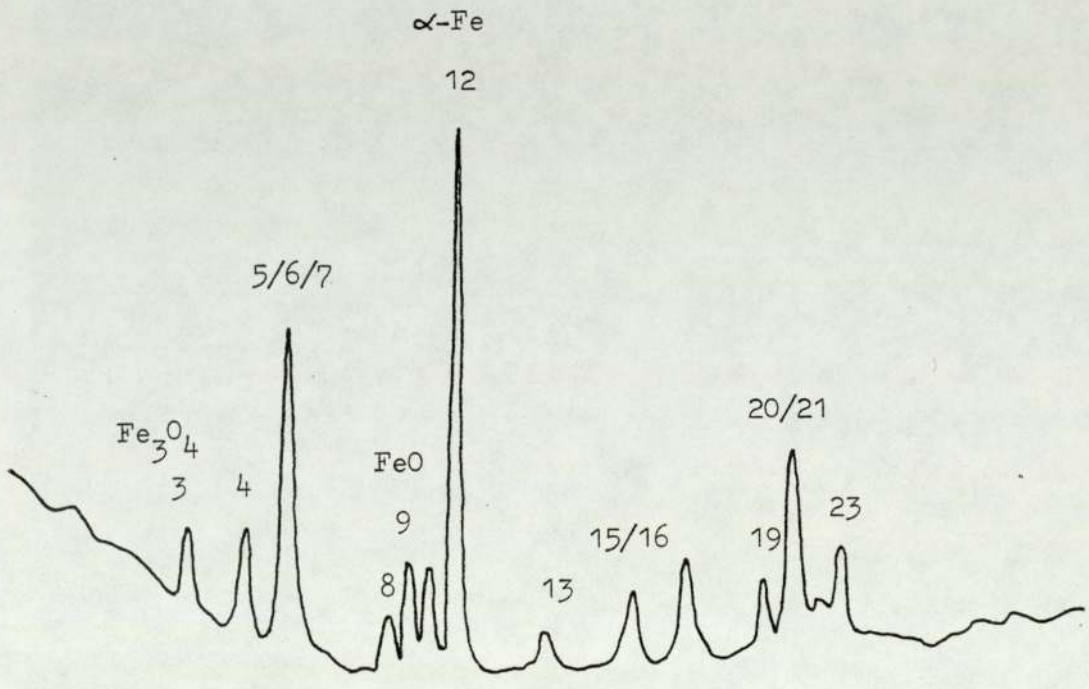

(b) 98.1N

FIGURE 3.25 Microdensitometer Traces of the Wear Debris from EN8 Experiments at 300°C.

(v) T_D = 400°C and 500°C

The major constituents of the wear debris at all loads were α-Fe_2O_3 and Fe_3O_4. No Feo was detected and α-Fe lines were barely visible. Microdensitometer results showed the peak height ratio of 2.703Å α-Fe_2O_3(diffraction line 4 in Table 3.13) and 2.52Å α-Fe_2O_3/Fe_3O_4 (diffraction lines 5/6 in Table 3.13) lines was approximately constant for all the loads considered. This indicated that the composition of wear debris did not vary with load. A typical microdensitometer trace from 400°C and 500°C experiments is shown in Figures 3.26(a) and (b) respectively.

3.7.2 EN31 Experiments

(i) Room Temperature and T_D = 100°C

The wear behaviour of EN31 steel at these temperatures was characterised by three different wear regimes. See Figure 3.2(a). Microdensitometer traces taken from powder patterns of wear debris produced in each of these wear regimes are shown in Figure 3.27. The debris was selected from 19.6N, 58.9N and 98.1N load experiments carried out at room temperature. The debris was irradiated with Cobalt Kα x-rays for 45 minutes at a potential and filament current of 40kV and 30mA respectively.

Figure 3.27(a) shows that in the first wear regime, at loads below 30N, the constituents of wear debris were α-Fe_2O_3, Fe_3O_4, FeO and α-Fe. For loads in the range of 30N to 80N (second wear regime) large increase in Fe_3O_4 was observed. A microdensitometer trace from 58.9N load experiment shows this quite clearly in Figure 3.27(b). However

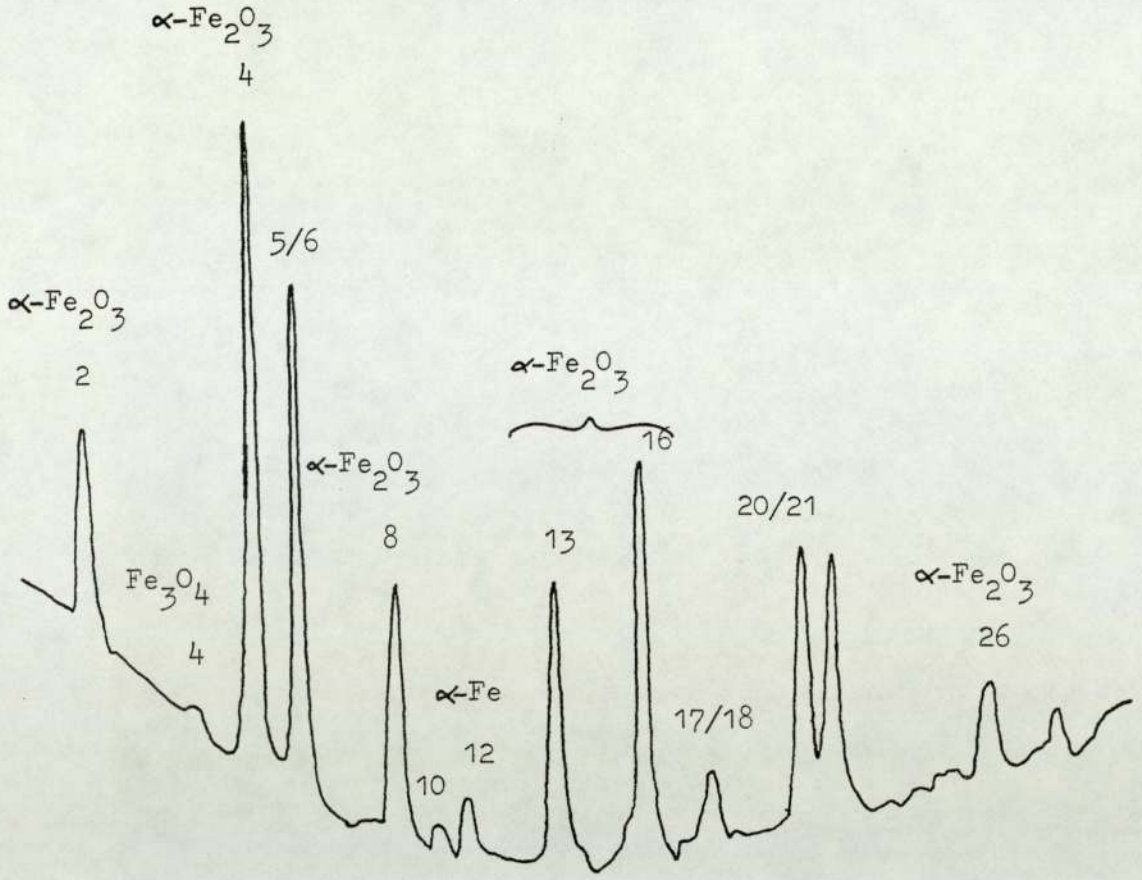

(a) 68.7N, 400°C

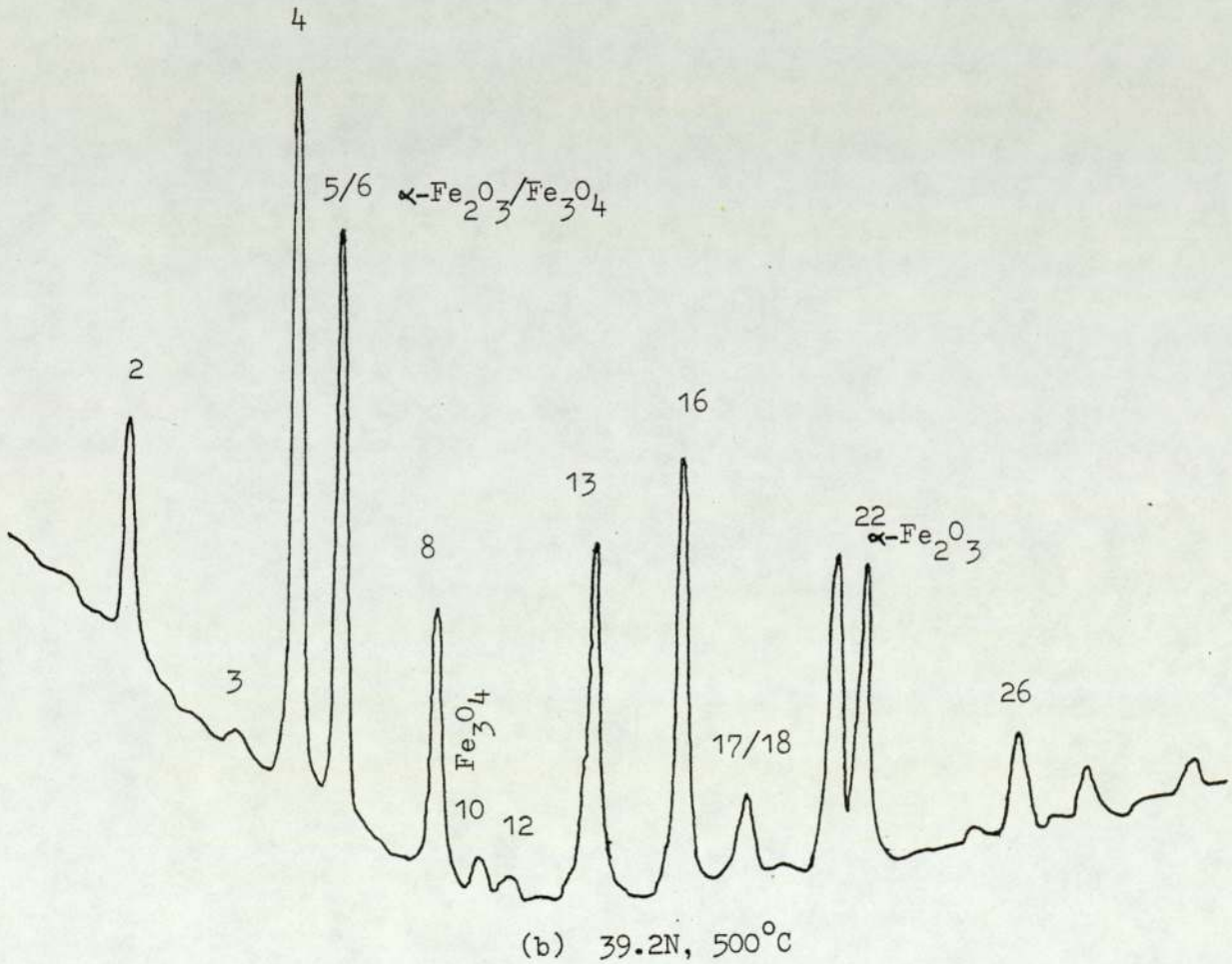

(b) 39.2N, 500°C

FIGURE 3.26 Typical Microdensitometer Trace of the Wear Debris from EN8 Experiments at 400°C and 500°C.

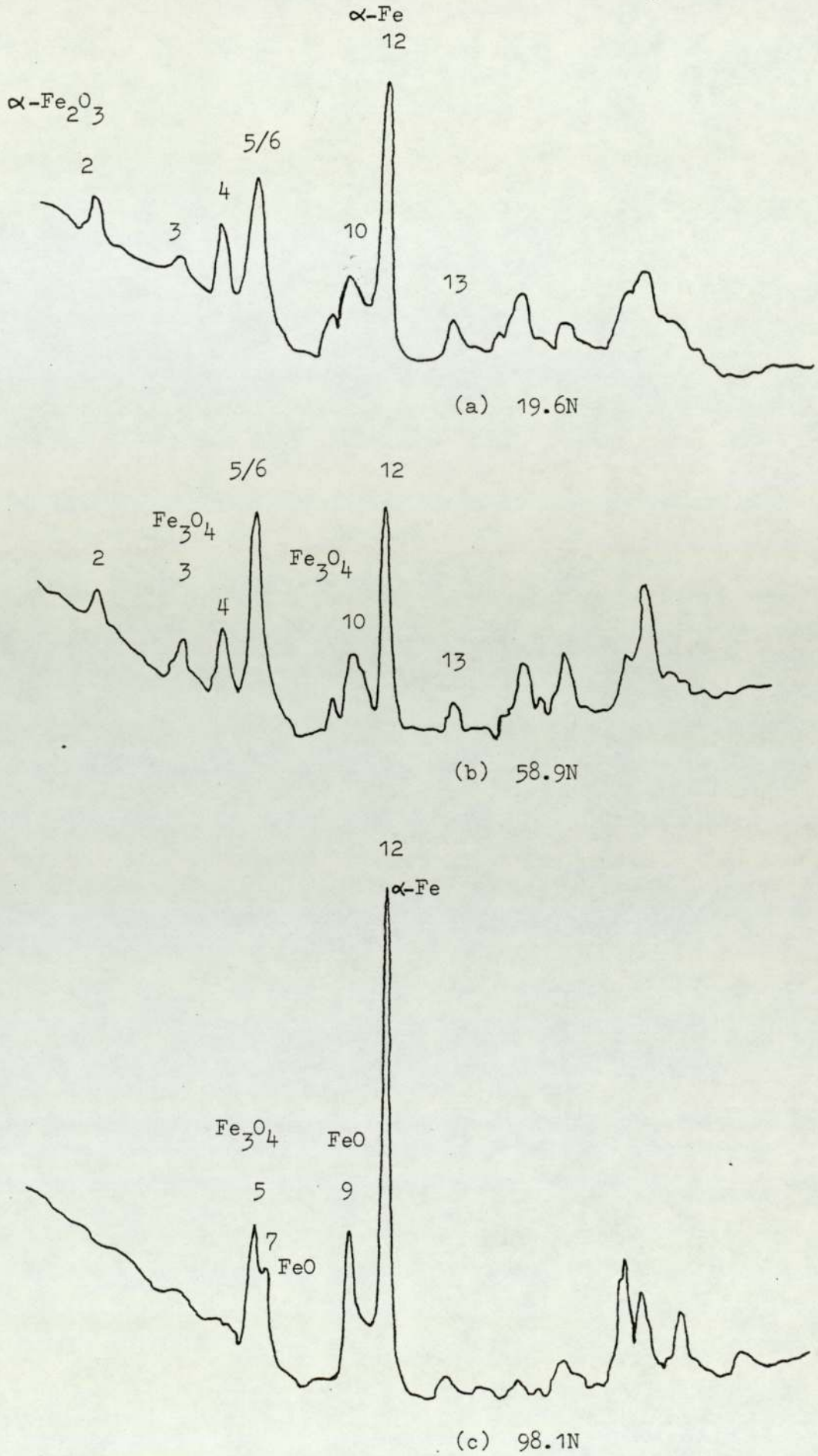

FIGURE 3.27 Microdensitometer Traces of the Wear Debris from EN31 Experiments at Room Temperature.

in the third wear regime occurring at loads greater than 80N, the wear debris was a mixture of FeO, Fe_3O_4 and α-Fe. See Figure 3.27(c). The disappearance of α-Fe_2O_3 lines is also apparent from this figure.

(ii) T_D = 200°C

For loads below 60N the composition of wear debris as analysed by x-ray diffraction was a mixture of α-Fe_2O_3, Fe_3O_4 and α-Fe. See Figure 3.28(a). This figure shows a microdensitometer trace for 24.5N load experiment. In 63.8N load experiment, the appearance of faint FeO lines was evident from powder diffraction pattern. The microdensitometer trace of the pattern showed an increase in α-Fe. Debris from all experiments carried out at loads higher than 63.8N showed an increase in FeO with load. However, at 83.4N, an increase in Fe_3O_4 oxide was observed. At the highest load employed (137.3N) the α-Fe_2O_3 lines were barely visible, as shown by the microdensitometer trace given in Figure 3.28(b).

(iii) T_D = 300°C

The debris from all the experiments at this disc temperature was a mixture of α-Fe_2O_3 and Fe_3O_4. Figure 3.29(a) shows a microdensitometer trace for 58.9N load experiment. Samples of debris from 157.0N experiment showed an increase in Fe_3O_4 oxide. No FeO lines were detected. See Figure 3.29(b).

(iv) T_D = 400°C and 500°C

The oxide detected was similar to that detected in the EN8 experiments at these temperatures, i.e.

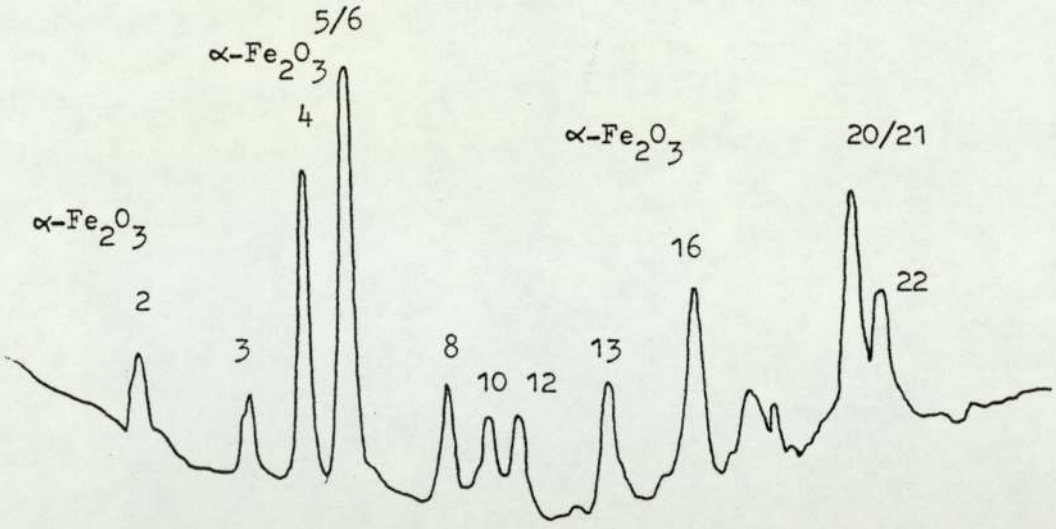

(a) 24.5N

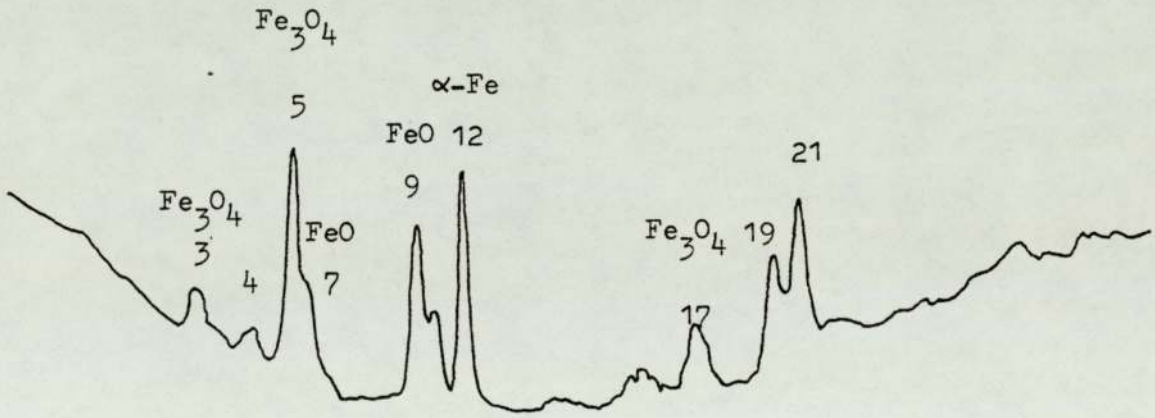

(b) 137.3N

FIGURE 3.28 Microdensitometer Traces of the Wear Debris from EN31. Experiments at 200°C.

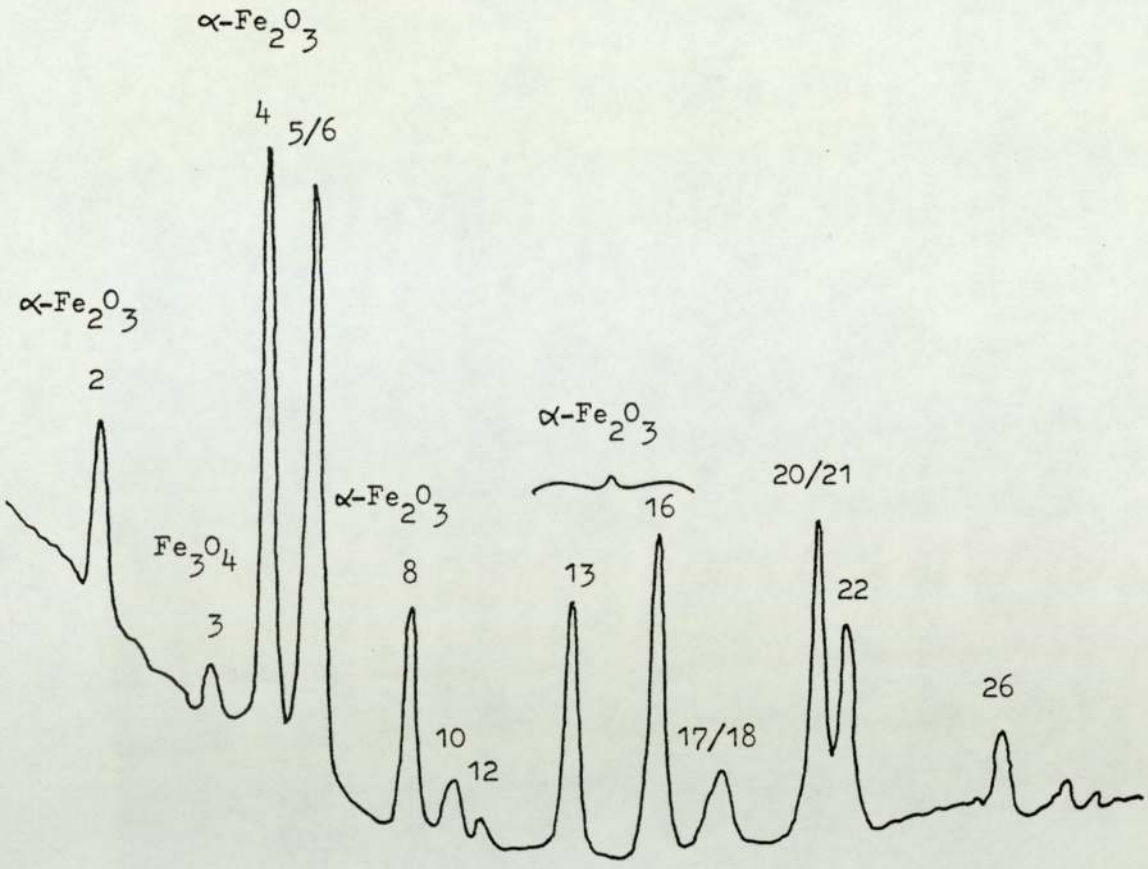

(a) 58.9N

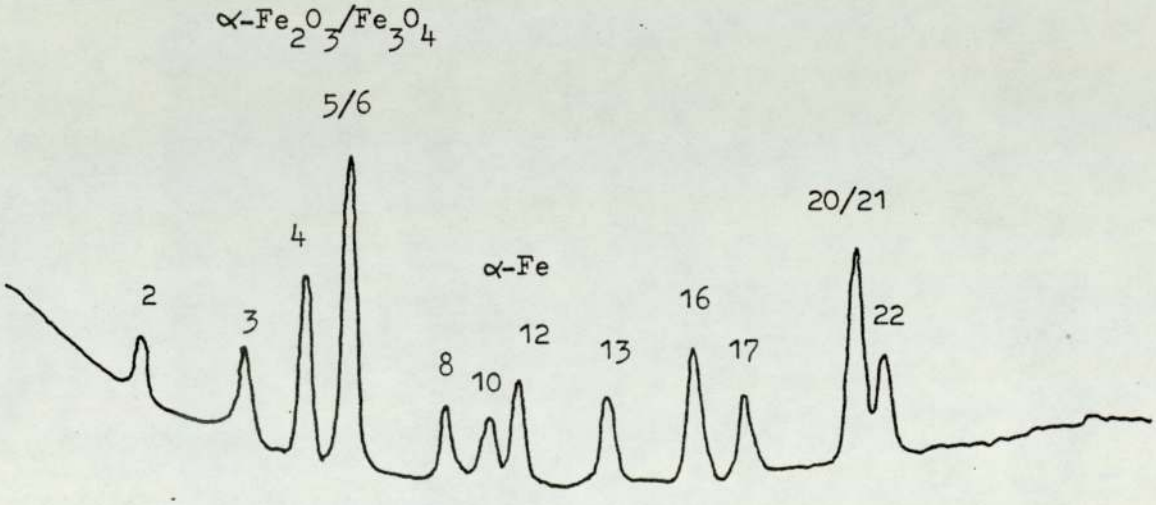

(b) 157.0N

FIGURE 3.29 Microdensitometer Traces of the Wear Debris for EN31 Experiments at 300°C.

a mixture of α-Fe_2O_3 and Fe_3O_4. The α-Fe lines were very faint and barely detectable. A typical microdensitometer trace taken from 58.9N load 400°C experiment is shown in Figure 3.30.

3.8 Glancing Angle X-ray Diffraction of the Worn Specimens

A glancing angle x-ray diffraction technique was used to study the surface films formed on worn pins. Diffraction lines on the x-ray pattern were measured using the α-Fe lines 110, 200, 211 and 220 as internal standard. The results showed that oxides detected on pin surfaces corresponded to those found in the wear debris. Compounds identified on worn pin surfaces and in the wear debris for selected EN8 and EN31 experiments are presented in Table 3.14. This technique also revealed that subsurface layers of some worn pins contained austenite (γ-Fe). This was evident from the detection of 2.08Å and 1.80Å lines on the x-ray pattern. Microdensitometer trace of the x-ray diffraction pattern of 58.9N load 200°C EN8 worn pin is shown in Figure 3.31. Confirmation of this was obtained from the absence of these two lines from x-ray diffraction pattern of an unworn pin. X-ray data indicated that austenite is present in the following experiments: at loads greater than about 30N and 50N for the EN8 experiments conducted at room temperature (and 100°C) and 200°C respectively; at loads greater than about 90N for the EN31 experiments conducted at room temperature, 100°C and 200°C. Therefore, the presence of austenite suggested that contact temperature must have been in excess of 730°C, i.e. the martensite - austenite transformation temperature. Welsh (39), in his comprehensive study of wear of plain carbon steels, observed that soft steels can undergo profound structural changes and intense surface hardening (600 - 850 VPN). It was assumed that this hard phase represented material transformed to austenite by local temperatures above the α-γ transformation point and then converted to martensite by rapid cooling.

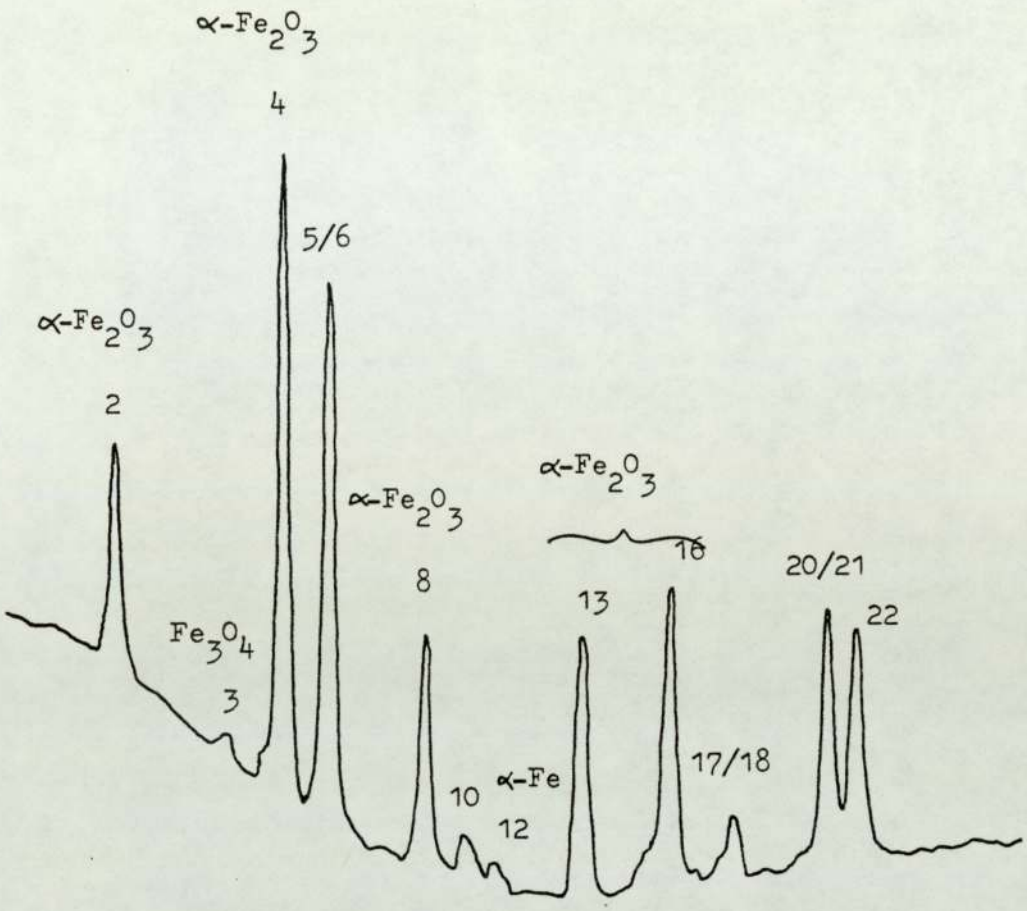

FIGURE 3.30 Typical Microdensitometer Trace of the Wear Debris from EN31 Experiments at 400°C and 500°C.

EXPERIMENTAL CONDITIONS			X-RAY DIFFRACTION ANALYSIS	
PIN	LOAD (N)	TEMPERATURE (^{o}C)	WEAR DEBRIS	PIN SURFACE
EN8	29.4	Room	FeO, α-Fe	FeO, α-Fe
EN8	39.4	Room	FeO, α-Fe	Fe_3O_4(T), FeO, α-Fe Austenite (T)
EN8	9.8	200	α-Fe_2O_3, Fe_3O_4 α-Fe	α-Fe_2O_3, Fe_3O_4 FeO (T), α-Fe
EN8	58.9	200	α-Fe_2O_3, Fe_3O_4 FeO, α-Fe	α-Fe_2O_3, Fe_3O_4 α-Fe, FeO, Austenite(T)
EN8	117.7	200	Fe_3O_4, FeO, α-Fe	Fe_3O_4, FeO, α-Fe Austenite
EN8	98.1	500	α-Fe_2O_3, Fe_3O_4 α-Fe (T)	α-Fe_2O_3, Fe_3O_4 α-Fe
EN31	29.4	Room	α-Fe_2O_3, Fe_3O_4 α-Fe, FeO (T)	α-Fe_2O_3, Fe_3O_4 α-Fe, FeO (T)
EN31	9.8	100	α-Fe_2O_3, Fe_3O_4 α-Fe	α-Fe_2O_3, Fe_3O_4 α-Fe
EN31	98.1	100	Fe_3O_4, FeO α-Fe	Fe_3O_4, FeO, α-Fe Austenite (T)
EN31	39.4	400	α-Fe_2O_3, Fe_3O_4 α-Fe (T)	α-Fe_2O_3, Fe_3O_4 α-Fe

T = Traces.

TABLE 3.14 Compounds Identified in the Debris and on Pin Surface by X-Ray Diffraction.

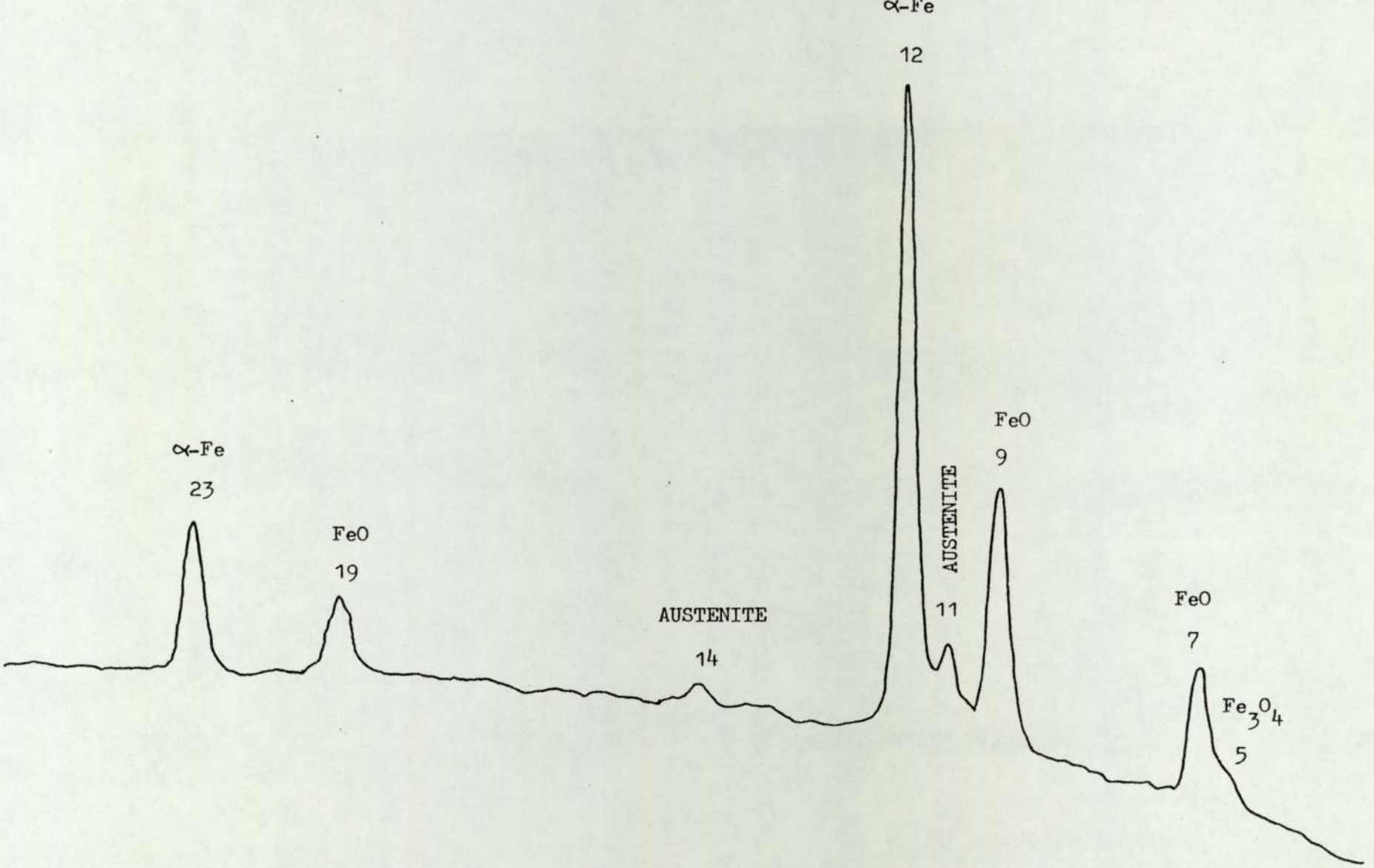

FIGURE 3.31 Microdensitometer Trace of Glancing Angle X-ray Diffraction Pattern of 58.9N Pin from EN8 Experiments at 200°C.

3.9 Proportional Analysis of Wear Debris

The intensity of a diffraction maximum depends upon the volume of the material irradiated and several other factors. From basic x-ray diffraction theory (99), it can be shown that the intensity of x-rays diffracted into a maximum at $2\theta_{hkl}$ to the undeviated direction is given by Equation 3.2:

$$I_x \alpha \left\{\frac{F_x^2 m L_p \exp(-2M)}{\nu_x^2}\right\} V_x A_\theta \qquad (3.2)$$

where

F_x is the structure factor of the component x

m is the multiplicity factor of the diffraction plane (hkl)

L_p is the Lorentz polarisation factor

exp(-2M) is the Debye-Waller temperature factor (a function of θ)

ν_x is the volume of the unit cell of substance x

V_x is the volume of substance x irradiated

and A_θ is the sample absorption factor, dependent upon angle of diffraction.

These terms are discussed in more detail in Appendix 1. Since for any sample only the relative intensities are required Equation 3.2 can be written as:

$$I_x = R_x V_x A_\theta \qquad (3.3)$$

where

$$R_x = \left\{\frac{F_x m L_p \exp(-2M)}{\nu_x^2}\right\} \qquad (3.4)$$

Following Averbach and Cohen (100), Quinn (97) showed that if graph of I_x/R_x is plotted against Bragg angle θ, a curve

should be obtained which represents the variation of A_θ with θ. Assuming that absorption of x-rays depend upon the mixture as a whole and not on the individual components giving rise to the maximum, then curves if I/R plotted against θ for two components (x and y) should be the same, except for a difference in ordinate representing the ratio of their volumes. Thus, at angle θ

$$\frac{I_{x/R_x}}{I_{y/R_y}} = \frac{V_x}{V_y} \qquad (3.5)$$

Taking logs of both sides of Equation 3.5 we get

$$\text{Log}_e \frac{V_x}{V_y} = \text{Log}_e \frac{I_x}{R_x} - \text{Log}_e \frac{I_y}{R_y} \qquad (3.6)$$

Thus if the logs of the ratio (I/R) are plotted against θ the difference in ordinates of the graphs gives the log of (V_{x/V_y}). The relative intensities can be measured fairly easily via a microdensitometer trace of the x-ray diffraction pattern. Typical microdensitor traces are shown in Figures 3.22 to 3.30. To a reasonably good approximation, Quinn (97) showed that the relative integrated intensity (when referred to the microdensitometer trace) is given by the product, "peak height" times "width of the peak at half its height". The factor R can be readily evaluated for crystalline substance of known structure (see Appendix 1).

Quinn et al. (46, 101,102) have applied this technique to the proportional analysis of wear debris, namely the proportional analysis of the wear debris formed during the unlubricated sliding of low-alloy medium-carbon steels. However, it was later shown (103) that the R values used by Quinn in his analysis were incorrect. The inconsistencies arose because of incorrect values used for the multiplicity factor (m). The corrected R values, recalculated by Rowson (103), are given in Appendix 1. Using these R values, Rowson showed that curves of I/R plotted against θ could be approximated to straight lines of positive slope. Figure 3.32

shows I/R versus plots for 100% standards of α-Fe, α-Fe_2O_3, Fe_3O_4 and FeO. The broken lines shown in this figure are lines of equal slope and the solid lines correspond to the lines that best fit the results. Clearly Figure 3.32 shows (apart from the fact that it is possible to get straight lines of positive slope) that the variation of A_θ with Bragg angle θ is approximately the same for iron and its three oxides.

An example of the method of proportional analysis taken from reference (103) is given in Figure 3.33. The following procedure is adopted to determine the percentage volumes of various constituents present in the wear debris. A component which has the most readily resolved diffraction pattern is chosen to serve as an internal standard. For example, in Figure 3.33 FeO is chosen as the internal standard. Consequence of the assumption made about the absorption factor A_θ, lines through the other components are drawn parallel to the internal standard. Then the ratios of the ordinates of the points relating to the other components with the corresponding ordinate of the standard are compared in order to obtain estimates of relative volume percentages. If lines of equal slopes are not drawn through the various components then different volume percentages at different angular position θ on the graph would be obtained.

In applying this method to the present work some alarming results were obtained. It was found that sometimes it was not possible to obtain I/R versus θ plots which gave lines of positive slope. Thus it appeared that the basic idea of proportional analysis was being contradicted.

It was decided to test the technique using pre-mixed standards of known percentage volume concentrations. These standards were prepared from α-Fe, α-Fe_2O_3, Fe_3O_4 and FeO powders. After mixing these powders into 50/50 proportions using a rotary mixture, x-ray diffraction analysis was carried out on samples taken from these 50/50 standards.

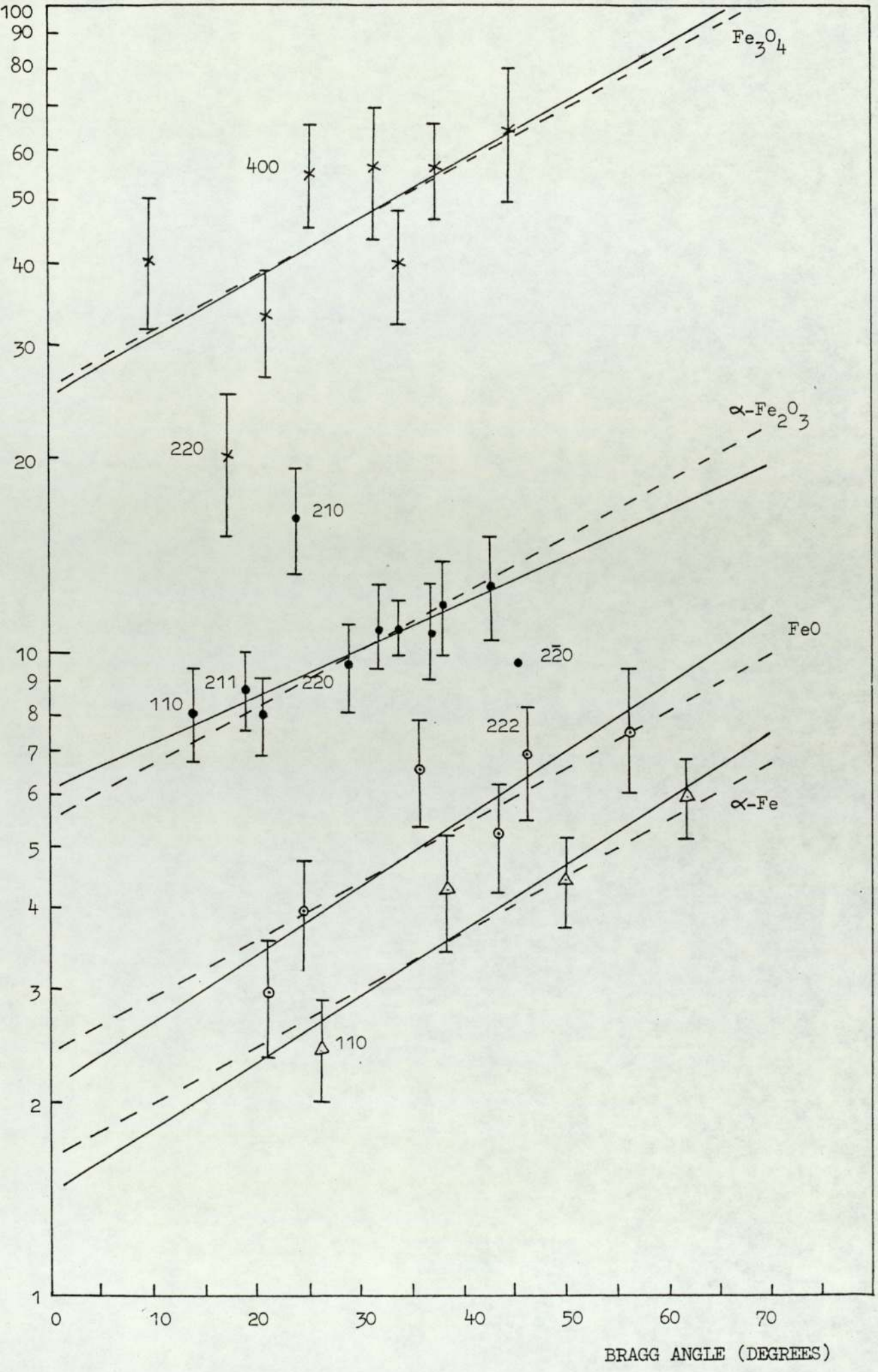

FIGURE 3.32 (I/R) Versus Bragg Angle for 100% Standards of α-Fe, α-Fe_2O_3, Fe_3O_4 and FeO.

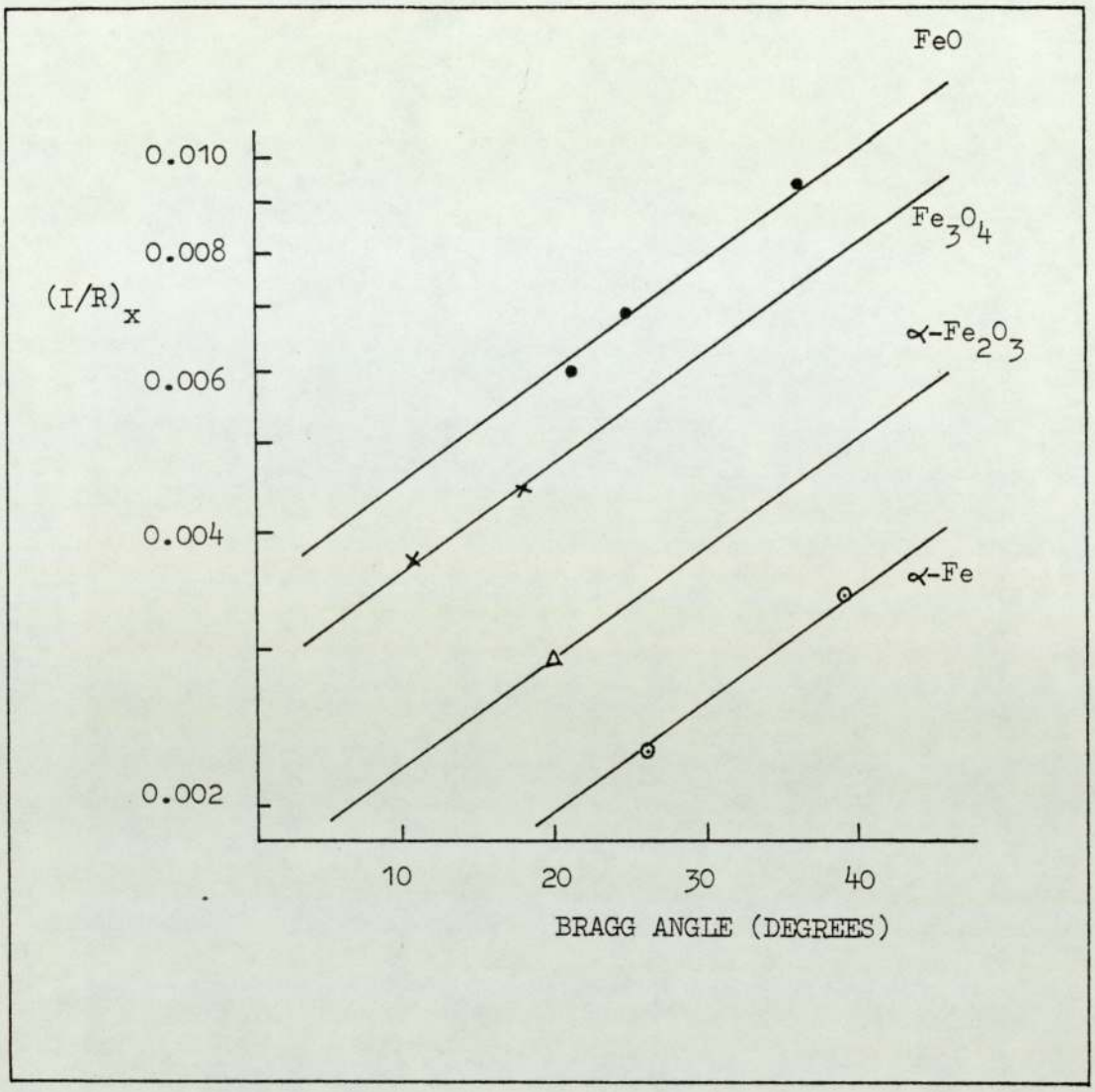

Using FeO as the Internal Standard:

$$V_{Fe_3O_4} / V_{FeO} = 0.00545/0.00700 = 0.77857$$

$$V_{\alpha\text{-}Fe_2O_3} / V_{FeO} = 0.00344/0.00700 = 0.49143$$

$$V_{\alpha\text{-}Fe} / V_{FeO} = 0.00235/0.00700 = 0.33571$$

$V_{FeO} = 100/ (1+0.77857+0.49143+0.33571) = 38.4\% = 38\%$

$V_{Fe_3O_4} = 38.4 \times 0.77857 = 29.9\% = 30\%$

$V_{\alpha\text{-}Fe_2O_3} = 38.4 \times 0.49143 = 18.9\% = 19\%$

$V_{\alpha\text{-}Fe} = 38.4 \times 0.33571 = 12.7\% = 13\%$

FIGURE 3.33 An Example of the Method of Proportional Analysis of Wear Debris (103)

Cobalt Kα radiation was used throughout. A typical set of results from 50/50 α-Fe_2O_3/FeO standard are given in Table 3.15 and Figure 3.34 gives the log(I/R) versus θ plot for these results. The calculated percentage volume for 50/50 α-Fe_2O_3/FeO standard, together with result from other 50/50 standards, are tabulated in Table 3.16. To eliminate the possibility of any uncertainty in the preparation of the standards, new 50/50 mixtures of both α-Fe_2O_3/α-Fe and Fe_3O_4/α-Fe were prepared. The calculated percentage volumes for these mixtures are also given in Table 3.16. Clearly this table shows that the calculated percentage volumes of these 50/50 standards are in poor agreement with the expected volumes, especially more so for the α-Fe/α-Fe_2O_3 and α-Fe/Fe_3O_4 mixtures. This is most disturbing because α-Fe, α-Fe_2O_3 and Fe_3O_4 are the main constituents found in debris produced during the wear of plain carbon steels. However, the agreement between the expected and calculated percentage volume for the α-Fe/FeO standard is very good. The reproducibility of the α-Fe_2O_3/α-Fe and Fe_3O_4/α-Fe results shown in Table 3.16 suggests that the R values used in the calculations are probably incorrect. The standard deviation given in this table is the error associated in the measurement of the relative integrated intensity, i.e. the area under the peak.

In calculating the value of R for a particular diffraction line, Quinn (97, 104) and then Rowson (10^3) had assumed that the atomic scattering factor f (used in the calculation of F_x) was independent of the incident wavelength λ, as long as the quantity $(\text{SIN } \theta)/\lambda$ was constant. This is not quite true. When the incident wavelength λ is nearly equal to the wavelength λ_k of the K absorption edge of the scattering element, then the atomic scattering factor of that element may be several units lower than it is when λ is very much shorter than λ_k(96). This correction for anomalous change Δf in scattering factor near an absorption edge is particularly important for iron atoms when Cobalt Kα radiation is used. A curve (taken from reference 96) showing the variation of Δf with λ/λ_k is given

OXIDE	d_{hkl} (Å)	θ°	I	R	I/R
α-Fe_2O_3	3.686	14.20	88±10	13.48	6.35±0.73
	2.703	19.50	329±27	36.18	9.09±0.74
	2.208	24.05	108±12	6.68	16.17±1.80
	1.843	29.20	170±16	15.10	11.26±1.05
	1.696	32.00	228±20	17.71	12.87±1.10
	1.6013	34.10	42±6	4.19	10.02±1.60
	1.4873	37.10	140±13	12.76	10.97±1.06
	1.4343	38.10	150±15	11.46	13.19±1.30
	1.2595	45.40	52±7	3.29	15.80±2.20
	1.1416	51.75	73±9	4.47	16.30±2.00
	1.1042	54.25	70±8	4.70	14.90±1.80
	1.0571	58.05	77±9	6.01	12.81±1.50
FeO	2.153	24.60	324±30	68.28	4.75±0.44
	1.523	36.05	248±23	37.41	6.63±0.63
	1.243	46.10	91±10	12.94	7.03±0.80
	1.077	56.25	81±9	8.24	9.83±1.10

TABLE 3.15 Proportional Analysis of a 50/50 Mixture of α-Fe_2O_3 and FeO.

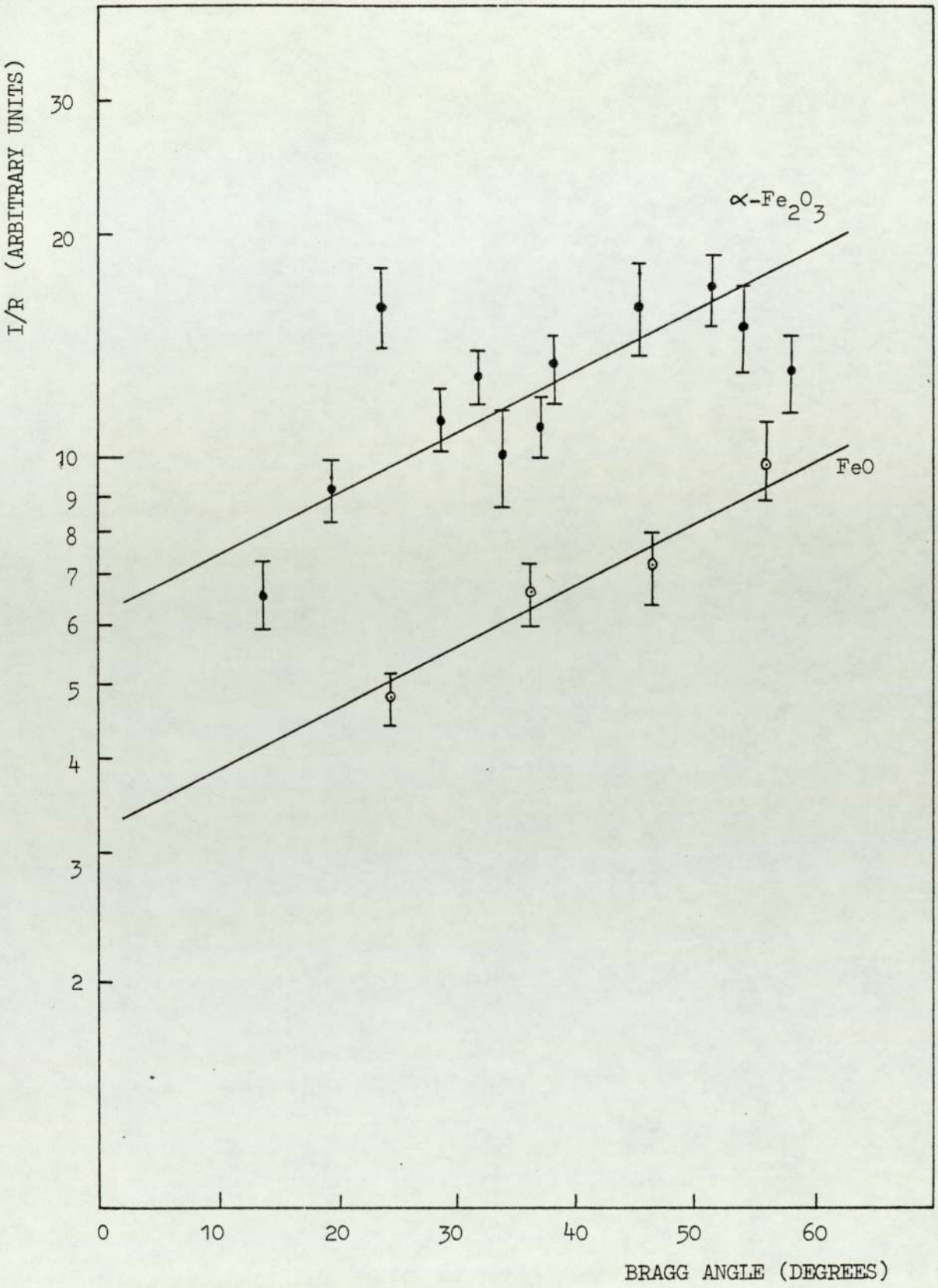

FIGURE 3.34 I/R Versus Bragg Angle for 50/50 Mixture of α-Fe_2O_3 and FeO.

50/50 MIXTURE (X - Y)	$(I_x/R_x)_\theta$	$(I_y/R_y)_\theta$	Calculated Volume (V_x-V_y) %
α-Fe_2O_3/FeO	11.8	6.0	(66-34) $\pm$ 7
Fe_3O_4/FeO	5.5	9.0	(38-62) $\pm$ 6
α-Fe_2O_3/Fe_3O_4	4.6	2.7	(37-63) $\pm$ 12
α-Fe/FeO	1.6	1.7	(48-52) $\pm$ 5
α-Fe_2O_3/α-Fe	17.1	2.5	(87-13) $\pm$ 3
	7.2	1.4	(84-16) $\pm$ 4
Fe_3O_4/α-Fe	12.2	2.1	(85-15) $\pm$ 5
	12.2	1.5	(89-11) $\pm$ 3

TABLE 3.16 Proportional Analysis of 50/50 Mixtures of α-Fe_2O_3 , Fe_3O_4 , FeO and α-Fe .

in Appendix 1. Because the variation of Δf with atomic number Z is not large, this curve can be used with fairly good accuracy to estimate the correction Δf which must be applied for any particular combination of wavelength and scattering element.

Following on from this work, Rowson (103) has recently recalculated the R values using atomic scattering factors corrected for anomalous scattering. These new R values, together with the original uncorrected R values of Rowson (103), are given in Appendix 1. These tables show that the new corrected R values are considerably lower (for some diffraction lines by a factor of nearly two) than the uncorrected R values. However, on using these new R values in the proportional analysis of the pre-mixed standards no significant difference was found in the calculated percentage volumes. The reason for this can best be explained if we consider the proportional analysis results for a 50/50 α-Fe_2O_3/α-Fe mixture shown in Figure 3.35. For the sake of comparison, this figure shows log (I/R) versus θ plots corresponding to uncorrected and correct R values. Referring only to the α-Fe_2O_3 and α-Fe lines corresponding to the uncorrected R values, the difference in ordinates of these two lines correspond to a ratio of $V\alpha$-Fe_2O_3/ $V\alpha$-Fe of 7.0 (±2.0). This gave the composition of the mixture as (87 ±4)% α-Fe_2O_3 and (13±4)% α-Fe. Similarly, for the corrected α-Fe_2O_3 and α-Fe lines the ratio of $V\alpha$-Fe_2O_3/ $V\alpha$-Fe is 6.4 (±1.5). This gave the composition of the mixture as (86±3)% α-Fe_2O_3 and (14±3)% α-Fe. Clearly, since the corrected R values simply increases the ordinates of α-Fe_2O_3 and α-Fe lines by approximately equal amounts (i.e. the difference in the ordinates remains the same) the values calculated for the percentage volume are not affected. Very much similar results were obtained for other standard mixtures.

The α-Fe_2O_3/Fe_3O_4 mixture was studied further by preparing various standards of different proportions. For this mixture only five diffraction lines on the x-ray diffraction

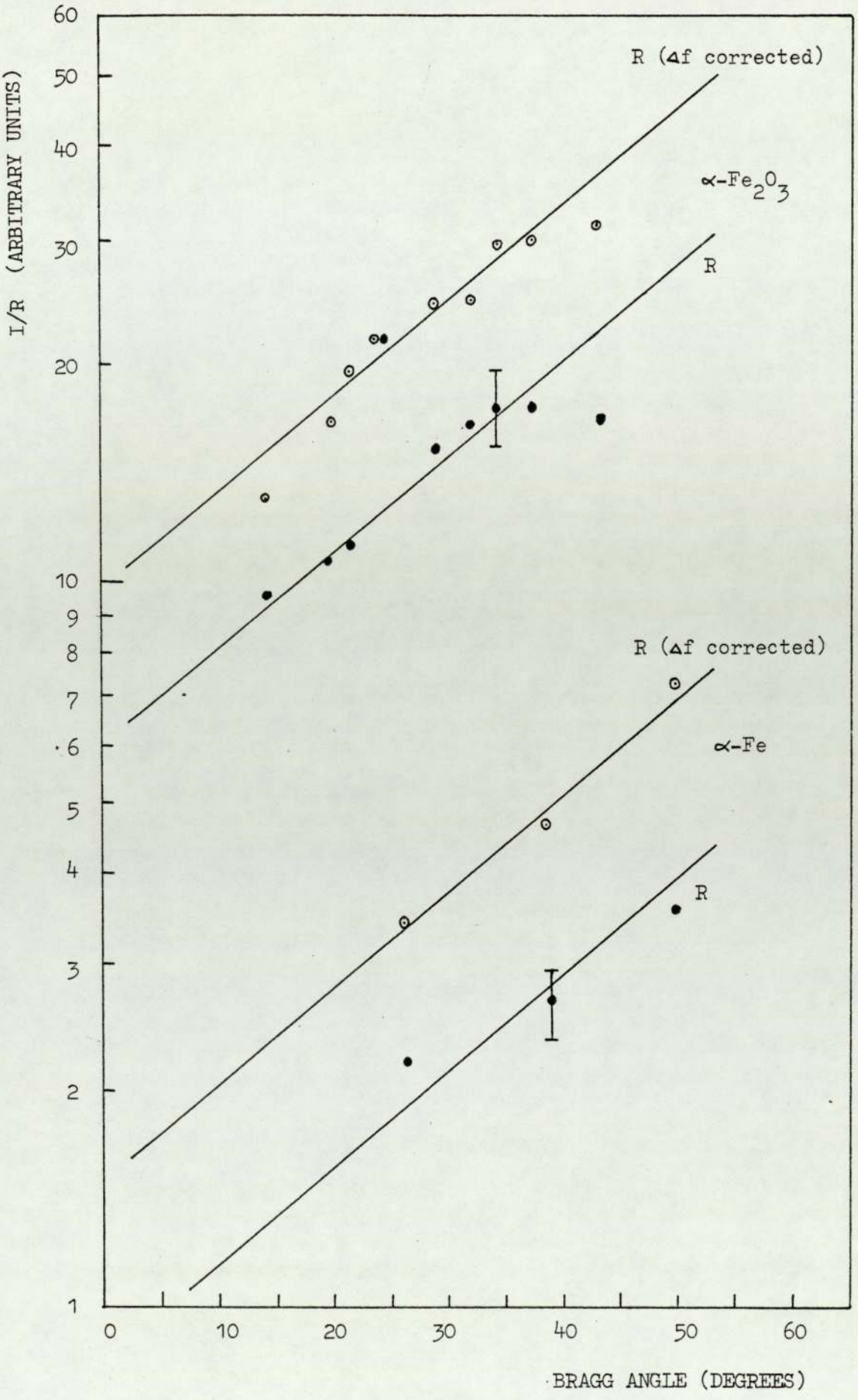

FIGURE 3.35 Proportional Analysis of a 50/50 Mixture of α-Fe and α-Fe_2O_3 using R Values Corrected for Anomolous Scattering (Δf).

pattern were available for proportional analysis. These were the (110), (211), (220) and (400), (220) lines from α-Fe_2O_3 and Fe_3O_4 respectively. All the other lines were either difficult to resolve because of overlapping or were too faint to be measured. This study showed that if the (220) line of Fe_3C_4 is not considered in the proportional analysis then consistently good results can be obtained for the calculated percentage volumes of the α-Fe_2O_3/Fe_3O_4 standards. These results are presented in Table 3.17. Corrected R values were used in the calculations. The omission of (220) diffraction line of Fe_3O_4 can be justified by referring to Figure 3.32. This figure shows log (I/R) versus θ plots for pure 100% standards of α-Fe, α-Fe_2O_3, Fe_3O_4 and FeO. Considering only the Fe_3O_4 standard it is clear from this figure that the point corresponding to (220) diffraction line is low compared with points from other diffraction lines. The (210) and $(2\bar{2}0)$ lines of α-Fe_2O_3 also show similar deviations from the α-Fe_2O_3 plot. However, if correct R values are used then these two lines are in good agreement with all the other diffraction lines on the log (I/R) versus θ plot for α-Fe_2O_3. In contrast, only a small improvement is obtained in the (220) diffraction line of Fe_3O_4 relative to other lines on the log (I/R) versus θ plot for this particular oxide.

We are now in the position to apply this technique to experiments in which the constituents of the wear debris were only α-Fe_2O_3 and Fe_3O_4, i.e. experiments carried out at 300°C, 400°C and 500°C. Figures 3.36 to 3.40 shows the calculated percentage volumes of α-Fe_2O_3 and Fe_3O_4 for these experiments plotted against applied load.

3.10 Scanning Electron Microscopy (SEM)

This section presents a selection of scanning electron micrographs of worn specimens and wear debris. During the course of these investigations several hundred micrographs were obtained, but obviously only a small number can be shown here. These have been selected to illustrate how the surface changed with load and temperature.

$Fe_3O_4/\alpha\text{-}Fe_2O_3$ STANDARD (% Volume)	$(I/R)_{Fe_3O_4}$	$(I/R)_{\alpha\text{-}Fe_2O_3}$	Calculated Volume $(Fe_3O_4/\alpha\text{-}Fe_2O_3)$ % ±8
20/80	3.1	16.0	17/83
25/75	3.9	10.5	27/73
40/60	4.2	9.2	32/68
50/50	6.1	7.8	44/56
75/25	8.0	4.2	66/34
80/20	9.8	2.2	82/18

TABLE 3.17 Proportional Analysis of $Fe_3O_4/\alpha\text{-}Fe_2O_3$ Standards.

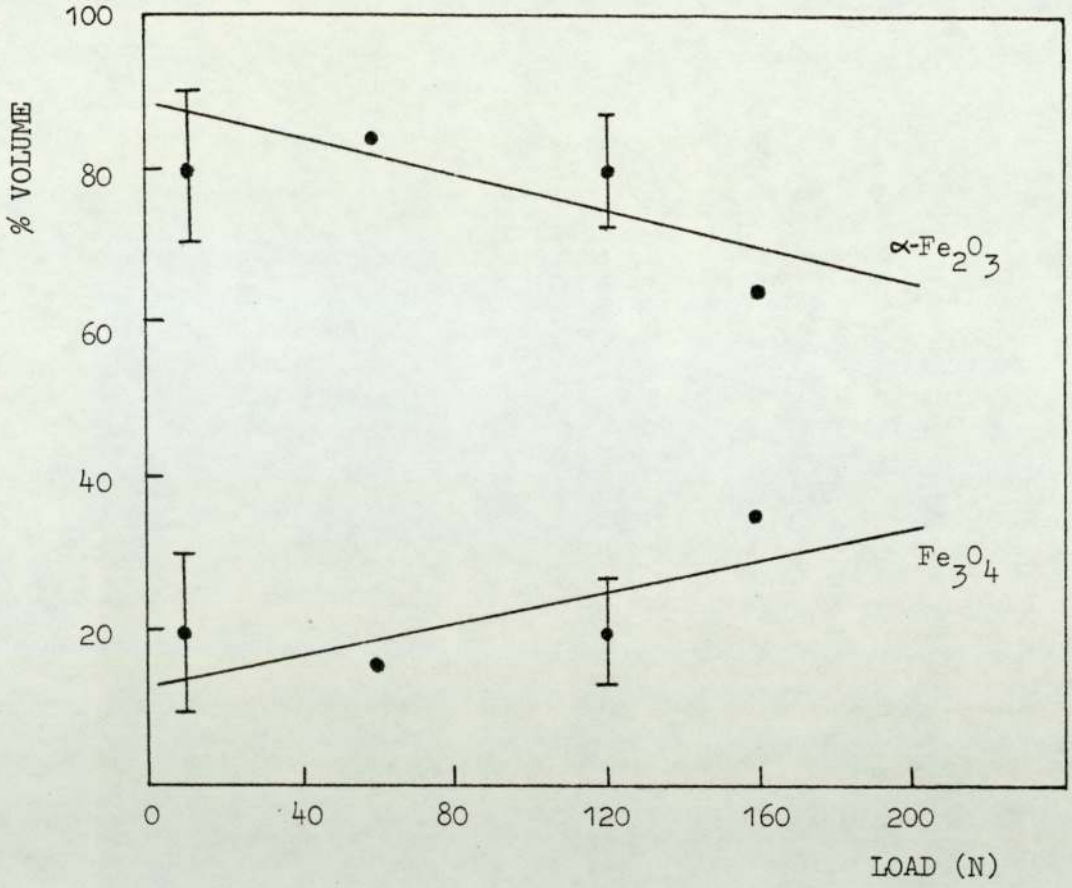

FIGURE 3.36 Percentage Volume of α-Fe_2O_3 and Fe_3O_4 in the Wear Debris from EN31 Experiments at 300°C.

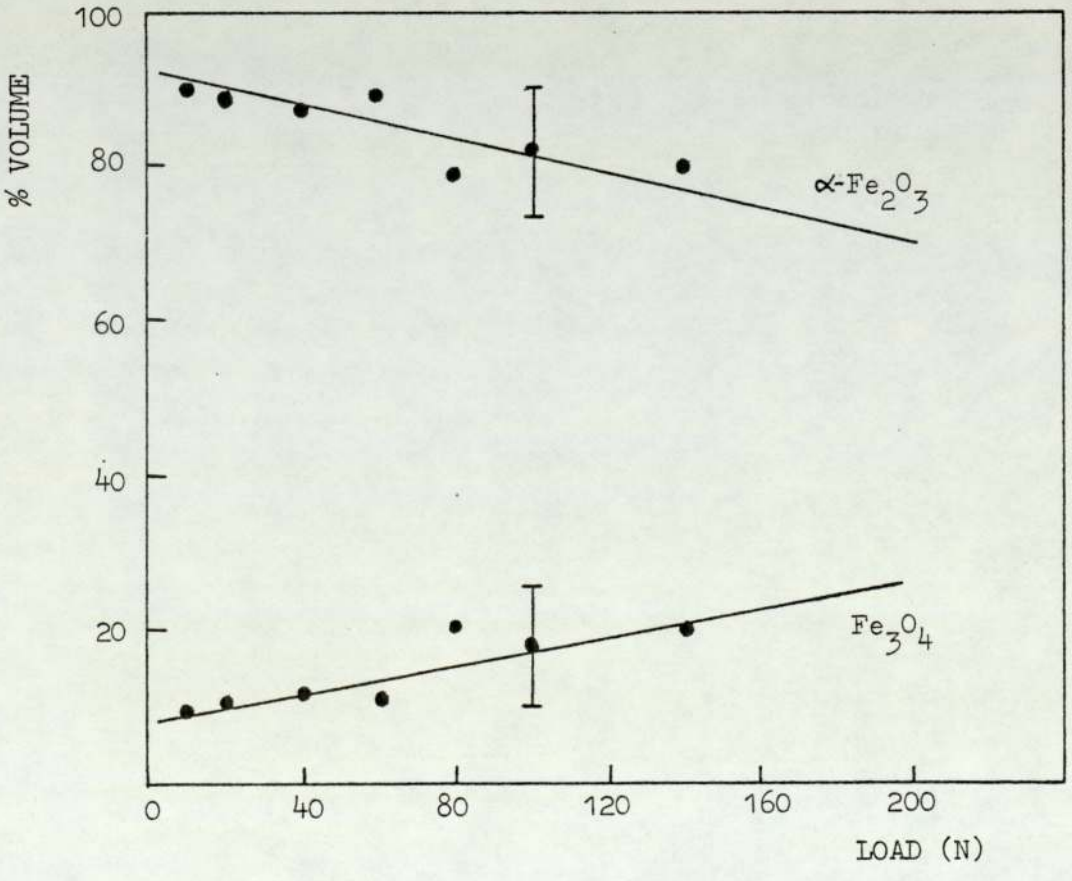

FIGURE 3.37 Percentage Volume of α-Fe_2O_3 and Fe_3O_4 in the Wear Debris from EN31 Experiments at 400°C.

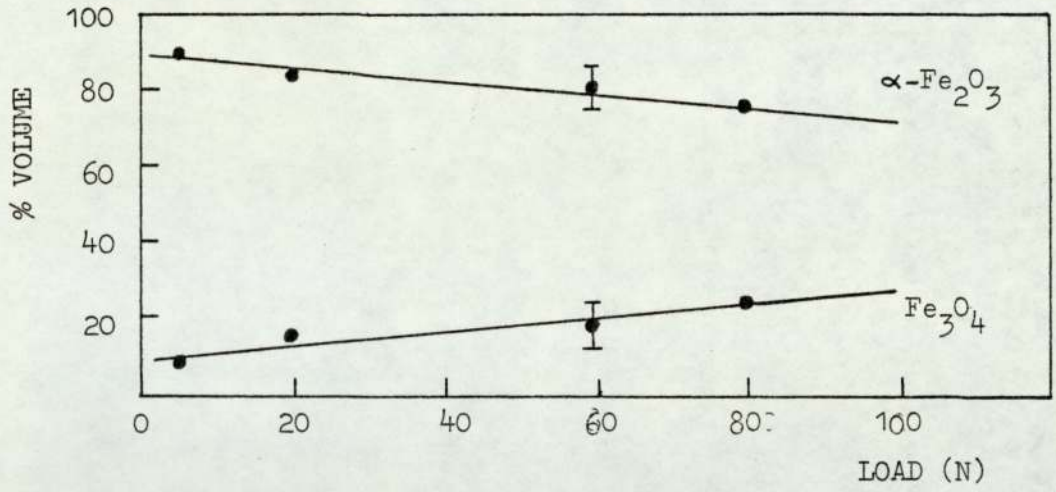

FIGURE 3.38 Percentage Volume of α-Fe_2O_3 and Fe_3O_4 in the Wear Debris from EN8 Experiments at 300°C.

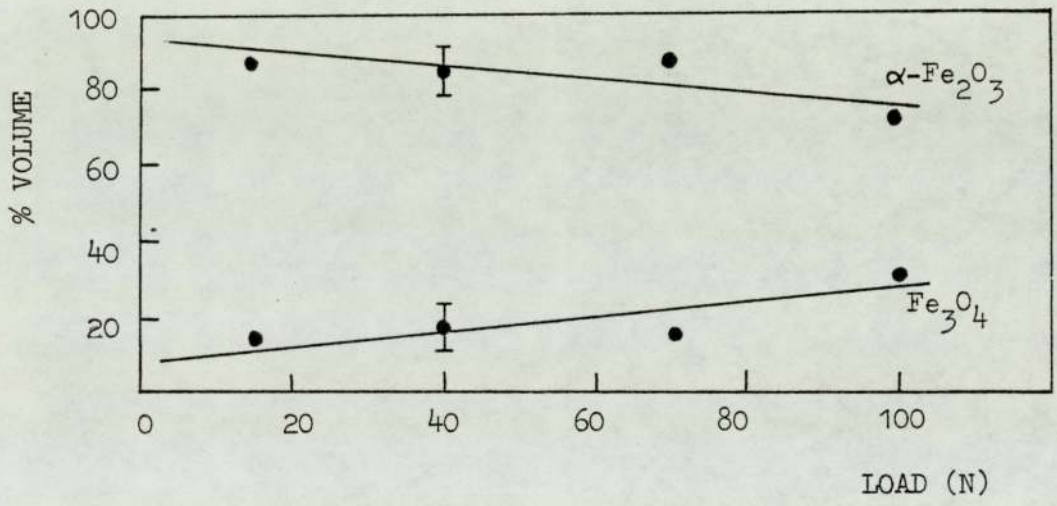

FIGURE 3.39 Percentage Volume of α-Fe_2O_3 and Fe_3O_4 in the Wear Debris from EN8 Experiments at 400°C.

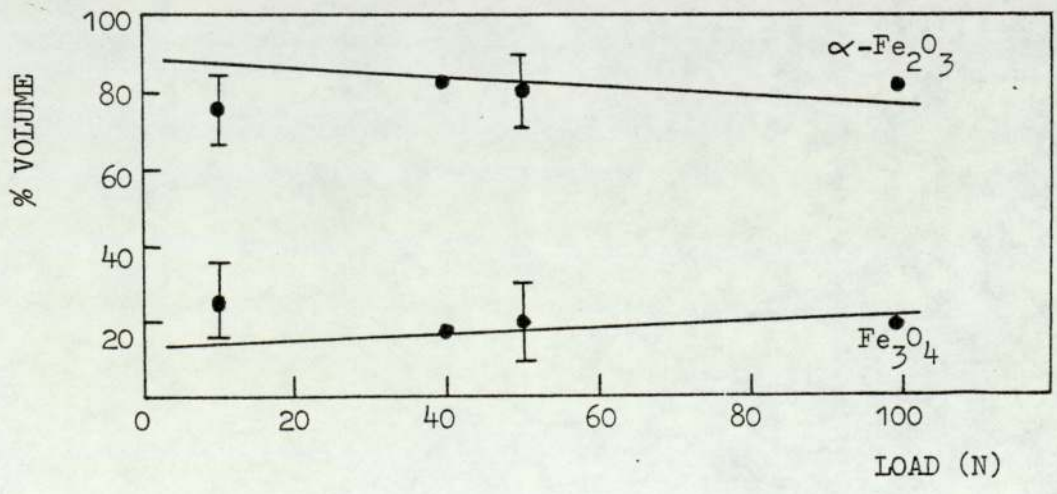

FIGURE 3.40 Percentage Volume of α-Fe_2O_3 and Fe_3O_4 in the Wear Debris from EN8 Experiments at 500°C.

3.10.1 Topographical Study of Worn Surfaces of EN8

The vast majority of the scanning electron micrographs of worn surfaces were obtained with the specimen surface inclined at an angle of 45° to the electron beam since this provided good contrast between surface features and was especially suitable for topographical studies.

The micrographs shown in Figure 3.41 were taken of worn surfaces from room temperature experiments (load 14.7N). It is clear from these micrographs that the pin surface is relatively smooth with damaged regions produced by the removal of the thin oxide film which covers the surface. In contrast, the disc surface is covered with debris and is heavily damaged.

Figure 3.42 shows the general pin topography from 100°C disc temperature experiments for loads below the transition load of 10N. The surface is covered with an oxide layer and is very smooth due to frictional contact, but surface damage due to the removal of oxide flakes has revealed relatively rougher areas. The highly oxidised nature of the pin surface confirms that wear at these loads was mild. As expected, for experiments carried out above this transition the appearance of worn surfaces was similar to the room temperature micrographs shown in Figure 3.41.

Shown in Figures 3.43 and 3.44 are micrographs taken of worn surfaces from the 200°C elevated temperature experiments. Figure 3.43 shows the topography of pin surface at loads of 24.5N and 39.2N respectively. These two loads were selected to illustrate worn pin surfaces on either side of the transition observed in the wear curve at this temperature (see Figure 3.1(a)). The micrographs for 39.2N load experiment shows that pin surface has been deeply gouged in the direction of sliding

(a) PIN

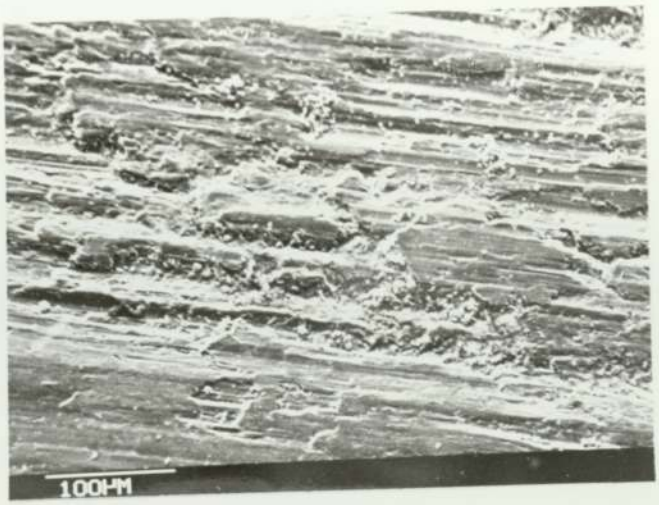

(b) DISC

FIGURE 3.41 Topography of Worn Pin and Disc Surface from EN8 Experiments at Room Temperature (14.7N).

FIGURE 3.42 Topography of Worn Pin from EN8 Experiment at 100°C (4.9N).

(a) 24.5N

(b) 39.2N

FIGURE 3.43 Topography of Worn Pin Surface from EN8 Experiments at 200°C.

(a) 24.5N

(b) 39.2N

FIGURE 3.44 Topography of Worn Disc Surface from EN8 Experiments at 200°C.

and is covered with loose debris produced by disruption of oxide film. In contrast the micrograph for the 24.5N experiment shows a surface mostly covered with an oxide film, apart from regions where oxide has flaked off revealing relatively rough areas and loose oxide particles. The corresponding micrographs obtained from disc surface at this temperature are shown in Figure 3.44.

Micrographs of specimens from 300°C experiments are shown in Figures 3.45 and 3.46. Both worn surfaces were heavily oxidised and smooth, but damage due to the separation of flake-like debris has occurred. See Figure 3.45. The damaged regions are covered with small oxide particles which are probably formed due to crushing of flake-like fragments. An area from which the oxide has flaked off is shown in Figure 3.45(b). The micrograph shows that the remaining oxide film appears to be lifting from the metal substrate and is heavily cracked. It is worth noting that these cracks run in a direction perpendicular to the sliding direction. The cracking of oxide film just before it breaks off is evident from Figure 3.46(a). A closer examination of this region showed that the thickness of the film is approximately 4μm. Separation of the oxide layer as observed from this micrograph suggests that either thermal or mechanical fatigue mechanism or differential volume expansion of the oxide and metal substrate are the possible causes. The absence of oxide film from 98.1N surface at 300°C, see Figure 3.46(b), could explain the high wear rate observed at this load. It was concluded that at this load the rate of removal of oxide was much greater than rate of production.

The micrographs taken of worn surfaces from 400°C and 500°C elevated temperature experiments showed very similar surface features. A typical micrograph from each member of the rubbing surfaces is shown in Figure 3.47. The surfaces are highly oxidised and smooth with

(a) PIN

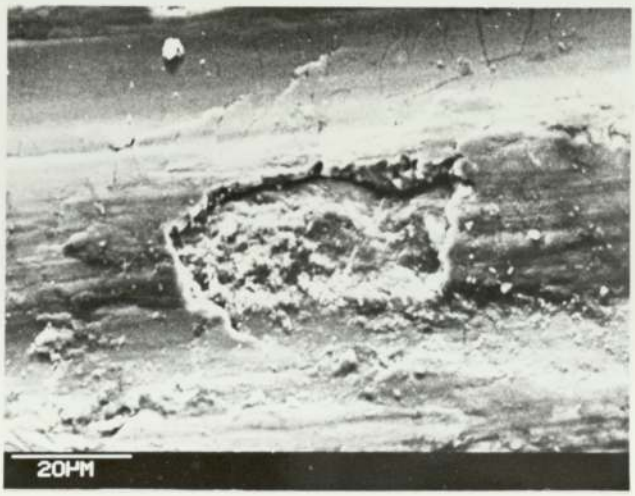

(b) DISC

FIGURE 3.45 Topography of Worn Pin and Disc Surface from 14.7N Load EN8 Experiment at 300°C.

(a) 78.5N

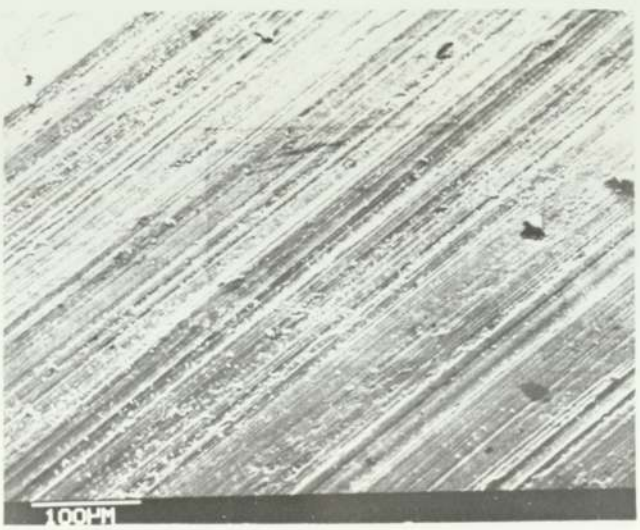

(b) 98.1N

FIGURE 3.46 Micrographs of Pin Surface from EN8 Experiments at 300°C.

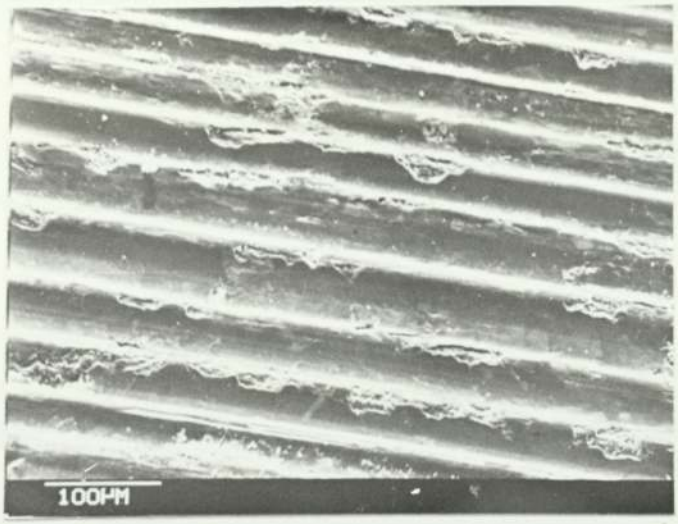

(a) DISC, 54.0N, 400°C.

(b) PIN, 98.1N, 500°C.

FIGURE 3.47 Typical Topographies of Worn Surfaces from EN8 Experiments at 400°C and 500°C.

damage occurring only by removal of flakes from the oxide film.

3.10.2 Topographical Study of Worn Surfaces of EN31

The micrographs shown in Figure 3.48 were taken of worn surfaces from room temperature experiments. Figure 3.48(a) shows the pin surface at 9.8N load, covered with smooth oxide islands standing out or above relatively rough, debris covered areas. Upon increasing the load, these oxide islands grow in size until almost a single oxide layer covers the whole pin surface. Micrographs of a 58.9N load pin surface shows this clearly in Figure 3.48(b). This micrograph also shows that the surface has suffered damage only in relatively few areas. Figure 3.49(a) shows the corresponding disc surface at this load. Disruption of the oxide film producing oxide flakes of various shapes and sizes but all having a well defined thickness of 3μm is illustrated in Figure 3.49(b). A change in topography of worn pins was detected for experiments carried out above 78.5N applied load. At these loads the pin surface had only a sparse covering of oxide film. This is illustrated clearly in Figure 3.48(c) which shows a typical micrograph of pin surface taken from 98.1N experiment. However, it must be noted that the micrograph given in this figure is at a higher magnification than those in Figures 3.48(a) and 3.48(b).

A micrograph of 300°C experiment pin shown in Figure 3.50, shows that heavy cracking and lifting of oxide film from the metal substrate has occurred. Areas from which oxide has recently flaked off are also evident from this figure. These areas are relatively rough and covered with loose debris probably formed by crumbling of large wear particles which have recently cracked and flaked off.

FIGURE 3.48 Micrographs of Pin Surface from EN31 Experiments at Room Temperature.

(a) 9.8N
(b) 58.9N
(c) 98.1N

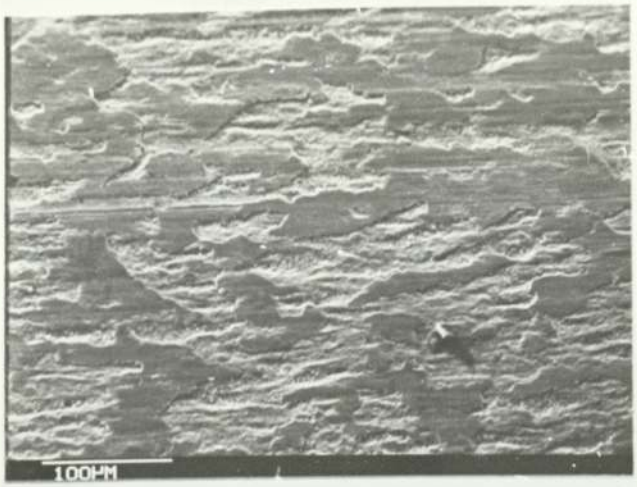

(a)

(b)

(c)

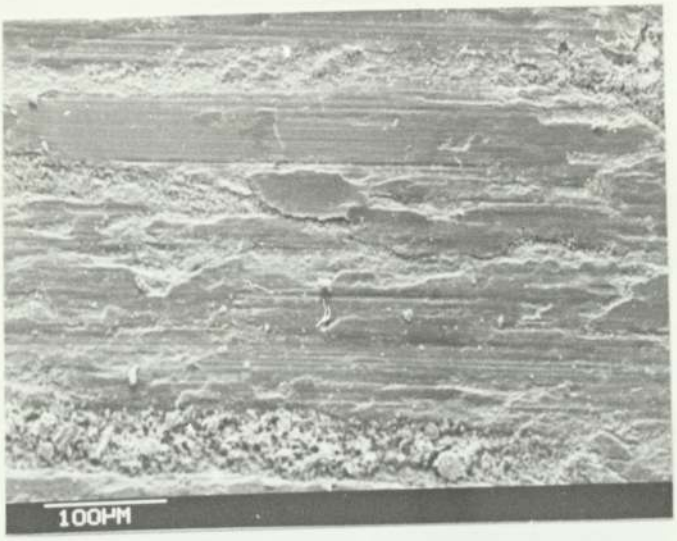

(a)

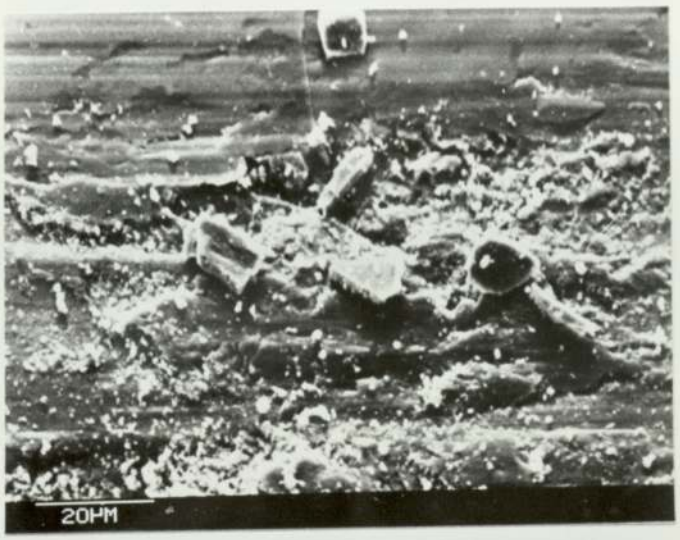

(b)

FIGURE 3.49 Micrographs of Disc Surface from 58.9N Load EN31 Experiment at Room Temperature.

FIGURE 3.50 Topography of Worn Pin Surface from 68.7N Load EN31 Experiment at 300°C.

A selection of micrographs obtained from 400°C and 500°C experiments are given in Figure 3.51. These micrographs shows that the surfaces are highly oxidised and smooth due to the mechanical action of the sliding process, with damage occurring only by the removal of oxide flakes. The damaged regions are rather rough and covered with debris. These features are similar to those shown for EN8 experiments in Figure 3.47.

3.10.3 Oxide Film Thickness Measurements

To study the nature of the surface oxide film in more detail it was necessary to view some areas with the specimen tilted at large angles (between 50° and 60°). At these large angles of tilt it was possible to make reasonably accurate measurements of the oxide layer thicknesses and in some instances see beneath them to view the pin substrate. Results of oxide film thickness for EN8 and EN31 wear experiments are tabulated in Tables 3.18 and 3.19 respectively. An average of at least ten separate measurements of different regions on the same specimen are given in these tables. However, for relatively few specimens an average of less than ten measurements was taken owing to the difficulty encountered in finding suitable oxide edges. The value given within the bracket in Tables 3.18 and 3.19 is the standard deviation of measurement. Out of approximately thirty available EN8 discs used in this work only four discs had studs inserted in them. This limited the number of experiments for which the oxide film thickness on the disc could be determined.

A small selection of some typical oxide edges found on worn pin surfaces are given in Figures 3.52 and 3.53. In general, the results showed that oxide film thickness on the worn specimens increased with applied load.

FIGURE 3.51 Topographies of Worn Surfaces from EN31 Experiments at 400°C and 500°C.

(a) PIN, 58.9N, 400°C
(b) DISC, 58.9N, 400°C
(c) PIN, 157.0N, 500°C

(a)

(b)

(c)

FIGURE 3.52 Typical Oxide Edges from EN8 Experiments.

(a) PIN, 49.1N, 300°C
(b) PIN, 19.6N, 300°C
(c) PIN, 58.9N, 400°C

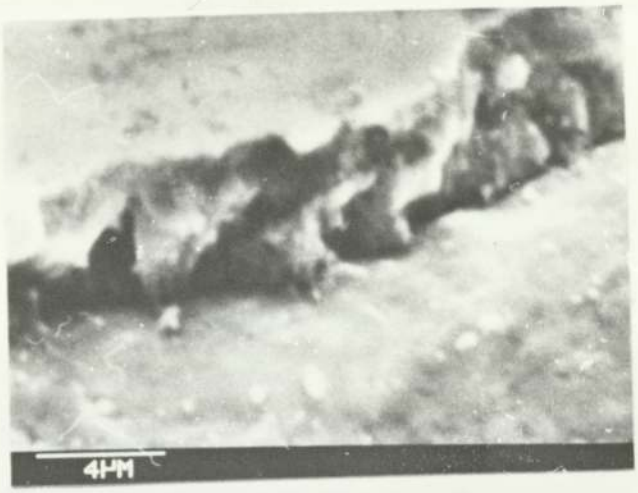

(a)

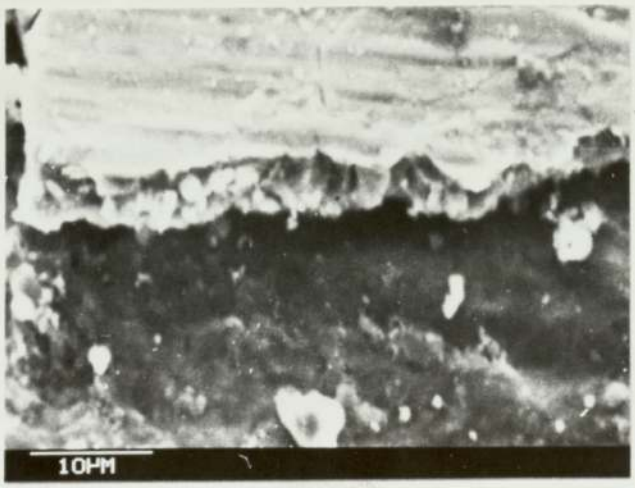

(b)

(c)

Experimental Condition	$\xi(\mu m)$
RT - all loads	<1.0
100°C - at 4.9N	0.5 (0.5)
100°C - at 8.3N	1.1 (0.7)

(a)

Load(N)	Oxide Film Thickness (μm)	
	Pin (ξ)	Disc (ξ^*)
9.8	1.9 (0.7)	1.6 (0.5)
14.7	3.5 (1.3)	-
24.5	2.5 (0.7)	2.4 (0.8)
49.1	2.2 (0.5)	-
58.9	2.5 (0.7)	-
78.5	3.0 (1.0)	-
83.4	2.4 (1.2)	2.6 (0.7)
88.3	3.1 (1.0)	-
117.7	2.1 (1.4)	-

(b)

Table 3.18. Oxide Film Thickness for EN8 Experiments

(a) Room Temperature and 100°C

(b) 200°C

Load(N)	Oxide Film Thickness (μm)	
	Pin (ξ)	Disc (ξ^*)
19.6	2.0 (0.5)	-
39.2	3.0 (0.5)	-
49.1	2.5 (0.5)	-
58.9	2.7 (0.7)	-
64.8	2.6 (0.6)	2.5 (0.9)
78.5	3.5 (0.5)	-

(c)

Load(N)	Oxide Film Thickness (μm)	
	Pin (ξ)	Disc (ξ^*)
7.4	2.4 (0.9)	-
14.7	2.0 (1.1)	3.0 (0.7)
24.5	2.2 (0.5)	-
29.4	3.4 (1.0)	2.8 (0.8)
39.2	3.2 (0.7)	-
54.0	4.0 (1.0)	3.6 (1.4)
68.7	4.0 (1.3)	-
98.1	4.8 (1.0)	-

(d)

Table 3.18. Oxide Film Thickness for EN8 Experiments

(c) 300°C
(d) 400°C

Load(N)	Oxide Film Thickness (μm)	
	Pin (ξ)	Disc (ξ^*)
9.8	2.2 (0.5)	-
14.7	2.4 (0.8)	3.6 (0.6)
19.6	2.4 (0.8)	
39.2	2.6 (0.7)	3.8 (0.8)
58.9	3.2 (1.1)	-
78.5	3.5 (1.4)	-
98.1	3.5 (0.5)	-

(e)

Table 3.18. Oxide Film Thickness for EN8 Experiments

(e) 500^{o}C

FIGURE 3.53 Typical Oxide Edges from EN31 Experiments.

(a) PIN, 39.2N, ROOM TEMPERATURE
(b) PIN, 19.6N, 400°C
(c) PIN, 19.6N, 400°C

(a)

(b)

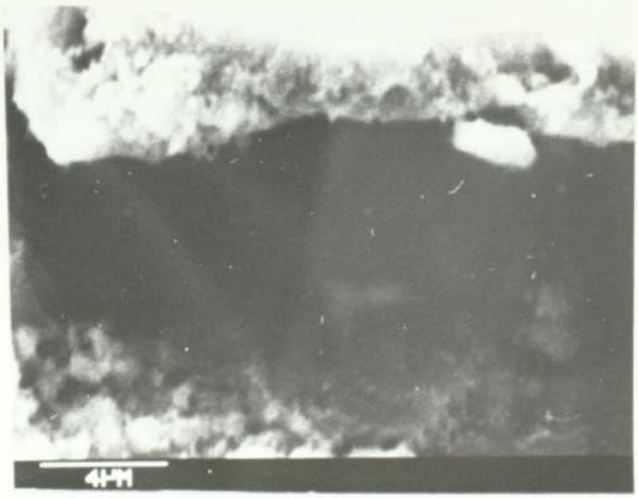

(c)

Load(N)	Oxide Film Thickness (μm)	
	Pin (ξ)	Disc (ξ^*)
9.8	1.1 (0.6)	-
19.6	1.8 (1.0)	3.0 (1.0)
24.5	1.3 (0.5)	-
29.4	3.0 (1.0)	-
34.3	2.5 (0.7)	-
39.2	3.0 (0.9)	3.8 (0.5)
58.9	3.2 (0.5)	2.9 (0.9)
78.5	2.9 (0.8)	2.8 (0.9)
98.1	1.3 (0.5)	-

(a)

Load(N)	Oxide Film Thickness (μm)	
	Pin (ξ)	Disc (ξ^*)
6.9	1.7 (0.5)	-
14.7	2.4 (0.7)	3.8 (0.8)
34.3	2.9 (0.7)	1.5 (0.4)
49.1	3.1 (0.4)	-
88.3	1.4 (1.0)	3.5 (0.7)

(b)

Table 3.19. Oxide Film Thickness for EN31 Experiments

(a) Room Temperature

(b) 100°C

Load(N)	Oxide Film Thickness (μm)	
	Pin (ξ)	Disc (ξ^*)
24.5	2.5 (0.5)	1.8 (0.5)
44.1	2.7 (0.4)	2.5 (0.5)
54.0	2.9 (0.8)	-
63.8	2.8 (0.9)	2.8 (0.8)
83.4	2.6 (1.0)	3.2 (0.7)
103.0	2.4 (1.1)	3.8 (0.7)

(c)

Load(N)	Oxide Film Thickness (μm)	
	Pin (ξ)	Disc (ξ^*)
9.8	2.1 (0.5)	-
14.7	2.8 (0.8)	2.4 (0.6)
39.2	2.9 (1.1)	-
58.9	3.4 (0.6)	-
68.7	3.4 (0.7)	3.0 (0.8)
117.7	3.9 (0.9)	-

(d)

Table 3.19. Oxide Film Thickness for EN31 Experiments

(c) 200°C

(d) 300°C

Load(N)	Oxide Film Thickness (μm)	
	Pin (ξ)	Disc (ξ^*)
9.8	2.3 (0.7)	-
14.7	2.5 (0.8)	2.9 (0.9)
19.6	2.8 (1.1)	-
39.2	2.8 (0.7)	-
58.9	3.9 (0.7)	3.8 (0.8)
78.5	3.8 (1.4)	-
98.1	5.1 (1.8)	-

(e)

Load(N)	Oxide Film Thickness (μm)	
	Pin (ξ)	Disc (ξ^*)
9.8	2.2 (0.6)	-
39.2	3.0 (0.8)	-
49.1	3.3 (0.5)	3.8 (1.1)
78.5	3.3 (0.9)	-
88.3	4.5 (1.0)	5.0 (2.0)
98.1	4.1 (1.0)	-
157.0	4.7 (0.8)	-

(f)

Table 3.19. Oxide Film Thickness for EN31 Experiments

(e) 400°C

(f) 500°C

3.10.4 Examination of Wear Debris

A selection of micrographs taken of wear debris are given in Figure 3.54. Micrographs such as these can provide useful information about both the shape and size of the wear debris. In scanning electron microscope non-conducting materials tend to charge up and show up somewhat brighter. Thus, the brightly revealed debris in these micrographs suggests that majority of wear particles are oxides.

Results of wear debris examination from all the experiments selected for analysis showed that the debris consists of flake-like fragments varying from approximately 10μm to 200μm in size. The much smaller debris seen in the micrographs covering these fragments was probably formed due to crushing of larger wear flakes. The dimensions of these wear fragments corresponds reasonably well to the damaged regions found on the specimen surfaces shown for example in Figures 3.41 to 3.51.

Figure 3.55 shows a typical wear flake from 300° C EN8 experiment whose size is approximately 100μm. On closer examination, the thickness was measured to be around 2μm. The surface of this fragment is smooth as a result of sliding contact between the rubbing members before it became detached to form a wear particle. In the bottom right hand corner of this micrograph the bottom surface of another wear fragment (the underlying oxide/metal interface) is clearly visible. As a result of separation from the wearing surface, the bottom surface of the wear fragment is rather rough and covered with small oxide particles.

One important conclusion emerging from this work was the thickness of wear fragments was found to lie within the range of oxide film thickness measured on

(a) EN8, 78.5N, 300°C

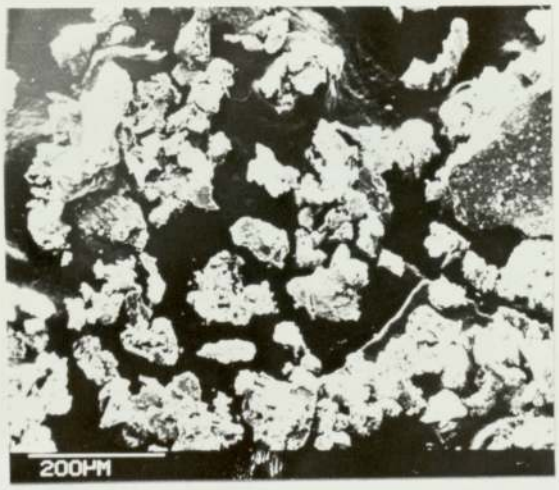

(b) EN31, 14.7N, 100°C

FIGURE 3.54 Scanning Electron Mircographs of Wear Debris.

FIGURE 3.55 Scanning Micrograph of Wear Flake (EN8, 49.1N, 300°C).

worn specimens, that is, between 1 to 5μm. This suggests, and agrees with the original assumption proposed by Quinn (44), that the oxide layer formed during wearing process fractures at a critical thickness to produce a wear particle.

3.10.5 Subsurface Observations

The microstructure was investigated by scanning electron microscopy of taper sections through worn pins. Micrographs shown in Figure 3.56(a) and (b) were taken of 9.8N and 39.2N pins from EN31 room temperature experiments respectively. The dark unetched regions seen in these micrographs are thought to be oxide films formed during wear. Microhardness measurement carried out on this region gave hardness in the range 490-567 VPN. The oxide film thickness can be estimated from Figures 3.56(a) and (b), and is 2.5±1.0μm and 7.0±1.0μm respectively. Although these values are higher than those given in Section 3.10.3, the general trend is still the same, i.e.an increase in oxide thickness with load in the range 20-80N.

A micrograph of a metallographic section through a 34.3N load pin from EN8 room temperature experiments is shown in Figure 3.57. Plastic flow of the subsurface material in the rubbing direction is clearly evident from this micrograph. Microhardness measurements of the subsurface showed it to be extremely work-hardened. Values of up to 927 VPN were recorded, the majority of the readings falling within the range 700-800 VPN. Such intense hardness is normally produced only by quenching from the austenite range, i.e. to give the martensite phase (38). X-ray diffraction analysis of 39.2N load pin taken from the same set of experiments confirmed the presence of austenite.

(a) 9.8N

(b) 39.2N

FIGURE 3.56 Scanning Electron Micrograph of Tapered Section through Worn Pin Surface from EN31 Experiments at Room Temperature.

FIGURE 3.57 Tapered Microsection through EN8 Room Temperature Pin (34.3N).

A typical micrograph showing the microstructure of an EN8 pin from 400° C temperature experiments is shown in Figure 3.58. A heavily deformed subsurface covered with an oxide layer is clearly evident from this micrograph. Similarly, the subsurface of an EN31 pin taken from 400 °C experiments is shown in Figure 3.59(a), and at higher magnification in Figure 3.59(b). The dark unetched regions seen in these micrographs (below the black bakelite) are thought to be surface grooves, produced during the initial running-in wear, covered with oxide. The separation of these grooves compares reasonably well with the talysurf profiles given in Section 3.6.

3.11 Auger Electron Spectroscopy (AES)

The technique of AES was employed to study concentration-depth profiles of worn pins. Composition profiles were obtained by sputtering with 2kV argon ions at a gas pressure of 5×10^{-5} torr. Approximate values for the relative concentrations of the elementss were obtained by measuring the peak to peak heights of selected Auger peaks and incorporating the appropriate sensitivity factors (98). A typical Auger spectrum is shown in Figure 3.60. The peaks considered in this analysis were 503eV and 703eV from oxygen and iron respectively. The topmost surface of worn specimens was found to contain carbon as a result of atmospheric contamination but this was quickly removed during the ion etching process (< 2 minutes). Figure 3.61 shows a typical secondary electron micrograph of pin surface (39.2N load EN8 pin at 400 °C) after it has undergone sputtering for some period of time. The corresponding oxygen map of this area (obtained by using the AES in its scanning mode and detecting the 503eV Auger electrons from oxygen) is given in Figure 3.62. It is clear from these two micrographs that the raised regions seen in Figure 3.61 are in fact oxide plateaux.

FIGURE 3.58 Tapered Microsection through Pin from EN8 Experiment at 400°C (54.0N).

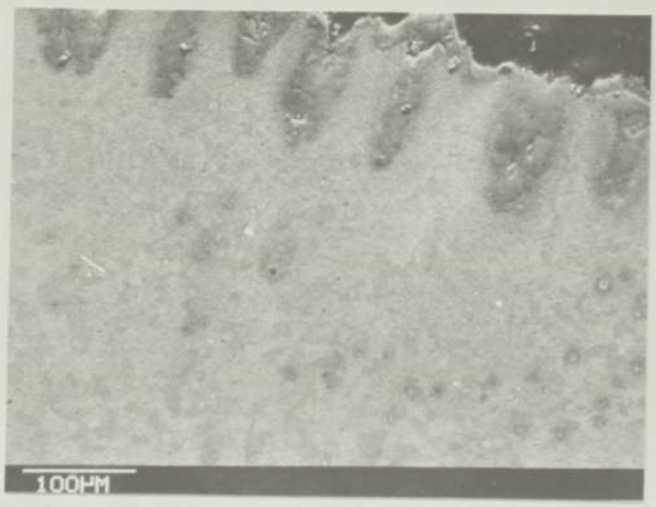

(a)

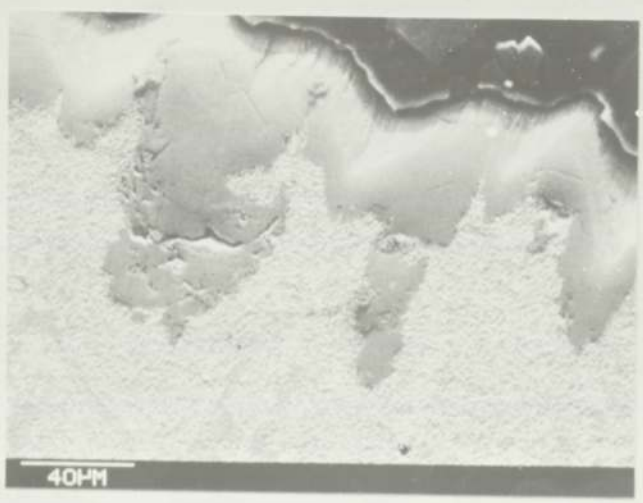

(b)

FIGURE 3.59 Tapered Microsection through Pin from EN31 at 400°C (58.9N).

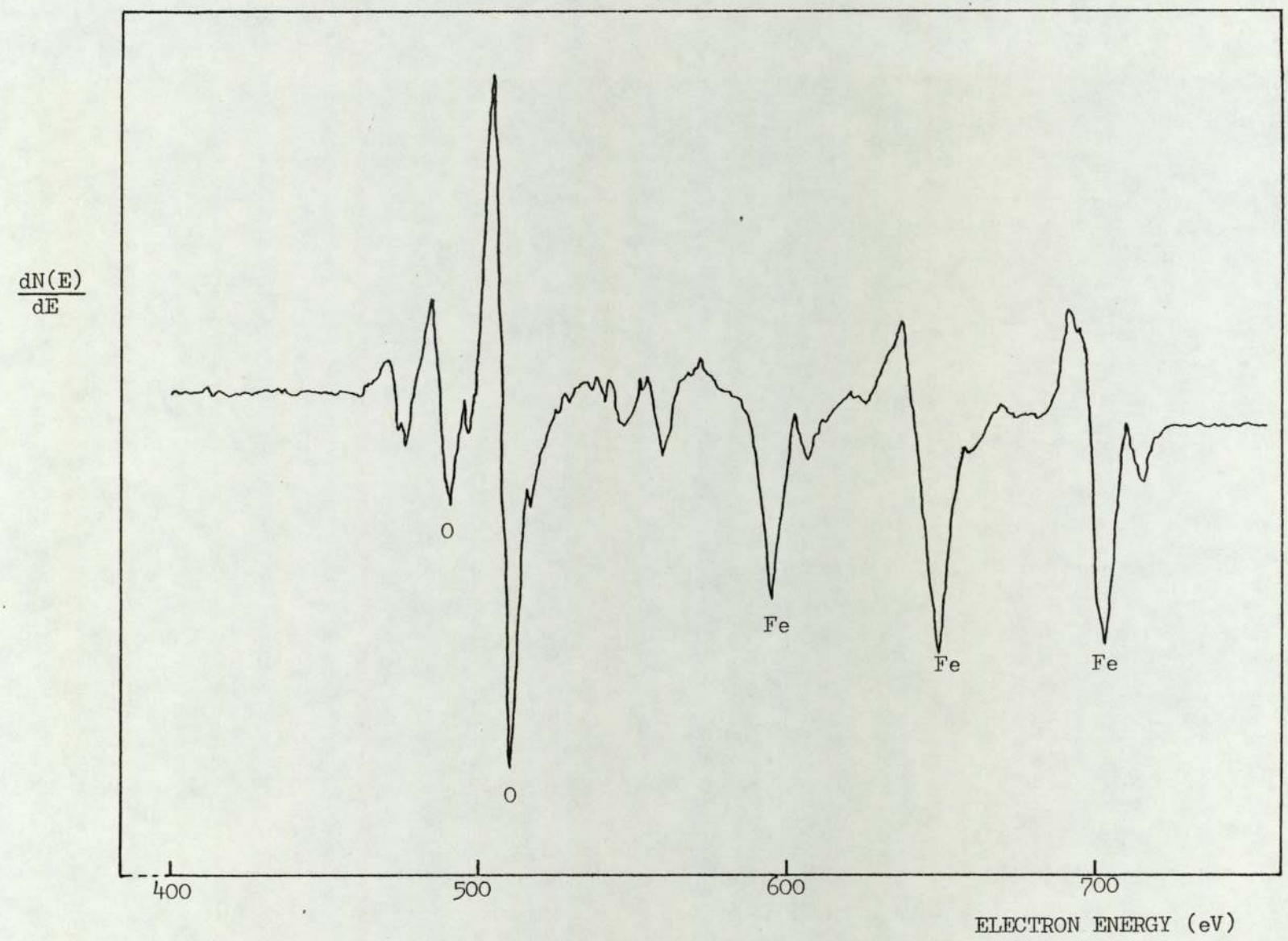

FIGURE 3.60 Typical Auger Spectrum (EN8, 39.2N, 400°C)

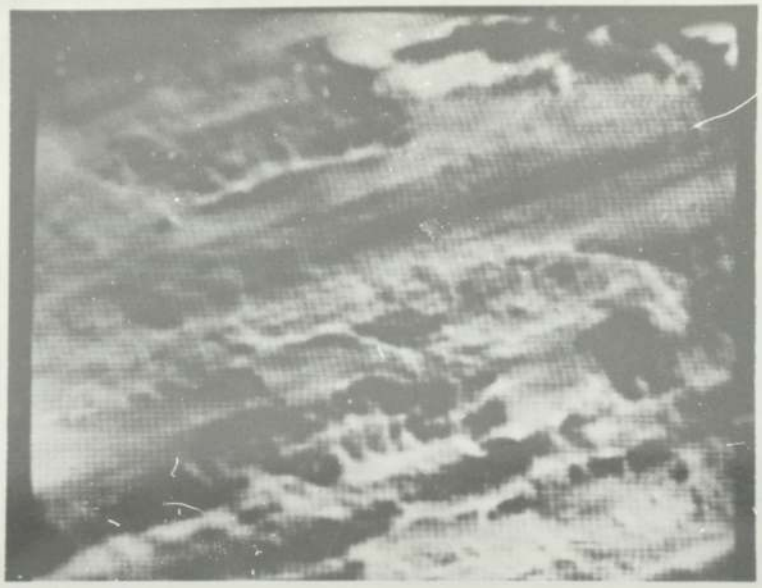

FIGURE 3.61 A Typical Secondary Electron Image of a Worn Surface after Argon Ion etching for 136 minutes (EN8, 39.2N, 400°C, 1000X).

FIGURE 3.62 Corresponding Auger Oxygen Map of the same Surface.

It is important to note that the concentration depth profiles were carried out on these oxide plateaux.

The results obtained from various worn pins using this technique are given in graphical form in Figures 3.63 and 3.64. These figures show the concentration of oxygen as a function of sputtering time (measured here in μAmin). The total sputtering time required to remove the oxide film present on a pin surface can be readily estimated from these figures. For example, from Figure 3.64, the total sputtering time for 24.5N and 58.9N load EN31 pins from room temperature experiments is 4×10^3 μAmin and 1.6×10^4 μAmin respectively. This suggests that for 58.9N pin a thicker oxide film is present on the pin surface. Confirmation of this can be found in Section 3.10.3. The SEM results given in this section showed that the oxide film thickness on 58.9N load pin, when compared with 24.5N, was three times as large. On the other hand, x-ray diffraction analysis of wear debris produced from the 58.9N load experiment (Section 3.7.2) showed that oxide had changed predominantly into Fe_3O_4. The oxide detected in 24.5N load experiment was a mixture of α-Fe_2O_3 and Fe_3O_4. Numerous workers (61-63) have shown that Fe_3O_4 adheres more strongly to the metal substrate than does α-Fe_2O_3. This leads us to conclude that the change in wear rate observed in EN31 room temperature and 100°C experiments (between applied loads 30-80N) was probably due to both an increase in oxide film thickness and change in oxide composition.

Although the composition profiles in this study are plotted against sputtering time (μAmin), it is hoped that in future work approximate values for the depth could be obtained by using experimentally derived sputtering yields for α-Fe_2O_3, Fe_3O_4 and FeO oxides.

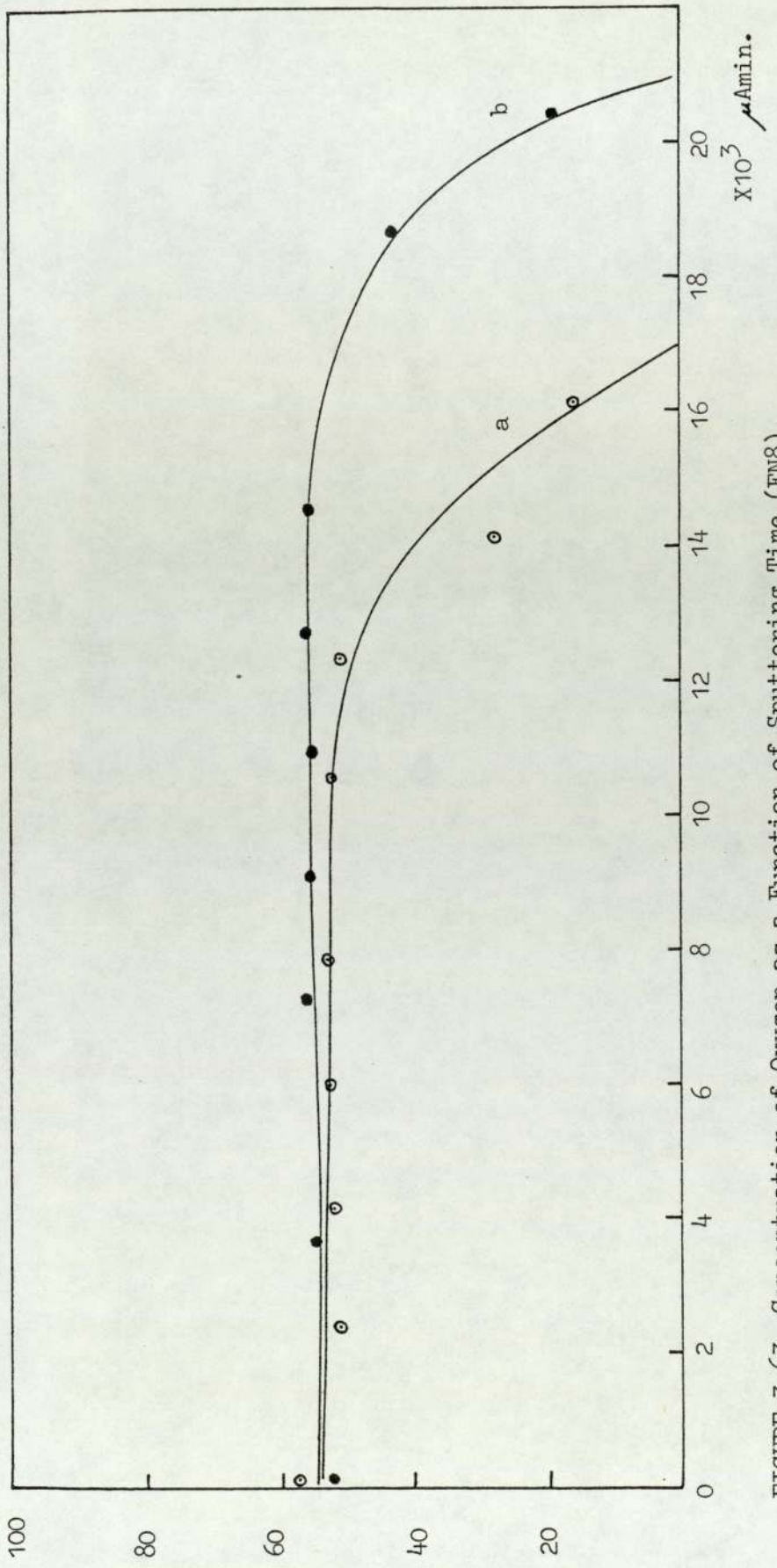

FIGURE 3.63 Concentration of Oxygen as a Function of Sputtering Time (EN8).

a) 39.2N, 400°C
b) 39.2N, 500°C

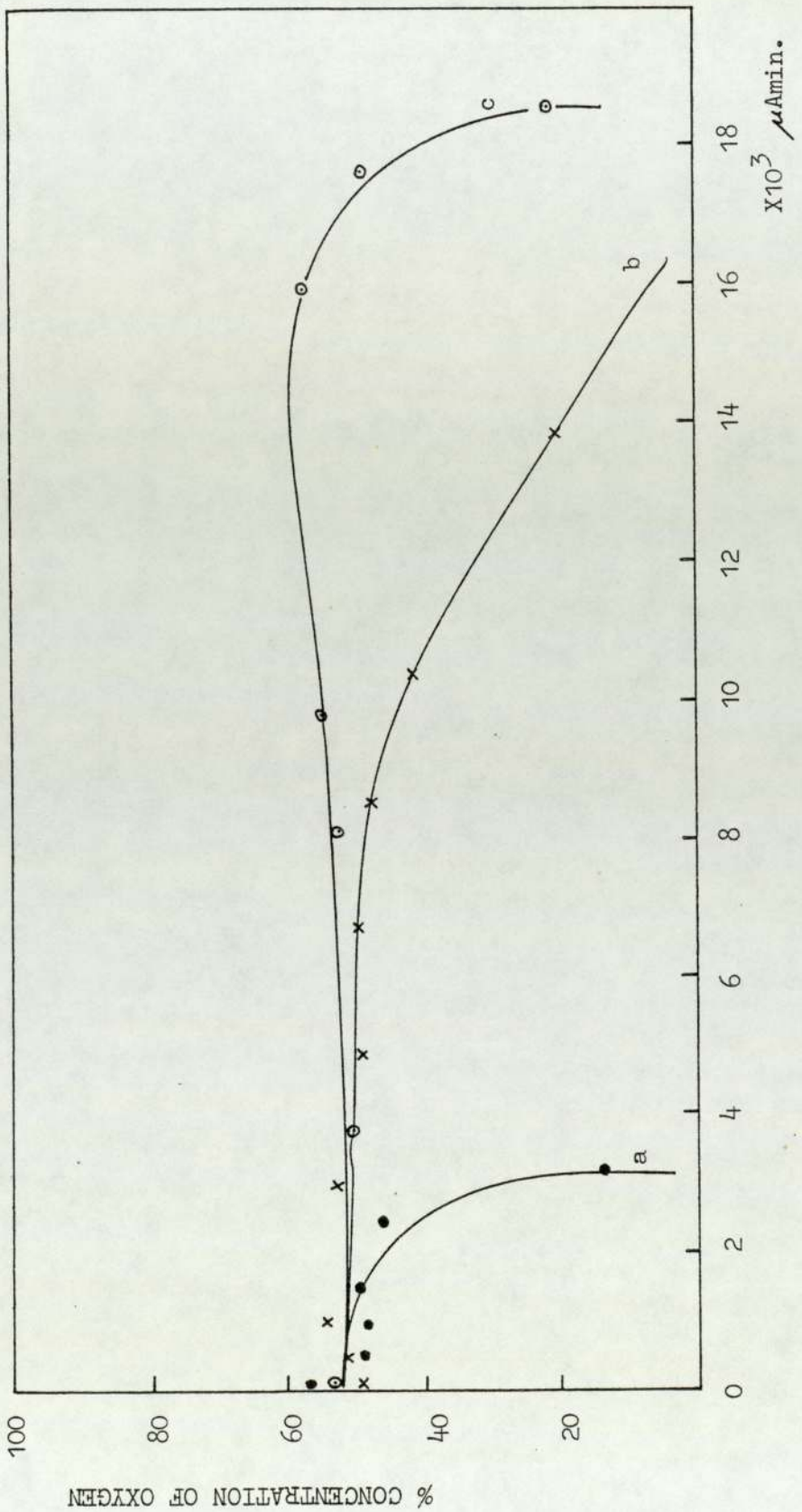

FIGURE 3.64 Concentration of Oxygen as a Function of Sputtering Time (EN31)

a) 24.5N, Room Temperature
b) 58.9N, Room Temperature
c) 39.2N, 400°C

CHAPTER 4

Theoretical Considerations

4.1 INTRODUCTION

A theoretical analysis is presented in Section 4.2, involving equations for the contact temperature and the division of heat at the sliding interface, to deduce the contact radius a, the number N of contacting asperities, the critical oxide film thickness ξ and the contact temperature T_c. The results from this analysis are presented in Section 4.4 in terms of the variation of these parameters with applied load. In Section 4.6 a modification to the oxidational wear theory (discussed in Section 4.5) is proposed to take into account the out-of-contact oxidation.

4.2 Theoretical Determination of Surface Parameters

The temperature at the real areas of contact between sliding interfaces is arguably the most important parameter to be determined since it controls the type of surface compositions being formed at these interfaces, as well as the rate at which they are being formed. In this section a method is proposed whereby the contact temperature (T_c), the number of contacts (N), the contact radius (a) and the critical oxide film thickness (ξ) can be deduced. The method involves equating average contact temperatures of rubbing surfaces and searching for values of a and ξ which give best comparison between the theoretical and experimental divisions of heat.

According to Archard (82) the theoretical division of heat along the pin is given by

$$\delta_{th} = \frac{T_m}{T_m + T_p} \qquad 4.1$$

where T_m is the "fictitious" flash temperature obtained assuming all the heat flow rate H_T (evolved at the sliding interface) is supplied to the disc only and T_p is a similar temperature deduced on the assumption that the heat is supplied at that rate to the pin only.

Quinn (88), following an approach very similar to that proposed by Grosberg and Mølgaard (87), has modified flash temperature equations developed by Archard (82) to take into account N circular areas of contact (of radius a) each with an oxide film thickness ξ. For the model suggested by Quinn, N is related to the contact radius through the relation:-

$$N = \frac{W}{\pi a^2 P_m} \qquad 4.2$$

where W is the applied load and P_m is the hardness of substrate metal. According to Quinn, one of these "fictitious" temperatures T_p can be expressed as

$$T_p = \frac{H_T}{4aK_sN} + \frac{H_T\xi}{N\pi a^2 K_o} \qquad 4.3$$

where K_s and K_o are the thermal conductivities of the substrate metal and oxide respectively. From the definition of flash temperature an expression can be obtained for the average contact temperature of the pin, namely

$$T_c\ (PIN) = T_s + \frac{H_1}{4aK_sN} + \frac{H_1\xi}{N\pi a^2 K_o} \qquad 4.4$$

where T_s is the general pin surface temperature and H_1 is the heat flow rate along the pin at the sliding interface. It is worth noting that the actual flash temperature of the pin is given by equation (4.3) with H_1 in place of H_T.

To deduce T_m, three equations could be relevant according to the speed of sliding (82). Quinn et al. (105) claim that the expression for medium speeds is probably suitable for most practical conditions, that is

$$T_m = (0.8605 - 0.1021 \frac{Va}{2\chi_s}) \frac{H_T}{4aNK_s} \qquad 4.5a$$

where χ_s is the thermal diffusitivity of the disc material and V is the linear speed. However, in the derivation of equation (4.5a) no oxide film was postulated for the disc asperities. The SEM evidence, however, given in Section 3.10.3, shows that even for the room temperature experiments an appreciable oxide film is present on the disc wear track. Thus, if an oxide film thickness ξ^* is assumed for the disc asperities, equation (4.5a) can be modified as follows

$$T_m = \frac{\alpha H_T}{4aNK_s} + \frac{\alpha H_T \xi^*}{N\pi a^2 K_o} \qquad 4.5b$$

where α is given by the expression

$$\alpha = (0.8605 - 0.1021 \frac{Va}{2\chi_o}) \qquad 4.6$$

and χ_o is the thermal diffusitivity of oxide. Therefore, from the definition of flash temperature, the average contact temperature for the disc is

$$T_c\,(DISC) = T_D + \frac{\alpha(H_T - H_1)}{4aNK_s} + \frac{\alpha(H_T - H_1)\xi^*}{N\pi a^2 K_o} \qquad 4.7$$

Equating the average contact temperatures given by equations (4.4) and (4.7), and eliminating N by using equation (4.2), an expression can be obtained for the contact radius, namely

$$a = \frac{-(B-G) \pm ((B-G)^2 - 4EJ)^{\frac{1}{2}}}{2E} \qquad 4.8a$$

where

$$G = \frac{0.8605P_m (H_T-H_1)}{WK_s} - \frac{0.1021P_m V(H_T-H_1)\xi}{2\chi_o K_o W} \qquad 4.8b$$

$$E = \frac{0.1021P_m V(H_T-H_1)}{2\chi_o K_s W} \qquad 4.8c$$

$$F = \frac{0.8605P_m \xi^* (H_T-H_1)}{K_o W} \qquad 4.8d$$

$$J = T_s + C - T_D - F \qquad 4.8e$$

$$B = \frac{H_1 P_m}{K_s W} \qquad 4.8f$$

and

$$C = \frac{H_1 P_m \xi}{K_o W} \qquad 4.9g$$

From equation (4.8a) two numerical values of the contact radius a are possible. However, simple calculations show that only the positive root of equation (4.8a) needs to be considered because the term (B-G) is always positive and the term J is always negative.

With the knowledge of critical oxide film thicknesses (ξ and ξ^*) and the physical properties, equation (4.8a) can be solved for the contact radius (a) using the heat flow data given in Tables 3.1 to 3.12. (This in turn can be substituted in equations 4.2 and 4.4 to give values of N and T_c respectively.) However, before such calculations can be carried out, the important question to ask is at what temperature should the temperature dependent physical properties P_m, K_s, K_o and χ_o be chosen. It was decided that the physical properties of the metal, K_s and P_m, should be chosen corresponding to the general

surface temperature. The variation of P_m (for both EN8 and EN31 materials) and K_s (for EN8) with temperature are illustrated in Figures 2.5 and 2.4 respectively. Without introducing a significant error in the calculations, the thermal conductivities of EN8 and EN31 can be considered to be the same. The temperature at which the physical properties of oxide (K_o and χ_o) should be taken is open to conjecture. However, it was thought that it would be more appropriate to take those corresponding at or near to the contact temperature. The effect of evaluating the physical properties at any other temperature between T_s and T_c has been investigated and will be discussed later.

Published work on thermal conductivity of iron oxides is limited mainly to a few determinations close to room temperature. Of the three possible oxides, no value is available for FeO, values for Fe_3O_4 between 0.0168 and 0.714 $Wcm^{-1}{}^{o}c^{-1}$ (106) have been reported, while for the oxide α-Fe_2O_3 values between 0.0252 and 0.147 $Wcm^{-1}{}^{o}c^{-1}$ (106) have been given. Mølgaard and Sweltzer (106) have shown that the thermal conductivity of α-Fe_2O_3 and Fe_3O_4 varies with temperature according to the relationship given by the following equations:-

$$K_o(\alpha\text{-}Fe_2O_3) = 0.0839 - 6.63 \times 10^{-5} T \qquad 4.9a$$

and

$$K_o(Fe_3O_4) = 0.0423 - 1.37 \times 10^{-5} T \qquad 4.9b$$

where K_o is $Wdeg^{-1}\,cm^{-1}$ and T is the absolute temperature in elvins. Unless otherwise stated the average of equations (4.9a) and (4.9b) was considered throughout this work, even when the oxide analysed was predominantly FeO.

The thermal diffusivity χ_o of the oxide is given by the expression

$$\chi_o = \frac{K_o}{\rho_o C_o} \qquad 4.10$$

where

K_o = thermal conductivity of oxide
ρ_o = density of the oxide
C_o = specific heat capacity of the oxide

Since no relevant data relating to the variation of C_o (and χ_o) with temperature was found in the literature, a value of $756 JK^{-1}K^{-1}$ (107) for the specific heat capacity was used throughout. It was also assumed that for any given oxide of iron, ρ_o is independent of temperature.

To assume that the physical properties of the oxide should be taken at the contact temperature necessitates the introduction of an iteration process in the calculations. The following iteration procedure was adopted in this work.

Due to the differences in the thermal and mechanical stresses experienced by the oxide film on the pin and disc asperities, the critical oxide thicknesses ξ and ξ^* will be different. However, for simplicity, and to make calculations manageable it was assumed that ξ is equal to ξ^*. Referring to the measured values of the oxide film thicknesses given in Tables 3.18 and 3.19 it becomes apparent that, within the error of the measurement, the values for ξ and ξ^* are approximately equal.

A value is assumed for the oxide film thickness $\xi(=\xi^*)$. In the first step of iteration the physical properties of oxide K_o and χ_o are calculated from equations (4.9) and (4.10) respectively at the general surface temperature T_s. On substituting these calculated values for χ_o and K_o, together with other relevant data, a value for contact radius is calculated from equation (4.8a). This value for contact radius is then consequently inserted into equations (4.2) and (4.4) to calculated the number of contacts N and the contact temperature T_c respectively. In the second step of iteration, new values for K_o and χ_o are recalculated at this

contact temperature and the above procedure repeated to generate new values for N and T_c, and so on. The iteration process is terminated when two subsequent contact temperatures are with 0.1% of each other. Then δ_{expt} (equation (3.1)) is compared with δ_{th} (equation (4.1)) before the whole iteration procedure is repeated for a different value of ξ. The value of ξ for which best comparison is obtained between δ_{expt} and δ_{th} is taken, together with the corresponding values for T_c, a, and N.

The computer program used to perform the iteration is given in Appendix 2. In this program the oxide thickness is varied from 0.5μm to 15μm in steps of 0.5μm.

The fact that the assumption that ξ is equal to ξ^* does not introduce any significant error in the calculations is shown in Table 4.1. This table shows that for a given value of ξ, δ_{th} is fairly insensitive to changes in ξ^*. The reason for this is that as ξ^* changes the product $\alpha\xi^*$ in equation (4.5b) remains approximately constant. The corresponding values for T_c and a are given in Tables 4.2 and 4.3 respectively.

4.3 Heat Transfer Across an Air Gap

Since the theoretical analysis given in Section 4.2 is based upon the division of frictional heat between the sliding members, consideration of heat flow along the pin other than from frictional heating of contact areas is important. Therefore, in elevated temperature experiments where T_D is greater than T_s (as a result of temperature drop across the oxide) substantial amounts of heat flow will occur through the air gap between the specimens (away from the contact areas). Hence, the experimentally measured heat flow rate H_1 entering the pin will consist of both a frictional heat component plus a heat transfer component from the externally heated disc. Consequently the theoretically predicted values of ξ will be very much lower than the actual values measured by SEM.

LOAD (N)	THEORETICAL DIVISION OF HEAT, δ_{th} (%)		
	(ξ^* = 2μm)	(ξ^* = 4μm)	(ξ^* = 8μm)
9.8	8.9	8.9	8.9
19.6	13.7	13.7	13.6
24.5	7.8	7.8	7.7
29.4	16.7	16.6	16.6
39.2	8.3	8.3	8.3
58.9	7.4	7.4	7.4
78.5	7.0	7.3	7.3
98.1	8.3	8.3	8.3
117.7	15.0	14.9	14.7

TABLE 4.1 Influence of ξ^* on Theoretical Division of Heat.

LOAD (N)	CONTACT TEMPERATURE, T_c (^{o}C)		
	($\xi^* = 2\mu m$)	($\xi^* = 4\mu m$)	($\xi^* = 8\mu m$)
9.8	473	484	490
19.6	437	447	453
24.5	487	496	502
29.4	509	525	534
39.2	568	575	579
58.9	626	634	638
78.5	742	618	622
98.1	709	722	730
117.7	769	794	818

TABLE 4.2 Influence of ξ^* on Contact Temperature

LOAD (N)	CONTACT RADIUS, a (μm)		
	(ξ^* = 2μm)	(ξ^* = 4μm)	(ξ^* = 8μm)
9.8	6.2	6.6	6.9
19.6	6.4	7.0	7.3
24.5	5.8	6.3	6.6
29.4	5.2	5.8	6.1
39.2	4.9	5.6	5.9
58.9	4.3	4.9	5.3
78.5	3.5	5.1	5.5
98.1	3.3	4.1	4.5
117.7	3.0	3.6	3.8

TABLE 4.3 Influence of ξ^* on Contact Radius

To determine the contribution of heat transfer component to H_1 requires calculations of heat transfer across the air gap by radiation, convection and conduction. Thomas and Probert (108) have given a condensed theoretical description of heat transfer across interfaces and a review of experimental results for some of the most often used engineering materials.

Heat transfer by radiation Q_r across an air gap can be readily determined by using the following modification of the Stefan-Boltzman equation (109)

$$Q_r = \frac{5.673 \times 10^{-8} A_a \quad (T_2^4 - T_1^4)}{1/e_1 + 1/e_2 - 1} \qquad 4.12$$

where e_1, e_2 = emissitives of the two surfaces
T_1, T_2 = absolute temperatures in kelvins
A_a = apparent pin area ($3.17 \times 10^{-5} m^2$)

Considering only the experiments in which T_D was greater than T_s and taking $e_1 = e_2 = 0.7$ (109) it was possible to show, using equation (4.12), that heat transfer by radiation can be neglected. For example, considering the 9.8N load EN8 experiment conducted at 500°C we have T_1 = 773K and T_2 = 687K. Hence from equation (4.12) Q_r = 0.13W. (cf. H_1 = 11.3W)

Since the air gap between the two surfaces will only be of the order of few microns, it is reasonable to assume that the main source of heat transfer will be conduction and not convection because the movement of the air within the gap will be restricted. Lang (110) has suggested that convection heat transfer is usually negligible for gap widths up to 6.35mm.

Heat transfer by conduction Q_{con} was determined using equation (4.13)

$$Q_{con} = \frac{K_a A_a}{X} \quad (T_D - T_s) \qquad 4.13$$

where K_a is the thermal conductivity of air, X is the width of air gap, and all the other terms have already been defined. To calculate Q_{con} the width of the air gap is required. In reference to talysurf profiles from 400°C and 500°C elevated temperature experiments (many of which gave $T_D > T_s$), it was possible to conclude that a typical value for the width of the air gap is likely to be within the 10-20μm range. A small selection of talysurf profiles are given in Section 3.6. Therefore, taking the thermal conductivity of air at T_s, Q_{con} was calculated for different widths of air gap for each experiment in which T_D was greater than T_s. The calculations showed that the contribution of Q_{con} to H_1 was significant, especially more so in the low load experiments where frictional heat evolved at the sliding interface was considerably less. For these experiments the experimental division of frictional heat δ_{expt} is given by equation (3.1) with $(H_1 - Q_{con})$ in place of H_1. Fortuitously it was found that Q_{con} values obtained for a 15μm air gap, when used in the theoretical analysis, gave consistently good agreement between the measured and theoretically predicted values of ξ. Therefore it was decided to use an air gap of 15μm throughout. Q_{con} values calculated for EN8 and EN31 500°C experiments are given in Tables 4.4 and 4.5 respectively.

4.4 Determined Values of T_c, a, N and ξ

This section gives the results of the theoretical analysis described in the previous sections. For the sake of comparison with the wear curves given in Figures 3.1 and 3.2, the results from this analysis are presented in terms of the variation with applied load of the contact temperature (T_c), the contact radius (a), the number of contacts (N) and the critical oxide film thickness (ξ). Although the theoretical analysis was performed on all the experiments that were carried out, results from only a selection of these experiments are given in this study.

LOAD (N)	H_1 (W)	Q_{CON} (W)	$H_1 - Q_{CON}$ (W)
9.8	11.3	9.3	2.0
14.7	11.4	9.1	2.3
19.6	12.6	6.9	5.7
39.2	11.5	6.7	4.8
58.9	12.9	4.9	8.0
78.5	13.5	4.3	9.2
98.1	13.5	3.7	9.6
117.7	13.0	3.1	9.9

TABLE 4.4 Heat Transfer Across an Air Gap by Conduction (Q_{CON}) for EN8 at 500^{o}C

LOAD (N)	H_1 (W)	Q_{CON} (W)	$H_1 - Q_{CON}$ (W)
9.8	10.7	9.7	1.0
19.6	12.7	5.0	7.7
39.2	13.4	5.7	7.7
49.1	13.5	3.2	10.3
58.9	14.5	3.2	11.2
78.5	13.9	4.8	9.1
98.1	14.9	2.6	12.3
117.7	14.6	0.7	13.9

TABLE 4.5 Heat Transfer Across an Air Gap by Conduction (Q_{CON}) for EN 31 at 500°C.

The computer predicted values of N, a, T_c, ξ and δ_{th} for EN31 room temperature experiments are given in Table 4.6 and in Figure 4.1. Table 4.6 shows that the agreement between δ_{th} and δ_{expt} is good. Shown in Figure 4.1(a) are curves of T_c and T_s plotted against applied load. It must be noted that in the calculation of T_c for loads up to 30N, the value used for the thermal conductivity K_o was that given by equation (4.9(a)). This was because the main constituent in the wear debris was α-Fe_2O_3. Figure 4.1(b) is a graph of the computed values of oxide film thickness ξ plotted against load. For the sake of comparison, the SEM measured values (from Section 3.10.3) are also plotted on the same graph. Although the computed values are slightly higher, both curves show a similar variation with load. The measured ξ values is around $1.4 \pm 0.5\mu m$ for loads less than 30N, $2.9 \pm 0.8\mu m$ for loads in the range 30-80N and $1.3 \pm 0.5\mu m$ for loads greater than 80N. The corresponding values of ξ predicted by the computer are $3.2 \pm 1.0\mu m$, $5.3 \pm 0.9\mu m$ and $4.0 \pm 0.5\mu m$ respectively. X-ray diffraction analysis of the wear debris showed that α-Fe_2O_3 was the main constituent for loads less than 30N, Fe_3O_4 for loads in the range 30-80N, and FeO for loads greater than 80N. Figure 4.1(c) is a graph of the number of contacts N which have emerged from the theoretical analysis. This graph shows that the increase in N is almost linear for loads up to about 100N. The deviation from linearity at 117.72N load can be best understood if we consider the values obtained for the contact radius shown in Figure 4.1(d). This figure shows that the contact radius decreases slightly with load for loads up to about 100N, that is, from a value of $6.5\mu m$ at 9.8N to $4.6\mu m$ at 98.1N. However, for the 117.7N experiment the contact radius changed abruptly to a value of $3.4\mu m$.

Computer results for EN31 experiments at $200^{\circ}C$ are given in Table 4.7 and Figure 4.2. Curves of T_c and T_s plotted against load are shown in Figure 4.2(a), and Figure 4.2(b) shows that the agreement between the predicted and measured ξ values is good, particularly more so in the 40-100N load

LOAD (N)	N	a (μm)	T_c (^{o}C)	ξ (μm)	δ_{th} (%)	δ expt (%)
9.8	30	6.5	481	3.0	8.8	8.5
19.6	61	6.5	438	2.0	13.7	11.4
24.5	78	6.4	498	4.5	7.7	6.8
29.4	134	5.4	506	2.0	16.6	13.9
34.3	142	5.6	564	4.0	9.4	8.5
39.2	161	5.6	576	4.5	8.2	7.3
58.9	281	5.2	637	6.0	7.3	6.7
78.5	457	4.7	703	6.5	6.9	6.1
98.1	576	4.7	675	5.0	10.4	8.4
117.7	1244	3.5	791	3.5	14.8	11.7

TABLE 4.6 Values of N, a, T_c, ξ and δ_{th} for EN31 at Room Temperature.

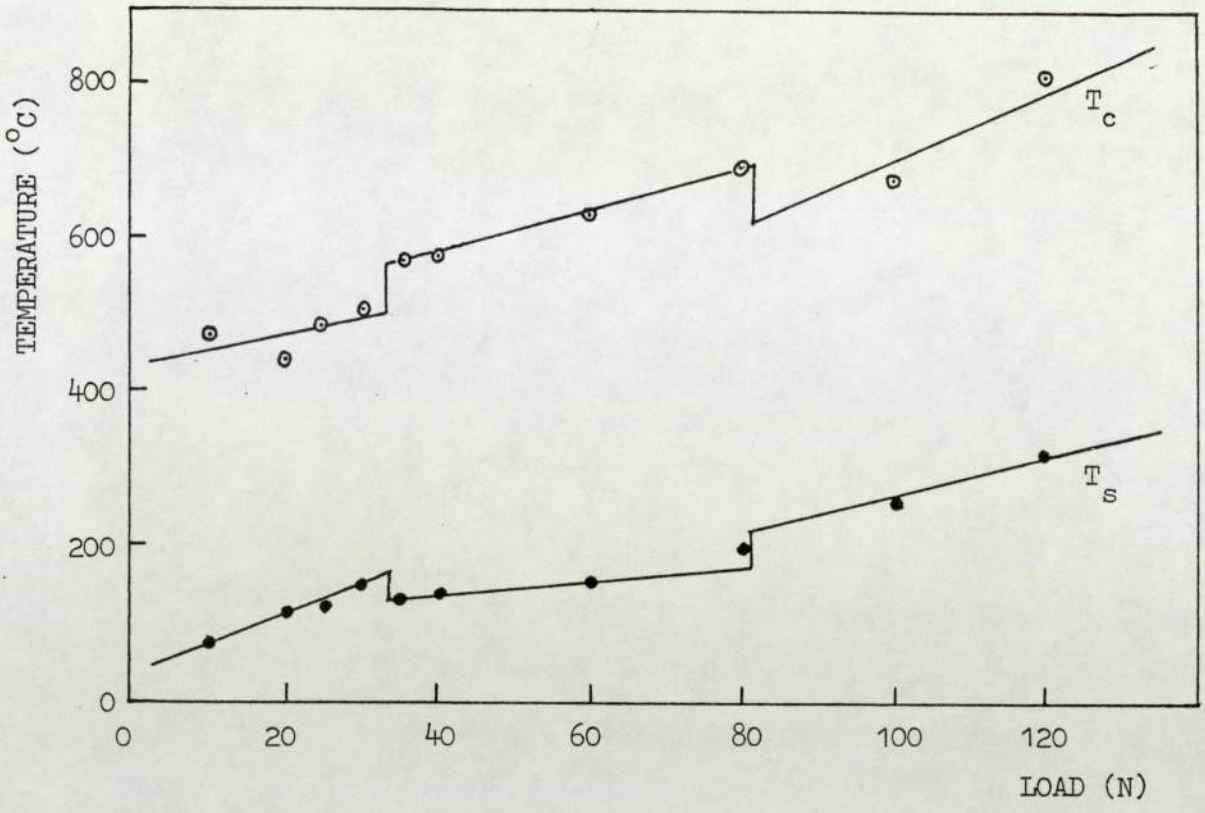

FIGURE 4.1 (a) Variation of Contact Temperature and General Surface Pin Temperature with Load for EN31 at Room Temperature.

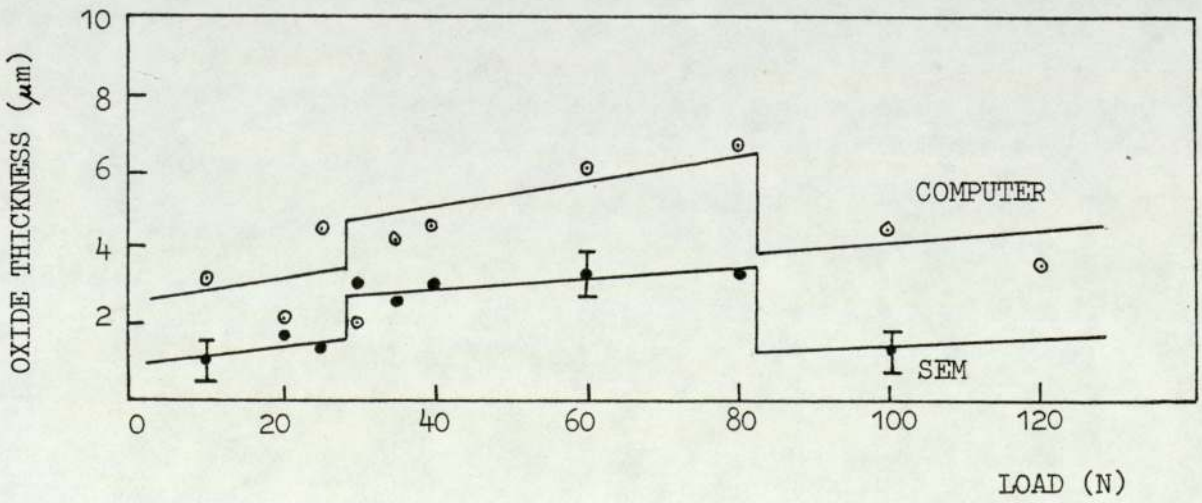

FIGURE 4.1 (b) Variation of Oxide Film Thickness with Load for EN31 at Room Temperature.

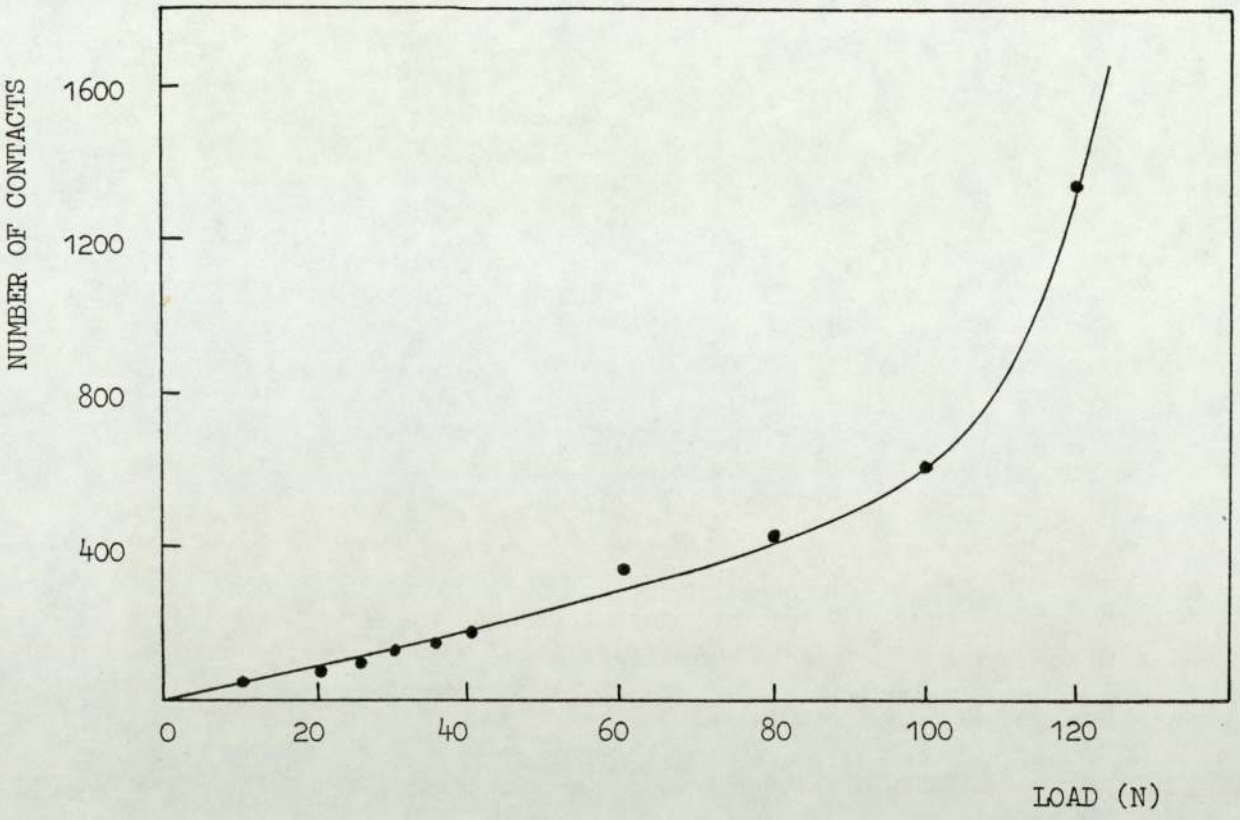

FIGURE 4.1 (c) Number of Contacts Versus Load for EN31 at Room Temperature.

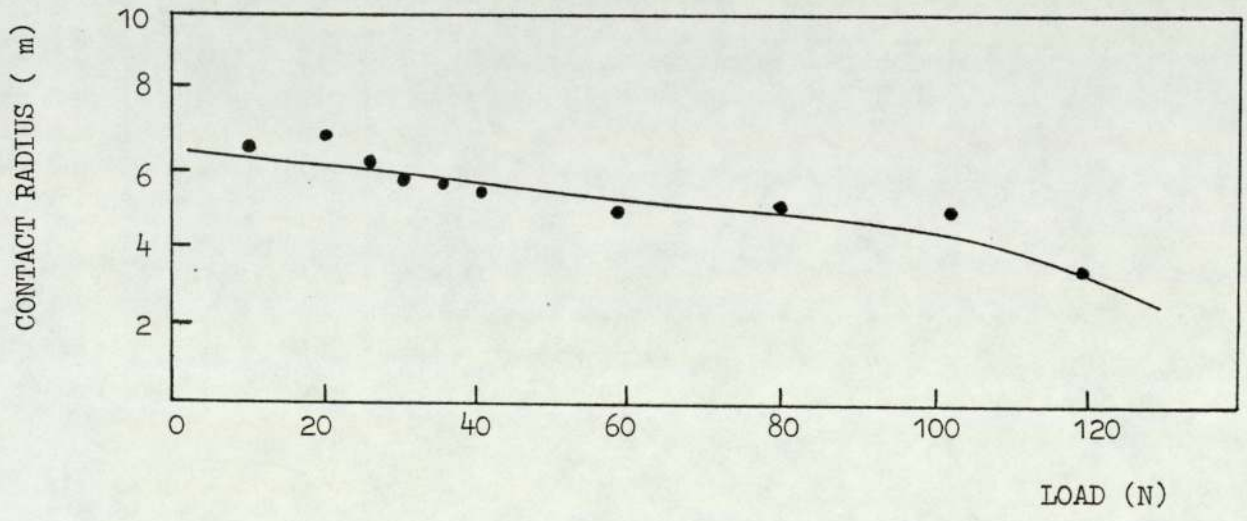

FIGURE 4.1 (d) Mean Contact Radius Versus Load for EN31 at Room Temperature.

LOAD (N)	N	a (μm)	T_c (^{o}C)	ξ (μm)	δ_{th} (%)	δ expt (%)
9.8	47	5.2	567	1.5	13.2	13.7
24.5	181	4.2	557	1.0	23.1	22.3
44.2	215	5.2	596	2.5	11.7	11.3
54.0	395	4.2	730	3.0	11.6	10.9
58.9	283	5.2	634	4.5	8.0	7.6
63.8	581	3.8	720	2.5	17.7	15.4
73.6	375	5.0	629	4.0	10.4	9.6
83.4	548	4.5	638	2.5	16.1	12.9
103.0	1046	3.6	766	3.0	16.2	13.4
137.3	1026	4.3	694	3.5	14.2	10.1

TABLE 4.7 Values of N, a, T_c, ξ and δ_{th} for EN31 at 200^{o}C.

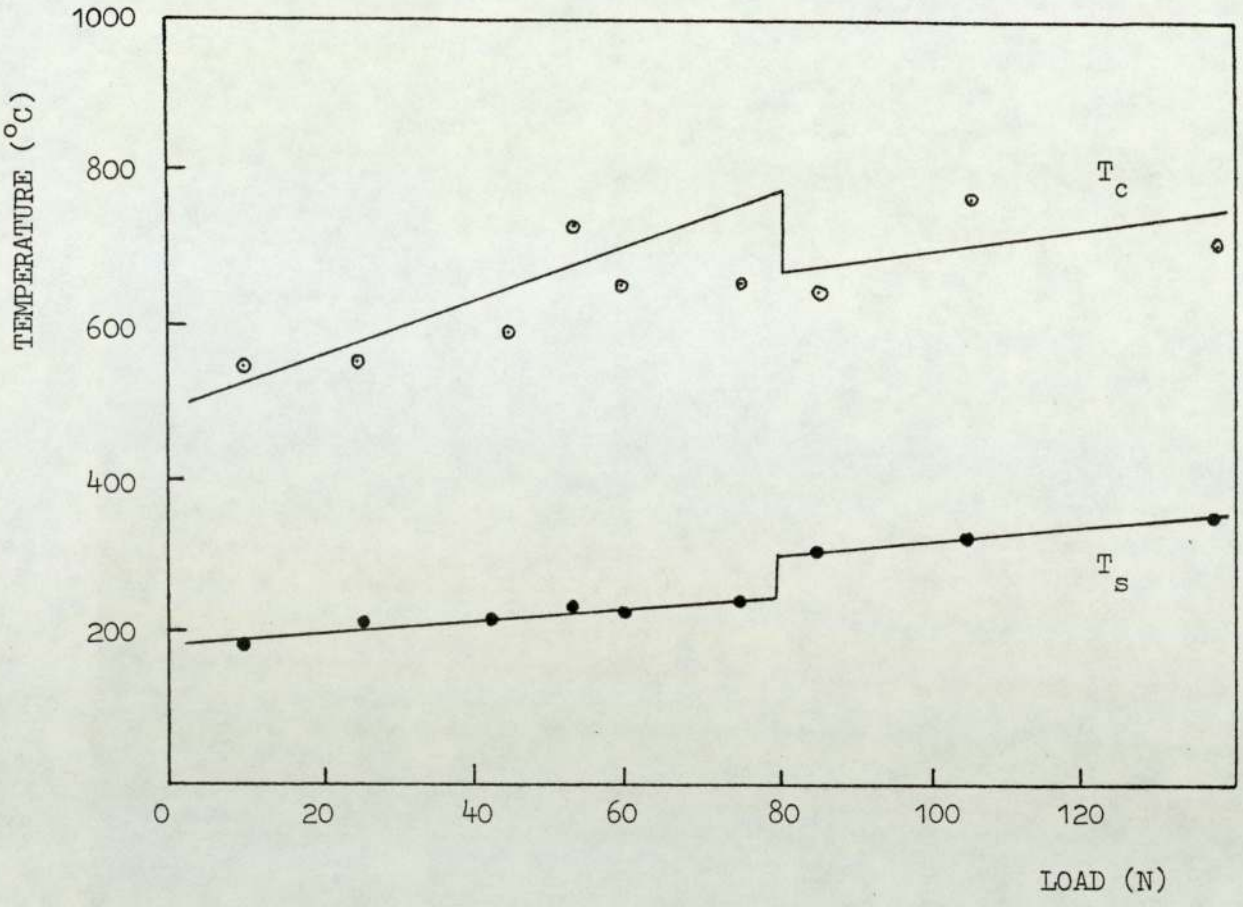

FIGURE 4.2 (a) Variation of Contact Temperature and General Surface Pin Temperature with Load for EN31 at 200°C.

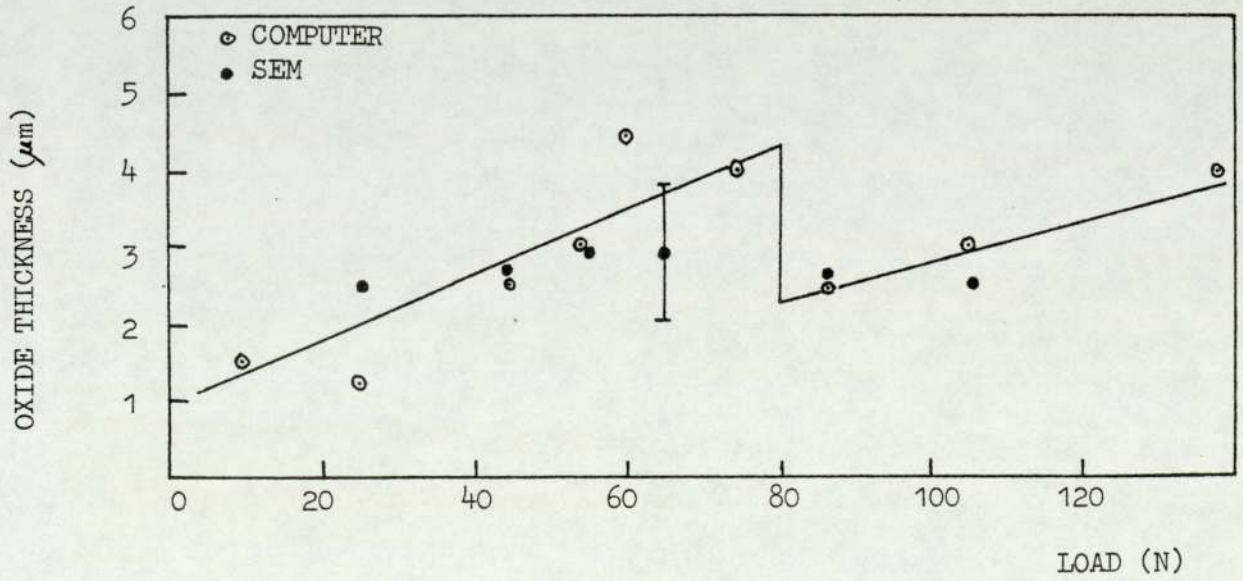

FIGURE 4.2 (b) Variation of Oxide Film Thickness with Load for EN31 at 200°C.

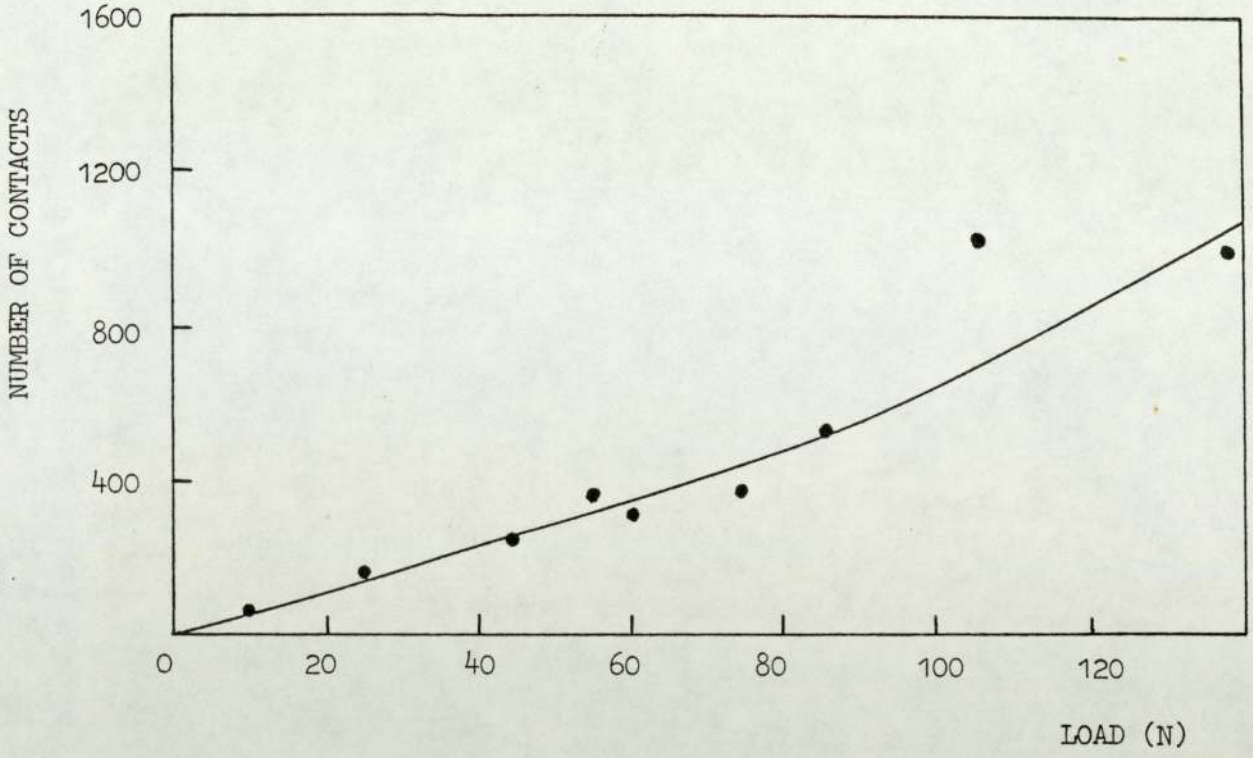

FIGURE 4.2 (c) Number of Contacts Versus Load for EN31 at 200°C.

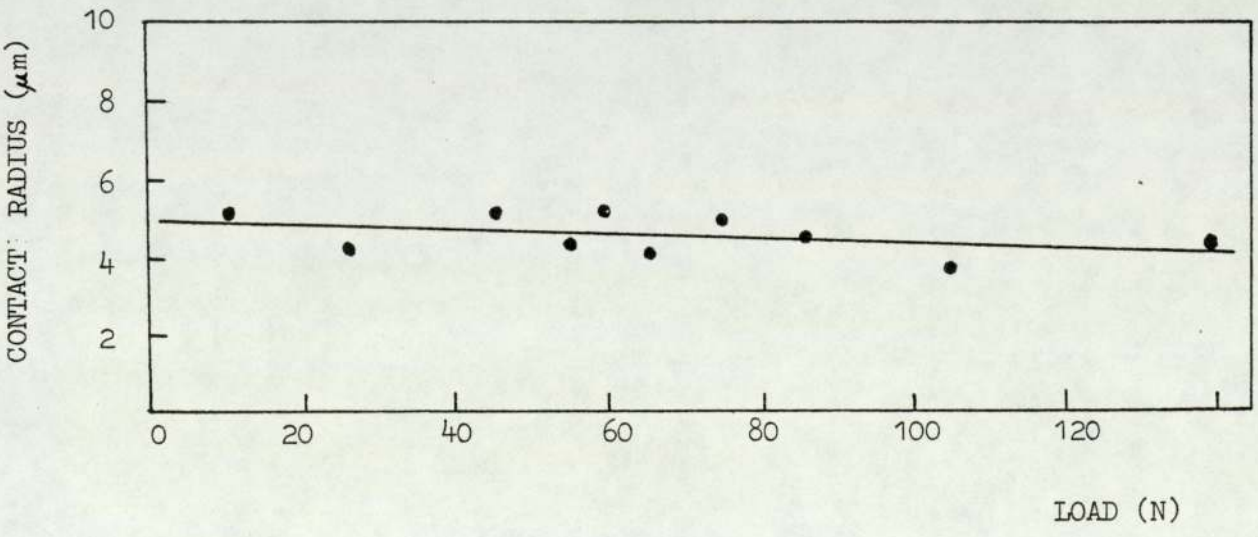

FIGURE 4.2 (d) Mean Contact Radius Versus Load for EN31 at 200°C.

range. Graphs of the number of contacts and the contact radius versus load are shown in Figures 4.2(c) and (d) respectively. The contact radius versus load curve (Figure 4.2(d)) shows a small but a steady fall with increasing load. The form of the N versus load graph (Figure 4.2(c)) is similar to that observed with the room temperature experiments shown in Figure 4.1(c).

The computer results for EN31 experiments at 500°C are given in Table 4.8 and Figure 4.3. The variation of T_c and T_s with load is shown in Figure 4.3(a). This figure shows that T_c varied linearly with load, in the same manner as T_s. Figure 4.3(b) shows that curves for both the measured and predicted ξ values show a very similar trend, that is ξ increases with increasing load. X-ray diffraction analysis showed that the wear debris was a mixture of α-Fe_2O_3 and Fe_3O_4, with Fe_3O_4 increasing with load. Figure 4.3(c) shows the graph of N versus load for the EN31 experiments at 500°C. The contact radius versus load curve for these experiments is shown in Figure 4.3(d). Comparison of Figures 4.1(c) and 4.2(c) with Figure 4.3(c) indicates that at any given load the number of contacts have increased with temperature. For example, for 9.8N load EN31 experiment at room temperature, 200°C and 500°C, the number of contacts was 30, 47 and 67 respectively.

Computer results for EN8 experiments at room temperature, 100°C, 200°C, 300°C, 400°C and 500°C were obtained and those at room temperature, 200°C and 500°C are given in Tables 4.9, 4.10 and 4.11 respectively.

The variation of contact temperature (T_c) and general surface temperature (T_s) with load for EN8 experiments at room temperature is shown in Figure 4.4(a). This figure shows that T_c varies linearly with load. The wear debris identified by x-ray diffraction consisted of FeO and α-Fe. Figure 4.4(a) shows that the T_c values for the room temperature experiments are (with the exception of 4.9N load experiment) in excess of 570°C, i.e. the formation temperature of FeO.

LOAD (N)	N	a (μm)	T_c (^{o}C)	ξ (μm)	δ_{th} (%)	δexpt (%)
9.8	67	4.7	722	3.0	5.4	7.4
19.6	708	2.2	672	0.5	34.1	39.4
39.2	632	3.3	736	1.5	22.4	26.0
49.1	1116	2.8	787	1.5	24.2	26.0
58.9	1083	3.1	739	1.5	23.6	25.6
78.5	1256	3.3	810	3.0	15.6	16.9
98.1	1492	3.5	759	2.5	17.9	18.7
107.9	2735	2.9	770	2.0	24.3	23.4
117.7	2226	3.2	818	3.0	16.9	17.2
137.3	3388	3.0	821	3.0	20.1	19.1
157.0	2915	3.4	799	3.5	16.5	15.8

TABLE 4.8 Values of N, a, T_c, ξ and δ_{th} for EN31 at 500^{o}C.

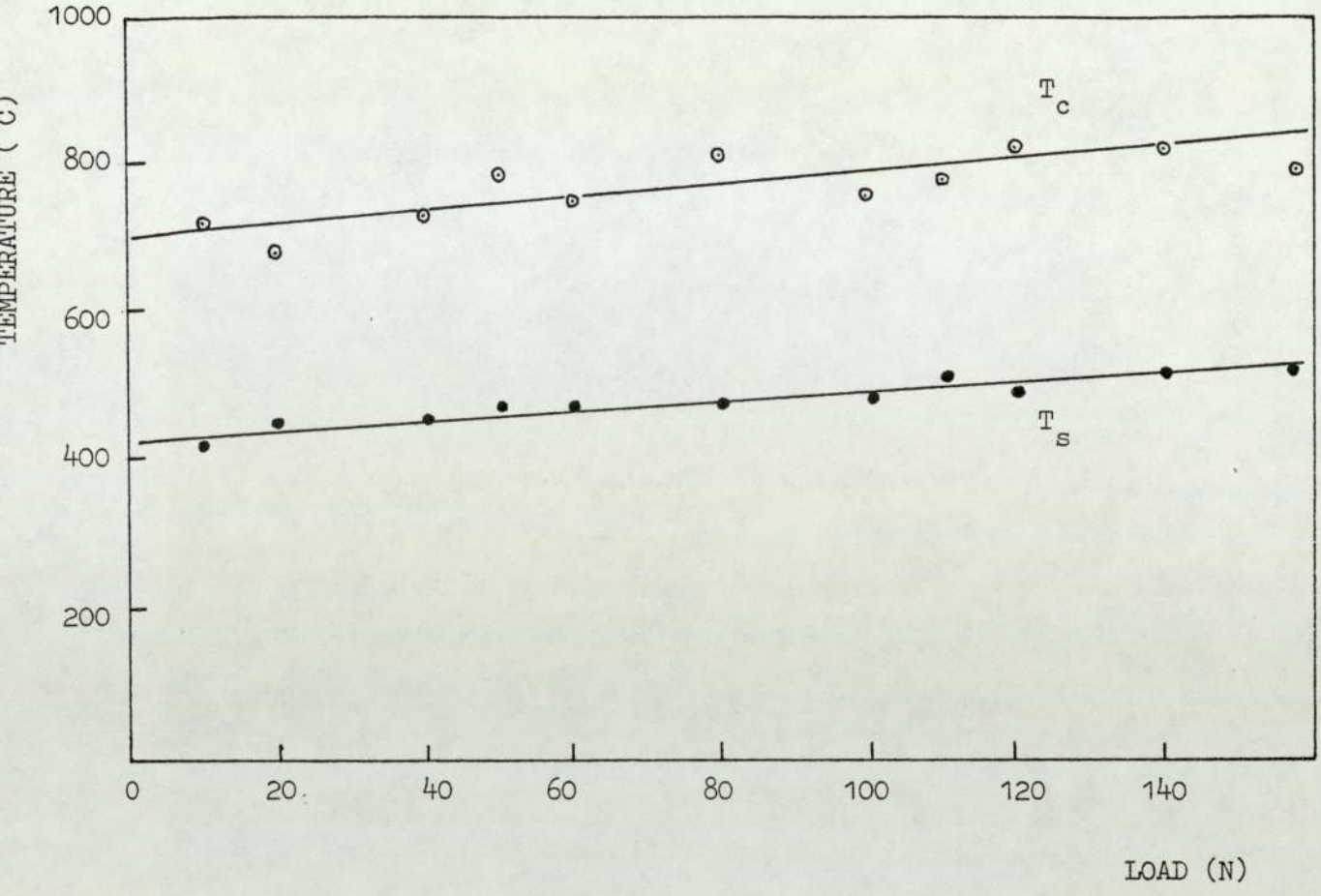

FIGURE 4.3 (a) Variation of Contact and General Surface Pin Temperature with Load for EN31 at 500°C.

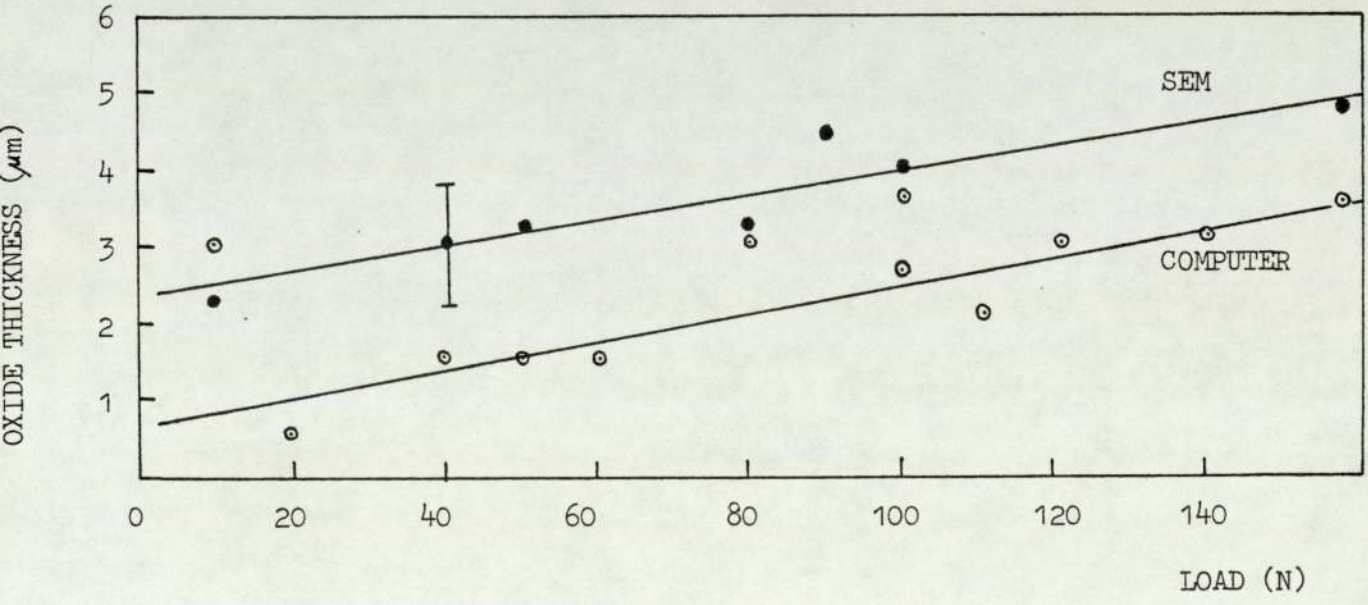

FIGURE 4.3 (b) Variation of Oxide Film Thickness with Load for EN31 at 500°C.

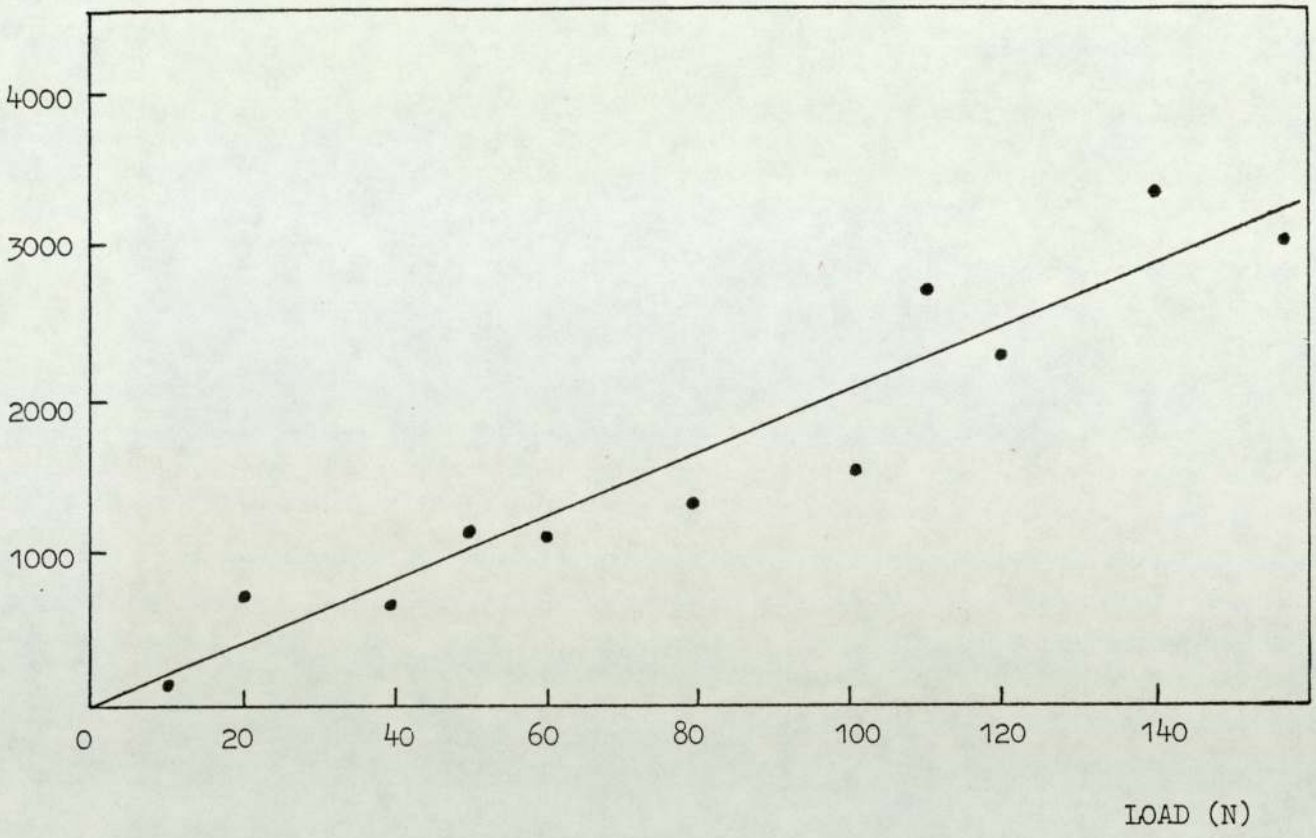

FIGURE 4.3 (c) Number of Contacts Versus Load for EN31 at 500°C.

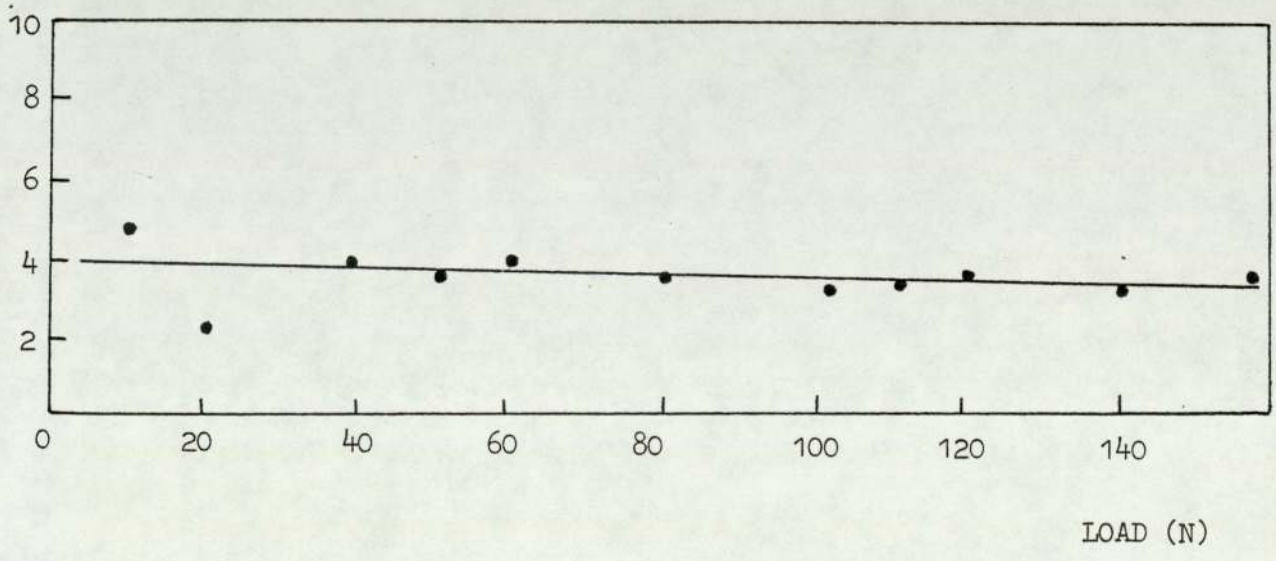

FIGURE 4.3 (d) Mean Contact Radius Versus Load for EN31 at 500°C.

LOAD (N)	N	a (μm)	T_c (^{o}C)	ξ (μm)	δ_{th} (%)	δ expt. (%)
4.9	19	6.0	548	3.5	6.4	6.1
14.7	91	4.8	574	2.0	17.0	14.9
29.4	254	4.0	622	2.5	21.3	17.8
34.3	448	3.3	576	1.5	29.3	22.4
39.2	887	2.5	615	1.5	33.4	24.7

TABLE 4.9 Values of N, a, T_c, ξ and δ_{th} for EN8 at Room Temperature.

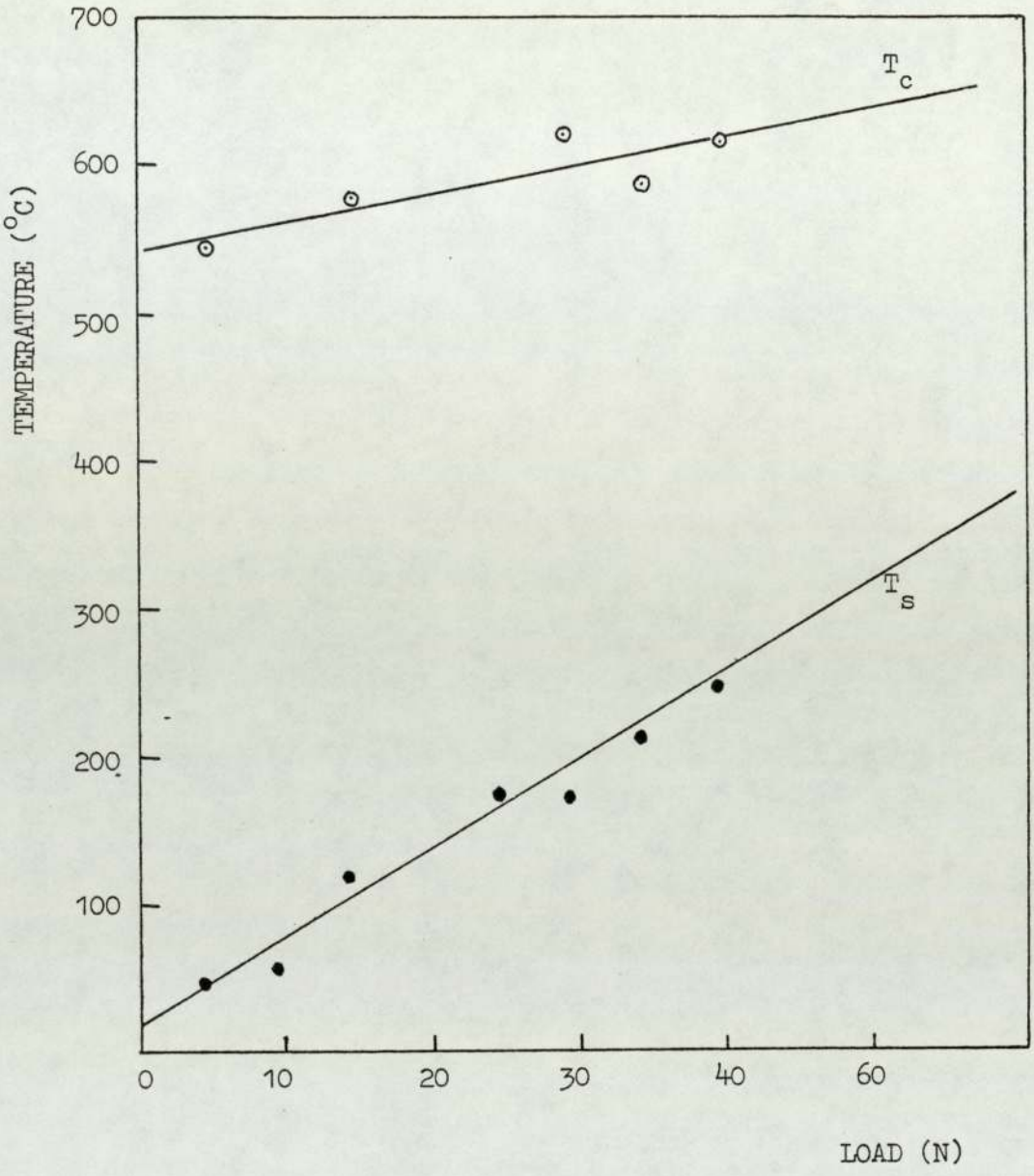

FIGURE 4.4 (a) Variation of Contact Temperature and General Surface Pin Temperature with Load for EN8 at Room Temperature.

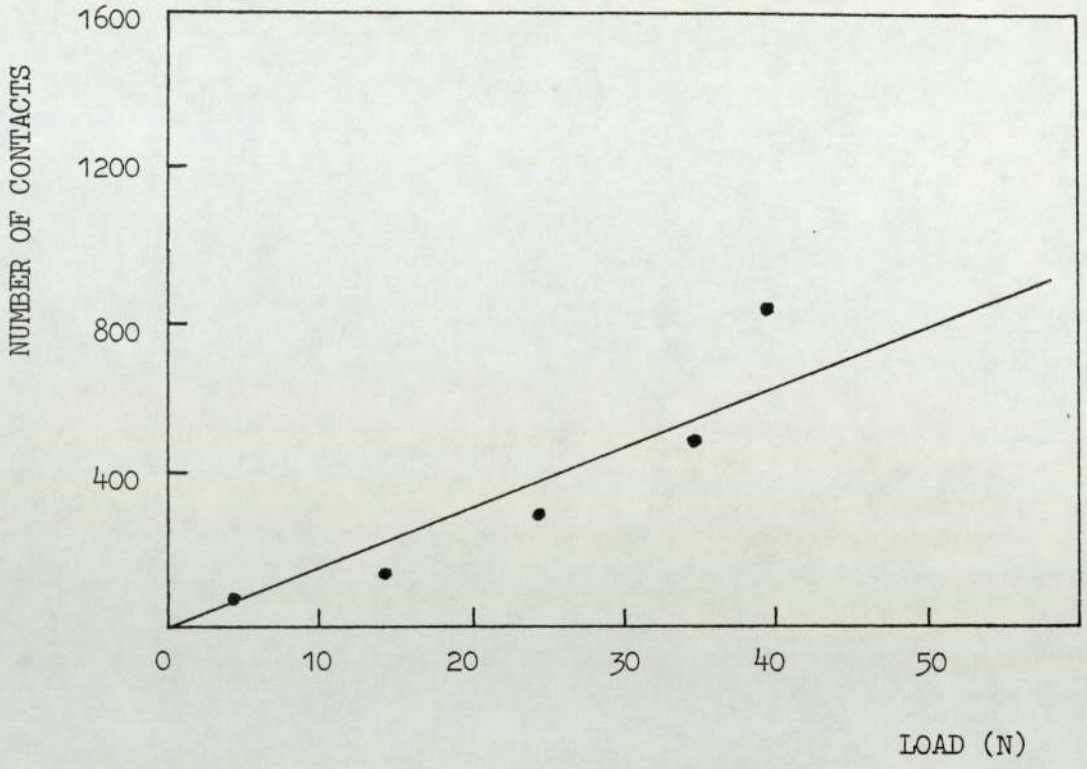

FIGURE 4.4 (b) Number of Contacts Versus Load for EN8 at Room Temperature.

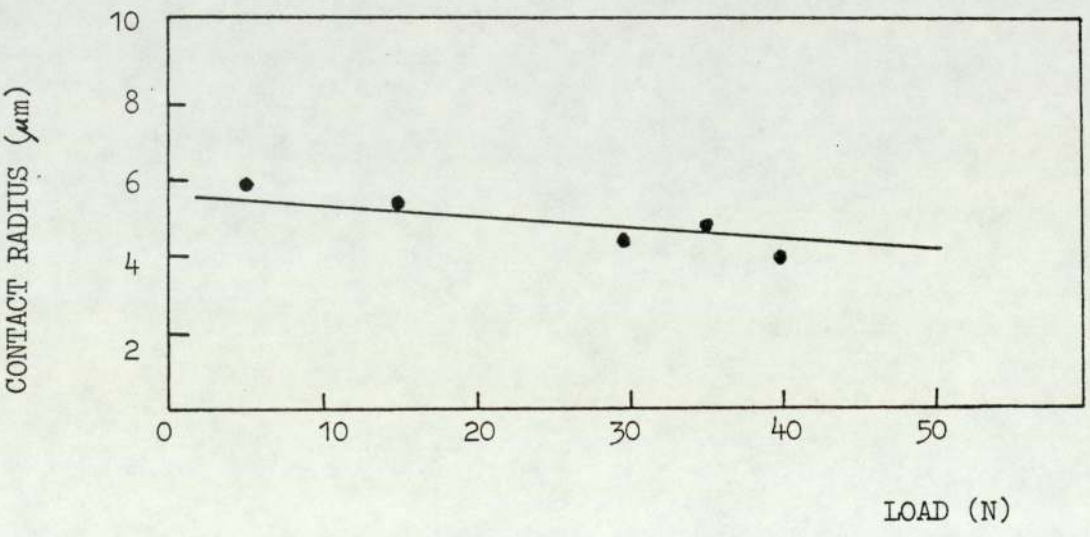

FIGURE 4.4 (c) Mean Contact Radius Versus Load for EN8 at Room Temperature.

Graphs of the number of contacts and the contact radius versus load for these experiments are shown in Figures 4.4(b) and 4.4(c) respectively.

The computer results for EN8 experiment at 200°C are given in Figure 4.5. Graphs of T_c and T_s versus load are given in Figure 4.5(a). This figure shows a transition in T_c and T_s at 35N load. Examination of the wear debris indicated that FeO was the predominant oxide in experiments carried out at loads greater than 35N. It is worth noting that values for T_c given in Figure 4.5(a) are greater than the formation temperature of FeO, even though at loads less than 35N only α-Fe_2O_3 and Fe_3O_4 were detected (with the possible exception of 29.4N experiment in which traces of FeO were found) in the wear debris. Nevertheless, the presence of FeO at 29.4N load suggests that T_c values of around 592°C determined for the low load experiments (<25N) are of the correct magnitude. Figure 4.5(b) shows the variation of measured and computed oxide film thickness with load. Graphs of the number of contacts and the contact radius versus load for EN8 experiments at 200°C are shown in Figures 4.5(c) and 4.5(d) respectively.

Figure 4.6 gives the computer results for EN8 experiments at 500°C. The variation of T_c and T_s with load is shown in Figure 4.6(a). It is obvious from this figure that T_c increases linearly with load in the same manner as T_s. The correlation between the measured and computed oxide film thickness for these experiments, as shown in Figure 4.6(b), is very good. This figure shows that the oxide film increases steadily with increasing load, that is, from 1.5μm at 9.8N to 4.5μm at 117.7N. X-ray diffraction analysis showed that the wear debris was a mixture of α-Fe_2O_3 and Fe_3O_4, with Fe_3O_4 increasing with load. Graphs of the number of contacts versus load is shown in Figure 4.6(c). Comparison of this figure with Figures 4.4(c) and 4.5(c) indicates that the number of contacts have increased with temperature, particularly more so at the higher loads. Figure 4.6(d) gives the contact radius

LOAD (N)	N	a (μm)	T_c (^{o}C)	ξ (μm)	δ_{th} (%)	δ expt (%)
6.9	37	5.2	599	3.5	11.3	13.1
9.8	46	5.5	592	5.0	5.8	6.9
19.6	95	5.4	592	6.0	5.8	6.7
29.4	172	4.9	652	5.0	7.1	7.9
39.2	240	4.8	660	2.5	13.9	13.0
49.1	270	5.0	620	2.0	17.2	15.5
58.9	485	4.1	702	3.0	17.0	15.9
68.7	505	4.3	678	5.0	10.6	9.7
78.5	495	4.7	642	5.5	9.1	8.5
83.4	631	4.3	672	3.5	15.3	13.6
88.3	631	4.4	657	4.0	13.5	12.1
98.1	1027	3.6	761	4.0	14.2	11.9
117.7	1225	3.7	739	3.0	18.7	14.7
137.3	1538	3.7	729	3.5	18.1	12.2

TABLE 4.10 Values of N, a, T_c, ξ and δ_{th} for EN8 at 200^{o}C.

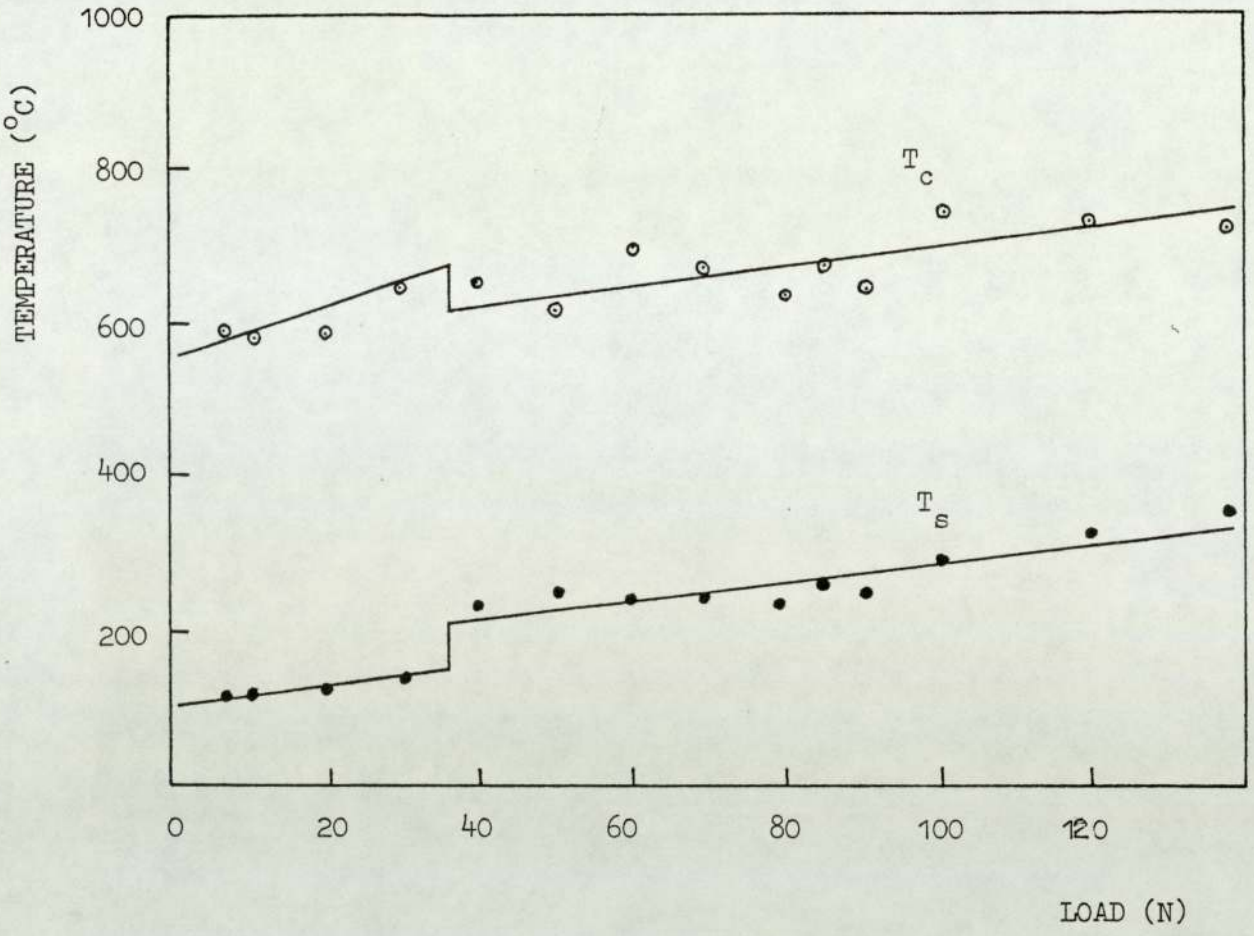

FIGURE 4.5(a) Variation of Contact Temperature and General Surface Pin Temperature with Load for EN8 at 200°C.

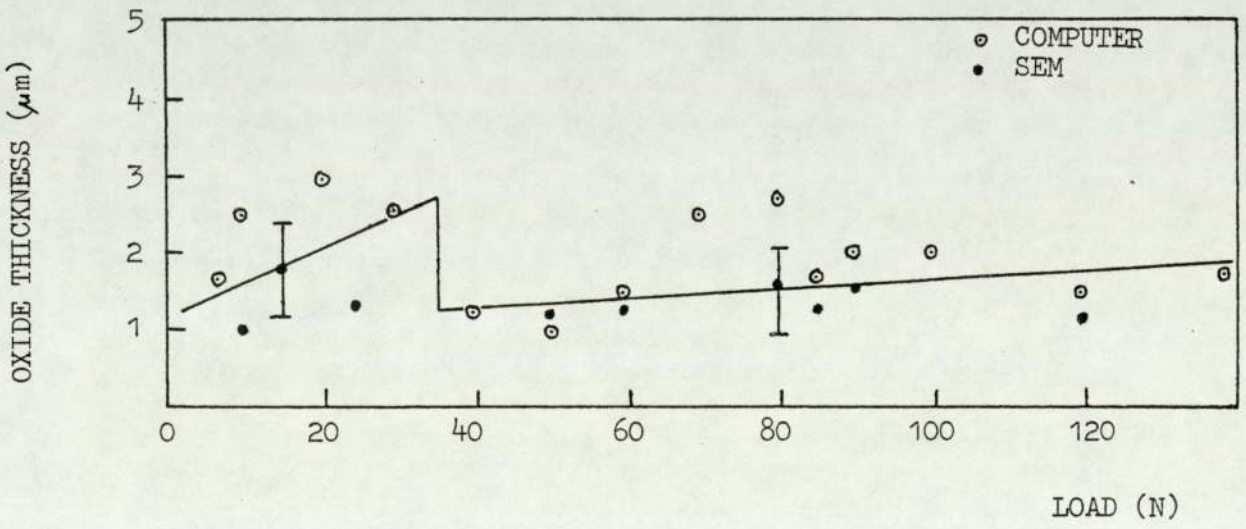

FIGURE 4.5 (b) Variation of Oxide Film Thickness with Load for EN8 at 200°C.

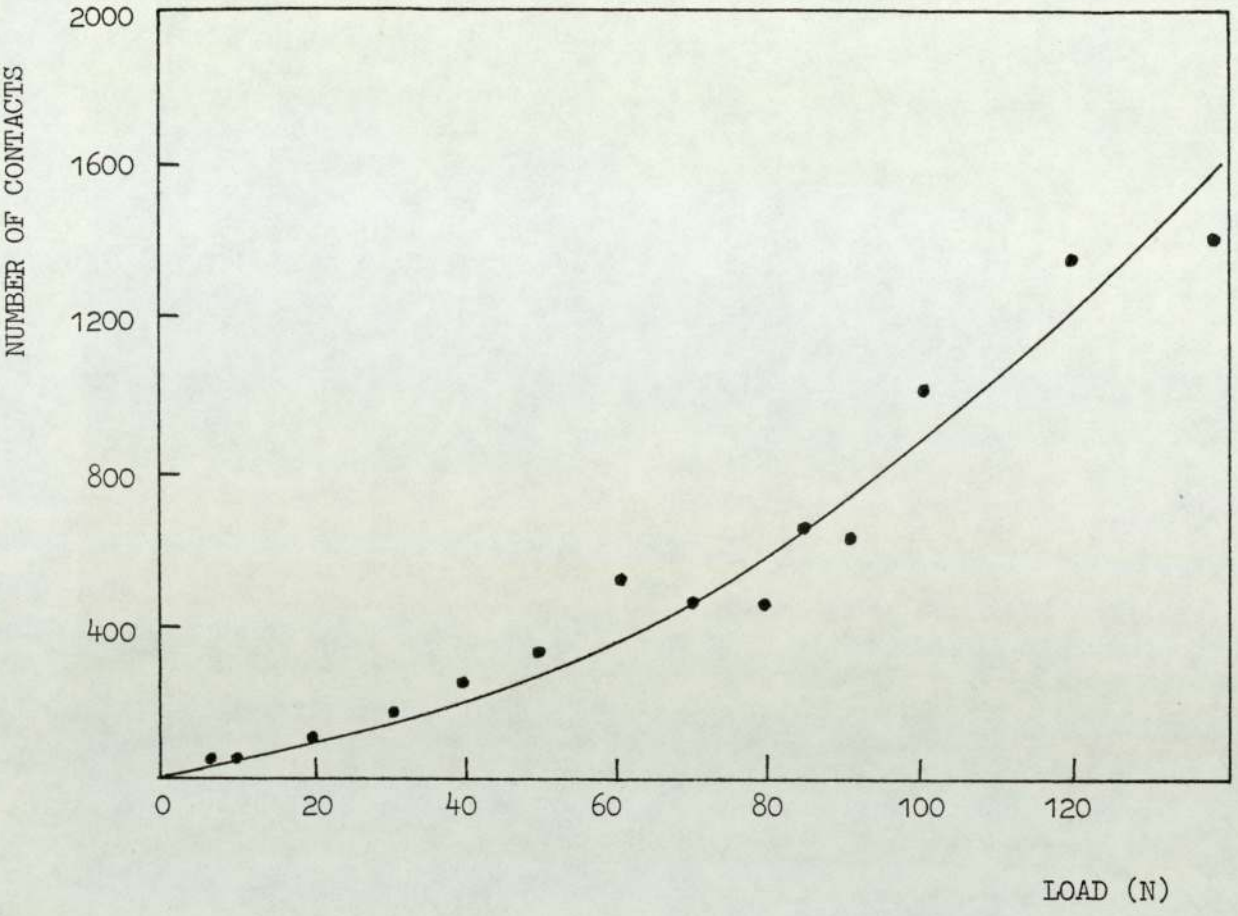

FIGURE 4.5 (c) Number of Contacts Versus Load for EN8 at 200°C.

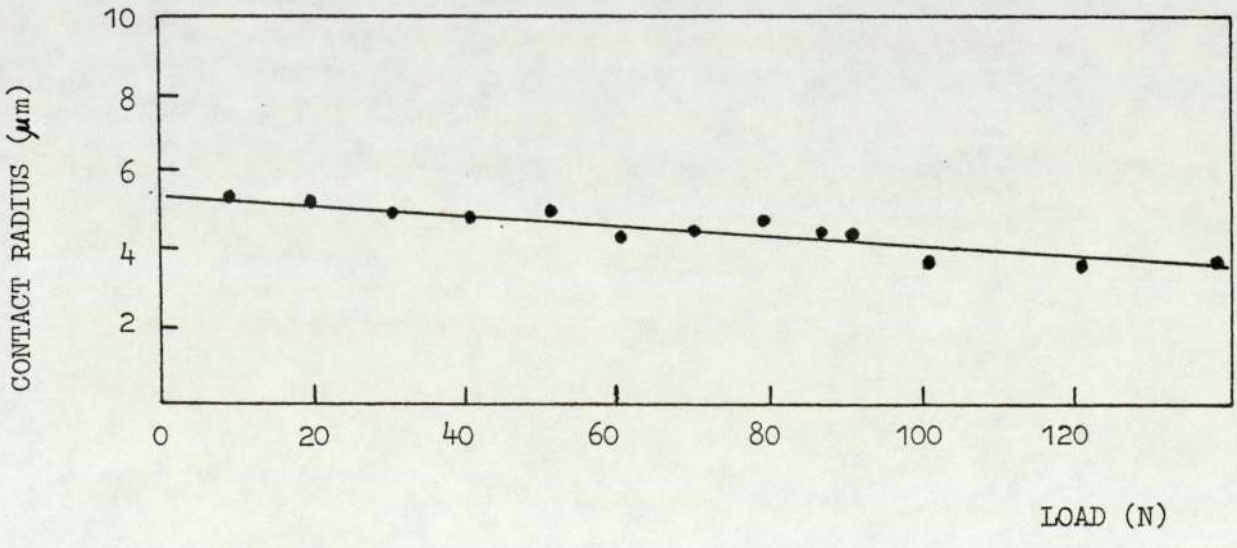

FIGURE 4.5 (d) Mean Contact Radius Versus Load for EN8 at 200°C.

versus load curve for the EN8 experiments at 500°C. As found with the EN31 experiments, the contact radius for the EN8 experiments (Figures 4.4(d), 4.5(d) and 4.6(d)) showed a small but steady decrease with load.

LOAD (N)	N	a (μm)	T_c (^{o}C)	ξ (μm)	δ_{th} (%)	δ_{expt} (%)
9.8	91	4.3	711	1.5	12.2	16.3
14.7	123	4.5	702	2.0	10.0	13.6
19.6	276	3.6	726	1.0	19.4	23.5
39.2	456	4.0	771	3.0	10.7	12.7
58.9	698	4.0	745	2.5	12.9	14.8
78.5	1143	3.5	822	3.0	12.5	13.8
98.1	1375	3.5	806	3.5	13.3	14.5
117.7	1534	3.9	774	4.5	10.8	11.7

TABLE 4.11 Values of N, a, T_c, ξ and δ_{th} for EN8 at 500^{o}C.

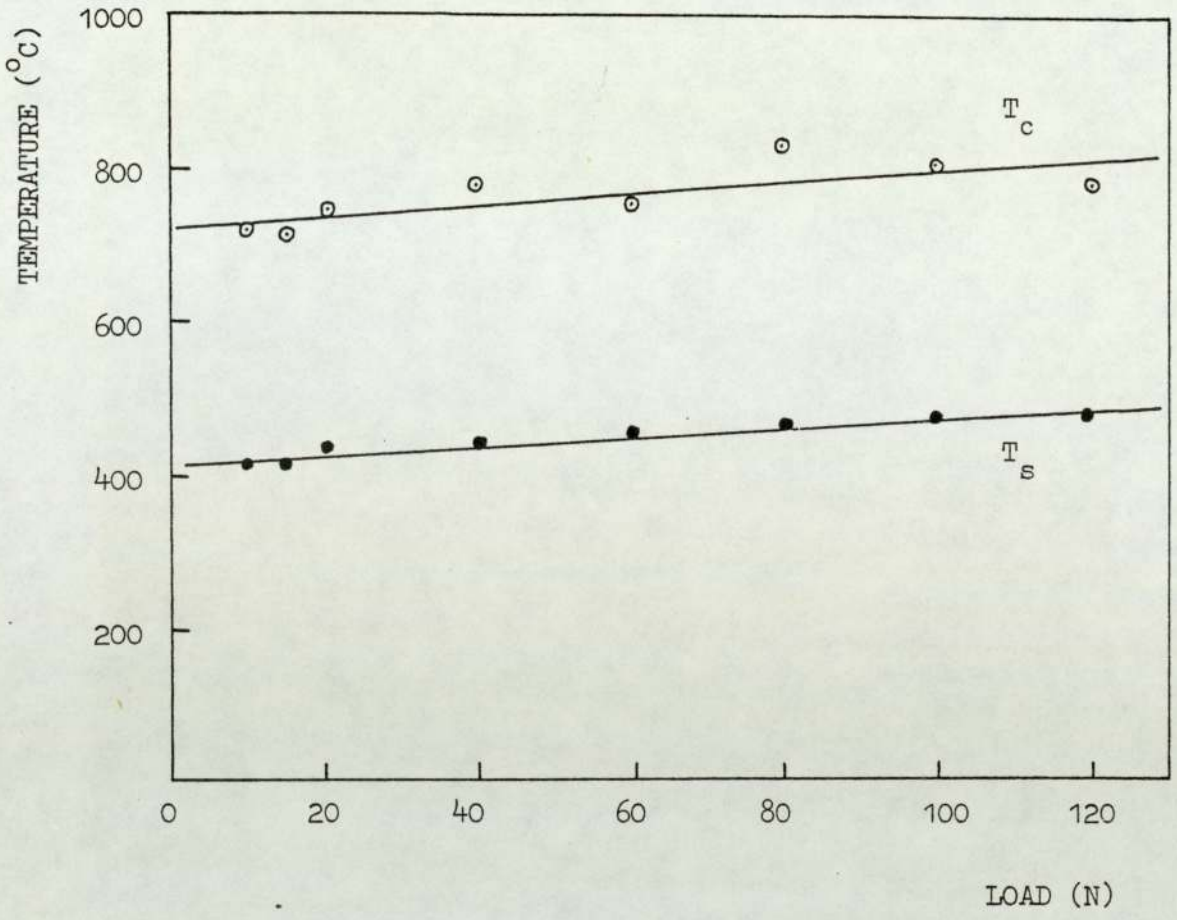

FIGURE 4.6 (a) Variation of Contact Temperature and General Surface Pin Temperature with Load for EN8 at 500°C.

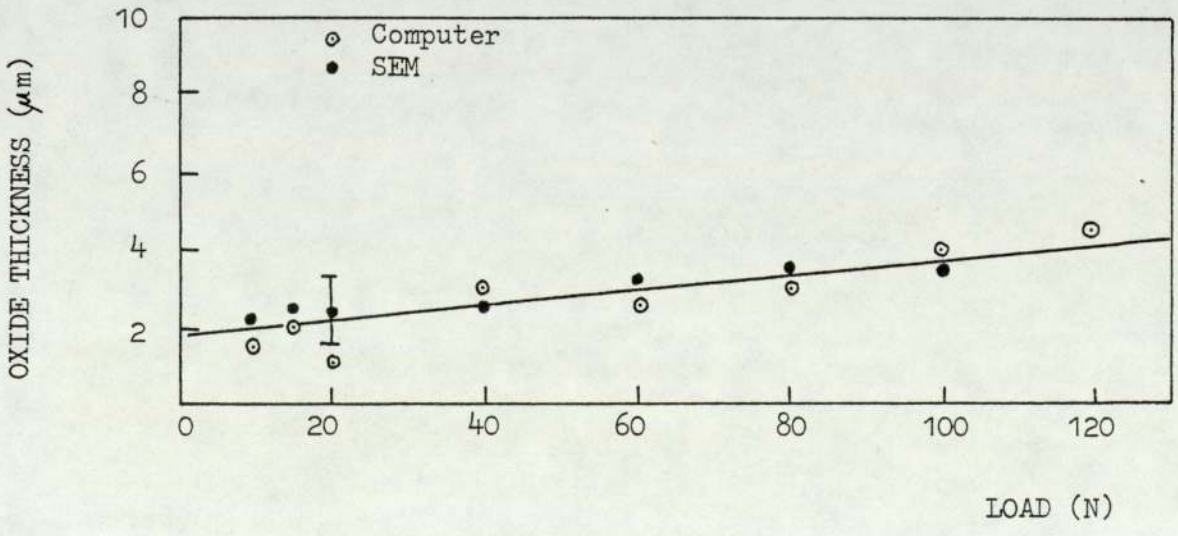

FIGURE 4.6 (b) Variation of Oxide Film Thickness with Load for EN8 at 500°C.

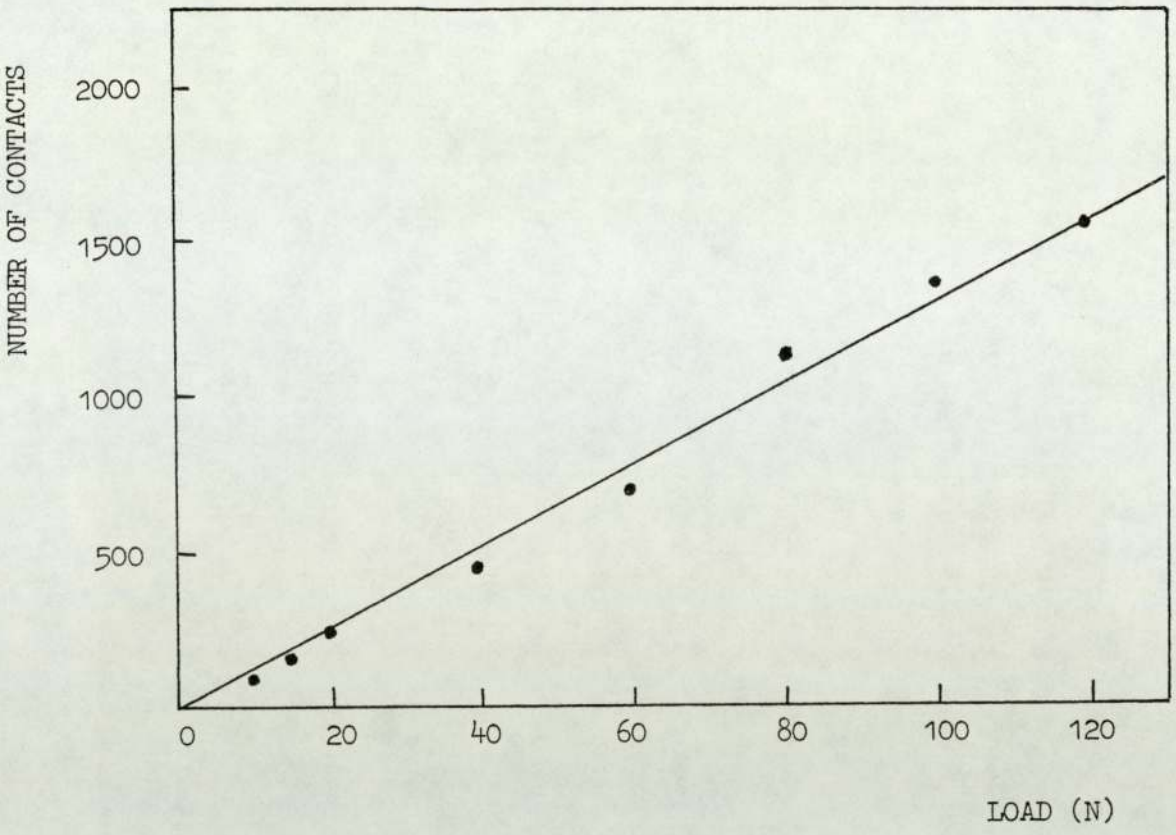

FIGURE 4.6 (c) Number of Contacts Versus Load for EN8 at 500°C.

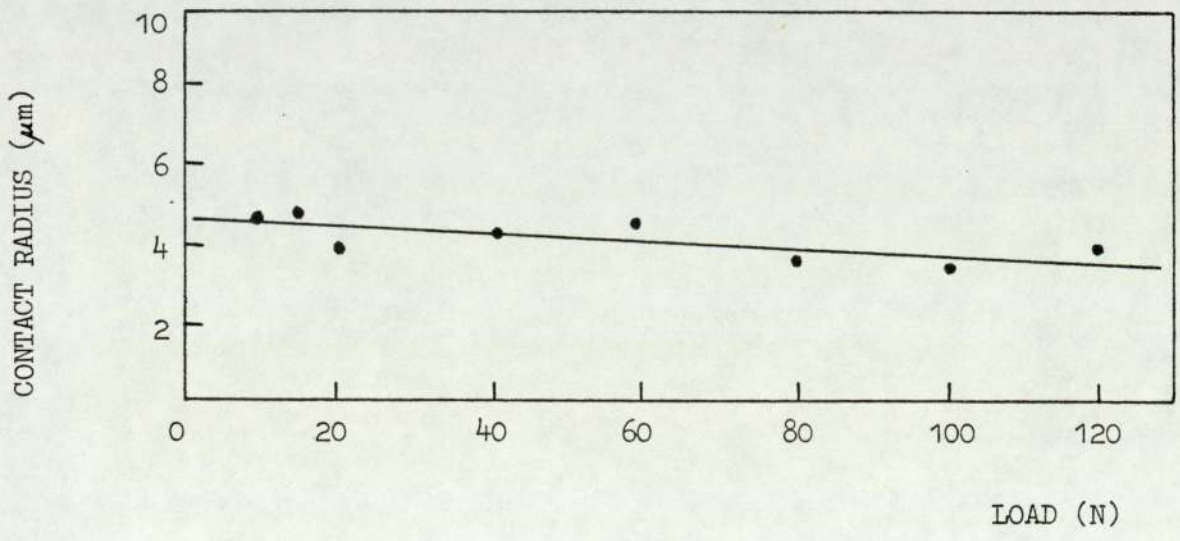

FIGURE 4.6 (d) Mean Contact Radius Versus Load for EN8 at 500°C.

4.5 An Oxidational Wear Theory

Implicit implication of the oxidational wear theory originally proposed by Quinn (44) is that rate of oxide growth is equal to the rate of removal. This theory is based on the Archard Wear Equation (111).

$$\omega = KA \qquad 4.14$$

where ω is the wear rate (measured in terms of volume removed per unit sliding distance), A is the real area of contact between the sliding surfaces, and K is the probability factor. Quinn assumed that, on the average, 1/K asperity encounters are necessary (at a given asperity contact) for a critical oxide film thickness ξ to build up before it becomes detached to form a wear particle. It was further assumed that each encounter adds to oxide thickness at a given asperity. If τ is the duration of a single wearing contact, then the total time (t_c) to produce a wear particle of thickness ξ is given by

$$t_c = \frac{\tau}{K} \qquad 4.15$$

but $\tau = d/V$, where d is the distance along which a wearing contact is made (assumed to be twice the contact radius, i.e. 2a) and V is the speed of sliding.

Hence

$$t_c = \frac{d}{VK} \qquad 4.16$$

Quinn (44) further assumed that oxidation proceeds at the contact at a rate which is parabolically dependent upon the total time of contact (t_c). This assumption is true for thick

films with diffusion mechanism responsible for oxidation. Thus, the mass per unit area of oxide growth Δm can be expressed through the parabolic relation (67) as

$$\Delta m^2 = k_p t_c \qquad 4.17$$

where k_p is the parabolic rate constant. To a good approximation, it can be assumed that

$$\Delta m = \xi f \rho \qquad 4.18$$

where ρ is the density of the oxide and f is the mass fraction of the oxide which is oxygen.

Eliminating t_c from equations (4.16) and (4.17), and using the above described value for Δm, one obtains

$$K = \frac{dk_p}{V\rho^2 f^2 \xi^2} \qquad 4.19$$

It is generally accepted (67) that the parabolic oxidation rate constant is exponently dependent on the temperture of oxidation (T_o), namely

$$k_p = A_p \exp(-Q_p/(R_g T_o)) \qquad 4.20$$

where A_p is the Arrhenius constant for parabolic oxidation, Q_p is the activation energy for parabolic oxidation and R_g is the gas constant.

The oxidational wear theory assumes (9) that the temperature (T_o) at which the real areas of contact oxidise is equal to, or not significantly different from, the contact temperature T_c. Thus, combining equations (4.19) and (4.20) and writing T_c for T_o, we get

$$K = \frac{dA_p \exp(-Q_p/(R_g T_c))}{V\rho^2 f^2 \xi^2} \qquad 4.21$$

Substituting the above expression for K into equation (4.14) and assuming real area of contact is approximately given by W/P_m in accordance with the plastic deformation hypothesis of Bowden and Tabor (6), one obtains

$$\omega = \frac{dWA_p \exp(-Q_p/(R_g T_c))}{P_m V \rho^2 f^2 \xi^2} \qquad 4.22$$

Recent work by Sullivan et alia (112) has shown that discrepancies observed in previous applications of equation (4.22) to the mild wear of low-alloy steels (44,46,88) were due to the incorrect assumption that oxidational constants measured under static conditions could be applied without change to tribological conditions. They showed that although the activation energies (Q_p) for static and sliding conditions are likely to be the same, the accompanying Arrhenius constants (A_p) will be different, leading to very different growth rates.

By very careful plotting of the static oxidation rates versus the reciprocal of the absolute temperature, derived from static oxidation studies on cold worked iron of Caplan and Cohen (68), Sullivan et alia (112) have revealed three distinct regions on the Arrhenius plot corresponding to three different oxide growth regimes. The corresponding values of A_p and Q_p from these plots for different temperature regions are given in Table 4.12. Inserting these values for Q_p into the computer search technique (88), they generated appropriate values of the Arrhenius constant relevant for oxidation during sliding. These "tribo-oxidation" A_p values are also given in Table 4.12. It is interesting to note that these "Arrhenius constants for wear" are quite different from the Caplan and Cohen (68) static oxidation values.

Recent work with low-alloy steels (105,112) has shown that equation (4.22) can be used to predict their wear behaviour provided appropriate A_p and Q_p values given in Table 4.12 are used according to the temperature range in which T_c occurs.

Oxide	α-Fe_2O_3	Fe_3O_4	FeO
Static Oxidation A_p $(KG^2m^{-4}S^{-1})$	1.5×10^6	3.2×10^{-2}	1.1×10^5
Tribo-Oxidation A_p $(KG^2m^{-4}S^{-1})$	1.1×10^{16}	1.7×10^3	1.5×10^8
Activation Energy $(KJmole^{-1})$	208	96	210

TABLE 4.12 Oxidation Constants Derived from Caplan and Cohen (68).

Oxide	α-Fe_2O_3	Fe_3O_4	FeO
Density (KGm^{-3})	5.24×10^3	5.21×10^3	5.7×10^3
f	0.3006	0.2885	0.2277

TABLE 4.13 Oxide Data

Using the computed values of T_c, a and ξ given in Section 4.4 for the EN31 room temperature experiments, together with the Q_p values from Table 4.12, A_p values appropriate to tribo-oxidation were calculated from equation (4.22). It is important to recall that for the EN31 experiments carried out at room temperature the main constituent in the wear debris, as analysed by x-ray diffraction (Section 3.7), were as follows:-

α-Fe_2O_3	< 30N
Fe_3O_4	between 30-80N
FeO	> 80N

The tribo-oxidation A_p values for the three iron oxides calculated with the EN31 room temperature results are given in Table 4.14. Also included in this table is the average value of A_p appropriate to each oxide. An important feature of this table is the value of A_p for α-Fe_2O_3 which is six orders of magnitude less than that given by Sullivan et al. (Table 4.12 and reference 112) but the values for Fe_3O_4 and FeO are in reasonably good agreement with their work. Relevant data for ρ and f appropriate to three oxides of iron is tabulated in Table 4.13.

4.6 Modifications to the Oxidational Wear Theory

The Quinn's oxidational wear theory, described in Section 4.5, is based on the assumption that negligible oxidation occurs at those parts of the sliding interfaces not actually in contact at any given instant. However, for the study of wear at elevated temperatures, where temperatures are induced externally as well as by frictional heating, then we can no longer neglect the "out-of-contact" oxidation. In this section the oxidational wear theory is developed further to take into account the contribution to oxide thickness by oxidation of a given region whilst it is "out-of-contact".

LOAD N	T_c °C	TRIBO-OXIDATION ARRHENIUS CONSTANT (A_p) $KG^2M^{-4}S^{-1}$		
		α-Fe_2O_3	Fe_3O_4	FeO
9.8	481	6.3×10^{10}	9.8×10^{2}	
19.6	438	1.9×10^{11}	1.0×10^{3}	
24.5	498	5.8×10^{10}	1.4×10^{3}	
29.4	506	9.8×10^{9}	2.8×10^{2}	
34.3	564	3.1×10^{9}	3.2×10^{2}	
39.2	576		3.2×10^{2}	
58.9	637		2.1×10^{2}	
74.5	703		0.7×10^{2}	
98.1	675		1.5×10^{2}	2.2×10^{8}
117.7	791			1.0×10^{7}
AVERAGE VALUE (A_p)		6.4×10^{10}	5.2×10^{2}	1.2×10^{8}
STANDARD DEVIATION		6.7×10^{10}	4.7×10^{2}	1.0×10^{2}

TABLE 4.14 Values of Tribo-Oxidation Arrhenius Constant for EN31 Room Temperature Results.

Consider a pin-on-disc geometry, and assume that under a given normal load W there are N asperities in contact at any instant of equal heights and of equal circular area (πa^2), where a is the radius of contact. If we further assume a uniform distribution of these contacts, then the number of contacts per unit area is given by

$$\eta = \frac{4N}{\pi D^2} \qquad 4.23$$

where D is the diameter of the pin. During the wearing process, a given asperity (diameter d) on the pin will generate an annulus of width d on the disc wear track. Hence, it follows from equation (4.23) that the number of contacts within this annulus is

$$\eta_d = \frac{8dR_m N}{D^2} \qquad 4.24$$

where R_m is the mean radius of the wear track. See Figure 4.7. Therefore, on average, each asperity on the pin will make η_d encounters per revolution.

Let us define a factor K*, analagous to Archard's K factor (1), as the probability of producing a wear particle per revolution. Thus, we can interpret 1/K* as the number of revolutions required to produce a critical oxide film thickness ξ on any given asperity before it becomes detached to form a wear particle. Therefore, it follows from equation (4.24) that the number of encounters required to produce a wear particle is

$$\frac{1}{K} = \frac{1}{K^*} \frac{8dR_m N}{D^2} \qquad 4.25$$

Hence the probability of producing a wear particle per single encounter is given by

$$K = \frac{K^* D^2}{8dR_m N} \qquad 4.26$$

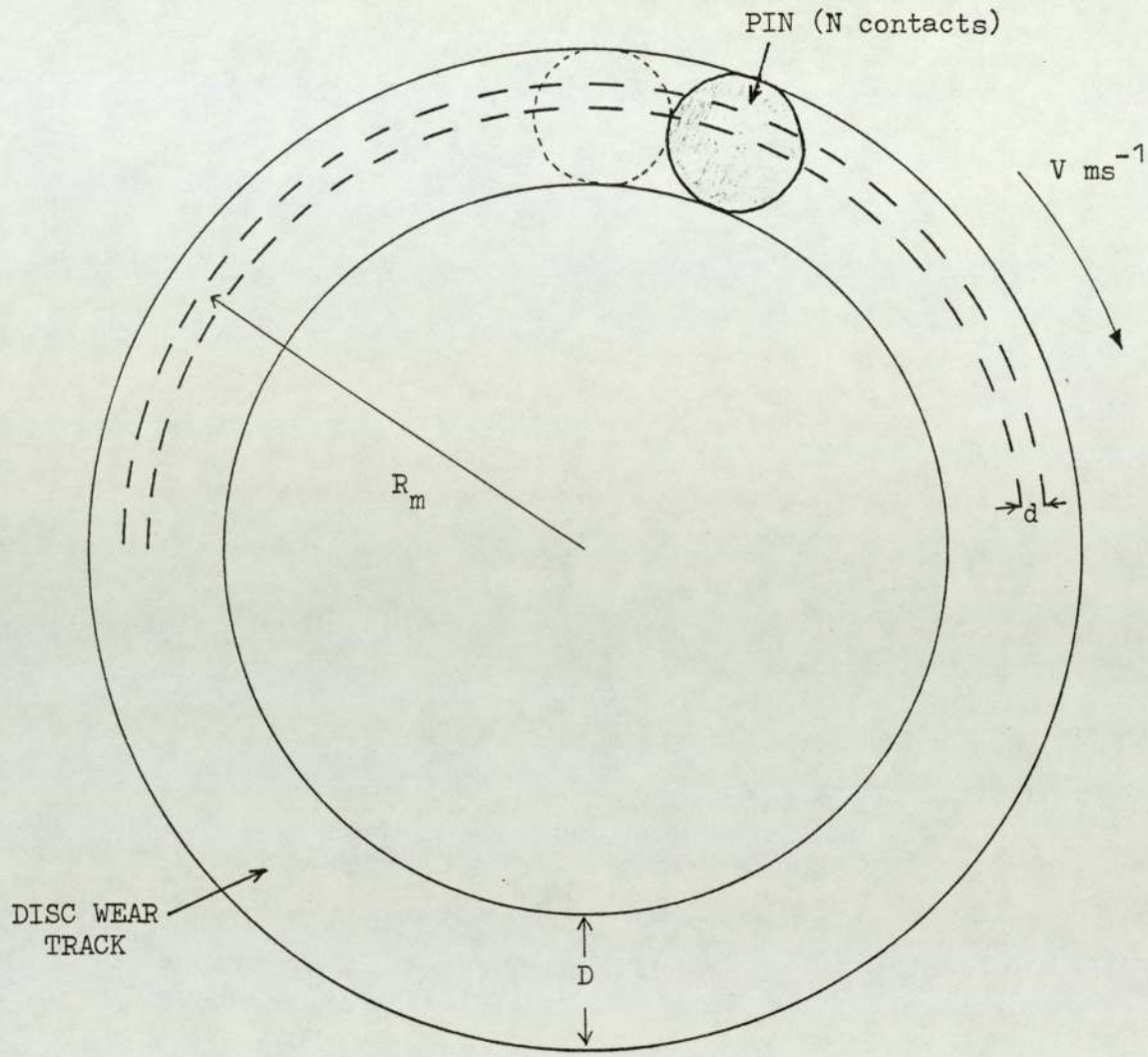

FIGURE 4.7 Pin-on-Disc Wear Geometry

It is now possible to deduce expressions for the times t_c and t_s for which the wearing asperity is at the contact temperature T_c and at the general surface temperature T_s respectively. Consider a single asperity on the pin surface. The time of oxidation at this asperity for one revolution is given by

$$t_r = t_{rc} + t_{rs} = \frac{2\pi R_m}{V} \qquad 4.27$$

where t_{rc} is the time at which the asperity is in contact, t_{rs} is the time whilst it is "out-of-contact" per revolution, and V is the linear sliding speed. Using equations (4.24) and (4.15), the contact time per revolution can be expressed as

$$t_{rc} = \frac{8R_m N}{V}\left(\frac{d}{D}\right)^2 \qquad 4.28$$

Hence, from equations (4.25) and (4.28), the total contact time t_c is

$$t_c = \frac{1}{K^*} t_{rc} = \frac{d}{VK} \qquad 4.29$$

It is interesting to note that this expression is the same as equation (4.16) and shows that the total time at contact temperature T_c is the sum of all the 1/K individual encounters each of duration d/V.

We can now obtain an expression for the time the asperity is "out-of-contact" in one revolution from equations (4.27) and (4.28), that is

$$t_{rs} = \frac{2\pi R_m}{V} - \frac{8R_m N}{V}\left(\frac{d}{D}\right)^2 \qquad 4.30$$

Hence, from equations (4.25) and (4.30), the time of oxidation at temperature T_s is given by

$$t_s = \frac{1}{K^*} t_{rs} = \frac{D^2}{4dKNV}\left\{\pi - 4N\left(\frac{d}{D}\right)^2\right\} \qquad 4.31a$$

To a good approximation it can be shown that

$$t_s = \frac{\pi D^2}{4dKNV} \qquad 4.31b$$

Let us assume that the critical oxide thickness ξ which builds up upon the asperity after $1/K^*$ revolutions is given by

$$\xi = \xi_c + \xi_s \qquad 4.32$$

where ξ_c and ξ_s are the oxide film thickness produced at temperatures T_c and T_s respectively.

For relatively thick oxide films (>0.5μm) it is reasonable to assume a parabolic rate of oxide growth at both temperatures T_c and T_s. Hence from equation (4.17) the mass uptake of oxygen per unit area at the contact temperature (Δm_c) is

$$\Delta m_c^2 = k_p(T_c)t_c \qquad 4.33$$

where $k_p(T_c)$ is the parabolic rate constant of oxidation at temperature T_c. Similarly, we can write an expression for the mass uptake of oxygen per unit area whilst the asperity is "out-of-contact" at the general surface temperature (Δm_s), namely

$$\Delta m_s^2 = k_p(T_s)t_s \qquad 4.34$$

where $k_p(T_s)$ is the parabolic rate constant at the temperature T_s. Since both the Arrhenius constant (A_p) and activation energy (Q_p) will have different values according to the temperature range (112), then the parabolic rate constants $k_p(T_c)$ and $k_p(T_s)$ can be expressed as

$$k_p(T_c) = A_p(T_c) \exp(-Q_p(T_c)/R_g T_c) \qquad 4.35$$

$$k_p(T_s) = A_p(T_s) \exp(-Q_p(T_s)/R_g T_s) \qquad 4.36$$

From equation (4.18), the mass uptake of oxygen at T_c and T_s is

$$\Delta m_c = f_c \rho_c \xi_c \qquad 4.37$$

$$\Delta m_s = f_s \rho_s \xi_s \qquad 4.38$$

Combining equations (4.32), (4.37) and (4.38) we get

$$\xi = \frac{\Delta m_c}{f_c \rho_c} + \frac{\Delta m_s}{f_s \rho_s} \qquad 4.39$$

Using equations (4.33) and (4.34), the above expression can be written as

$$\xi = \frac{(k_p(T_c)t_c)^{\frac{1}{2}}}{f_c \rho_c} + \frac{(k_p(T_s)t_s)^{\frac{1}{2}}}{f_s \rho_s} \qquad 4.40$$

By substituting for t_c and t_s from equations (4.29) and (4.31b) respectively, equation (4.40) becomes

$$\xi = \left\{\frac{k_p(T_c)d}{VK}\right\}^{\frac{1}{2}} \frac{1}{f_c \rho_c} + \left\{\frac{\pi k_p(T_s)D^2}{4dKNV}\right\}^{\frac{1}{2}} \frac{1}{f_s \rho_s} \qquad 4.41$$

Squaring this equation and rearranging to obtain an expression for K, namely

$$K = \frac{k_p(T_c)d}{Vf_c^2 \rho_c^2 \xi^2} + \frac{\pi k_p(T_s)D^2}{4dNVf_s^2 \rho_s^2 \xi^2} + \frac{D}{Vf_c \rho_c f_s \rho_s \xi^2}\left\{\frac{\pi k_p(T_c)k_p(T_s)}{N}\right\}^{\frac{1}{2}} \qquad 4.42$$

Substituting this expression for K into equation (4.14) and assuming $A = W/P_m$, the theoretical wear rate is given by

$$\omega = \frac{Wdk_p(T_c)}{P_m Vf_c^2 \rho_c^2 \xi^2} + \frac{\pi WD^2 k_p(T_s)}{4P_m dNVf_s^2 \rho_s^2 \xi^2} + \frac{WD}{VP_m f_c \rho_c f_s \rho_s \xi^2}\left\{\frac{\pi k_p(T_c)k_p(T_s)}{N}\right\}^{\frac{1}{2}} \qquad (4.43)$$

It is interesting to note that if we assume negligible "out-of-contact" oxidation, then equation (4.43) reduces to

Quinn's original expression for the wear rate given by equation (4.22). In a simplified form, equation (4.43) can be written as

$$\omega_{th} = \omega_{\alpha} + \omega_{\beta} + \omega_{\gamma} \qquad 4.44$$

where ω_{α}, ω_{β} and ω_{γ} relate to the first, second and third terms of equation (4.43) respectively.

4.7 Contribution from the "Out-of-Contact" Oxidation

In this section the contribution to the theoretical wear rate ω_{th} from the "out-of-contact" oxidation (ω_{β} and ω_{γ}) is examined.

Let us consider the EN8 experiments conducted at 200°C. From the evidence of x-ray diffraction analysis given in Section 3.7, it is possible to list the oxides produced during the "out-of-contact" oxidation at the general surface temperature T_s and at the contact temperature T_c as follows:-

"In-contact"	Fe_3O_4<40N; FeO >40N
"Out-of-contact"	α-Fe_2O_3<85N; Fe_3O_4>85N

Using the values of A_p and Q_p appropriate to the oxides produced during the contact and out-of-contact periods from Table 4.14, together with the computed values of T_c, ξ, a and N from Section 4.3, the terms ω_{α}, ω_{β} and ω_{γ} were calculated for all the 200°C EN8 experiments conducted. These are given together with experimental values of wear rate ω_{expt} in Table 4.15. Clearly, it is evident from this table that at general surface temperatures around 300°C both ω_{β} and ω_{γ} terms are comparable with ω_{α} indicating the importance of "out-of-contact" oxidation at these temperatures. Relevant data relating to f_c, ρ_c, f_s, and ρ_s (where the subscripts c and s relate to the type of oxide produced at T_c and T_s respectively) is given in Table 4.13.

Load (N)	T_s (°C)	ω_α	ω_β	ω_γ	ω_{th}	ω_{expt}
		$X10^{-13}(m^3m^{-1})$				
9.8	120	3.5	-	-	3.5	1.8
19.6	131	4.7	-	-	4.7	2.9
29.4	142	23.0	-	0.001	23.0	4.2
39.2	238	15.0	0.003	0.4	15.0	19.0
49.1	250	10.0	0.014	0.7	10.7	26.0
58.9	242	47.0	0.002	0.7	47.7	35.0
68.7	247	10.0	0.014	0.2	10.0	42.0
78.5	234	3.9	0.001	0.1	4.0	56.0
83.4	269	22.0	0.02	1.4	23.4	63.0
88.3	258	12.0	5.6	18.0	35.6	63.0
98.1	304	17.0	26.0	114.0	157.0	77.0
117.7	337	220.0	140.0	360.0	720.0	79.0
137.3	362	150.0	210.0	360.0	720.0	91.0

TABLE 4.15 Wear Rate Predicted by Oxidational Wear Theory for EN8 at 200°C

On considering the 400°C and 500°C experiments (assuming that FeO and Fe_3O_4 oxides are produced at T_c and T_s respectively), the wear rate predicted by equation (4.43) was always approximately 3-4 orders of magnitude higher than the experimental wear rate ω_{expt}. For example, using the 58.9N load results from 500°C EN8 experiment, the values calculated for ω_α, ω_β and ω_γ were 2.3×10^{-11}, 4.0×10^{-10} and $1.9 \times 10^{-10}\ m^3m^{-1}$ respectively. The experimentally measured wear rate for this load was $6.0 \times 10^{-13}\ m^3m^{-1}$.

In experiments where the major influence upon wear is from the "out-of-contact" oxidation, the important question to ask is whether most of the oxide grows at T_s. To answer this question let us consider the results from 58.9N load EN8 experiment at 500°C for the following discussion.

From equations (4.33) and (4.37) the oxide thickness after a single encounter at temperature T_c is given by

$$\xi_c = \frac{1}{f_c \rho_c} \{k_p(T_c)\tau\}^{\frac{1}{2}} \qquad 4.45$$

where $\tau = d/V$. Substituting for $k_p(T_c)$ from equation (4.35), we get

$$\xi_c = \frac{1}{f_c \rho_c} \{A_p(T_c)\exp(-Q_p(T_c)/R_g T_c)\frac{d}{V}\}^{\frac{1}{2}} \qquad 4.46$$

For the 58.9N load EN8 experiment at 500°C, T_c = 1018K, T_s = 730K and d = 8μm (i.e. $\tau = 4 \times 10^{-6}$sec.). Assuming that the oxide produced during the contact period is FeO and using the appropriate tribo-oxidation A_p values given in Table 4.14, the oxide thickness after a single encounter is

$$\xi_c \text{ (single encounter)} = 6.9 \times 10^{-8}m$$

Similarly, the oxide thickness (on the pin at temperature T_s) produced during one revolution of the disc is given by

$$\xi_s = \frac{1}{f_s \rho_s} \{A_p(T_s)\exp(-Q_p(T_s)/R_g T_s) t_r\}^{\frac{1}{2}} \qquad 4.47$$

where t_r is the time for one revolution and is equal to 0.157 seconds. Hence, assuming the "out-of-contact" oxide to be Fe_3O_4, the oxide thickness after one revolution is

$$\xi_s \text{ (one revolution)} = 2.2 \times 10^{-6}\text{m}$$

The number of encounters each asperity makes per revolution can be calculated from equation (4.24) and is about 55 for the experiment being considered in our discussion. Hence, the oxide thickness produced at T_c after 55 encounters (or one revolution) is

$$\xi_c \text{ (one revolution)} = 5.0 \times 10^{-7}\text{m}$$

Therefore we can conclude that in one revolution the contribution of ξ_s to the critical oxide film thickness ξ is approximately four times greater than that from ξ_c.

Clearly, this discussion has shown that most of the oxidation will occur during the "out-of-contact" period, i.e. the oxide film on a given asperity will reach a critical thickness after undergoing only a few encounters. Hence the oxide film produced under these conditions will have a lower degree of surface disruption (i.e. lower dislocation density and vacancy diffusivity) than that produced on a wearing surface where "out-of-contact" oxidation is negligible. Therefore under these conditions it would be more appropriate to use an Arrhenius constant which is similar to that derived from statically grown oxide films.

Using the statically derived A_p values appropriate to the oxide produced during the contact and "out-of-contact" periods (i.e. FeO and Fe_3O_4 respectively) from Table 4.14, together with the computed values of T_c, ξ, a and N from

Section 4.3, the terms ω_α, ω_β and ω_γ were calculated for both EN8 and EN31 experiments conducted at 500°C. The results are given together with experimental values of wear rate ω_{expt} in Tables 4.16 and 4.17 for EN8 and EN31 respectively.

Load (N)	ω_α	ω_β	ω_γ	ω_{th}	ω_{expt}
			X $10^{-13}(m^3m^{-1})$		
9.8	0.1	0.3	0.2	0.6	1.4
14.7	0.1	0.2	0.2	0.5	1.6
19.6	0.3	0.7	0.9	1.9	1.9
39.2	0.2	0.1	0.3	0.6	3.6
58.9	0.3	0.3	0.5	1.1	6.0
78.5	1.2	0.2	1.0	2.4	7.7
98.1	0.8	0.2	0.8	1.8	8.3
117.7	0.3	0.1	0.4	0.8	11.0

TABLE 4.16 Wear Rate Predicted by Oxidational Wear Theory for EN8 at 500°c

Load (N)	ω_α	ω_β	ω_γ	ω_{th}	ω_{expt}
	X 10^{-3} (m^3m^{-1})				
9.8	-	0.1	0.1	0.2	1.5
19.6	0.2	3.9	1.5	5.6	2.2
39.2	0.3	0.6	0.8	1.6	2.9
49.1	1.0	0.8	1.8	3.6	3.3
58.9	0.4	0.9	1.3	2.6	5.0
78.5	0.8	0.2	0.9	1.9	6.7
98.1	0.5	0.5	1.0	2.0	8.5
107.9	1.0	1.1	2.1	4.2	8.6
117.7	1.4	0.4	1.4	3.2	7.6
137.3	1.8	0.5	1.9	4.3	13.0
157.0	1.1	0.4	1.3	2.8	17.0

TABLE 4.17 Wear Rate Predicted by Oxidational Wear Theory for EN31 at 500°C

CHAPTER 5

DISCUSSION

5.1 Introduction

The wear of EN8 and EN31 steels is discussed in Section 5.2 with reference to scanning electron microscopy, x-ray diffraction and heat flow results reported in Chapter 3.

In Section 5.3, the friction results are explained in terms of the adhesion theory.

Hardness and subsurface observations are discussed in Section 5.4 in relation to work-hardening and phase transformation of the subsurface layers.

Discussion of surface parameters in relation to wear and previous investigations is given in Section 5.5. In addition, the effect of taking the physical properties of the oxide at any other temperature between T_s and T_c in the theoretical analysis is considered.

The relative importance of static and tribo-oxidation Arrhenius constants for oxidation in wear at different ambient temperatures is discussed in Section 5.6.

Finally, Section 5.7 brings together all the points from the early sections in an attempt to form an hypothesis on the mechanisms of the mild wear of low alloy steels.

5.2 Wear Behaviour

Under all the conditions of unlubricated sliding investigated in this work the wear mechanism was oxidational.

5.2.1 Wear of EN8

For the experiments carried out at room temperature (without external heating) scanning electron microscopy (Figure 3.41) showed that the pin surface was covered with a thin oxide film ($<1.0\mu m$). X-ray data revealed that the oxide was FeO and the presence of α-Fe in the debris indicated that the oxide film is broken down ocassionally giving rise to some intermetallic contact. Since the general surface temperature for all loads was less than 250°C, the presence of FeO in the debris and on the surface indicated that temperatures in excess of 570°C had been reached at the real areas of contact. The results reported by Dunckley (93, 113) for EN8 steel sliding against itself at $2ms^{-1}$ without external heating are consistent with the present work. Dunckley found no transitions in the wear curve and the debris consisted of FeO and α-Fe.

The wear behaviour at 100°C was characterised by two distinct wear regimes, the transition between these two regimes occurring at a load of 10N (Figure 3.1(a)). In the experiments carried out at loads above 10N the appearance of worn surfaces was similar to that found in the room temperature experiments, and the debris consisted of FeO and α-Fe. But at loads below 10N the worn surfaces were heavily oxidised and x-ray diffraction analysis revealed that both debris and surface oxides consist of an Fe_3O_4, α-Fe_2O_3 mixture. Also in comparison with the room temperature results the amount of α-Fe present in the debris was considerably less. Hence for the experiments carried out at loads below 10N the greater rate of out-of-contact oxidation induced by external heating reduces the degree of intermetallic contact between the surfaces.

The effect of increasing the bulk disc temperature to 200°C was to increase the transition observed

at 100°C to 35N (Figure 3.1(a)). Similarly, Lancaster (34) found that a transition in the wear rate versus load curve (i.e. mild to severe) of 60/40 brass sliding on hardened tool steel occurs at a critical load, the magnitude of which increases with the temperature. Lancaster suggested that an increase in surface temperature facilitates the formation of a protective oxide film. This work tends to support this view. For loads less than 35N the worn surfaces were covered with an oxide film and damage occurring at relatively few areas (Figures 3.43(a) and 3.44(a)). The debris was almost entirely oxidised and consisted of α-Fe_2O_3 and Fe_3O_4, but traces of α-Fe were also found. Microdensitometer measurements showed that the amount of Fe_3O_4 present in the debris was appreciably greater than that present in the 100°C experiments carried out below the transition load of 10N. Numerous workers (61-63) have shown that Fe_3O_4 is associated with good surface protection and hence is more beneficial on wear reduction than α-Fe_2O_3.

For the 200°C experiments carried out at loads greater than 35N the worn surfaces had only sparse covering of oxide. The debris consisted of FeO, Fe_3O_4, α-Fe_2O_3 and α-Fe, with FeO becoming more predominant as the load increased and no α-Fe_2O_3 was detected at loads greater than 85N. Microdensitometer results showed that compared with the 200°C experiments carried out at loads below 35N the amount of α-Fe present in the debris had increased, indicating there is some intermetallic contact. Compared with the room temperature experiments however, the main α-Fe diffraction lines are weaker indicating that greater proportion of the wear particles are in fact oxides. Although frictional heating (H_T) increased steadily with load, the rate of heat flow H_1 along the pin at the sliding interface increased abruptly at 35N (Table 3.3), confirming that there was some intermetallic contact. Consequently there was a sudden increase in general surface temperature T_s of the pin at this load, as shown in Figure 3.10. However, it must be noted that the abrupt increase in H_1 at 35N may also be due to the fall in oxide thickness at this load (Figure 4.5(b)) since this will allow more heat

to be conducted through the asperities of the pin.

X-ray diffraction examination of the wear debris revealed that for the 300°C experiments carried out at loads up to 88.3N the main constituents in the debris were α-Fe_2O_3 and Fe_3O_4. At 98.1N load the wear rate increased dramatically (Figure 3.1(a)). The debris changed character and consisted of predominantly FeO and α-Fe. An SEM micrograph of the pin from this particular load (Figure 3.46(b)) showed the surface was relatively free from an oxide film. In contrast, SEM micrographs taken from experiments carried out below the transition showed heavily oxidised surfaces. Unfortunately no heat flow data was recorded for the 98.1N experiment because both thermocouples T_A and T_B (see Figure 2.3) came loose during the running-in period. Nevertheless, the appearance of FeO on the surface and in the debris indicates that a sudden increase in T_s and H_1 is expected at this load similar to that observed in the 200°C experiment at a load of 39.2N. Furthermore, the reduction of oxide film will result in more heat being conducted into the pin with a consequent sudden increase in the general surface temperature of the pin. Similar transitions in the wear rate, T_s and H_1 have been reported by Quinn et al. (105, 112) in their work on the wear of low alloy steels. They have attributed the transitional behaviour to changes in the oxide phases formed during wear, and found that high wear rates were associated with FeO and α-Fe_2O_3. Hence the transition observed in the wear rate versus load curve for the 100°C, 200°C and 300°C experiments is attributed to the appearance of significant amounts of FeO on the sliding surfaces.

In the experiments conducted at disc temperatures of 400°C and 500°C the wear rate versus load curve showed no transition over the load range covered by this investigation. At all loads the worn surfaces were covered with an oxide film and the debris was entirely oxide. X-ray diffraction analysis revealed that both debris and surface oxides consist of an Fe_3O_4, α-Fe_2O_3 mixture. Heat flow analysis showed that at low loads the general surface

temperature of the pin T_s was lower than the disc temperature, the latter was kept constant by external heating. This was due to the fact that the oxide film present on the pin surface reduces the heat flow through the contacting pin asperities. One surprising feature of these higher temperature experiments was that proportional analysis showed that the major oxide constituent was α-Fe_2O_3 in a region where one would expect more Fe_3O_4 to be present in the mixture. Similarly, Dunckley (113) found that compared with the low temperature experiments the debris from the experiments conducted at 500°C contained a much higher proportion of α-Fe_2O_3 oxide. X-ray photoelectron spectroscopy study of Fe_3O_4 (114) has shown that oxidation in air can occur to a significant extent to convert this oxide to α-Fe_2O_3. Therefore it may be concluded that the predominant oxide produced at the general surface temperature is Fe_3O_4 but this oxide degenerates to α-Fe_2O_3. Support for this was found in the visual examination of the wear debris from these experiments which showed a change in colour from dark brown to red on cooling to room temperature. The same arguments apply to the EN31 experiments conducted at these temperatures.

5.2.2 Wear of EN31

The wear behaviour at room temperature and 100°C was characterised by three distinct wear regimes (Figure 3.2(a)), and the transitions between these regimes were found to be associated with change in the type of oxide formed on the surface and consequently present in the debris. In the first wear regime, occurring at loads below 30N, x-ray diffraction analysis showed that the predominant oxide was α-Fe_2O_3. SEM analysis showed the surface covered with oxide plateaux, smooth due to wear, standing above relatively rough debris covered metallic areas (Figure 3.45(a)). That the plateaux are in fact oxide and not metal with an oxide covering is confirmed by the results of the Auger spectroscopy. Upon increasing the load, these oxide plateaux grow in size until in the second wear regime, occurring between 30-80N, an almost single

oxide layer covers the whole pin surface with very little disruption (Figure 3.48(b)). X-ray data showed that the debris in this region was predominantly Fe_3O_4. Clearly the good wear reduction properties of this oxide explains the lower wear rates observed in the second wear regime. In the third wear regime, occurring at loads greater than 80N, the debris was predominantly FeO. SEM studies showed that at these loads the surface had only a sparse covering of oxide (Figure 3.48(c)). Hence the change in topography suggests that FeO is probably far less adherent than either α-Fe_2O_3 or Fe_3O_4.

It is interesting to note that for the room temperature and 100°C experiments T_s varied with load (Figure 3.12) in a similar fashion to the variation of wear rate with load. In particular, when there was an abrupt change in the wear rate due to a change in wear regime, there was also an abrupt change in T_s. Clearly this is due to the change in surface conductance (i.e. oxide coverage) which accompanies any change in wear regime. For example, the thicker films and better surface coverage of the Fe_3O_4 oxide in the second wear regime result in less heat being conducted into the pin. Consequently there is a sudden decrease in the bulk surface pin temperature when this oxide is present.

The effect of elevating the disc temperature to 200°C produced a significant change in the wear behaviour of EN31 (Figure 3.2(b)). Only a single transition occurred in the wear curve at a load of little over 80N. For loads below the transition the constituents of the wear debris as analysed by x-ray diffraction was a mixture of α-Fe_2O_3, Fe_3O_4 and α-Fe. Compared with the room temperature and 100°C experiments carried out at loads below 80N the amount of α-Fe_2O_3 present in the debris had increased due to the increased out-of-contact oxidation. It is also worth noting that for these loads the composition of the debris was very similar to the debris from 200°C EN8 experiments carried out at loads below 35N, thus indicating a similar wear mechanism. For the 200°C experiments carried out at loads immediately above the transition, the debris consisted

of Feo, Fe_3O_4, α-Fe_2O_3 and α-Fe. As the load increased Feo became more predominant and at the higher loads α-Fe_2O_3 was barely detectable. SEM analysis of worn surfaces from experiments carried out at loads below the transition showed the surface covered with an oxide film with damage occurring only in relatively few areas. In contrast, SEM micrographs of worn surfaces taken from experiments carried out at loads above the transition showed the surface had only a sparse covering of an oxide film, thus increasing the possibility of metallic contact between the two surfaces.

In the experiments conducted at 300°C the transition occurred in the wear rate versus load curve at a load of 135N. Unlike the lower temperature experiments however no FeO was detected either in the debris or on the surface at loads above the transition. That is, at all loads both debris and surface oxides consisted of an Fe_3O_4, α-Fe_2O_3 mixture (Figure 3.29). This is because the majority of oxide is formed during the out-of-contact periods at the general surface temperature. However, the magnitude of the wear rate at loads greater than 135N (in relation to the 200°C wear results) suggests that FeO is probably produced in the wearing situation but due to relatively slow cooling of the contacts this oxide degenerates to the lower oxides. This is discussed in detail in Section 5.5.

In the experiments conducted at disc temperatures of 400°C and 500°C SEM analysis showed that worn surfaces were covered with an oxide film (Figure 3.51), the thickness of which increased from about 2μm at low loads to about 5μm at high loads. As in the case of EN8 experiments the general pin surface temperature at low loads is lower than the disc temperature because of the presence of this oxide film. X-ray diffraction analysis showed that both debris and surface oxides consist of an Fe_3O_4, α-Fe_2O_3 mixture. The absence of FeO in these experiments even though very high temperatures are reached at the real areas of contact is explained in Section 5.5.

5.3 Friction

At the start of each experiment the coefficient of friction μ was comparatively large, and the wear was of the severe metallic form. However, frictional heating (and external heating in elevated temperature experiments) caused rapid oxidation of the surfaces which resulted in a rapid decrease in μ and the wear rate decreased by well over 2 orders of magnitude. This running in phase was not studied in detail.

In general, the results show that μ peaked at low loads and then tended to decrease with increasing load (Figures 3.5 and 3.6). A similar reduction of μ with load for the unlubricated sliding steels has been reported by many workers (72, 93, 102). If μ is taken as the ratio of the shear strength s_f of the junction and the substrate hardness P_m (equation 1.14), the temperature applicable to s_f is the contact temperature T_c whereas the general surface temperature T_s will be applicable to P_m (6). Since both T_c and T_s increase in a similar manner with load, and because both the shear strength and the hardness terms tend to vary with temperature in the same manner (6), this indicates that μ should be insensitive to load variation. Talysurf analysis of worn surfaces show the surfaces are generally rougher at low loads because at higher loads the contacting asperities become flattened under the influence of the applied load. Hence, this suggests that the gradual decrease in μ with load is probably due to the reduction in the contribution of the ploughing component to the frictional force as the load increases. But it must be noted that the fall in μ may also be due to the greater amount of oxidation at the real areas of contact resulting from the increased frictional heating at higher loads (87).

For both EN8 and EN31 steels at any given load, μ decreases with increasing bulk temperature of the disc (Figures 3.7 and 3.8). This decrease is attributed to the formation of protective oxide films between the two rubbing surfaces, that is, the effective shear strength of the interface s_f is reduced with increasing oxide coverage as the temperature increases.

It is interesting to note that unlike the wear results no transitions were found in the corresponding friction results. This indicates that although friction is a surface effect it does not vary much from one oxide to another.

5.4 Hardness and Subsurface Observations

Metallographic examination of pin surface revealed that an oxide layer existed between the bakelite and the bulk material (Figure 3.56). Microhardness measurement indicated that the hardness of this layer (480 - 567 VPN) is the same as that measured on the oxidised region of the pin surface. The thickness of this layer (as calculated from the angle of taper) is of the same order as the measured thickness of the oxide film when the surface was directly examined using the SEM. For experiments conducted at room temperature and elevated temperatures below 400°C, the microhardness measurements of the substrate just below this oxide layer gave hardness values greater than 400 VPN, due to work-hardening (Figures 3.18 and 3.19). According to Welsh (39), during running-in the hardness of the metal surface increases until a critical hardness dependent on the material composition is exceeded. This hardness (normally in the range of 340 to 425 VPN for steels) indicates that the substrate possesses the strength necessary to support an oxide film. Hence, the experimental evidence suggests that at ambient temperatures below 400°C mild oxidational wear occurs by the removal of oxide debris from an oxide film supported on a work-hardened substrate.

At disc temperatures of 400°C and 500°C there was no evidence of subsurface hardening of the pin, due possibly to less work-hardening of subsurface layers at these temperatures. SEM micrographs taken of tapered sections of samples from these experiments appears to show surface

grooves, produced during the initial running-in period, covered with oxide (Figures 3.58 and 3.59). The separation of these grooves compares reasonably well with the talysurf profiles given in Figures 3.20 and 3.21. The hardness of these regions could not be obtained even at the smallest indenter load because the surface cracked under the load. Similar problems were encountered when the microhardness of the oxide on the surface was measured. Hence this confirms that these regions are indeed oxide. For both EN8 and EN31 the hardness of the substrate just below the oxide is of the order of the original bulk hardness value. It is worth recalling that the wear mechanism at these temperatures was purely oxidational. Therefore it may be concluded that at elevated temperatures the rate of oxidation is more important than the subsurface hardness changes for the onset of mild wear.

At high loads and low ambient temperatures, metallographic examination of pin surfaces revealed severe plastic flow of subsurface material in the direction of sliding (Figure 3.57). Microhardness measurements of the subsurface indicated it to be extremely work-hardened. Values of up to 927 VPN were recorded, the majority of the readings falling within the range 700-800 VPN. Several workers (38, 43, 115) have shown evidence that ferrous surfaces, rubbed under practical conditions or in test equipment, can produce gross structural changes and intense hardening of the surface layers. Welsh (38) suggested that this hard phase represented material transformed to austenite by local temperatures above the $\alpha - \gamma$ transformation point and then converted to martensite by rapid cooling. Examination of the pins using a glancing angle x-ray diffraction technique revealed that the subsurface layers of some pins contained austenite. It may therefore be concluded that during wear process the contacting asperities are raised very quickly to austenitisation temperatures, typically in 10^{-3} and 10^{-4} seconds (6), and when contact ceases these asperities are quenched very rapidly by the colder sublayers. A minimum temperature of about 730°C would be required to give hardening in this way. The results emerging from the theoretical analysis given in Section 4.2

clearly show that temperatures of such magnitude are readily attained at the contact areas during the wear process.

Microhardness measurements showed that the hardness decreases with depth below the surface (Figures 3.18 and 3.19) until the original hardness of the substrate is reached, that is, 250 VPN and 280 VPN for EN8 and EN31 respectively. The depth to which the subsurface is work-harden increases with load. Eyre and Baxter (116) have reported similar microhardness versus depth results for a 0.24% carbon steel.

5.5 Surface Parameters in Relation to Wear

An important feature emerging from the theoretical analysis is that there appears to be some correlation between the predicted contact temperature T_c and the oxide phases present on the surface and in the wear debris. For example, the predicted contact temperatures exceed 600°C when FeO is present in the debris. It is known that FeO forms at temperatures of 570°C and above. It is also possible to find transitions in the values of T_c corresponding to transitions in the wear rate due to change in oxide. For example, in EN31 experiments conducted at room temperature transitions occur at about 30N (α-Fe_2O_3 to Fe_3O_4) and 80N (Fe_3O_4 to FeO). The results show that slightly higher contact temperatures are to be expected if the oxide present is Fe_3O_4 (or Fe_3O_4/α-Fe_2O_3 mixture) since this oxide forms a thicker film with better coverage.

Confirmation that the predicted T_c values of around 750°C at high loads are of the correct order of magnitude was found in the presence of austenite in the subsurface layers of the pins from these experiments. However, in some of the experiments in which austenite was detected, the predicted T_c value was only around 700°C (e.g. 137.3N EN31 experiment at 200°C). It must, however, be appreciated that calculations of this type only give an indication of the magnitude of the temperatures at contacting

asperities. Furthermore, the predicted T_c value is the average contact temperature of the contacting asperities, since changes in the coefficient of friction with sliding distance and variation of oxide film thickness are not considered. Hence, the maximum temperature developed during sliding at some contacting asperities may be well in excess of 700°C.

For the experiments conducted at disc temperatures of 300°C, 400°C and 500°C the contact temperature values indicated that FeO should be present on the surface and in the wear debris. However, only the low temperature oxides α- Fe_2O_3 and Fe_3O_4 were detected. There are two reasons for this result. The first is that in order for FeO to be retained the oxide must be quenched very rapidly. If the surface temperature is low rapid quenching occurs after asperity contact and FeO is retained, but if surface temperatures are high then relatively slow cooling of the contacts occurs and FeO degenerates to α-Fe_2O_3 and Fe_3O_4, leaving only these oxides in the debris and on the surface. If this were the only process occurring, however, high wear rates associated with the FeO oxide would be expected in this temperature range when in fact wear rates are relatively low. Thus, the most important reason for the Fe_3O_4 α-Fe_2O_3 mixture being found in this temperature range is that the majority of surface oxidation occurs out-of-contact at the general surface temperature.

Another important feature emerging from this work is the increase in the number of contacting asperities N beneath the pin with increasing applied load. In addition, the results indicate that the number of contacts increase with bulk disc temperature. The rapid increase in N at higher loads is due to the fall in the hardness P_m of the substrate at temperatures greater than 300°C (Figure 2.5). However, for the experiments conducted at 500°C no deviation from linearity was observed in the N versus load graph due to the small increase in T_s with increasing load, i.e. P_m does not vary greatly.

It is interesting to note that the contact radius showed a small decrease with increasing load and under all experimental conditions was found to lie within the 2-7μm range. These computed values of contact radii are in good agreement with those reported by Quinn et. al.(105) for EN8 steel using an interative technique based upon the oxidational wear theory. They suggested that the contact radius of each asperity contact is approximately constant for a given material combination (and possibly for a given range of oxide formation). It was also suggested that the number of contacts is linearly dependent upon the load for a given oxide range. Rabinowicz (7) reports that the contact radius for copper and steel surfaces, as determined by a number of different methods, varies over a narrow range from 3μm to 15μm approximately. Kragelskii (3) has shown that contact points increase in number to a much greater extent than does the area of a single contact (i.e. πa^2). Archard and Hirst (2) have reached the same conclusion, that there is little change in the area of the individual contact points when the load is increased by N increases.

The predicted values of oxide film thickness show very good agreement with measured values using a scanning electron microscope. In general, both sets of results show an increase in thickness with increased load with obvious transitions where there has been a change in oxide type.

If the temperature-dependent physical properties of the oxide (K_o and χ_o) are taken at any other temperature between T_c and T_s, then the predicted values of contact temperature and oxide film thickness are higher than the values predicted if the properties are chosen corresponding to the contact temperature. The predicted values of T_c, ξ, a, N and δ_{th} for EN31 experiments carried out at room temperature when physical properties of the oxide are taken at half way between the contact temperature and general surface temperature are given in Table 5.1. It is clear from this table and Figure 5.1 that the predicted values of T_c are approximately 400°C higher than the values pred-

LOAD (N)	N	a (μm)	T_c ($^{\circ}$C)	ζ (μm)	δ_{th} (%)	δ_{expt} (%)
9.8	29	6.6	882	6.5	8.6	8.5
19.6	76	5.8	904	5.0	12.4	11.4
24.5	76	6.5	877	9.5	7.3	6.8
29.4	133	5.4	882	4.5	15.2	13.9
34.3	172	5.1	1138	9.0	8.9	8.5
39.2	197	5.1	1160	10.0	7.7	7.3
58.9	291	5.1	1145	12.5	7.0	6.7
78.5	389	5.1	1120	13.0	6.6	6.1
98.1	590	4.6	1135	10.0	9.3	8.4
117.7	879	4.2	1076	6.5	14.0	11.7

TABLE 5.1 Predicted Values of Surface Parameters when the Physical Properties are taken at $(T_c+T_s) / 2$ for EN31 at Room Temperature.

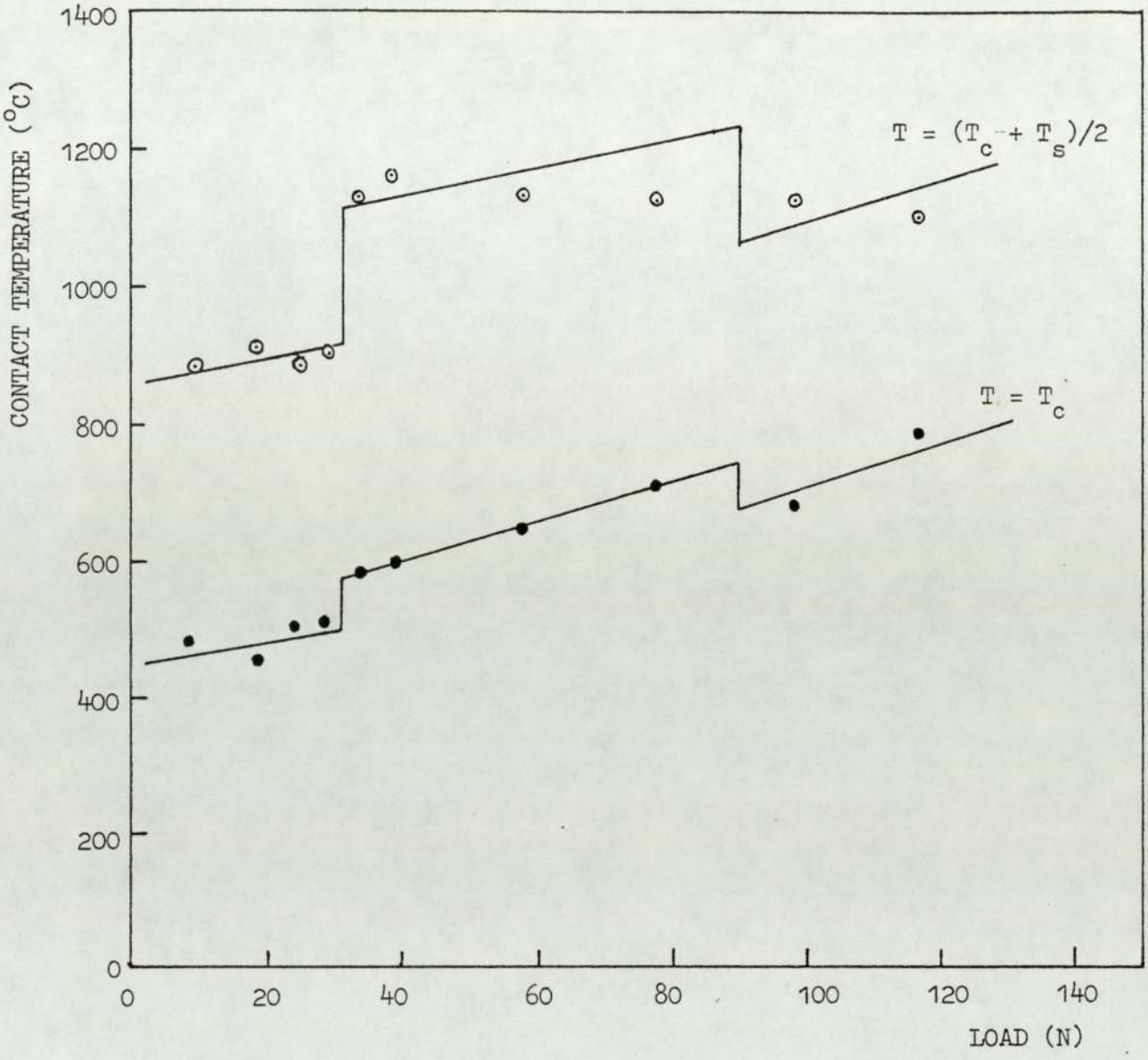

FIGURE 5.1 Predicted Values of Contact Temperature when the Physical Properties of the Oxide are taken at half way between the Contact and General Surface Temperature.

icted when the physical properties are taken at the contact temperature. It was found that as the temperature at which the properties are chosen varies from T_c to T_s, the predicted values of T_c and ξ gradually increase and they reach a maximum value (i.e. $T_c > 6000^{\circ}C$, $\xi > 100\mu m$) when the physical properties are taken corresponding to the general surface temperature. Earles and Powell (41, 84, 85) showed, using the Jaeger-Archard flash temperature theory, that if the temperature dependent properties are taken corresponding to room temperature, then the predicted flash temperatures (and therefore the contact temperatures) are too high for their physical significance to be explained. Alternatively, they showed that if it is postulated that the properties should be taken corresponding to the contact temperature of the asperities, then the predicted contact temperatures are lower than those which are known to occur from evidence provided by thermocouple measurements of subsurface temperatures. Earles and Powell proposed that the physical properties should be taken at the temperature of the substrate just below the asperities, that is, at the general surface temperature. But Cocks suggested in the discussion of (84) that the "correct" temperature at which to determine the physical properties of the asperity should be somewhere between the general surface temperature and the contact temperature. However, it is important to note that in their analysis Earles and Powell ignored the effect of an oxide film, which they otherwise demonstrated is present on the rubbing surfaces. This tends to invalidate their calculations because the thermal properties of a thin surface layer can have a marked influence on the temperature of the surface (80). For example, the presence of a low thermal conductivity film such as an oxide film will increase the surface temperature. The findings of this investigation show that in order to predict surface parameters which give a reasonable representation of the processes occurring at the sliding surface then the temperature dependent properties of the oxide and substrate should be taken at the contact (or something very near to this) and general surface temperature respectively.

5.6 Oxidation in Wear

Under conditions of mild oxidational wear the growth of the oxide film is controlled by a parabolic rate law (47). This involves the inward diffusion of oxygen ions and the outward diffusion of metal ions (67). The Arrhenius constant (A_p) and the activation energy (Q_p) for parabolic oxidation will both depend on the type of oxide which is predominant in the wear process. Sullivan et alia (112) have shown that although the activation energy is not expected to differ in static and tribological conditions, the corresponding Arrhenius constant (which depends on surface conditioning, void and dislocation and other factors (67)) will be very different in the tribological situation.

The findings of this investigation suggests that the relative importance of static and tribo-oxidation Arrhenius constants for oxidation in wear at different ambient temperatures is as follows. Since at low ambient temperatures the majority of the oxide is formed at the contact temperature, the crystalline structure of the oxide film is greatly disrupted due to the mechanical and thermal stresses associated with the rubbing action. The number of dislocations, the number of vacancies and their mobility will be large. Therefore the rate of growth of the oxide film is quite different to that measured under static conditions. Thus under these conditions the Arrhenius constant deduced for tribo-oxidation (Table 4.14) is applicable to oxidation during wear. At high ambient temperatures, however, most of the oxidation on a given asperity occurs during the out-of-contact period at the general surface temperature. Therefore the oxide produced under these conditions will have a lower degree of surface disruption (due to the reduction in mechanical and thermal stresses) than that produced entirely at the contact temperature. Thus in tribological situations where the majority of the oxide is formed out-of-contact at the general surface temperature it is more appropriate to use an Arrhenius constant which is similar to that derived from static oxidation experiments.

5.7 General Discussion on the Mild Wear of Steels

Under all loads and temperature conditions investigated in this work the mechanism which was prevalent in the wear process was mild oxidational wear. The transition from one wear regime to another was found to be associated with change in the type of oxide formed on the surface. The results show that Fe_3O_4 gives better protection and hence lower wear rates than either α-Fe_2O_3 or FeO. Considering, for example, the EN31 experiments conducted at room temperature (Figure 3.2(a)) the predominant oxide below the first transition is α-Fe_2O_3. The transition then corresponds to a change in oxide type of Fe_3O_4. The second transition corresponds to the appearance of significant amounts of FeO at the wearing surface. Similarly the transition associated with the 200°C and 300°C experiments correspond to changes from region of Fe_3O_4 and α-Fe_2O_3 mixtures to regions containing FeO. If the portion of the wear rate versus load curve for the EN31 room temperature experiments corresponding to the α-Fe_2O_3 region, below 30N is extrapolated into the Fe_3O_4 region a wear rate of approximately twice the measured value might be expected. That is, under similar conditions if it were possible to have either α-Fe_2O_3 or Fe_3O_4 present then the latter would be expected to have an associated wear rate equal to half of the former. The same observation is true when significant amounts of FeO appear in the debris, that is after the second transition. As can be seen from the room temperature, 200°C and 300°C curves of Figures 3.2(a) and (b) an increase in wear rates of approximately two times is apparent. Scanning electron microscopy studies showed that Fe_3O_4 forms a thicker oxide film with greater surface coverage and less disruption than does either α-Fe_2O_3 or FeO. This better coverage and increased film thickness undoubtedly combine to give the oxide containing Fe_3O_4 a greater protective capability.

The differences in wear behaviour between EN8 and EN31 low alloy steels is probably due to the small amount of chromium present in the latter. The presence of chromium

tends to suppress the formation of the FeO and tends to push the Fe_3O_4-FeO transition to higher temperatures and hence higher loads. For example, FeO was detected in all the EN8 experiments carried out at room temperature. It is interesting to note that the predicted values of contact temperature for these experiments are around 600°C. However, in the case of EN31 experiments carried out under similar conditions significant amounts of FeO was only detected at loads greater than 80N when the predicted values of contact temperature exceeded 675°C.

The experimental evidence suggests that the mechanism of oxidational wear particle formation is similar to that described by Quinn (44) in which an oxide film of critical thickness is formed and then becomes detached due to a fatigue process involving thermal and mechanical stresses at the oxide-metal interface. At low ambient temperatures the important temperature which controls wear is that of the contact, that is the majority of the oxide is formed at the contact temperature (or something very near to this). This is consistent with the results reported by Kawamoto and Okabayashi (117) who showed that when the mean surface temperature is relatively low (e.g. below about 200°C-250°C for carbon steels) then wear mainly depends on the contact temperature. As the ambient temperature increases, however, the out-of-contact oxidation becomes increasingly important and this eventually becomes the predominant controlling mechanism at temperatures above 300°C. One feature that shows this is so is the movement of the transition to higher loads as disc temperature increases and eventually disappearing altogether at 400°C and 500°C. The only explanation for this is the increasing out-of-contact oxide formed at the general surface temperature. If out-of-contact oxidation was not taking place, that is only T_c important, then the transition load would move in the opposite direction with temperature. Thus, although high contact temperatures are achieved in the experiments conducted at 400°C and 500°C, the majority of oxide is formed at T_s giving the protective predominantly Fe_3O_4 layer and consequently low wear rates.

It is interesting to note that results obtained from the modified oxidational wear theory (Table 4.15) clearly show that the out-of-contact oxidation becomes important at T_s greater than about 300°C.

CHAPTER 6

CONCLUSIONS

Using a pin on disc wear test rig experiments were conducted on the mild wear of EN8 and EN31 steels at loads varying from 5 to 160N and at disc temperatures up to 500°C. It was found that transitions occur in the wear rate versus load curves at certain critical loads, the magnitude of which increase with temperature. Powder x-ray diffraction analysis of debris and glancing angle x-ray diffraction analysis of the surfaces show that these transitions in wear rate correspond to changes in oxide composition. The spinel oxide Fe_3O_4 was found to give better protection than either the rhombohedral oxide α-Fe_2O_3 or the wustite FeO; estimated wear rate being a factor of two lower when Fe_3O_4 was present. Surface examination showed that the spinel oxide produced thicker films with greater surface coverage and less disruption. In contrast, the appearance of the surfaces where the predominant oxide was either α-Fe_2O_3 or Fe_3O_4 was very similar. That is, they consist of patchy oxide plateaux, smooth due to wear, above relatively rough debris covered metallic areas.

The fact that the transition load increased with temperature and disappeared at temperatures of 400°C and 500°C indicates the increasing importance of out-of-contact oxidation (occurring at the general surface temperature) with increase in temperature and this eventually becomes the dominant mechanism at temperatures above 300°C. Scanning electron micrographs of surfaces generated in both EN8 and EN31 experiments conducted at 400°C and 500°C show remarkably similar surface characteristics. For both materials the surfaces were smooth and heavily oxidised with damage occurring by removal of flake like particles from the oxide film. This is a typical feature of oxidational wear.

The results from the modified oxidational wear theory supports the experimental finding that out-of-contact oxidation becomes important at general surface temperatures greater than about 300°C.

At high ambient temperatures (i.e. 300°C - 500°C) all the FeO produced in the wearing situation degenerates to α-Fe_2O_3 and Fe_3O_4 due to the relatively slow cooling of the contacts, leaving only these oxides in the debris and on the surface. In addition, at these temperatures the predominant oxide produced at the general surface temperature is Fe_3O_4 but oxidation in air can occur to convert most of this oxide to α-Fe_2O_3.

In tribological conditions where the important temperature in oxide formation is that of the contact, the appropriate Arrhenius constant which is applicable to the rate of growth of the oxide film is that deduced for tribo-oxidation. However, if most of the oxidation occurs at the general surface temperature then Arrhenius constant derived from static oxidation experiments may be applied to tribological situations.

For both the steels investigated in this work the coefficient of friction μ decreases with increasing load and temperature. The gradual decrease in μ with load is probably due to the reduction in the contribution of the ploughing component to the frictional force as the load increases, whereas the decrease in μ with temperature is attributed to the formation of protective oxide film between the two rubbing surfaces. Although friction is a surface effect the results show that it does not vary much from one oxide type to another.

Scanning electron microscopy of wear debris from all the experiments showed it to consist of laminar particles varying in size to about 200μm. The thickness of these particles was found to lie within the range of measured values of oxide film thickness on pin and disc surfaces, that is, between 1 and 5μm.

An important feature borne out by the heat flow analysis is the similarities between the variations of wear rate and general surface temperature (T_s) with load. Abrupt changes in wear rate are always accompanied by abrupt changes in T_s. This is due to the change in surface conductance which accompanies any change in wear regime. For elevated temperatures consideration must also be given to heat flow through the air gap between the pin and disc. This only occurs in tribological conditions where the general surface temperature of the pin is lower than that of the disc. Calculations indicate that although convection and radiation effects are negligible, there is a considerable contribution to heat flow into the pin from conduction through the air gap. Hence under these conditions the experimentally measured heat flow (H_1) entering the pin consists of a measured component due to conduction through the contacting asperities plus a component due to conduction through the air gap.

Microhardness measurements show that during sliding the subsurface is work-hardened to a depth which increases with load. In addition, the technique of glancing angle x-ray diffraction revealed the presence of austenite in the subsurface layers of some of the samples, indicating that temperatures in excess of 730°C had been attained at the contact areas during the wear process. At disc temperatures of 400°C and 500°C the rate of oxidation is more important than the subsurface hardness changes for the onset of mild wear.

In the recent past there has been some controversy about the nature of the plateaux observed in experiments of this type. Questions have been raised as to whether they consisted entirely of oxide or whether they were metallic with a thin oxide coating. The work described here using scanning Auger spectroscopy clearly shows that these plateaux are entirely oxide.

Before any conclusions can be drawn on the proportional analysis of wear debris more work is required. A possible area of further work is the proportional analysis of pre-

mixed samples using a diffractometer. Since the diffractometer needs a much larger sample than the powder camera this will reduce any uncertainties in sample preparations. Hence the results should be more reliable.

The theoretical analysis developed in order to estimate values of otherwise unobtainable parameters was thought to have produced successful results since not only did estimated contact temperatures correspond to those expected for the oxides produced on the surface, but the values of oxide thickness obtained show very good agreement with measured values. In addition, it is possible to find transition in the values of contact temperature and oxide film thickness corresponding to transitions in the wear rate when type of oxide formed on the surface changes. The number of contacts (N) is found to increase both with load and temperature but the corresponding values for the contact radius only show a little change.

In conclusion, the experimentally measured results and theoretically deduced surface parameters presented in this work seem to give a reasonable representation of the processes occurring at the sliding surfaces.

Clearly, in order to understand more fully the unlubricated wear of low alloy steels at elevated temperatures more work is required along the lines of this present investigation. The recommendations for future work are to investigate the wear behaviour of these steels at different sliding speeds and at high ambient temperatures in a region where the predominant oxide produced at the general surface temperature is expected to be FeO. The findings of this present study suggests that the presence of chromium in steels may have a marked effect on their wear behaviour. Hence, it would be interesting to investigate the wear and oxidation rates of steels containing different amounts of chromium. Obviously, an area which requires further work is the oxidation occurring during wear. Do oxide films produced under tribological conditions differ from those produced under static conditions? Is the relative proportion of α-Fe_2O_3 and

Fe_3O_4 detected in the high temperature wear experiments similar to that found in static oxidation experiments at the same temperature? It is hoped that these questions and many more will be answered by using techniques such as transmission electron microscope, Auger electron spectroscopy and x-ray photoelectron spectroscopy to study the oxide films produced under static and tribological conditions. Finally, the modified expression for the theoretical wear rate will have to be investigated further, perhaps by using results of wear experiments with other metals which oxidise readily under tribological situations.

APPENDIX 1

Intensity of Powder Diffraction Line

The basic expression for the intensity of a diffraction maximum is given in equation 3.2. There are six factors affecting the relative intensity of the diffraction lines on a powder pattern.

(i) The Structure Factor, F

For a set of planes (hkl) the structure factor F_{hkl} is given by

$$F^2_{hkl} = \left\{\sum_{i=1}^{n} f_i \cos 2\pi(hx_i + ky_i + lz_i)\right\}^2 + \left\{\sum_{i=1}^{n} f_i \sin 2\pi(hx_i + ky_i + lz_i)\right\}^2$$

where n is the number of atoms in the unit cell
x,y,z relate to the atomic positions
and f is the atomic scattering factor

F is, in general, a complex number, and it expresses both the amplitude and phase of the resultant wave. Its absolute value $|F|$ gives the amplitude of the resultant wave in terms of the amplitude of the wave scattered by a single electron, i.e.

$$|F| = \frac{\text{amplitude of the wave scattered by all the atoms of a unit cell}}{\text{amplitude of the wave scattered by one electron}}$$

Thus the intensity of the beam diffracted by all the atoms of the unit cell in a direction predicted by the Bragg law is proportional simply to $|F|^2$, the square of the amplitude of the resultant beam.

The atomic scattering factor f is defined as the ratio of the amplitude of the x-ray wave scattered by an atom compared with the amplitude scattered by an electron. The variation of f with $(\sin\theta)/\lambda$ for oxygen and iron atoms is given in Figure A1. From this figure the value of f corresponding to each diffraction maxima can be found.

When the incident wavelength λ is nearly equal to the wavelength λ_k of the K absorption edge of the scattering element, the atomic scattering factor f should be corrected for anomolous scattering by an amount Δf. Figure A2 shows approximately how Δf varies with λ/λ_k. To a good approximation, the change in Δf is independent of scattering angle and therefore is a constant for all lines on the diffraction pattern. Hence the f versus $(\sin\theta)/\lambda$ curve given in Figure A1 can be corrected for this anomolous change in scattering factor near an absorption edge by adding, algebraically, the same value of Δf to all the ordinates.

(ii) Debye-Waller Temperature Factor, exp(-2M)

Atoms undergo thermal vibration about their mean positions even at the absolute zero of temperature, and the amplitude of this vibration increases as the temperature increases. Thermal agitation decreases the intensity of a diffracted beam because it has the effect of smearing out the latticeplanes. The Debye-Waller temperature factor varies from unity, for maxima with very small Bragg angles, down to about 0.65 for larger Bragg angles, as shown in Figure A3 for iron at 20°C.

(iii) Absorption Factor, A_θ

In all diffraction techniques the incident and diffracted beams passing through the specimens are partially absorbed, so that the diffracted beams are less intense than they would be with a completely

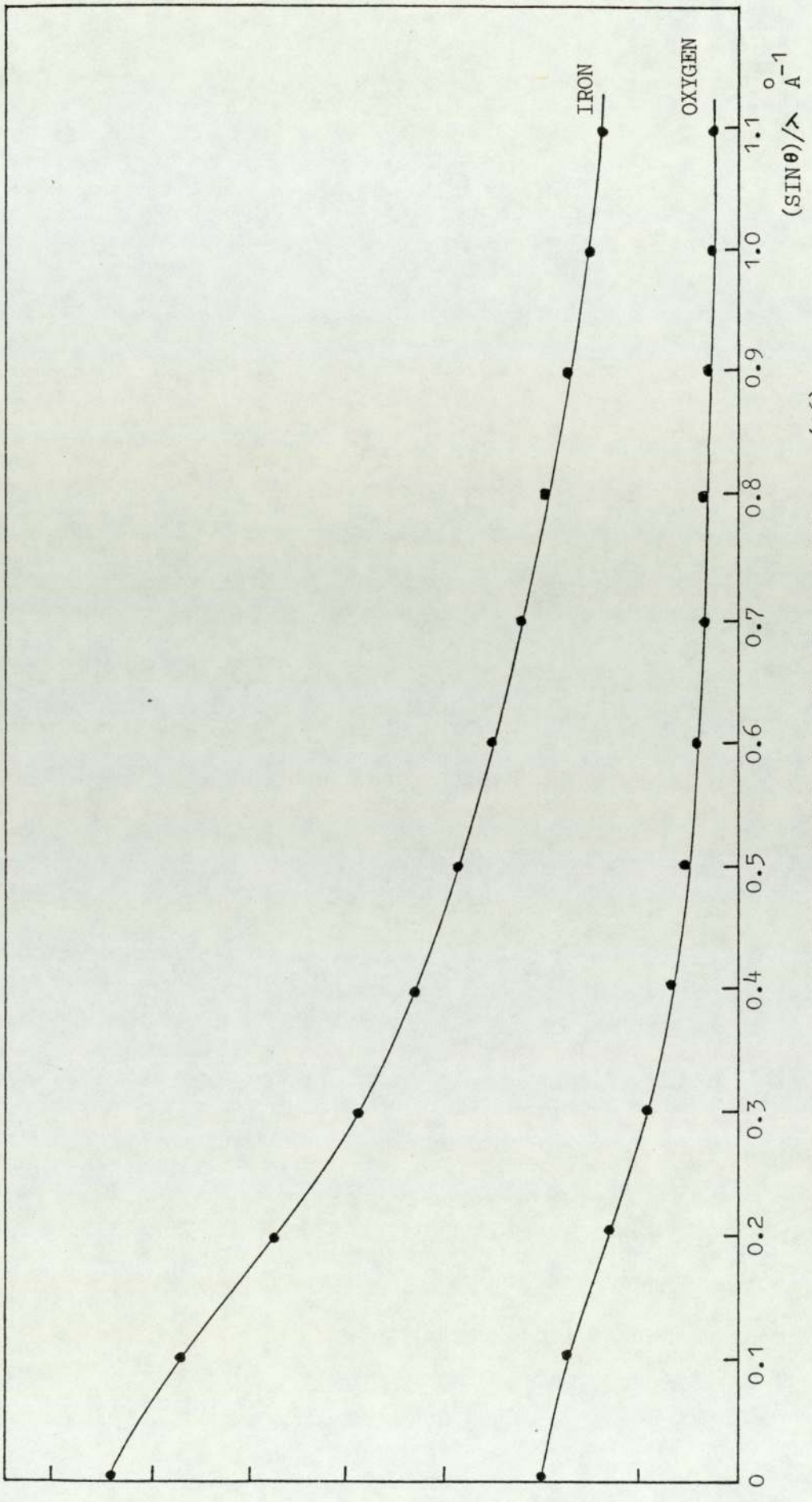

FIGURE A1 Atomic Scattering Factors for Iron and Oxygen (26).

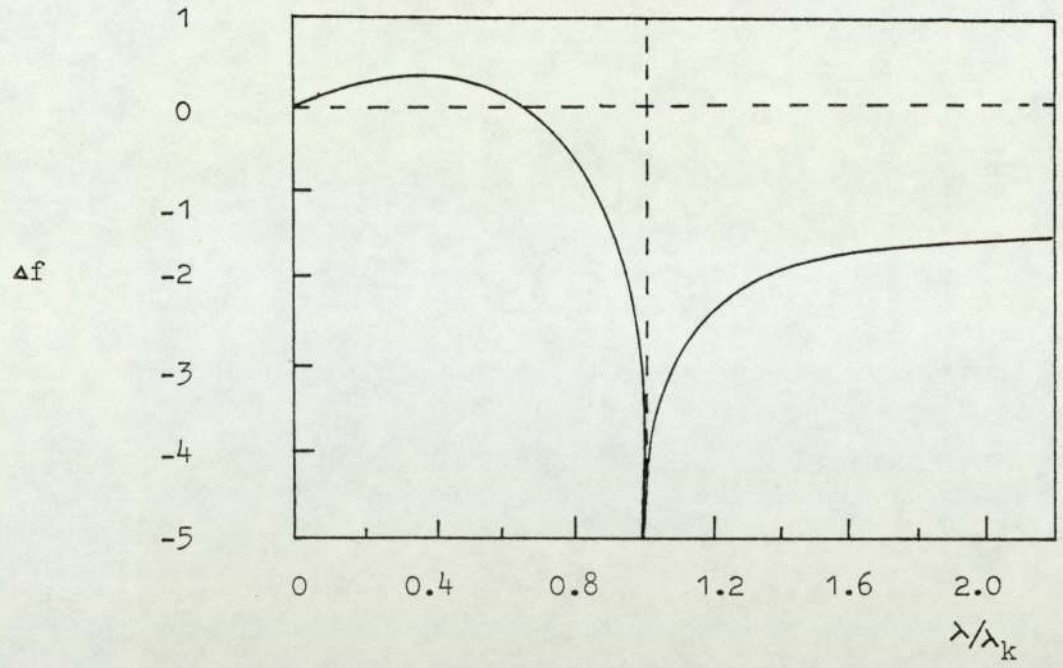

FIGURE A2 Variation of Δf with λ/λ_k (26).

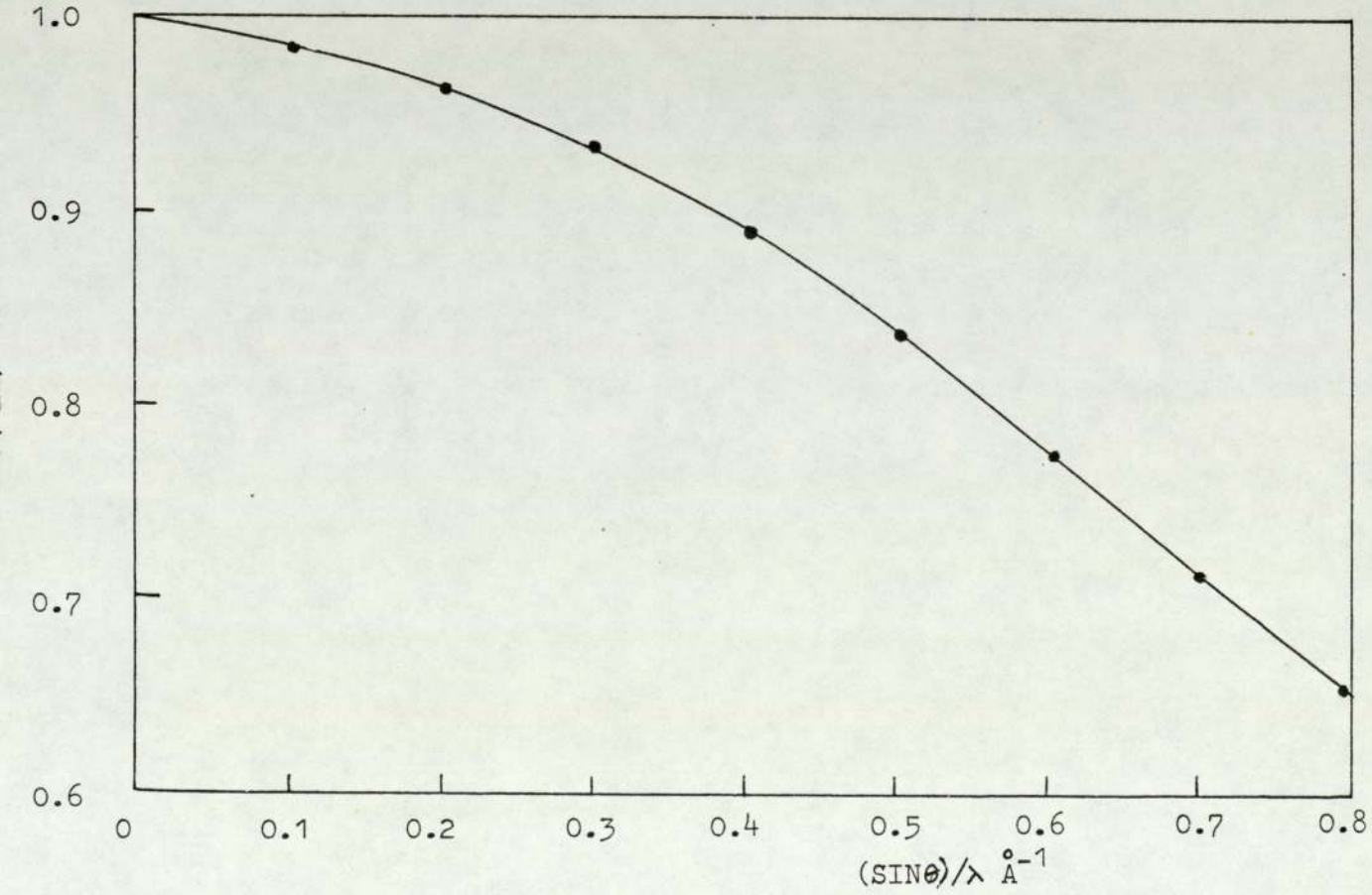

FIGURE A3 Temperature Factor exp(-2M) of Iron at 20°C as a Function of $(\sin\theta)/\lambda$ (26).

nonabsorbing specimen. Bradley (118) gives a method, involving complicated mathematics, which makes it possible to calculate the absorption factor for cylindrical powder samples with an accuracy of at least 1%. Using Bradley's method, the variation of A_θ with Bragg angle for α-Fe_2O_3 is given in Figure A4. It is interesting to note that within the range $20^\circ<\theta<60^\circ$ this curve has the same form as log(I/R) versus θ plots.

(iv) Polarization Factor

For unpolarized incident beam, such as that produced from an x-ray tube, the relative intensity of the diffraction lines is modified by a factor

$$\tfrac{1}{2}\,(\,1 + \cos^2 2\theta\,)$$

This is called the polarization factor.

(v) Lorentz Factor

It is a correction factor which takes into account the fact that a perfect crystallite can reflect a monochromatic beam of x-rays not only under Bragg condition (i.e. $2d_{hkl}\sin\theta = \lambda$) but also with smaller intensities, at angles deviating some seconds of arc from the exact Bragg value. Hence the diffraction lines on an x-ray pattern will have a finite width. That is, the intensity of each reflection is spread over an finite angle. It also takes into account that at angles approaching $2\theta = 90^\circ$ the circumference of the diffracted cone of x-rays is greatest, therefore the integrated intensity per unit length of diffraction line is reduced.

For a cylindrical specimen, the Lorentz factor is

$$\frac{1}{4\sin^2\theta\cos\theta}$$

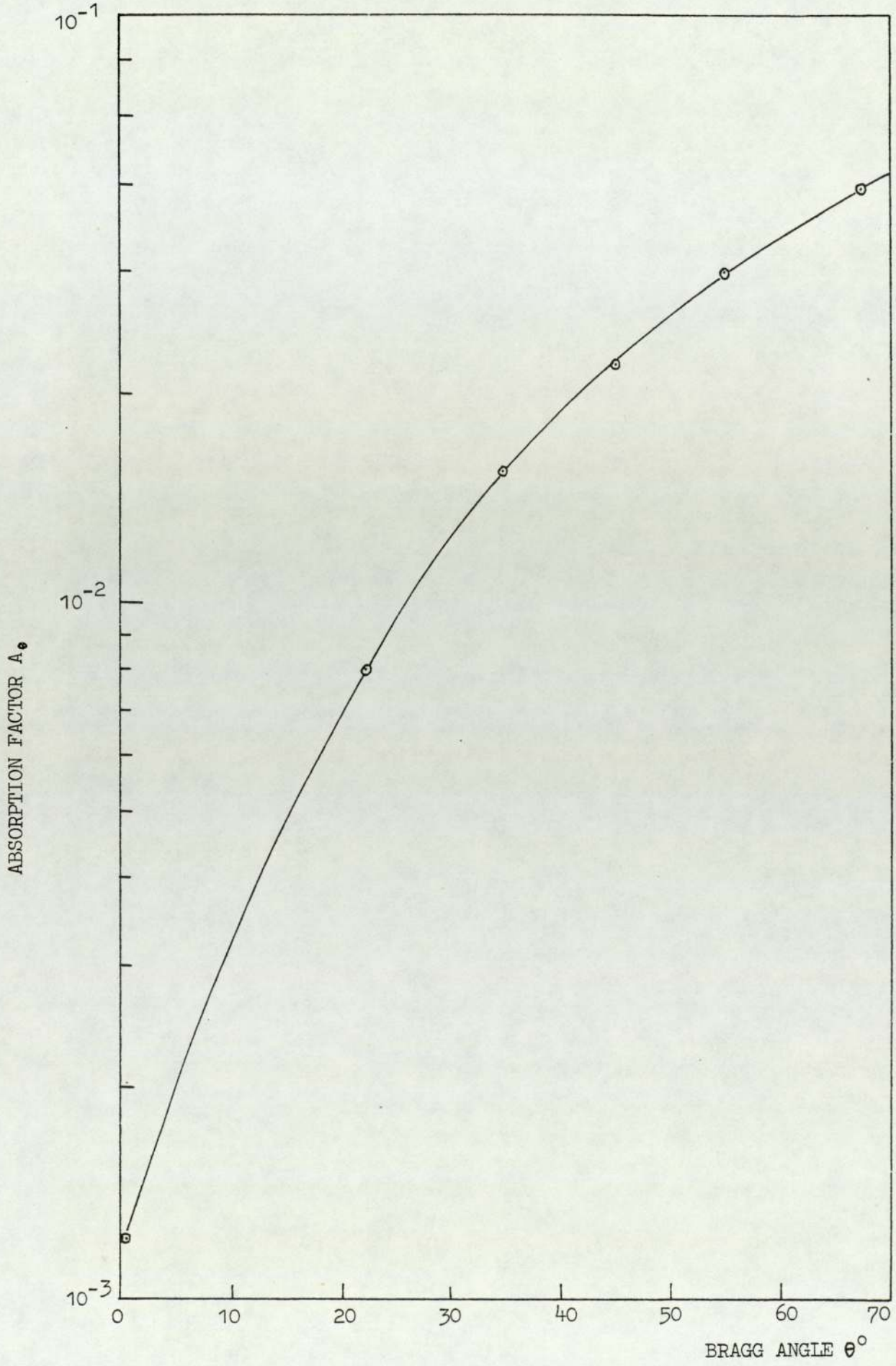

FIGURE A4 Absorption Factor A_θ

The Lorentz and polarization factors are combined to give the combined Lorentz-polarization factor which, with a constant factor of $\frac{1}{8}$ omitted, is given by

$$L_p = \frac{1 + \cos^2 2\theta}{\sin^2\theta\cos\theta}$$

Values of this factor are given in Figure A5 as a function of θ. The overall effect of these geometrical factors is to decrease the intensity of reflections at intermediate angles compared to those in forward or backward directions.

(vi) Multiplicity Factor, m

The multiplicity m for a powder photograph is the number of equivalent planes having the same combination of h, k, l in their Miller indices. The value of m depends on the crystal system. For instance, the cubic planes (100) have a multiplicity of 6, since there are 6 equivalent (100) planes, namely (100), $(\bar{1}00)$, (010), $(0\bar{1}0)$, (001) and $(00\bar{1})$. In a tetragonal crystal, the (100) and (001) planes do not have the same spacing, so that the value of m for {100} planes is reduced to 4 and the value for {001} planes to 2.

Calculation of R Values

The R values may be evaluated for crystalline substances of known structures as follows:-

(a) Index the lines on the x-ray powder photograph of the specimen for each component x and measure the d_{hkl} spacings. Use the x-ray Powder Data files to identify the components.

(b) For a given component, measure the Bragg angle θ for the diffraction maximum to be

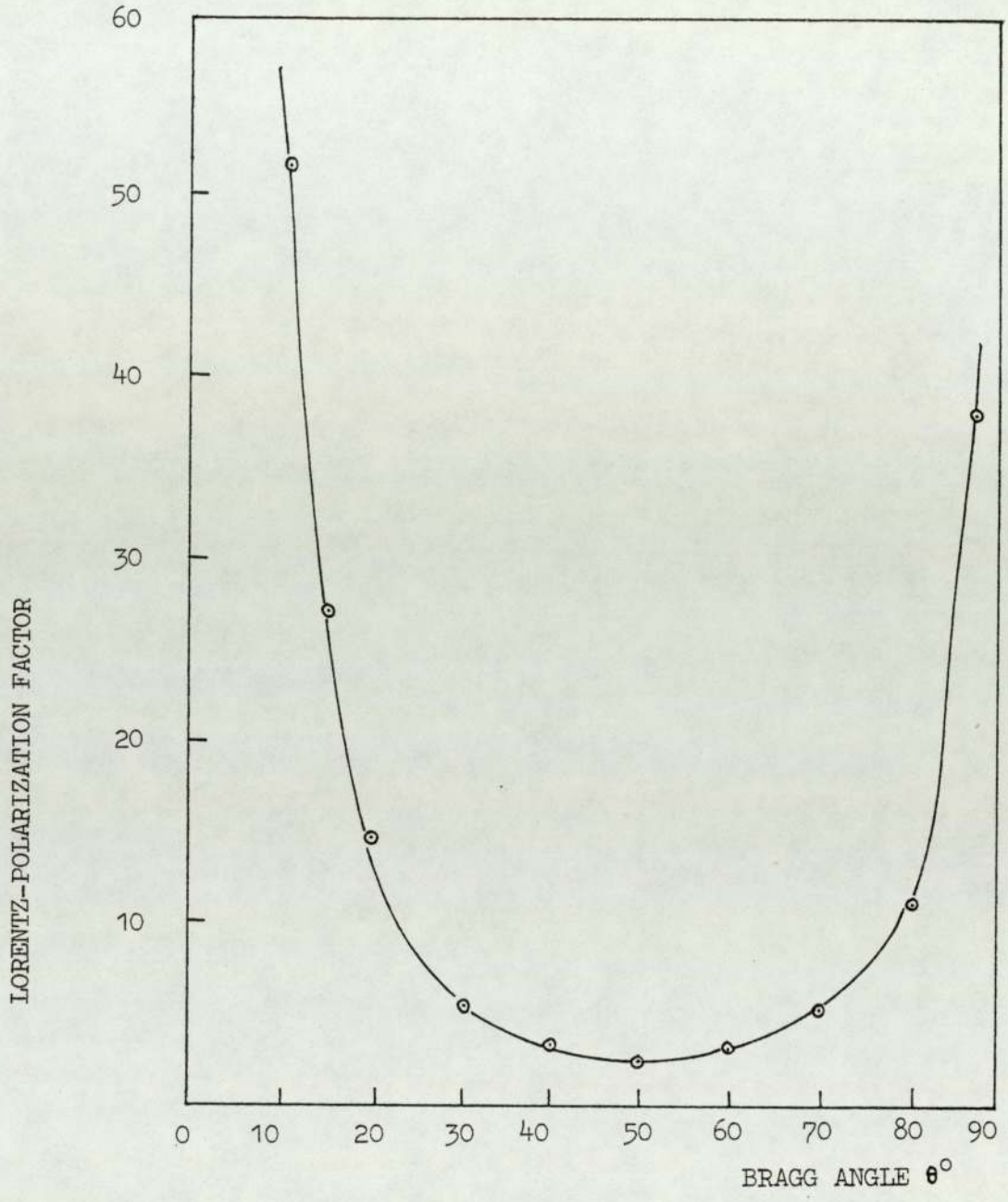

FIGURE A5 Lorentz-polarization Factor (26).

considered and compute $(\sin\theta)/\lambda$, where λ is the wavelength of the radiation used.

(c) Compute the unit cell volume v_x using the equations given in reference (96).

(d) Read off the value for the Lorentz-polarization factor L_p from Figure A5.

(e) Read off the value for the Debye-Waller temperature factor, exp(-2M), from Figure A3.

(f) Use reference (119) to find the atomic coordinates (x_i, y_i, z_i) for the position of the atoms within the unit cell for the component under consideration.

(g) Calculate the structure factor.

(h) Use the tables in reference (96) to find the multiplicity factor m.

(i) Calculate the value of R_x.

Tables A1, A2, A3 and A4 shows the R values calculated by Rowson (103), together with the R values corrected for anomalous scattering factor Δf, for α-Fe, FeO, Fe_3O_4 and α-Fe_2O_3 respectively.

hkl	d_{hkl} (A^o)	R	R (Δf correction)
110	2.0268	196.20	124.40
200	1.4332	28.48	15.95
211	1.1702	68.13	32.98
220	1.0134	35.77	15.48
310	0.9064	192.96	83.65

TABLE A1 R values for α-Fe (Structure BCC, $a_o = 2.8664A^o$).

hkl	d_{hkl} (A^o)	R	R (Δf correction)
111	2.486	46.52	24.86
200	2.153	68.28	48.78
220	1.523	37.41	24.42
311	1.299	17.70	7.22
222	1.243	12.94	7.66
400	1.077	8.24	4.30
331	0.988	18.18	5.98
420	0.963	42.79	20.77

TABLE A2 R values for FeO (Structure NaCl cubic, $a_o = 4.307\ A^o$)

hkl	d_{hkl} (A^o)	R	R (Δf correction)
111	4.850	5.84	4.48
220	2.967	26.62	17.96
311	2.532	58.35	37.79
400	2.099	12.66	10.27
422	1.715	6.47	3.94
511 + 333	1.616	19.56	11.50
440	1.485	26.94	17.45
620	1.328	1.31	0.68
533	1.281	5.95	2.96
444	1.212	2.15	1.51
642	1.122	2.20	1.10
731 + 553	1.093	18.96	8.73
800	1.050	6.00	3.27
822 + 660	0.9896	3.31	1.43
662	0.9632	3.91	0.95
840	0.9386	7.55	4.81

TABLE A3 R values for Fe_3O_4 (Structure spinnel - Al_2MgO_4, a_o = 8.396 A^o).

hkl	d_{hkl} (A^o)	R	R (Δf correction)
110	3.686	13.48	10.18
211	2.703	36.18	23.11
$\bar{1}10$	2.519	28.92	16.85
210	2.208	6.68	6.69
220	1.843	15.10	9.64
321	1.697	17.71	11.72
332 + 12$\bar{1}$	1.601	4.19	2.45
310	1.487	12.76	7.30
211	1.454	11.46	7.28
224	1.351	1.10	0.50
334	1.313	5.01	2.70
2$\bar{2}$0	1.260	3.29	1.45
303 + 114	1.229	1.48	0.40
31$\bar{1}$	1.215	0.33	0.33
134 + 10$\bar{3}$	1.191	2.61	1.44
244	1.165	2.89	1.28
23$\bar{1}$	1.142	4.47	1.89
024	1.104	4.70	2.51
222	1.077	0.71	0.48
235	1.057	6.01	2.61
400	1.040	1.73	0.58
512 + 31$\bar{2}$	0.990	3.38	1.65
141 + 554	0.960	13.27	4.38
511 + 12$\bar{3}$	0.952	8.80	3.55
223 + $\bar{1}$04	0.932	0.48	0.48
154	0.909	20.60	9.64

TABLE A4 R values for α-Fe_2O_3 (Structure Rhombohedral, a_r = 5.4367 A^o, α = 55.2043^o)

APPENDIX 2

```
100 REM      PROGRAM "S.S. ATHWAL"
110 REM    DETERMINATION OF SURFACE
120 REM           PARAMETERS
130 OPEN1,4
140 PRINT#1,"  SURFACE PARAMETERS  "
150 PRINT#1," A=CONTACT RADIUS"
160 PRINT#1,"TC=CONTACT TEMPERATURE"
170 PRINT#1," N=NUMBER OF CONTACTS "
180 PRINT#1,"FP=OXIDE THICKNESS    "
190 CLOSE1
200 READ W,TS,TD,H1,HT,PM
210 CO=750: U=2: RH=5.21E3: F=0.2885
220 OPEN1,4
230 PRINT#1,""
240 PRINT#1,""
250 PRINT#1,"LOAD=";W;"TEMP(TD)=";TD
260 DE=H1/HT
270 I=0
280 DE=INT(DE*1000+.005)/1000
290 PRINT#1,"EXPT. DIVISION OF HEAT=      ",DE
300 CLOSE1
310 IF TS>200 THEN GOTO 330
320 KS=52.5-7.5*TS/365 : GOTO 340
330 KS=56-22.5*TS/620
340 HD=HT-H1
350 B=H1*PM/(KS*W)
360 G1=.8605*HD*PM/(KS*W)
370 G2=.1021*HD*PM/W
380 F1=.8605*HD*PM/W
390 E1=.1021*HD*PM/(KS*W)
400 FOR PP=0.1 TO  5 STEP 0.5
410 FP=PP*1E-6
420 FD=PP*1E-6
430 PRINT"FP=";FP
440 T=TS
450 KM=4.23-1.37E-3*(T+273)
460 KH=8.39-6.63E-3*(T+273)
470 KO=(KM+KH)/2
480 XO=KO/(RH*CO)
490 C=H1*PM*FP/(KO*W)
```

```
490 C=H1*PM*FP/(KO*W)
500 E=E1/XO
510 F=F1*FD/KO
520 G=G1-G2*FD/(XO*KO)
530 BG=B-G
540 X=BG*BG-4*E*(TS+C-TD-F)
550 IF X<=0 GOTO 730
560 X1=SQR(X)
570 A=(X1-BG)/(2*E)
580 TC=TS+C+(B*A)
590 PRINT A,TC
600 IF A<0 THEN GOTO 730
610 IF TC<0 THEN GOTO 730
620 IF TC>1500 THEN GOTO 730
630 IF ABS(TC-T)<=(T/1000)THEN GOTO 650
640 T=TC : GOTO 450
650 TP=HT*PM*A/(KS*W)+HT*PM*FP/(KO*W)
660 AL=.8605-.1021*A/XO
670 TM=AL*HT*PM*A/(KS*W)+AL*HT*PM*FD/(KO*W)
680 DT=TM/(TM+TP)
690 PRINT".........DT=";DT
700 I=I+1 : IF I=1 THEN GOTO 720
710 IF ABS(DT-DE)>ABS(DZ-DE)THENGOTO 730
720 DZ=DT:TZ=TC:AZ=A:EP=FP:XX=XO
730 NEXT
740 IF I=0 THEN GOTO 840
750 N=W/(PM*3.14*AZ*AZ)
760 N=INT(N*10+0.5)/10
770 TZ=INT(TZ*10+0.5)/10
780 DZ=INT(DZ*1000+.005)/1000
790 OPEN1,4
800 PRINT#1,"THEORETICAL DIVISION OF HEAT=",DZ
810 PRINT#1,"N=";N;"FP=";EP;"TC=";TZ;"A=";AZ
820 CLOSE1
830 GOTO 870
840 OPEN1,4
850 PRINT#1," NO SOLUTION FOUND "
860 CLOSE 1
870 GOTO 200
880 END
890 DATA 29.4,153,71,5.71,40.2,2.49E9
900 DATA 39.2,140,80,4.14,56.42,2.49E9
910 DATA 58.9,158,109,4.85,72.22,2.48E9
920 DATA 78.5,192,121,5.91,94,2.48E9
930 DATA 98.1,226,136,6.34,89.1,2.5E9
940 DATA 117.7,311,159,12.8,109.16,2.46E9
```

REFERENCES

1. ARCHARD J.F., Contact and rubbing of flat surfaces, *J. Appl. Phys.*, 24 (1953) 981.

2. ARCHARD J.F. and HIRST W., The wear of metals under unlubricated conditions, *Proc. Roy. Soc.*, A236 (1956) 397.

3. KRAGELSKII I.V., *Friction and Wear*, Butterworths (1965), Washington D.C.

4. RIGNEY D.A. and GLAESER W.A., *Source Book on Wear Control Technology*, ASM Engineering Bookshelf (1978), Ohio.

5. BURWELL J.T., Survey of possible wear mechanisms, *Wear*, (1957) 119.

6. BOWDEN F.P. and TABOR D., *The Friction and Lubrication of Solids*, Clarendon Press, Oxford, Part I (1954), Part II (1964).

7. RABINOWICZ E., *Friction and Wear of Materials*, John Wiley and Sons (1965), New York.

8. RABINOWICZ E. and TABOR D., Metallic transfer between sliding metals, *Proc. Roy. Soc.* (London), A208 (1951), 455.

9. QUINN T.F.J., The role of oxidation in the mild wear of steel, *Brit. J. Appl. Phys.*, 13 (1962) 33.

10. TAO F.F., A study of oxidation phenomena in corrosive wear, *ASLE Trans.*, 12 (1969) 97.

11. AVIENT B.W.E., GODDARD J. and WILMAN M., An experimental study of friction and wear during abrasion of metal, *Proc. Roy. Soc.*, A258 (1960) 159.

12. RABINOWICZ E., DUNN L.A. and RUSSELL P.G., A study of abrasive wear under 3-body conditions, *Wear*, 4 (1961) 345.

13. HALLING J., *Principles of Tribology*, Macmillan Press Limited (1975).

14. SARKAR A.D., *Friction and Wear*, Academic Press Inc. (London) Limited (1980).

15. BARNETT R.S., Fretting and fretting corrosion, *Lubrication*, 41 (1955) 85.

16. WRIGHT K.H.R., An investigation of fretting corrosion, *Proc. Instn. Mechn. Engrs.* 1B (1952/53) 556.

17. HURRICKS P.L., The fretting wear of mild steel from 200°C to 500°C, *Wear*, 30 (1974) 189.

18. KAYABA T. and IWABUCHI A., The fretting wear of 0.45% carbon steeel and austenitic stainless steel from 20°C up to 650°C in air, *Proc. ASME Conf. on Wear of Materials* (1981) p229, San Francisco,U.S.A.

19. FINK M., Wear oxidation - a new component of wear, *Trans. Am. Soc. Steel Treating*, 18 (1930) 204.

20. ROSENBERG S.J. and JORDAN L., *J. Res. Nat. Bur. Stand.*, Washington, 13 (1934) 267.

21. MAILANDER R. and DIES K., Contribution to the study of wear phenomena, *Archiv. f. Eisenhuttenuesen*, 16 (1943) 385.

22. DIES K., Processes taking place during wear in conditions of pure sliding and dry friction, *Reibung und Versheiss*, No. 7DI Verlag (Berlin), (1939).

23. SIEBEL E. and KOBITZSCH R., *Verschleisscheinungen bei gleitender trocker Reibung*, VKI Verlag (Berlin) (1941).

24. HOLM R., *Electric Contacts Handbook*, Springer-Verlag (1958), Berlin.

25. BURWELL J.T. and STRANG C.D., On the empirical law of adhesive wear, *J. Appl. Phys.*, 23 (1952) 18.

26. RABINOWICZ E. A quantitative study of the wear process, *Proc. Phys. Soc.*, B66 (1953) 229.

27. GREEN A.P., Friction between unlubricated metals: A theoretical analysis of the junction model, *Proc. Roy. Soc.*, A228 (1955) 181.

28. GREENWOOD J.A. and TABOR D., Deformation properties of friction junctions, *Proc. Phys. Soc.* (London), B68 (1955) 609.

29. KERRIDGE M., Metal transfer and the wear process, *Proc. Phys. Soc.* (London) B68 (1955) 400.

30. KERRIDGE M. and LANCASTER J.K., The stages in a process of severe metallic wear, *Proc. Roy. Soc.* (London), A236 (1956) 250.

31. ARCHARD J.F. and HIRST W., The wear of metals, *Sci. Lub.*, November (1959).

32. HIRST W. and LANCASTER J.K., Surface film formation and metallic wear, *J. Appl. Phys.*, 27 (1956) 1057.

33. MOORE A.J.W. and TEGART W.J.McG., Effect of included oxide films on the structure of the Beilby layer, *Proc. Roy. Soc.* A212 (1952) 458.

34. LANCASTER J.K., The influence of temperature upon metallic wear, *Proc. Phys. Soc.* (London), B70 (1957) 112.

35. HIRST W. and LANCASTER J.K., The influence of speed on metallic wear, *Proc. Roy. Soc.* (London), A259 (1960) 288.

36. LANCASTER J.K., The formation of surface films and the transition between mild and severe wear, *Proc. Roy. Soc.* (London), A273 (1963) 466.

37. ARCHARD J.F. and HIRST W., An examination of a mild wear process, *Proc. Roy. Soc.* (London), A238 (1957) 315.

38. WELSH N.C., Frictional heating and its influence on wear of steels, *J. Appl. Phys.*, 28(9) (1957) 960.

39. WELSH N.C., The dry wear of steels, Parts I and II, *Philos. Trans. Roy. Soc.* (London), A257 (1965) 31.

40. EARLES S.W.E. and HAYLER M.G., Wear characteristics of some metals in relation to surface temperature, *Wear*, 20 (1972) 51.

41. EARLES S.W.E. and POWELL D.G., Surface temperature and its relation to periodic changes in sliding condition between unlubricated steel surfaces, *Trans. ASLE*, 11 (1968) 109.

42. POWELL D.G. and EARLES S.W.E., Wear of unlubricated steel surfaces in sliding contact, *Trans. ASLE*, 11 (1968) 101.

43. EYRE T.S. and MAYNARD D., Surface aspects of unlubricated metal-to-metal wear, *Wear*, 18 (1971) 301.

44. QUINN T.F.J. The effect of "hot-spot" temperatures on the unlubricated wear of steel, *Trans. ASLE*, 10 (1967) 158.

45. QUINN T.F.J., Dry wear of steels as revealed by electron microscopy and x-ray diffraction, *Proc. Inst. Mech. Engrs.* 182 (3N) (1967-68) 203.

46. QUINN T.F.J., An experimental study of the thermal aspects of sliding contacts and their relation to the unlubricated wear of steel, *Proc. Inst. Mech. Engrs.* 183 (3P) (1968-69) 129.

47. QUINN T.F.J., Oxidational wear, *Wear*, 18 (1971) 413.

48. SUH N.P., The delamination theory of wear, *Wear*, 25 (1973) 111.

49. SUH N.P. et al., Further investigation of the delamination theory of wear, *Trans. ASME*, F96, (1974) 631.

50. JAHANMIR S., SUH N.P. and ABRAHAMSON E.P., Microscopic observation of the wear sheet formation by delamination wear, *Wear*, 28 (1974) 235.

51. CHILDS T.H.C., The sliding wear mechanisms of metals - mainly steels, *Tribology International*, 13 (1980) 285.

52. WHITEHEAD J.R., Surface deformation and fracture of metals at light loads, *Proc. Roy. Soc.*, A201 (1950) 109.

53. WILSON R.W., Influence of oxide films on metallic friction, *Proc. Roy. Soc.* A212 (1952) 450.

54. WILSON R.W., The contact resistance and mechanical properties of surface films on metals, *Proc. Roy. Soc.*, B68, (1955) 625.

55. COCKS M., The effect of compressive and shearing forces on the surface films present in metallic contacts, *Proc. Roy. Soc.*, B67 (1954) 238.

56. COCKS M., Role of atmospheric oxidation in high speed sliding phenomena - I, *J. Appl. Phys.*, 28(8) (1957) 835.

57. COCKS M., The role atmospheric oxidation in high speed sliding phenomena - II, *Trans. ASLE*, 1 (1958) 101.

58. MØLGAARD J., A discussion of oxidation, oxide thickness and oxide transfer in wear, *Wear*, 40 (1976) 277.

59. STOTT F.H., LIN D.S. and WOOD G.C., The structure and mechanism of formation of the 'glaze' oxide layers produced on Nickel-based alloys during wear at high temperatures, *Corrosion Science*, 13 (1973) 449.

60. STOTT F.H. and WOOD G.C., The influence of oxides on the friction and wear of alloys, *Tribology International*, 11 (1978) 211.

61. GOOD J.N. and GODFREY D., Changes found on run-in and scuffed surfaces of steel, chrome plate and caste iron, NASA Techn. Note 1432, (1947).

62. BISSON E.F., JOHNSON R.L. and SWIKERT M.A., Friction, wear and surface damage of metals as affected by solid surface films, NASA Techn. Note 3444, (1955).

63. CLARK W.T., PRITCHARD C. and MIDGLEY J.W., Mild wear of unlubricated hard steels in air and carbon dioxide, *Proc. Instn. Mechn. Engrs.*, 182 (3N) (1967) 97.

64. CORNELIUS D.F. and ROBERTS W.H., Friction and wear of metals in gases up to 600°C, *Trans. ASLE*, 4(1) (1961) 20.

65. QUINN T.F.J., SULLIVAN J.L. and ROWSON D.M., New developments in the oxidational theory of the mild wear of metals, *Proc. ASME Conf. on Wear*, Dearbon, Michigan, April (1979).

66. MØLGAARD J., The activation energy of oxidation in wear, *Wear*, 41 (1977) 263.

67. KUBASCHEWSKI O. and HOPKINS B.E., *Oxidation of metals and alloys*, Butterworths, London, 1962.

68. CAPLAN D. and COHEN M., The effect of cold work on the oxidation of iron from 100°C to 650°C, *Corr. Sci.*, 6 (1966) 321.

69. CARTER R.E. and RICHARDSON F.D., An examination of the decrease of surface-activity method of measuring self diffusion coefficients in wustite, *J. Metals*, 6 (1954) 1244.

70. YOSHIMOTO G. and TSUKIZOE T., On the mechanism of wear between metal surfaces, *Wear*, (1957-58) 472.

71. ARCHARD J.F., A review of wear studies, NASA Symposium in Interdisciplinary Approach to Friction and Wear, Paper 5, (1967) 267.

72. EARLES S.W.E. and POWELL D.G., Variation in friction and wear between unlubricated steel surfaces, *Proc. Instn. Mechn. Engrs.*, 181 (pt 30) (1966-67) 171.

73. EARLES S.W.E. and POWELL D.G., Stability of self-generated oxide films on unlubricated ENIA steel surface, *Proc. Instn. Mechn. Engrs.* 182 (3N) (1968) 167.

74. TENWICK N. and EARLES S.W.E., A simplified theory of oxidative wear, *Wear*, 18 (1971) 381.

75. ARONOV. V., Kinetic characteristics of the transformation and failure of the surface layers of metal under dry friction, *Wear*, 41 (1977) 205.

76. BOWDEN F.P. and RIDLER K.E.W., A note on the surface temperature of sliding metals, *Proc. Roy. Soc.*, A151 (1936) 431.

77. FUREY M.J., Surface temperatures in sliding contact, *Trans. ASLE*, 1 (1964) 133.

78. BLOK H. Determinations of surface temperatures under extreme pressure lubricating conditions, *Proc. World Congr. Petrol.* (Paris), 2 (1937) 471.

79. BLOK H. Theoretical study of temperature rise at surfaces of actual contact under oiliness lubricating conditions, *Inst. Mechn. Engrs., (Proc. General Discussion on Lubrication and Lubricants)*, 2 (1937) 222.

80. JAEGER J.C., Moving sources of heat and the temperature at sliding contacts, *Proc. Roy. Soc.* (New South Wales), 56 (1942) 203.

81. HOLM R., Calculation of the temperature development in a contact heated in the contact surface, and the application to the problem of the temperature rise in a sliding contact, *J. Appl. Phys.* 19 (1948) 361.

82. ARCHARD J.F., The temperature of rubbing surfaces, *Wear*, 2 (1959) 438.

83. BARBER J.R., Distribution of heat between sliding surfaces, *J. Inst. Mechn. Engng. Sci.*, 9(5) (1967) 351.

84. EARLES S.W.E., HAYLER M.G. and POWELL D.G., A comparison of surface temperature theories and experimental results for high speed dry sliding, *Trans. ASLE*, 14 (1971) 135.

85. POWELL D.G. and EARLES S.W.E., An assessment of surface temperature predictions in the high speed sliding of unlubricated SAE 1113 steel surfaces, *Trans. ASLE*, 15(2) (1972) 103.

86. GROSBERG P., McNAMARA A.B. and MØLGAARD J., The performance of ring travellers, *J. Text. Inst.*, 56 (1965) T24.

87. GROSBERG P. and MØLGAARD J., Aspects of the wear of spinning travellers: The division of heat at rubbing surfaces, *Proc. Instn. Mechn. Engrs.*, 181(3L) (1966-67) 16.

88. QUINN T.F.J., The division of heat and surface temperature at sliding steel interfaces and their relation to oxidational wear, *Trans. ASLE*, 21 (1978) 78.

89. WILSON J.E., STOTT F.H. and WOOD G.C., The development of wear-protective oxides and their influence on sliding friction, *Proc. Roy. Soc.* (London), A369 (1980) 557.

90. RIGNEY D.A. and HIRST J.P., Plastic deformation and sliding friction of metals, *Wear*, 53 (1979) 345.

91. TABOR D., Friction - The present state of our understanding, *J. Lubrc. Techn.*, 103 (1981) 169.

92. QUINN T.F.J., The role of oxide films in the friction and wear behaviour of metals, Paper presented at Conference on Microscopic Aspects of Adhesion and Lubrication, Paris, 14-18th Sept. (1981).

93. DUNCKLEY P.M. and QUINN T.F.J., The effect of elevated temperatures and speed upon the wear of mild steel, *Trans. ASLE*, 19(3) (1978) 221.

94. ROWSON D.M. and QUINN T.F.J., Frictional heating and the oxidational theory of wear, *J.Phys. D: Appl. Phys.*, 13 (1980) 209.

95. SMITHELLS C.J., *Metals Reference Handbook, Vol. 3*, 4th edition, Butterworths (1967).

96. CULLITY B.D., *Elements of X-ray Diffraction*, Addison-Wesley Co., (1959), London.

97. QUINN T.F.J., *Advances in X-ray Analysis, Vol. 10*, p310-327, Plenum Press, (1967), New York.

98. DAVIS L.E., MACDONALD N.C., PALMBERG P.W., RIACH G.E. and WEBER R.E., *Handbook of Electron Spectroscopy*, Physical Electronics Industries, Minnesota (1976).

99. KLUG H.P. and ALEXANDER L.E., *X-ray Diffraction Procedures*, Wiley (1954) New York.

100. AVERBACH B.L. and COHEN M., X-ray determination of retained austenite by integrated intensities, *Metals Technology*, T.P. 2342 (1948).

101. QUINN T.F.J. and WOOLLEY J.L. The unlubricated wear of 3% Cr - ½% Mo steel, *Lub. Eng.*, 26 (1970) 312.

102. QUINN T.F.J., BAIG A.R., HOGARTH C.A. and MÜLLER H., Transitions in the friction coefficients, the wear rates, and the composition of the wear debris produced in the unlubricated sliding of chromium steels, *Trans. ASLE*, 16(4) (1972) 239.

103. ROWSON D.M., Private communication, University of Aston, Birmingham.

104. QUINN T.F.J., *The Application of Modern Physical Techniques to Tribology*, Newnes-Butterworths (1971), London.

105. QUINN T.F.J., ROWSON D.M. and SULLIVAN J.L. Application of the oxidational theory of mild wear to the sliding wear of low alloy steel, *Wear*, 65 (1980) 1.

106. MØLGAARD J. and SMELTZER W.W., Thermal conductivity of magnetite and hematite, *J. Appl. Phys.*, 42(9) (1971) 3644.

107. Chemical Rubber Co., *Handbook of Chemistry and Physics*, 44th edition.

108. THOMAS T.R. and PROBERT S.D., Thermal contact of solids, *Chem. Process Eng.*, 47 (1966) 51.

109. DIAMANT R.M.E., *Insulation Deskbook*, Heating and Ventilating Publications Limited (1977), Croydon.

110. LANG P.M., Calculating heat transfer across small gas-filled gaps, *Nucleonics*, 20 (1962) 62.

111. ARCHARD J.F., Single contacts and multiple encounters, *J. Appl. Phys.*, 32 (1961) 1420.

112. SULLIVAN J.L., QUINN T.F.J. and ROWSON D.M., Developments in the oxidational theory of mild wear, *Tribology International*, 13 (1980) 153.

113. DUNCKLEY P.M., Ph.D. Thesis, (1977), University of Aston, Birmingham.

114. ALLEN G.C. et al., X-ray photoelectron spectroscopy of iron-oxygen systems, *J. of the Chemical Soc.* (Dalton), Part II (1974) 1525.

115. WILSON F. and EYRE T.S., Metallographic aspects of wear, *Metals Mater.*, 3(3) (1969) 86.

116. EYRE T.S. and BAXTER A., The formation of white layers at rubbing surfaces, *Tribology*, 5 (1972) 256.

117. KAWAMOTO M. and OKABAYASHI K., Study of dry sliding wear of cast iron as a function of surface temperature, *Wear*, 58 (1980) 59.

118. BRADLEY A.J., The absorption factor for the powder and rotating-crystal methods of x-ray crystal analysis, *Proc. Phys. Soc.* (London), 47 (1935) 879.

119. WYCKOFF R.W.G., *Crystal Structures (Vols. 1-5)*, Interscience Publishers (1963), New York.